Realizing Enhanced Toughness in Block Copolymer Modified Brittle Plastics

A Dissertation
SUBMITTED TO THE FACULTY OF
UNIVERSITY OF MINNESOTA
BY

Tuoqi Li

IN PARTIAL FULFILLMENT OF THE REQUIREMENTS
FOR THE DEGREE OF
DOCTOR OF PHILOSOPHY

Frank S. Bates and Lorraine F. Francis

August, 2016

Acknowledgements

Il y avait certainement quelqu'un que tu avais dans ta jeunesse,

jamais tu ne lui oublierai.

On August 13, 2011, it was the beautiful summer sunshine welcoming me when I stepped out from the Minneapolis airport. Exhausted from the long flight but overwhelmingly exited as I was at that time, I expected to have a new chapter of my life in a completely strange environment, barely thinking of the challenges and hardships waiting ahead. Sometimes, we can select which route to go, but life itself sets all the ups and downs on the way, leaving no more choices for us but saying "C'est la vie." Now, looking back at my five-year pathway, I feel like being blessed, because it is not only what you experienced but also who you encountered that shape you, both physically and mentally. Thanks to all of you, who enriched my Minnesota memories with warmth like sunshine besides the bitter coldness.

"He who teaches me for one day may be considered my father-figure for life." Firstly, I would like to extend my gratitude to my advisors: Prof. Frank Bates and Prof. Lorraine Francis, who act as the "father" and "mother" during this great period of intellectual and personal growth for me. Frank, your passion and enthusiasm can cheer me up like Beethoven's energetic symphony; Lorraine, your patience and serenity can calm me down like Chopin's comforting nocturne. You have been a tremendous source of inspiration and encouragement and your efforts guide me to the place where I am.

"Live and learn." Secondly, I really want to thank Prof. Chris Macosko, who influenced my life on multiple faces. Chris, partially because of you, I decided to join University of Minnesota five years ago. As a world-famous and respectable scholar, you generously offered me lots of help, suggestions and opportunities on my research and job hunting, although you are not my advisor. As my mentor during Bible study, you kindly shared your stories and thoughts, shaping my minds at a profound level. There is always more to learn from you. I will try to live gratefully and devoutly as you do.

"We are a team. Whatever you lack, I got you." Thirdly, it is a great fortune for me to have so many fantastic and helpful people around during the past years. I want to sincerely acknowledge my collaborators on research projects: Dr. Feng Zuo, Dr. Michael Heinzer, Dr. Jiuyang Zhang, Dr. Erica Redline, Debbie Schneiderman, Alex Mannion and Siyao He. You are amazing. I also would like to thank Dr. Athanasios Touris, Dr. Karen Haman and Dr. Jie Lu for teaching me polymer synthesis, Dr. Carmelo Declet-Pérez, Dr. Chris Thurber and Dr. Sangwoo Lee for inspiring suggestions and hands-on help during my experiments, Dr. Kyungtae Kim, Dr. Tim Gillard and Matt Irwin for the help during SAXS experiments at Argonne, Dr. David Giles, Wieslaw Suszynski and Fang Zhou for the training and help on many facilities, Prof. Marc Hillmyer, Prof. Bill Gerberich and Prof. Andres Stein for useful suggestions to my projects, and all current members and alumni in my two wonderful research groups. Whatever I lack, those brilliant persons can always get me, making my school life much easier. Thank you all!

"Friendship marks a life even more deeply than love." Pour Boxin and Yunlong, vous êtes mes surprises fantastiques, des amis qui m'acceptent comme je suis. Toutes les

fautes futiles, ne dont plus que mes souvenirs à vie. Thank all of you for blending various colors into my plain life: Yutao, Andrew & Jincheng, Weihua, Lian, Liangliang, Yiming, Jun & Yuyang, En & Hongyun, Tianqi, Yan, and Han. Thank you for your accompanying during my Bible study: Bo, Mengen and Yuezhou. Thank you for your encouragement and great help during my job hunting: Jing, Ankit, Jingwen and Sipei. Thank you for our everlasting friendship: Zichao, Huize, Xiangyang and Zixuan!

"I do not try to be better than anyone else. I only try to be better than myself." Lastly but most importantly, I need to thank one person, myself, for trekking through the jungle of self-denial and depression, not being crumpled nor giving up. I finally understand, there is a doomed reason for trudging our selected route in the manner that we did; I finally believe, there is also a destined direction for our path to go. I should always keep one point in mind, to be true to myself and to progress every day.

"I suppose in the end, the whole of life becomes an act of letting go, but what always hurts the most is not taking a moment to say goodbye." So, at this special moment for myself, sincerely, I just want to say,

Merci, merci pour vos présences dans ma vie!

Dedication

Pour mes parents et moi-même

Abstract

The great commercial importance of several brittle plastics continuously drives research efforts to be devoted to fabricating well defined structures in these materials for effectively toughening them. Amphiphilic block copolymers can be appropriately designed to generate nanometer scaled structures in a brittle plastic matrix at relatively low loadings (< 5% by weight). The resultant nanostructured plastics exhibit significant toughness enhancement without sacrificing other desirable properties such as transparency, stiffness and use temperature. The goal of this dissertation is to understand the nanostructure formation of block copolymers and the consequent toughening effect under various conditions.

In this work we designed different types of block copolymer modifiers in concert with several commercially important brittle plastics, including epoxy thermosets and poly(lactide) (PLA) thermoplastics. The block copolymer toughening strategy was first established in bulk epoxies as well as in epoxy coatings through a model system study with the Jeffamine resin. Two distinct types of diblock copolymers formed spherical micelles in cured bulk epoxies and 15 μm thick coatings, but the process of solvent-casting affected the micelle size and distribution in the coating. The toughness enhancement observed in bulk epoxies (up to 5-fold increase in the critical strain energy release rate G_{Ic}) successfully translated to coatings, as evidenced by the over 40% increase in the coating abrasive wear resistance with only 5 wt.% of modifiers. Transmission electron microscopy (TEM) revealed that similar toughening mechanisms as those in bulk epoxies (micelle cavitation and matrix shear yielding) still held in thin

coatings. Moreover, the hardness, modulus, transparency and glass transition temperature (T_g) of modified coatings were not appreciably affected compared to unmodified ones.

Based on this model system study, we proceeded to investigate the commercially viable Cardolite resin system that is more complex thermodynamically but industrially relevant. A series of poly(ethylene oxide)-*b*-poly(butylene oxide) (PEO-PBO) diblock copolymers were synthesized at fixed composition (31% PEO by volume) and varying molecular weight expanding on a commercial product under the tradename Fortegra™ 100. Direct application of this product resulted in little improvement of the poor fracture toughness of the cured material. Modification of the resin formulation and curing protocol led to the development of well-defined spherical and branched wormlike micelles in cured resins. Thermodynamic interactions and the curing reaction together controlled the micelle formation as evidenced by small angle x-ray scattering (SAXS) measurements. A 9-fold increase in G_{Ic} over the neat bulk epoxy, and an over 30% improvement in the coating abrasive wear resistance over the unmodified coating were achieved at 5 wt.% loading of wormlike micelles.

We then took one step further to explore the toughening efficacy of block copolymer micelles in hybrid composite systems in the presence of a second type of modifier, rigid graphene fillers with amine-functionalization. Both types of modifiers were well dispersed in cured epoxies with no observable interactions under TEM. The crosslink density of the epoxy network strongly affected the toughening effect. In the matrix with the lowest crosslink density, the combination of micelles and graphene drastically enhanced the G_{Ic} value to 19 times that of the neat material with no reduction

in the elastic modulus and T_g. Additionally, hybrid ternary composites exhibited a synergistic toughening effect, revealing some positive mutual interference to the toughening mechanisms noted for micelles and graphene particles.

Lastly, we extended the block copolymer toughening strategy to the PLA thermoplastic matrix. A low molar mass PEO-PBO diblock copolymer was uniformly dispersed as short cylindrical micelles in a commercial high molecular weight glassy PLLA plastic. This structure formation resulted from the negative Flory-Huggins interaction parameter (χ) between PEO and PLLA. Those micelles could effectively toughen the matrix through concurrent cavitation, crazing and shear yielding. At only 5 wt.% of loading, micelles led to a greater than 10-fold increase in the tensile toughness and notched Izod impact strength over the neat PLLA in the glassy state. This toughening effect was retained in plastic films prepared with modified blends via a film blowing process.

Table of Contents

List of Tables

List of Figures

Chapter 1

Introduction

1.1 Nanostructured plastics: general remarks

The few commodity plastics that occupy the majority of market share (e.g. polyethylene, polypropylene, polystyrene and polyvinylchloride) are produced at millions of metric tons annually, but they are under growing pressure to offer tailored property profiles for various service conditions.[1] Because of it, the utilization of blended polymeric materials begins dominate in many applications due to their unique combinations of properties difficult or even impossible to achieve otherwise.[2]

In the portfolio of properties, toughness is a crucial one and germane to almost every class of materials that find utility in society, including synthetic plastics. Toughness characterizes the material capability to resist crack propagation by absorbing and dissipating energy during plastic deformation prior to ultimate fracture.[3] It has been a longstanding issue related with intrinsically brittle plastics (e.g. polystyrene or epoxy resins) that have low crack initiation energy (low un-notched toughness) and low crack

propagation energy (low notched toughness).[4, 5] Development of new polymers with intrinsic ductility can lead to tough plastics, but it is often not economically justified. The other option takes advantage of polymer blends to toughen those brittle plastics. This toughening strategy relies on the assumption that the deformation mechanisms operative in a particular polymer would stimulate the response of the blend to applied loading to induce an extensive plastic deformation and therefore large energy absorption and dissipation.[6] In polymer blends, there are three important structural components: continuous phase, dispersed phase, and interfaces. These determine the microstructure and stress transfer within the blend. They can strongly affect the toughness via various morphological as well as micromechanical parameters.

Morphological parameters have a critical impact on toughness. Unlike homopolymers, polymer blends are endowed with structural heterogeneity, which permits the formation of some specific morphology that can realize toughening (e.g. nanoscale particles dispersed in the matrix) by allowing local yielding events and deformation processes to simultaneously take place in a large volume of the loaded material.[7]

The key to obtaining inexpensive and tough plastics often lies in designing blends precisely structured at the appropriate scale from existing polymers. The preferable structural scale is the nanometer regime, because unless the refractive index of dispersed phase matches that of the continuous phase, toughened plastics with micron-size dispersed phases lose optical transparency. However, technical difficulties arise during the fabrication of nanostructures. On one hand, dispersing a homopolymer A in an immiscible homopolymer B usually requires strong shearing (e.g. intense mechanical

stirring) to produce micrometer-sized features through droplet-breakup. Generating sub-micron finer dispersions is challenging.[8, 9] On the other hand, when the polymer B is a thermosetting polymer, the formation of nanostructures in this matrix polymer seems to be promising. Because prior to the condensation of the precursors, those small molecules act as a solvent that tends to more effectively mix with the homopolymer A compared to the case of mixing two long-chain polymers. Unfortunately, the growing network of polymer B is very likely to expel any kinds of inclusions initially solubilized in the precursor mixture.[10, 11] Consequently, the coalescence of fine dispersions leads to large domains again in the final thermosetting plastics.

The utilization of block copolymers as the dispersed phase can alleviate those aforementioned problems and help to fabricate transparent and super-tough nanostructured plastics. In bulk block copolymers, the local segregation between different blocks can yield molecular-scale domains of nanometer size.[12, 13] When mixed with other brittle plastics, block copolymers are capable of self-assembling into various equilibrium or even non-equilibrium morphologies at different length scales (nanometer to micrometer) in the final polymer blend. The process of microstructure formation as well as the toughening efficacy of dispersed block copolymer phase strongly depends on the chemistry of block copolymers, the type of plastic to be toughened, and also the method of incorporating the block copolymer into the plastic. They will be described thoroughly in subsequent sections.

Additionally, toughness is also significantly influenced by a range of micromechanical mechanisms, including crazing,[6, 14, 15] cavitation,[16-18] shear yielding,[19, 20]

and plasticity of polymer crystal.[21-23] They can be engaged in the deformation of polymer blends, on a nano- or microscale, resulting in a great overall energy absorption. As mentioned above, the deformation mechanisms that operate in a particular polymer blend are not only subject to the dispersed phase, but also depend on the continuous phase, i.e., the plastic to be toughened. For instance, the basic mechanisms involved in plastic deformation of glassy amorphous thermoplastics are crazing and shear yielding,[14, 19] but in semicrystalline plastics, crystallographic mechanisms can play a role, primarily by slips along and transverse to the chain direction in crystal lamellae.[24, 25] Contrary to thermoplastics, highly crosslinked thermosetting plastics are not crazable and have to activate other deformation mechanisms like shear yielding.

Our goal is to produce nanostructured plastics reinforced by block copolymer dispersions hopefully with no sacrifice in transparency, rigidity, hardness, and glass transition temperature. We are particularly interested to see the toughening efficacy of dispersed block copolymer particles in different types of polymer matrices (the continuous phase), including thermosetting plastics (epoxy resins), glassy amorphous thermoplastics (poly(D,L-lactide)) and semicrystalline thermoplastics (poly(L-lactide)). The following sections summarize approaches to empolying block copolymers to toughen epoxy thermosets and poly(lactide) thermoseplastics.

1.2 Toughening epoxy thermosets with block copolymers

Epoxy resins typically form polymer networks through the reaction between an epoxy monomer containing multiple epoxide groups and a crosslinker with specific

functional groups. Epoxy monomers are generally diglycidyl ether of bisphenol A (DGEBA), derived from the reaction of bisphenol-A with epichlorohydrin. The crosslinker, also referred to as hardener or curing agent, are available with a wide variety of selections,[10, 26] including those containing amines, amides, novolacs, and carboxylic acids.[27] The network structure and ultimate properties can be tailored by judiciously choosing the resin ingredients and curing protocol. For example, altering the chemical structure of an amine curing agent can readily tune the glass transition temperature (T_g) of the epoxy matrix from 127 ℃ to 189 ℃.[28] Epoxy resins are employed due to their excellent durability, chemical and thermal stability, good adhesion to various substrates and high rigidity.[29-33] These desirable properties make epoxy resins attractive for industrial applications and have motivated fundamental research for over two decades.

The commercial importance of epoxy resins continued to grow with an annual increase of 7.7% in the overall demand during 2009-2013. The global market for epoxy resins is projected to reach 3.03 million tons by the year of 2017.[29] As one of the most important classes of thermoset polymers, epoxy resins, with many outstanding properties, have been widely used in such areas as adhesives, protective coatings and paintings, automative and aircraft components, and encapsulating materials in the electronics industry.[34-36] However, the network structure makes glassy epoxy materials intrinsically brittle and therefore prone to fracture failure at a low stress level, which severely limits their applications. This brittleness arises from the reduced chain mobility caused by the constraint of crosslinks,[37] which prohibits deformation processes prior to ultimate fracture, decreasing the amount of energy that can be absorbed or dissipated.

Chapter 1

A traditional way of improving the fracture toughness of epoxy materials is to incorporate rubbery modifiers as a dispersed phase. In a recent review, Pearson et al.[16] has summarized the large body of literature on rubber toughened epoxies. Generally, there are two types of rubbery phases being used: liquid rubbers, like amine- or carboxyl-terminated butadiene acrylonitrile (ATBN or CTBN), and preformed rubber particles composed of a rubbery core and a glassy thin shell.[38] The liquid rubbers are initially miscible with epoxy precursors, but are expelled by the growing network, resulting in macrophase separated rubbery domains with a characteristic size ranging from tens of microns to hundreds of microns.[39, 40] It brings in the side effect that the resultant plastics become opaque as mentioned above. On the other hand, addition of rubber particles provides control over the morphology and dimension of the dispersed phase. However, a satisfactory improvement in toughness usually requires high loadings of rubber particles (ca. 20 wt.%), which can significantly reduce the elastic modulus, hardness and T_g of the resin.[38, 41, 42] In brief, the toughness enhancement with this traditional strategy is accompanied by detrimental effects on other resin properties, detracting from many applications, especially in coating products.

Block copolymers have emerged as an attractive solution to realizing well defined nanostructure and improved toughness in epoxy thermosets. Over a decade ago, it was discovered that amphiphilic block copolymers can self-assemble into long-range ordered structures like lamella, gyroid and hexagonally-packed cylinder in uncured epoxy resins.[43-45] Analogous to low molecular weight surfactants, amphiphilic block copolymers are designed so that the epoxy precursor can selectively solvate the epoxy-philic sub-

domain, while the unfavorable interactions with the epoxy-phobic block(s) promote self-assembly.[46] The rich morphological behavior exhibited in block copolymer/epoxy precursor blends parallels the phase behavior observed in AB/A block copolymer/homopolymer systems.[47] This discovery provides an effective approach to creating nanostructured epoxy plastics since the preformed microstructures are thermodynamically stable and can be preserved in the cured thermosets even when heated up to 200 ℃.[48, 49]

Following this self-assembly approach, Bates and many coworkers have extensively dealt with block copolymers composed of epoxy-philic poly(ethylene oxide) (PEO)[46, 48, 50-62] or other polar blocks[36, 54, 61, 63] , and added them at relatively low loadings (< 5 wt.%) to epoxy formulations. In this case, thermodynamic interactions drive amphiphilic block copolymers to form micellar structures in the melt-blending stage, and these micelles become fixed into the epoxy network resulting in a nanostructured plastic that lacks long-range order. Figure 1.1 illustrates this process schematically.

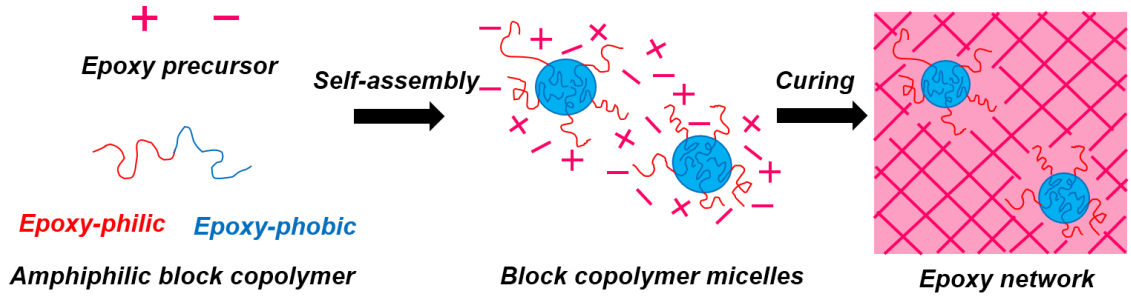

Figure 1.1 Formation of micellar structures in epoxy plastics.

The micellar structure has been proven to provide remarkable improvements in toughness. Engineering studies have shown that addition of just 5 wt.% of block copolymers can raise the critical strain energy release rate (G_{Ic}) of the cured product by up to 20 times that of the unmodified material.[48, 50-53, 64] Additionally, block copolymer modifiers can mitigate the reductions in resin modulus and T_g, due to the low required loading.[53, 63, 65]

The toughening efficacy of block copolymers is found to be dependent on the associated microphase separated nanostructures in the cured epoxy resins, including spherical micelles, wormlike micelles, and bi-layer vesicles. Figure 1.2 depicts these different configurations, and shows that the morphological transition is primarily controlled by the composition of the block copolymer.[53, 54, 65] Several authors[51-53, 61] have demonstrated that wormlike micelles are more desirable for toughening than spherical micelles with a difference of up to 250% in critical stress intensity factor (K_{Ic}) in favor of the former. Additionally, the toughening effect of vesicles varies a lot among different epoxy systems.[11, 45, 52, 53, 61] Therefore, the preceise control of block copolymer final morphology is critical for the goal of toughening the resultant epoxies.

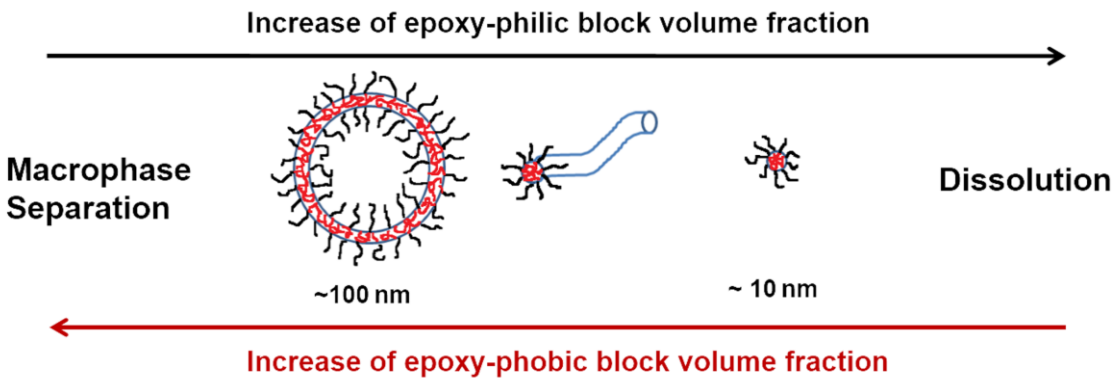

Figure 1.2 Self-assembled structures upon addition of small amounts of amphiphilic block copolymers to epoxies (from left to right): bi-layer vesicles, wormlike micelles, and spherical micelles. The epoxy-philic and epoxy-phobic blocks are denoted by black and red, respectivley. The interface is colored by blue. The direction of black (red) arrow points to the increase of epoxy-philic (-phobic) block volume fraction.

Over the last decade, extensive studies in literature have been devoted to the field of nanostructured epoxies with block copolymers, and specifically to the phase behavior and factors that control the resulting morphology of the blends, and also to the underlying toughening mechanisms. Apart from the self-assembly approach cited above, several groups, including Zheng and coworkers,[66-71] have also developed a reaction-induced microphase separation approach to fabricate nanostructured epoxies. They employed a linear or star-shaped block copolymer containing a block that was initially miscible with the epoxy precursor, but displayed an upper critical solution temperature (USCT). During curing at elevated temepratures, the block copolymer tended to microphase separate to form various microstructures, for instance, a "raspberry-like" or "onion-like" morphology.[72, 73] Leibler and coworkers[1, 2, 74, 75] used block copolymers containing specific funtional groups that can react with the resin components to finely tune and

control the morphology. In this case, both the thermodynamic interactions between different components and the reaction kinetics of the reactive block with the epoxy resin and of crosslinking of the resin itself, strongly affected the formation of nanophases. The control of reaction induced morphologies in bulk epoxy thermosets[76-82] or even in thin films[83-86] remains as a topic of great interest to-date. Unfortunately, those interesting morphologies were usually obtained at relatively high block copolymer concentrations (> 10 wt.%), and the authors did not report their influences on epoxy mechanical properties.

On the other hand, there have been a few in-depth studies aimed at understanding the toughening effect of block copolymers in epoxies[45, 52-54, 87-90] as well as the influences on toughness from factors like network crosslink density and deformation rate.[48, 59, 60] These reports have proposed the main toughening mechanism in rubbery-core micelle modified epoxies to be cavitation induced shear yielding of the matrix.[50, 91-95] Specifically, in the process zone ahead of a crack tip, the effect of high hydrostatic stresses drives micelles to cavitate within their rubbery cores, leaving voids in the network. The presence of voids helps decrease the constraint to deformation of the surrounding matrix material. Accordingly, local plastic deformation can readily occur, further promoting the shear yielding and shear band formation in the matrix. As a consequence, greater amounts of energy are required to propagate the primary crack. Based on this determination, the latest work[91, 93, 96] in the Bates group systematically investigated the deformation process of epoxy materials modified with rubbery and glassy core micelles via *in situ* small-angle x-ray scattering (SAXS) experiments. This comparative approach provided a framework for separating the role of cavitation in the

toughening mechanism. Findings showed that the rubbery core micelles underwent a dilatational process while the glassy core micelles deformed with constant volume, confirming the cavitation in rubbery nanodomains. However, glassy core micelles also afforded toughening, although less effective than that of rubbery ones. That has been explained by a network disruption mechanism, namely, in the region spanned by the micelle corona there exists network disruption that can also initiate matrix plastic deformation, but to a lesser extent than cavitation.[49, 91, 96]

Until now, most of the studies have emphasized the application of block copolymers in several model epoxy systems,[10, 11] with potentially limited practical utility. Also, a comprehensive understanding of the block copolymer toughening mechanism under various conditions is still lacking. Important issues include: (*i*) how observed toughness enhancement of bulk nanostructured epoxies translates to coating applications where thickness plays a crucial role, (*ii*) how block copolymers function in a composite with the presence of other modifiers like rigid fillers. This dissertation explores the block copolymer toughening strategy in more complex epoxy systems with direct implications for understanding and designing commercial products. This strong connnection with application is one of the principle attributes of the work.

1.3 Toughening PLA thermoplastics with block copolymers

Poly(lactide) (PLA), a compostable bioderived polyester, can be produced at a cost and scale that makes it an attractive replacement for nondegradable petroleum-derived

thermoplastics as introduced in Section 1.1.[97] It has been used in such applications as textile and disposable containers (e.g. bottles and cups).[98, 99] Despite possessing relatively high strength and modulus, PLA is intrinsically brittle, which severely inhibits the utilization in markets like films and food packaging, where toughness is essential.[99-101]

Various strategies to toughen PLA have been developed over the last ten years, including plasticization,[102-105] copolymerization,[106] blending with flexible polymers,[107-110] addition of rigid fillers,[111-113] and changing the poly(lactide) molecular orientation.[114] Plasticization involves adding a monomeric, oligomeric or low moleculer weight polymeric plasticizer to PLA to enhance its flexibility. Plasticizers usually are miscible with PLA, like polyethylene glycol (PEG)[115-118] and citrate esters,[102, 119] which have been most commonly investigated. The loading of plasticizer is usually higher than 10 wt.% for a satisfactory toughening effect. Unfortunately, incorporation of plasticizers often severely depresses the T_g of PLA, restricting the service temperature of these materials.[97, 115] Statistical or block copolymers can be generated by the copolymerization of lactide monomer with other cyclic ester or lactone monomers, and this offers attractive options for significantly improving the mechanical performance of PLA.[120-125] However, comonomer cost can prohibit the use of PLA copolymers for single use applications such as food packaging.

As mentioned in Section 1.1, fabricating polymer blends is a much more economical and convenient way to toughen this PLA thermoplastic. Previously, various polymers have been added as the dispersed phase into PLA, including polycaprolactone,[107, 126] poly(butylene succinate),[127] polyurethane elastomers,[128] soybean oil derivatives,[129] linear

low density polyethylene (LLDPE),[108, 130] and acrylonitrile-butadiene-styrene (ABS).[131] The immiscibility between these dispersed phases and PLA requires the addition of a compatibilizer to stablize the interface, and it typically results in micron-sized domains, reducing the transparency of the polymer blends.

Again, the utilization of block copolymers as the dispersed phase is the key to fabricating nanostructured PLA blends with enhanced toughness. This versatile and potentially low-cost strategy has been successfully employed to toughen polystyrene (PS).[132, 133] Leibler et al.[1] prepared "nanostructured" PS with the self-assembly of polystyrene-*b*-polybutadiene-*b*-polystyrene (SBS) block copolymers. Such materials are transparent and much tougher than neat PS. However, because the PS homopolymer is much longer than the styrene block within the SBS triblock, this nanostructure is not in equilibrium and the polymer blend may become opaque if annealed. (See below.)

Technical challenges with this strategy arise when designing appropriate block copolymers. The block copolymer must be amphiphilic with respect to the PLA homopolymer matrix, similar to the case of block copolymer/epoxy blend. It is natural to select PLA as the matrix-philic block to form the micelle corona, which causes no enthalpic penalty for mixing ($\Delta H_{mixing} = 0$), since the Flory-Huggins interaction parameter χ between the PLA block and the PLA homopolymer equals zero. The other matrix-phobic block(s) should possess a positive χ with the matrix polymer forming the micelle core. In this case, if the matrix PLA homopolymer has a higher molecular weight than that of the PLA block, long homopolymer chains would barely penetrate the corona region formed by short blocks, because it reduces the translational entropy ($\Delta S_{mixing} <$

0),[134, 135] resulting in $\Delta G_{mixing} > 0$, i.e., immiscibility between the corona block and matrix. Consequently, macrophase separation of the block copolymer would occur. The annealed SBS/PS polymer blend mentioned above is an example. Therefore, we have to make the PLA block much longer than the PLA homopolymer in order to stabilize the dispersion of micelles. However, addition of block copolymers with very high molecular weight can dramatically increase the system viscosity, limiting the processibility of polymer blends. The solution to these problems lies in the selection of the matrix-philic block, which should exhibit a negative χ with the matrix homopolymer. We postulate that this enthalpic attraction between the corona chain and homopolymer counteracts the unfavorable entropic effects, allowing the homopolymer to wet the corona, which favors dispersion, despite the disparate molecular sizes.[134-137] Consequently, low molecular weight block copolymers can generate dispersed micelles in the blend with commercially viable high molar mass PLA plastics. It is worthy to note that the crystallization of poly(L-lactide) (PLLA) can disrupt all micellar structures due to the lose of attractive interations.

Unlike the non-crazable epoxy resin, plain PLA plastic in the glassy state deforms first by crazing, then immediately undergoes shear banding without observable cavitation. The deformation mechanism in rubber-toughened glassy thermoplastics can be a good reference for our block copolymer/PLA blends. Kowalczyk et al.[138] prepared glassy PLA blends with immiscible poly(1,4-*cis*-isoprene) and found that crazing in the PLA matrix was accompanied by the cavitation within rubber domains, which further promoted the shear deformation of PLA. Three micromechanical mechanisms acting in

sequence were believed to produce the substantial improvement in drawability and impact strength of modified blends. In this dissertation, we continue to explore the fundamental aspects leading to toughness in block copolymer modified PLA materials in the form of bulk plastics as well as thin films.

1.4 Thesis overview

The commercial importance of toughened plastics continuously drives research efforts devoted to fabricating various structures and understanding the structure-property relationship in these materials. Our work is no different in that sense. However, we have employed the unique properties of block copolymers in concert with various commercially viable plastics to achieve well-defined nanostructures and superior toughness in the bulk state as well as in thin films.

The work presented in this dissertation has been divided into two parts and seven chapters. The first part (Chapter 2 to 5) focuses on understanding the block copolymer modified epoxy thermoset materials from various aspects. Firstly, chapter 2 introduces the basic set of experimental procedures and techniques including synthesis, sample preparation and characterization that are common to all polymer blend systems described in this dissertation. This chapter also presents the fundamental principles of some major characterization techniques.

Chapter 3 describes a model system study designed to establish the block copolymer toughening strategy in bulk thermosets as well as in thin epoxy coatings. The Jeffamine-

epoxy system being used is relatively simple in terms of thermodynamics and curing kinetics, and the nanostructure formation primarily relies on the block copolymer self-assembly. A very important result is that the toughness enhancement observed in bulk materials can successfully translate to coatings as thin as 15 μm, which has been quantified from the improvement in the coating abrasive wear resistance. This chapter provides some fundamental background for the toughening mechanism of micelles in coatings during abrasion.

In chapter 4 we investigate the commercially viable Cardolite-epoxy system that is more complex thermodynamically but directly connected to industrial applications. This chapter summarizes our successful engineering of a commercialized block copolymer product to provide superior toughening effect through the comprehensive integration of mixing thermodynamics, curing kinetics, and optimization of structure formation. We have confirmed the importance of processing variables by showing their morphological and mechanical property consequences in cured bulk and coating products. The approach presented in this chapter is valuable in designing other thermoset materials endowed with exceptional properties at manageable cost.

In chapter 5, we take one step further to explore the toughening efficacy of block copolymer micelles in hybrid composite systems with the presence of a second modifier, graphene fillers. The crosslink density of the epoxy network is tunable, which strongly affects the toughening effect in cured composites. At the lowest crosslink density, block copolymer/graphene/epoxy ternary composites exhibit an interesting synergistic toughening effect, revealing additional micromechanical mechanisms in our materials.

The second part of this dissertation (Chapter 6) extends the block copolymer toughening strategy to poly(lactide) thermoplastics. We still focus on controlling nanostructures derived from the block copolymer/homopolymer phase behavior in the melt state and quickly vitrified into the glassy thermoplastic. In this case, the crazable polymer matrix makes the deformation process and toughening mechanism different from that of thermoset epoxies. Finally, Chapter 7 presents a summary of the work and offers a few suggestions to future research directions.

Chapter 2

Materials and experimental methods

2.1 Introduction

This chapter introduces the materials and experimental methods used in this work. First brief descriptions of the thermoset and thermoplastic polymers that act as the brittle matrix to be toughened, including two different types of epoxy thermosets and a poly(lactide) thermoplastic, are presented, followed by a description of the synthesis of three distinct types of amphiphilic diblock copolymers designed as toughening agents using anionic polymerization techniques. Then sample preparation methods to incorporate those diblock modifiers into different polymer matrices are described. Last we detail the techniques utilized in characterizing the modified plastics. Microstructure was investigated through transmission electron microscopy (TEM) and small-angle X-ray scattering (SAXS). The thermal analysis was conducted with differential scanning calorimetry (DSC). Mechanical properties were further characterized using various methods depending on the matrix polymer and the specimen dimension (bulk *versus* coating), but in this chapter particular emphasis is given to standard fracture tests,

dynamic mechanical spectroscopy (DMS) measurements for bulk thermosets and nanoindentation, abrasion tests for coatings. In-depth fractography studies employed the use of scanning electron microscopy (SEM) to probe toughening mechanisms.

In general, our description summarizes those techniques that are common to all research chapters (Chapters 3-6), while details for the specific matrix polymers and associated block copolymer modifiers and the subsequent sample preparation protocols can be found in the experimental section for those chapters. Any characterization technique specific to a single given research chapter (e.g. the Izod impact strength test for poly(lactide) thermoplastic materials, Chapter 6) is listed in the experimental section of that chapter.

2.2 Description of the polymer matrices

2.2.1 Epoxy thermosets: Jeffamine system and Cardolite system

Two different types of epoxy resins were used as the thermoset polymer matrix to be toughened in this work: one is a model system, Jeffamine thermoset, and the other one is a commercially viable system, Cardolite thermoset. The Jeffamine system cures at high temperatures and is utilized for understanding the structure-property relationship in bulk materials and how observed property enhancement of bulk materials translates to thin coatings. The Cardolite system is designed for fast curing under ambient conditions and has been widely used in industry for coating applications.

The major difference between these two thermoset systems is the curing agent being used. As mentioned above, the first curing agent, Jeffamine, is designed for high temperature curing, which completes the network formation at 120 ℃. The merit of this epoxy system is that block copolymer modifiers self-assemble into different morphologies while being melt blended with the epoxy precursor, and the curing reaction appears to only play a role to fix those pre-formed structures.[95] For the separation between epoxy condensation and thermodynamically-driven structure formation, this Jeffamine thermoset is selected as the model system. On the other hand, the commercially viable Cardolite thermoset is more complex than Jeffamine in terms of the system thermodynamics and curing kinetics, but this bio-derived curing agent, Cardolite, is also more relevant with industrial applications.

2.2.2 Thermoplastic polymer: poly(lactide)

The block copolymer toughening strategy established with epoxy thermosets can be readily extended to modifying brittle thermoplastic polymers. In this work, we select poly(lactide) (PLA) as the thermoplastic matrix to be toughened. As a compostable bio-derived polyester, PLA can be produced at a cost and scale that makes it an attractive replacement for nondegradable thermoplastics, but pristine PLA is brittle and unsuitable for use in applications where high ductility is required.[97-99] Therefore, PLA is an ideal candidate to be included into the portfolio of block copolymer toughened plastics. There are two PLA isomers being used: isotactic poly(L-lactide) (PLLA) and atactic poly(D,L-

lactide) (PDLLA). The PLLA and PDLLA homopolymers have similar number average molecular weight and dispersity, but the major difference is that PDLLA cannot crystallize.

2.3 Synthesis of block copolymers

Three different types of diblock copolymers were synthesized and evaluated as the toughening agents for the aforementioned thermoset and thermoplastic polymer matrices. They are poly(2-vinyl pyridine)-*b*-poly(1,2-butadiene) (P2VP-PB) and poly(ethylene oxide)-*b*-poly(ethylene-*alt*-propylene) (PEO-PEP) that is used to toughen the Jeffamine thermoset, and poly(ethylene oxide)-*b*-poly(butylene oxide) (PEO-PBO) that modifies the Cardolite thermoset and the poly(lactide) thermoplastic. These diblocks are all designed to be amphiphilic with respect to the associated polymer matrix, and they are composed of a "matrix-philic" block (P2VP or PEO) and a "matrix-phobic" block (PB or PBO). Ideally, all diblocks would generate micelles in polymer matrices with the "matrix phobic" block forming the core and the "matrix-philic" block as the corona. The synthesis technique for these diblocks is anionic polymerization, and detailed procedures for each type are described below. Monomer purification was based on well-established practices,[139] and solvents used for polymer synthesis were purified by standard column methods.[140]

2.3.1 Poly(2-vinyl pyridine)-*b*-poly(1,2-butadiene) P2VP-PB

The P2VP-PB diblock was synthesized via sequential anionic polymerization using tetrahydrofuran (THF) as the solvent, and the synthetic scheme is presented in Figure 2.1. Purified 1,3-butadiene monomer was first initiated using *sec*-butyllithium and reacted at –60 ℃ for 1 h, followed by the addition of purified 2-vinyl pyridine monomer. Under these conditions 92% of butadiene monomers were incorporated into the polymer through 1, 2-addition; the remaining 8% were through 1,4-addition. The second block was allowed to grow for another 30 min, before the termination with methanol. The product was precipitated in distilled water, a poor solvent, at room temperature, and freeze-dried under vacuum for 48 h.

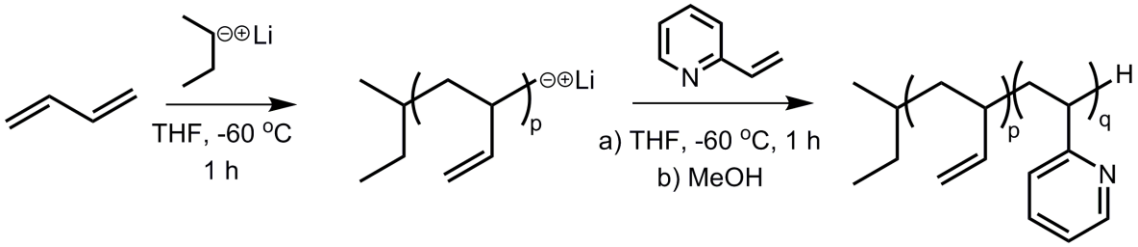

Figure 2.1 Synthetic scheme used to prepare poly(1,2-butadiene)-*b*-poly(2-vinyl pyridine) diblock copolymers. In the first step only 1,2-addition of butadiene repeat units is shown. The following abbreviation were used: THF for tetrahydrofuran, and MeOH for methanol.

2.3.2 Poly(ethylene oxide)-*b*-poly(ethylene-*alt*-propylene) PEO-PEP

The two step polymerization protocol followed in preparing PEO-PEP diblock copolymer has been previously reported,[141] and the synthetic scheme is shown in Figure

2.2. Purified isoprene monomer was first initiated using *sec*-butyllithium in cyclohexane as the solvent, and the reaction was conducted at 40 ℃ for 8 h. The resultant polyisoprene product showed 93% 1,4-addition and 7% 3,4-addition. Ethylene oxide (EO) monomer was then added to the living polyisoprene with a three- to five-fold excess and allowed to react for another 24 h before termination with methanol. Under these conditions the living polymer can be end-capped by a hydroxyl group.[142] After termination, the polymer product was recovered by evaporation of cyclohexane using a rotary evaporator followed by further drying in a vacuum oven overnight at 40 ℃. The catalytic hydrogenation of polyisoprene into poly(ethylene-*alt*-propylene) was completed in a high pressure reaction vessel, where ~ 10 g of hydroxyl-capped polyisoprene were dissolved in 500 mL of cyclohexane with 2 g of platinum/rhenium (Pt/Re) catalyst on silica support. The hydrogenation reaction was carried out under 625 psi of hydrogen at 100 ℃ for 12 h.[91] After that, the polymer solution was filtered to remove the catalyst and concentrated using a rotary evaporator. Residual solvent was removed by drying in a vacuum oven overnight at 80 ℃. Full saturation of the polyisoprene precursor was verified by ^{1}H NMR.

Addition of ethylene oxide units to the first block requires the hydroxyl-terminated polymer precursor to be re-initiated. In this case, the polymer precursor was re-dissolved in THF at 45 ℃ and carefully titrated with freshly prepared potassium naphthalenide until a light green color was achieved in the solution and persisted for at least 1 h. At this point purified EO monomer was slowly added into the reactor and the polymerization was allowed to proceed for 48 h at 45 ℃ prior to termination with acidic

methanol. THF was removed using a rotary evaporator and the product was re-dissolved in chloroform, and filtered to remove residual solids. Finally, the PEO-PEP product was isolated by evaporation of chloroform using a rotary evaporator followed by freeze-drying with benzene three times.

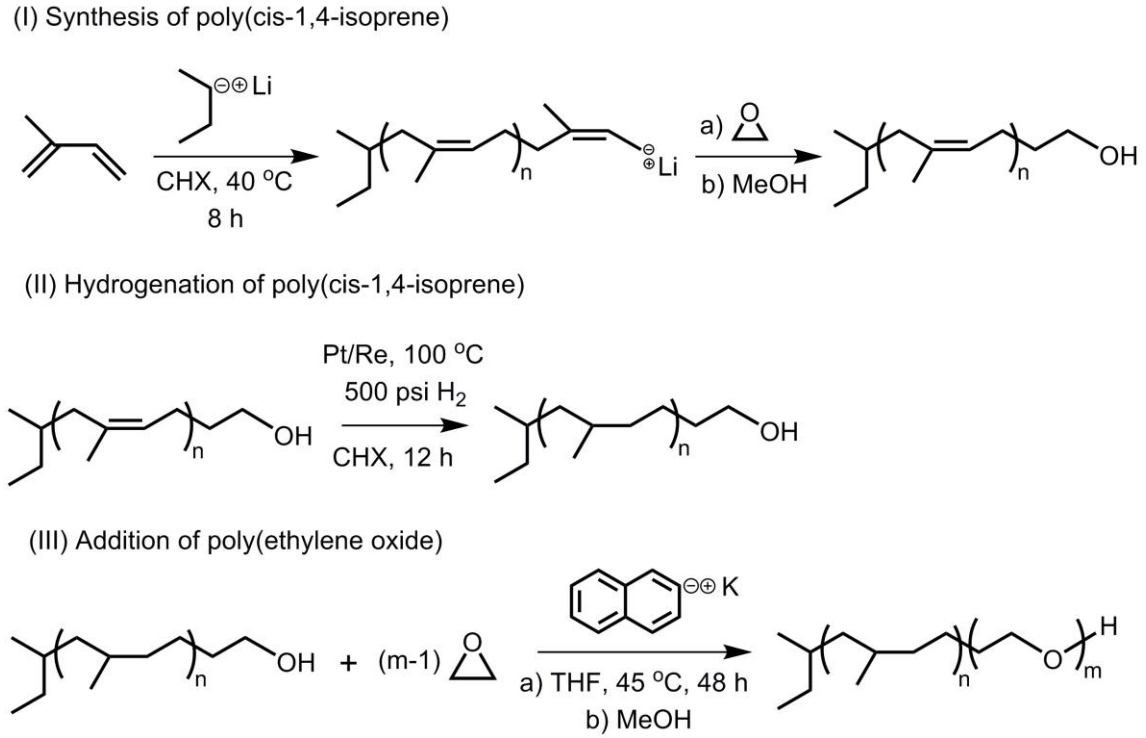

Figure 2.2 Synthetic scheme used to prepare poly(ethylene-*alt*-propylene)-*b*-poly(ethylene oxide) diblock copolymers. The first step was to synthesize a hydroxyl-terminated poly(*cis*-1,4-isoprene) precursor. Only 1,4-addition of isoprene repeat units is shown above. The second step was to hydrogenate this polymer to obtain a saturated polymer precursor. In the third step, the polymer precursor was used as a macro-initiator for the addition of ethylene oxide monomers. The following abbreviation was used: CHX for cyclohexane, MeOH for methanol, and THF for tetrahydrofuran.

2.3.3 Poly(ethylene oxide)-*b*-poly(butylene oxide) PEO-PBO

PEO-PBO diblock copolymers were synthesized via sequential anionic ring-opening polymerization of butylene oxide (BO) followed by reinitiation and addition of ethylene oxide (EO) using a modified version of the method reported by Allgaier et al.[143] Figure 2.3 presents the synthetic scheme. BO monomer was pre-dried over CaH_2 followed by addition of an *n*-butyllithium then distilled into a sealed burette. The initiator potassium *tert*-butanolate (KOt-Bu) in THF was added to a Schlenk flask, completely dried under dynamic vacuum, and then pressurized with purified argon. Crown ether 18-Crown-6 (18C6) was first freeze-dried from benzene then dissolved into purified toluene at a concentration of about 0.4 g/mL. Sufficient 18C6/toluene solution was injected into the Schlenk flask containing the KOt-Bu solid to produce a clear, gold-colored solution with a 3:1 18C6:KOt-Bu molar ratio. Purified toluene was then injected into the Schlenk flask followed by addition of BO monomer. The weight ratio of toluene to BO was between 2:1 and 1:1 for the higher and lower molecular weight products, respectively. The polymerization reaction was conducted at room temperature for about 20 h, and then terminated with acidic methanol. Toluene was removed using a rotary evaporator and the product was re-dissolved into chloroform, and filtered to remove residual solids followed by at least four washings with distilled water to completely remove residual initiator and crown ether. Finally, the poly(butylene oxide) (PBO) product was isolated by evaporation of chloroform using a rotary evaporator followed by freeze-drying with benzene three times. Addition of the second PEO block followed a similar procedure as described above

in the synthesis of PEP-PEO diblock. EO monomer was condensed into a flask, degassed, and reacted with *n*-butyl lithium twice before being distilled into a burette. The purified PBO homopolymer was re-initiated with potassium naphthalenide in THF under argon atmosphere, making a clear light green solution. EO monomer was then slowly added into the reactor to avoid transient pressure and the mixture was allowed to react for 24 h at 45 ℃, and was then terminated with acidic methanol. The final PEO-PBO diblock copolymer was recovered and purified in a similar way to that of the PBO homopolymer as described above. A series of PEO-PBO diblocks were prepared for the modification of the Cardolite thermoset or the poly(lactide) thermoplastic.

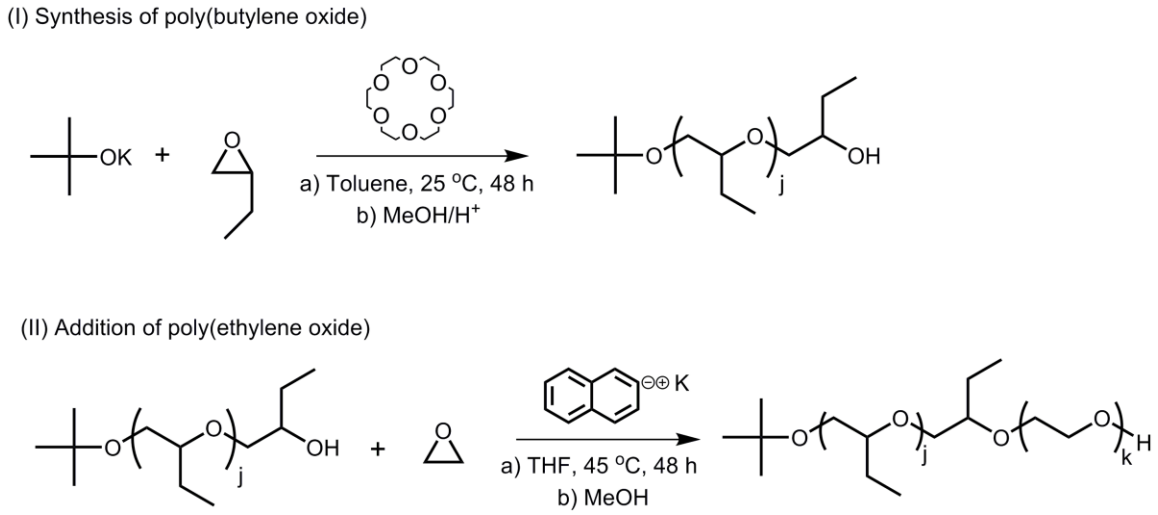

Figure 2.3 Synthetic scheme used to prepare poly(butylene oxide)-*b*-poly(ethylene oxide) diblock copolymers. In the first step a hydroxyl-terminated poly(butylene oxide) homopolymer was synthesized, and the addition of crown ether was critical for controlling the molecular weight and dispersity. In the second step, this homopolymer was used as a macro-initiator for the addition of ethylene oxide monomers. The following abbreviation were used: THF for tetrahydrofuran, and MeOH for methanol.

2.4 Sample preparation

The sample preparation protocol varies among different systems, primarily depending on the polymer matrix being used and the specimen dimension being adopted (bulk *versus* coating). Therefore, the description of associated sample preparation is detailed in the experimental section of subsequent chapters. Here, we just give a brief overview.

For the two epoxy thermosets, different formulations were obtained by either melt blending or solvent casting block copolymer modifiers into epoxy precursors. Then, full formulations were degassed and allowed to directly cure under different conditions to attain bulk samples, or underwent a pre-cure process prior to being re-dissolved in casting solvents to make thin coatings. For the poly(lactide) thermoplastic, blends of PLA homopolymer and diblock copolymers were prepared by both solvent and melt blending, and then those polymer blends were melt compounded or injection molded to make bulk specimens, or were extruded to films via a film blowing process.

It is noted that in the Cardolite and poly(lactide) systems, processing variables during sample preparation can greatly affect the modifier morphology and consequent toughening efficacy in the final product. Therefore, in those systems, it is also critical to engineer an optimized processing route besides designing the modifier chemistry, in order to achieve improved properties for the products.

2.5 Microstructure characterization

The microstructures of all modified polymer matrices were characterized using transmission electron microscopy (TEM) with respect to the block copolymer morphology and distribution. Ultrathin sections cut from block copolymer modified plastics were used so that the electron beam can pass through the specimen. Contrast in TEM is derived from differences in electron density between phases which determines their ability to scatter incoming electrons. It is noted that TEM micrographs are planar projections of three-dimensional objects, so complementary techniques like scattering are often employed for definite assignment of morphology. Additionally, small-angle x-ray scattering (SAXS) allowed us to investigate the block copolymer morphology at different stages during the curing reaction for the thermoset polymer systems. Details about TEM and SAXS specimen preparation for different polymer matrices, block copolymer modifiers, and sample dimensions (bulk *versus* coating) are described below.

2.5.1 Transmission Electron Microscopy (TEM)

Cured bulk thermoset samples were sectioned at room temperature on a Reichert Ultramicrotome S fitted with a Micro Star diamond knife, producing ultrathin sections (ca. 70-90 nm) that were floated onto distilled water and collected onto copper grids. On the other hand, modified bulk thermoplastic samples were cryo-sectioned at −100 ℃

using the same ultramicrotome but with Model FC-S cryo-attachments. Ultrathin frozen sections (ca. 100 nm) were directly collected onto copper grids.

Cured epoxy coatings were first carefully removed from the substrates using a fresh razor blade. A thin layer of platinum was sputtered onto the coating/air free surface to label this interface for TEM. The free-standing epoxy films were embedded in medium grade LR White Resin (Ted Pella) to create samples that were then microtomed in a similar manner to the bulk thermoset samples. The blown poly(lactide) films were embedded and microtomed in the same way.

Copper grids with TEM specimens were then vapor stained. This step is critical to increase the contrast for better imaging. P2VP-PB modified Jeffamine samples were stained with 2 wt.% OsO_4 aqueous solution for 23 min. Other samples containing PEO-PEP or PEO-PBO were all vapor stained with 0.5 wt.% RuO_4 aqueous solution for 15 min. After staining, specimens were imaged using an FEI Tecnai T12 transmission electron microscope with 120 kV accelerating voltage.

2.5.2 Small Angle X-ray Scattering (SAXS)

The SAXS experiments were conducted at Argonne National Laboratory using beamline 12-ID-B with a 14 keV radiation energy (wavelength λ = 0.886 Å) and a sample-to-detector distance of 6 m. The data were collected on a CCD area detector (Pilatus 2M). Liquid samples were sealed in 1.5 mm quartz capillaries with a high-temperature silicone-based sealant. These capillaries were placed in a home-made heating

stage to maintain the isothermal curing conditions for the thermoset polymers. All measurements were taken with a 1 s exposure time and the data were reported in units of arbitrary intensity. In all cases the scattering patterns were cylindrically symmetric and were therefore reduced to the one-dimensional form of intensity versus scattering wave vector magnitude, $q = 4\pi\lambda^{-1}\sin(\theta/2)$, where θ is the scattering angle. System structural features were extracted from those one-dimensional SAXS profiles using the Igor package provided by NIST.[144] A detailed description of the fitting models being used are presented below.

Intensity of scattered radiation. At a given scattering wave vector the intensity of scattered radiation $I(q)$ can be expressed as follows when the particle concentration is low:

$$I(q) = (\Delta\rho)^2 \times N \times P(q) \times S(q) \tag{2.1}$$

where $\Delta\rho$ is the difference between the scattering length densities of the micelle core and the micelle corona/matrix (or liquid epoxy precursors), N is the number of scattering particles, $P(q)$ is the form factor for a given shape, and $S(q)$ is the structure factor that accounts for interparticle interactions and approaches unity in dilute systems and increases as the particle concentration increases.

The correlation length fitting model. In several mixtures of PEO-PBO diblock copolymers with the Cardolite epoxy precursor, the obtained 1D SAXS profiles display a low-q feature ($q < 0.15$ nm^{-1}) that characterizes large size clusters, and a high-q feature (0.15 nm$^{-1} < q < 1$ nm^{-1}) that characterize block copolymer chains. In those cases, the following correlation length model[145] is employed for data fitting:

$$I(q) = \frac{A}{q^n} + \frac{C}{1+(q\lambda)^m} + B \tag{2.2}$$

where two multiplicative factors A and C, the incoherent background B, two exponents, n and m, and the correlation length λ are fitting parameters. The first term describes Porod scattering from weakly segregated block copolymer clusters, and the second term is a Lorentzian function describing scattering from polymer chains, reflecting the polymer/solvent interactions. For simplification, we treat the chain of PEO-PBO as a homopolymer chain, so only one Lorentzian function term was included in the fitting model, and the correlation length characterizes the interactions between diblocks and liquid epoxy precursors.

To summarize, the correlation length model requires a total six fitting parameters: *n*, *m*, λ and three factors *A, B, C*.

The hard sphere fitting model. In systems where block copolymers form spherical micelles, the structural characteristics of the micelles can be obtained using a hard sphere model with polydispersity correction for the micelle core radius. A detailed description of this model has been previously documented.[146, 147] This model assumes a spherical homogeneous micelle core with Gaussian distribution in radius and corona chains attached to the core surface. The intermicellar interactions are approximated by hard sphere interactions. In this model, the coherent scattering intensity is expressed as:

$$I(q) = \int D(R_c)(P_{sph}(q) + A^2_{sph}(q)[S(q)-1])dR_c \tag{2.3}$$

where R_c is the spherical core radius and its polydispersity is normalized with a Gaussian distribution $G(R_c)$, $P_{sph}(q)$ is the spherical form factor, $A_{sph}(q)$ gives the form factor

amplitude of the radial scattering length distribution of the micelle, and $S(q)$ is the structure factor of monodisperse hard spheres with the Percus-Yevick closure approximation.

Here the form factor $P_{\text{sph}}(q)$ is the sum of four parts: the form factor of spherical core, the form factor of Gaussian corona chains, the cross term between core and corona chains, and the cross term between corona chains. Therefore, the function of $P_{\text{sph}}(q)$ is written as:

$$\begin{aligned} P_{sph}(q) &= N_{agg}^2 \beta_{core}^2 A_{core}^2(q) + N_{agg} \beta_{corona}^2 P_{chain}(q) \\ &+ 2N_{agg}^2 \beta_{core} \beta_{corona} A_{core}(q) A_{corona}(q) + N_{agg}(N_{agg} - 1) \beta_{corona}^2 A_{corona}^2(q) \end{aligned} \tag{2.4}$$

where N_{agg} is the aggregation number of one micelle. β_{core} and β_{corona} are the excess scattering length of core and corona blocks, defined as $\upsilon_{\text{block}} \times (\rho_{\text{block}} - \rho_{\text{solvent}})$, with υ_{block} being the volume of the associated block and ρ being the scattering length density. $A_{\text{core}}(q)$ is the core form factor that can be expressed as:

$$A_{core}^2(q) = \Phi^2(qR_c) \exp(-q^2 \sigma_{\text{int}}^2) \tag{2.5}$$

with

$$\Phi(qR_c) = 3[\sin(qR_c) - (qR_c)\cos(qR_c)] / (qR_c)^3 \tag{2.6}$$

and σ_{int} being the interfacial thickness. $P_{\text{chain}}(q)$ is the Debye function for the corona chains that are assumed to be Gaussian chains:

$$P_{chain}(q) = \frac{2[\exp(-q^2 R_g^2) - 1 + q^2 R_g^2]}{q^4 R_g^4} \tag{2.7}$$

with R_g being the radius of gyration of the corona chain. $A_{corona}(q)$ is the form factor of corona chains, which is given as the normalized Fourier transform of the radial density distribution function of the corona chains $\rho_{corona}(r)$ that is composed of two spline functions $\rho_1(r)$ and $\rho_2(r)$:

$$A_{corona} = \frac{4\pi \int \rho_{corona}(r) \frac{\sin(qr)}{qr} r^2 dr}{4\pi \int \rho_{corona}(r) r^2 dr} \exp(-q^2 \sigma_{int}^2 / 2) \tag{2.8}$$

$$\rho_{corona}(r) = \frac{\rho_1(r) + a_1 \rho_2(r)}{1 + a_1} \tag{2.9}$$

Returning to Equation (2.3), $A_{sph}(q)$ gives the form factor amplitude of the radial scattering length distribution of the micelle, which can be expressed as:

$$A_{sph}(q) = N_{agg}(\beta_{core} A_{core}(q) + \beta_{corona} A_{corona}(q)) \tag{2.10}$$

where N_{agg}, β_{core}, β_{corona} and $A_{corona}(q)$ are as described above.

The structure factor $S(q)$ of monodisperse hard spheres with the Percus-Yevick approximation is written as:

$$S(q) = \left[1 + 24\phi_{hs} \frac{J(2qR_{hs})}{2qR_{hs}} \right]^{-1} \tag{2.11}$$

where R_{hs} is the effective radius of hard spheres and ϕ_{hs} is the volume fraction of hard spheres, and $J(x)$ is expressed as:

$$\begin{aligned} J(x) = {} & a / x^2 [\sin x - x \cos x] + b / x^3 [2x \sin x + (2 - x^2) \cos x - 2] + \\ & c / x^5 [-x^4 \cos x + 4((3x^2 - 6) \cos x + (x^3 - 6x) \sin x + 6)] \end{aligned} \tag{2.12}$$

where

$$a = \frac{(1+2\phi_{hs})^2}{(1-\phi_{hs})^4} \tag{2.13}$$

$$b = -6\phi_{hs}\frac{(1+\phi_{hs}/2)}{(1-\phi_{hs})^4} \tag{2.14}$$

$$c = \frac{1}{2}a\phi_{hs} \tag{2.15}$$

Lastly, the Gaussian distribution of core radius R_c follows the relationship below:

$$D(R_c) = \frac{1}{\sqrt{2\pi}\sigma_R}\exp[-\frac{(R_c - \langle R_c \rangle)^2}{2\sigma_R^2}] \tag{2.16}$$

where $<R_c>$ is the mean core radius and σ_R is the standard deviation.

To summarize, the hard sphere model requires a total of nine fitting parameters: N_{agg}, R_c and σ_{int} as in $P_{sph}(q)$ and $A_{sph}(q)$, R_g as in $P_{sph}(q)$, a_1 and s as in $A_{sph}(q)$, R_{hs} and ϕ_{hs} as in $S(q)$, and σ_R as in $D(R_c)$.

The core-shell cylinder fitting model. In systems where block copolymers form cylindrical or wormlike micelles, the structural characteristics of the micelles can be obtained using a core-shell cylinder model, where micelles are treated as polydisperse, right circular cylinders with a core-shell scattering length density profile. The shell thickness, *t*, on the cylinder radial surface is independent of that on the cylinder flat end face, and the latter contributes little to the overall scattering due to the large length, *L*. Polydispersity of the cylinder core radius, R_c, is calculated with a log-normal distribution. The overall scattering intensity can be expressed as:

$$I(q) = \int D(R_c)P_{cyl}(q)dR_c \tag{2.17}$$

where $D(R_c)$ is the Gaussian distribution of core radii, as shown in Equation (2.16), $P_{cyl}(q)$ is the cylindrical form factor. Here the structure factor comes at a low-q region (q $< 10^{-3}$ Å^{-1}) that is out of our SAXS spectrum. Therefore, the structure factor is taken as 1 and length polydispersity is not considered for this model.

The cylindrical form factor $P_{cyl}(q)$ is given by:

$$P_{cyl}(q) = \frac{\varphi}{V_{shell}} \int_0^{\pi/2} f^2(q,\alpha)\sin(\alpha)d\alpha \tag{2.18}$$

where φ is the background scale, V_{shell} is the volume of the cylinder shell, α is the angle between the cylinder and the scattering wave vector q, and $f(q, \alpha)$ is expressed as:

$$\begin{aligned} f(q,\alpha) = {} & 2(\rho_{core} - \rho_{shell})V_{core} j_0(qH\cos\alpha)\frac{J_1(qR_c\sin\alpha)}{qR_c\sin\alpha} + \\ & 2(\rho_{shell} - \rho_{solvent})V_{shell} j_0[q(H+t)\cos\alpha]\frac{J_1[q(R_c+\mathrm{t})\sin\alpha]}{q(R_c+\mathrm{t})\sin\alpha} \end{aligned} \tag{2.19}$$

where $j_0 = \sin(x)/x$, $V_{core} = \pi R_c^2 L$, $V_{shell} = \pi(R_c + \mathrm{t})^2 L$, $H = L/2$, and $J_1(x)$ is the first order Bessel function. In these calculations, it is assumed that $L/R_c >> 1$. Finally, the form factor is normalized by the total particle volume such that:

$$P_{cyl}(q) = \frac{\varphi}{V_{cyl}}\left\langle f^2 \right\rangle \tag{2.20}$$

where < > denote an average over all possible orientations of the cylinders.

To summarize, the core-shell model requires a total four fitting parameters: R_c, σ_{Rc}, t and L.

2.6 Thermal analysis

Differential Scanning Calorimetry (DSC). The thermal properties like the glass transition (T_g), crystallization (T_c) and melting (T_m) temperatures of block copolymer modified plastics were analyzed using a Q1000 differential scanning calorimeter (TA Instruments). There are some minor differences in the specimen preparation for different systems, as described below.

For epoxy thermosets, the extent of curing reaction was also determined. Cured bulk or free-standing coating samples (3.5-9 mg) were placed in hermetically sealed aluminum pans, and first heated at a rate of 10 ℃/min to 300 ℃ and equilibrated for 5 min to ensure full curing and to erase any thermal history in the material. A lack of an exothermic curing peak (apex at 200-220 ℃) on the first heating trace was taken to indicate a fully cured sample. However, in some cases, if an exothermic curing peak was recorded, the area of this peak was used to quantitatively estimate the extent of the curing reaction. Samples were then cooled to 0 ℃ and heated once more to 300 ℃, at a rate of 10 ℃/min in both cycles. The T_g, T_c and T_m were always determined during the second heating traces, and the reported values in this work represent an average of three measurements on three identical specimens obtained from the same sample.

In the PEO-PBO modified Cardolite thermoset, additional experiments with the blends of diblock copolymers with the epoxy monomer or curing agent were conducted with DSC. There liquid and nonreactive samples were annealed at 150 ℃ for 3 min, then

cooled down to −100 ℃ and subsequently measured while heating back to 150 ℃, at a rate of 10 ℃/min in all cycles.

For block copolymer modified PLA thermoplastics, samples were first heated at a rate of 10 ℃/min to 180 ℃ and held for 5 min to melt the polymer blends and erase any thermal history, and then cooled to −100 ℃ and heated back to 180 ℃ at 10 ℃/min. The reported T_g, T_c and T_m values were also determined from the second heating runs, and were averaged over three identical specimens from the same sample.

It is worthy to note that to compare the thermal properties and other mechanical properties (see below) of the neat materials with those of modified samples, a *t*-test with a threshold for statistical significance set to 0.05 was employed.

2.7 Mechanical performance evaluation

As mentioned in the introduction section of this chapter, the mechanical performance of modified plastics was evaluated using various techniques, depending on the matrix polymer and the specimen dimension (bulk *versus* coating). Any characterization technique specific to a single given research chapter (e.g. the impact strength test in Chapter 6) is listed in the experimental section of that chapter. Therefore, we herein summarize those techniques common to Chapters 3-5, and particular emphasis is on the standard fracture test for bulk thermosets, and nanoindentation and abrasion tests for coatings.

2.7.1 Compact tension test

The fracture toughness of neat and modified bulk epoxy thermosets was quantified using a linear elastic fracture mechanics (LEFM) approach. Measurements were conducted following the compact tension ASTM standard D 5045 protocol. Fully cured epoxy plaques were used to prepare compact tension specimens. Prior to the test, a sharp pre-crack was initiated ahead of the machined notch in each specimen by tapping a fresh razor blade that was previously immersed into liquid nitrogen. Specimens were then pulled to failure at room temperautre on an Instron tensile tester (Model 1011) at a cross-head speed rate of 10 mm/min. The critical stress intensity factor (K_{Ic}) as the fractrue toughness of the matierial was calculated from the peak force (P_{max}) required to propagate the crack and the specimen geometry,

$$K_{Ic} = \frac{P_{max}}{BW^{1/2}} f(\frac{a}{W}) \tag{2.21}$$

where the subscript *I* indicates that the crack opening is mode I, *B* is the specimen thickness, *W* is the specimen width, *a* is the initial crack length, and *f(a/W)* is a geometric factor provided in the ASTM standard D 5045. A schematic of the compact tension test specimen is presented in Figure 2.4 and the geometry information is also labelled in the figure.

ASTM standard D 5045 requires several criteria for verifying the validity of the LEFM approach to determine fracture toughness. First, during the fracture test, the specimen should exhibit a linear relationship between load and displacement followed by a catastrophic failure (i.e., rapid crack propagation). For our thermoset polymer systems,

representative load *versus* displacement curves obtained from compact tension tests are shown in Figure 2.5, where the behavior of the neat and block copolymer modified materials follows the required trend.

Second, in the calculation of K_{Ic} following Equation (2.21), we have verified the selection of peak force P_{max} or the effective maximum force P_Q determined by following the ASTM procedures. Figure 2.6 presents an example of interpreting the load *versus* displacement curve to calculate K_Q. A best straight line (AB) was to fit the curve to determine the initial compliance, C, which is given by the reciprocal of the slope of line AB. A second line (AB') with a compliance 5% greater than that of line (AB) was drawn from the same intercept point A. When the maximum load that the specimen was able to sustain, P_{max}, fell within lines (AB) and (AB'), P_{max} was used to calculate K_Q. Otherwise, the intersection of line (AB') and the load *versus* displacement curve, P_Q, was used. Furthermore, when $P_{max}/P_Q < 1.1$, P_Q was always used in the calculation of K_Q. However, if $P_{max}/P_Q > 1.1$, the test was invalid. This restriction limits the magnitude of the ambiguity in the point of crack extension.

Third, the following relationship was also used to check the calculated K_Q values:

$$B > 2.5\left(\frac{K_{Ic}}{\sigma_y}\right)^2 \tag{2.22}$$

where σ_y is the material yield stress determined from a tensile test. This restriction guarantees that the plastic zone size is no more than 2% of the uncracked ligament width, validating plane strain conditions and justifying LEFM analysis. Therefore, the reported

K_Q values in this work can reflect the fracture toughness, K_{Ic}, of neat and modified thermoset materials.

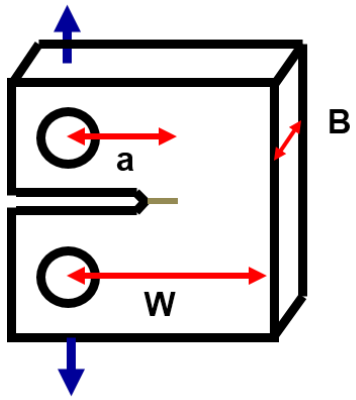

Figure 2.4 Schematic of compact tension test specimen. Typical dimensions for the specimen are B = 3.5 to 6.5 mm, W = 12 mm and a = 6 mm.

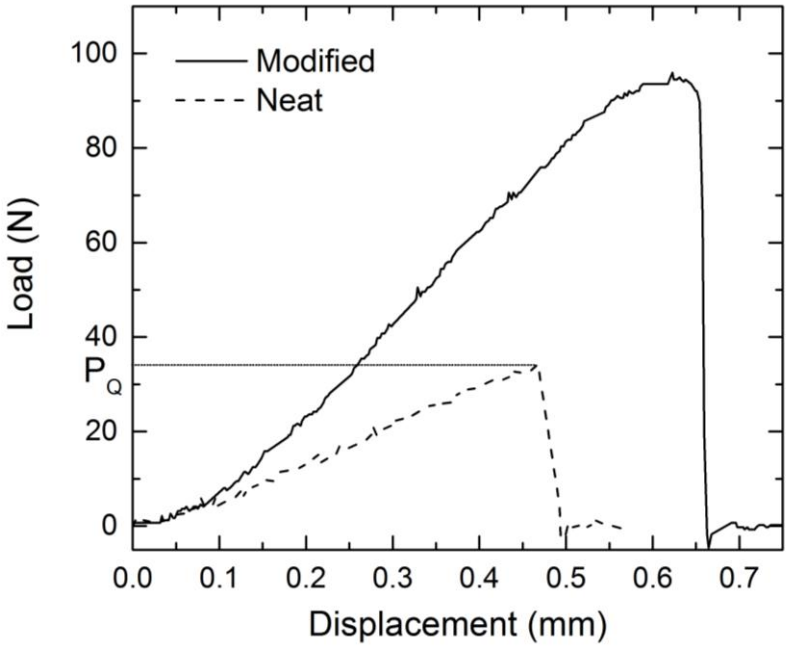

Figure 2.5 Typical load *versus* displacement curves obtained from compact tension tests for neat epoxy thermosets (dashed line) and block copolymer toughened epoxies (solid line). The linear relationship between load and displacement, and the catastrophic failure of the materials justify the use of LEFM for analysis.

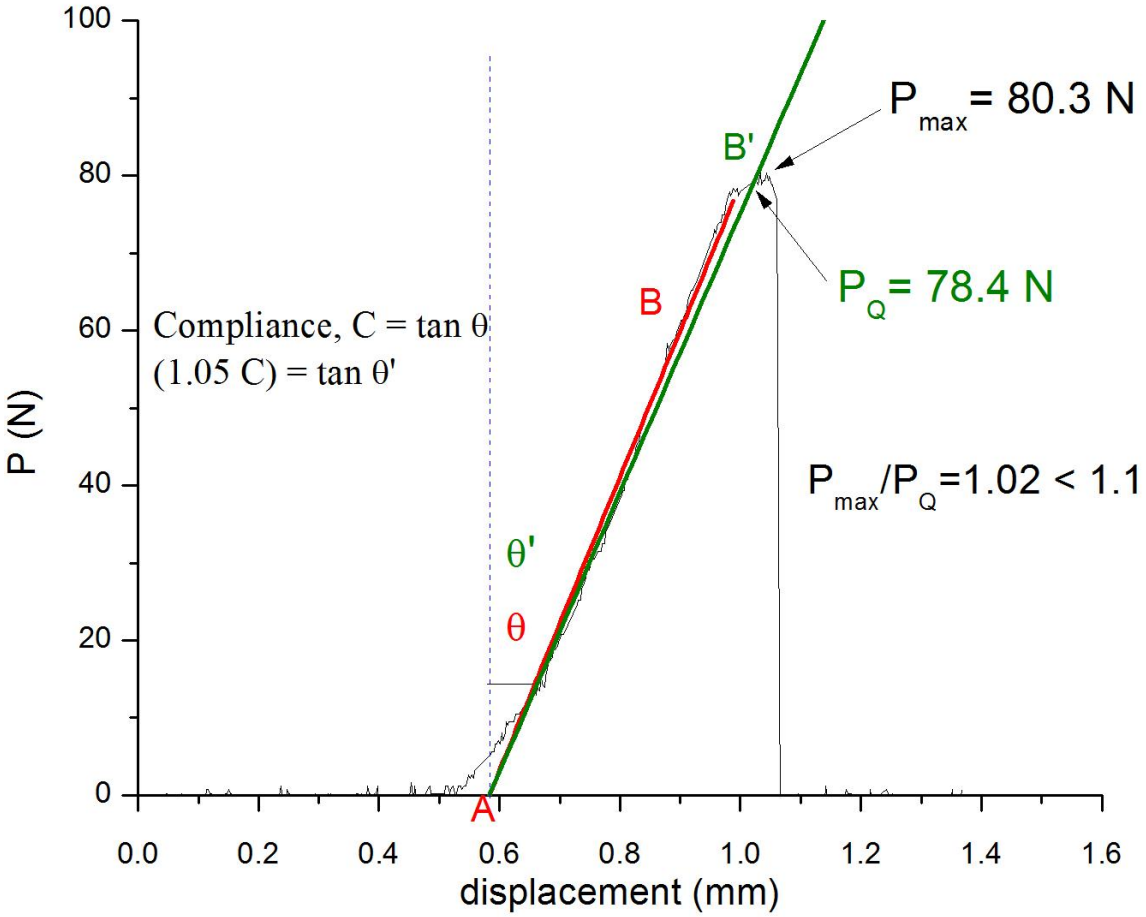

Figure 2.6 Determination of compliance and force from the load *versus* displacement curve obtained from compact tension tests. The compliance, C, is the reciprocal of the slope of the linear fitting line AB, and line AB' has a compliance 5% greater than that of line AB. In this example, the maximum load that the specimen can sustain, P_{max} does not fall with the lines AB and AB', and $P_{max}/P_Q < 1.1$, so the test is valid and P_Q should be used in the calculation of K_Q, following Equation (2.21).

In this work, we will also report the critical strain energy release rate (G_{Ic}) as the fracture energy per unit crack advancing area of the material, which can be determined by the following relationship under the plane strain condition:

$$G_{Ic} = \frac{K_{Ic}^2}{E}(1-\nu^2) \tag{2.23}$$

where E is the modulus of the material and ν is the Poisson's ratio taken as 0.34.[148] It is noted that Equation (2.23) only holds under the plane strain condition. The quantity G_{Ic} has a SI unit of J/m^2, and therefore it is much more physically appealing than the more obscure K_{Ic} that is in $MPa\cdot\sqrt{m}$. Accordingly G_{Ic} can be interpreted as the energy penalty for opening a new fracture surface within the material. Each reported value of K_{Ic} or G_{Ic} was averaged over at least five experimental values obtained from five identical specimens for each sample.

2.7.2 Dynamic Mechanical Spectroscopy (DMS)

The linear mechanical response of glassy polymers can be easily characterized using dynamic mechanical spectroscopy (DMS) measurements. During DMS experiments, it is typical to apply a sinusoidal strain of controlled frequency to the specimen and record the oscillating stress response. In our study we are interested in the dynamic elastic modulus (E^*), which can be resolved into a storage modulus (E') and a loss modulus (E''), reflecting the material's in-phase and out-phase response to the applied oscillatory strain, respectively. In glassy materials, the value of E^* is dominated by the storage component E'. Room temperature elastic moduli of neat and modified plastics were determined using a DMA-8000 (PerkinElmer) instrument with a three-point bending configuration. Rectangular shaped bars with dimensions of 40×4×2 (mm) were prepared from solid bulk plastics. Tests were carried out under a frequency of 10 rad/s and multi-strain between 0.01 and 0.1%. Each reported value of room temperature

modulus was averaged over five experimental values obtained from five identical specimens for each sample. To compare the value difference between different samples, a *t*-test with a threshold for statistical significance set to 0.05 was used.

2.7.3 Nanoindentation for coatings

Nanoindentation is a commonplace tool for the measurement of mechanical properties at small scales with high-resolution load-displacement data.[149] During a typical nanoindentation test, a micron-sized indenter tip is pressed into the test material's surface with a prescribed loading and unloading profile, and the applied force (P) and penetration displacement (h) are simultaneously recorded. Figure 2.7 shows an illustration of this process, and also a scanning electron microscope (SEM, see below) image of the indentation left on the material surface after fully retrieving the tip. Emphasis is given to the load-displacement curve, often referred to as the P-h curve, such as depicted in Figure 2.8. It is a typical data set obtained with a Berkovich indenter, where the deformation during loading is assumed to be both elastic and plastic, and only the elastic displacements are recovered during unloading. It has been proven that this technique does not apply to materials in which plasticity reverses during unloading.[150] Our epoxy coatings being tested are brittle in nature, giving the elastic response during unloading, and therefore facilitates the analysis with nanoindentation.

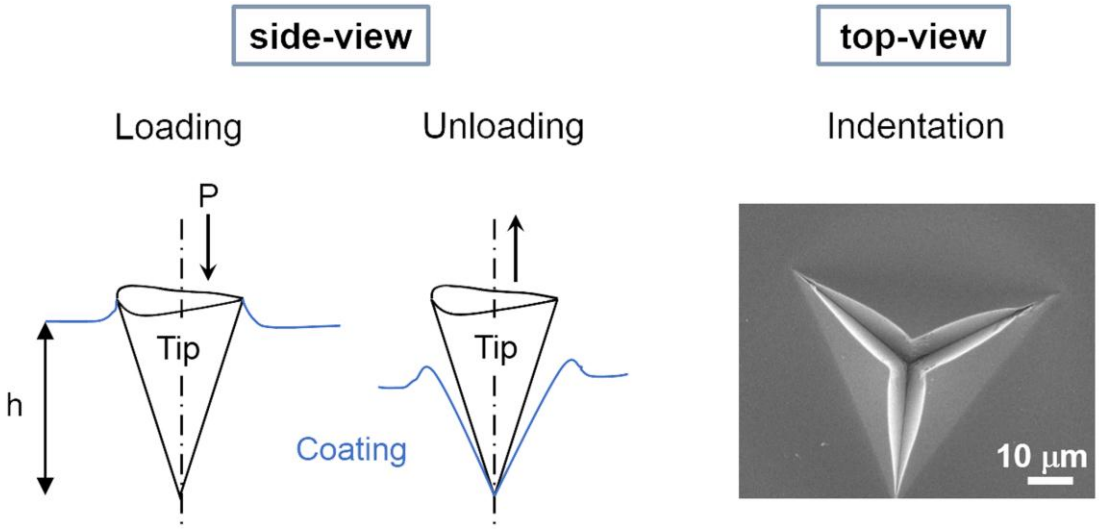

Figure 2.7 Schematic illustration of the nanoindentation testing. (Left) side-view of the indenter tip in the process of loading and unloading. The applied force (P) and penetration displacement (*h*) are simultaneously monitored and recorded. (Right) representative scanning electron microscope (SEM) image of an indentation left on the surface of an epoxy coating specimen after retrieving the indenter tip.

There are several critical parameters measured from the *P*-*h* curves: the maximum load, P_{max}, the maximum displacement, h_{max}, the elastic unloading stiffness, $S = dP/dh$, defined as the slope of the unloading curve during the initial stage of unloading (see Figure 2.8), and the final depth, h_f, which is the permanent depth of penetration after fully retrieving the indenter tip. The accuracy of indentation modulus (*E*) and hardness (*H*) measurements depends on how well these parameters can be measured experimentally.[150] The procedure adopted to quantify *E* and *H* is based on the unloading process as mentioned above. The basic assumption is that the contact periphery between the indenter tip and the testing material sinks in by some amount h_s that can be given by:

$$h_s = \varepsilon \frac{P_{max}}{S} \tag{2.24}$$

where ε is a constant dependent on the indenter geometry.

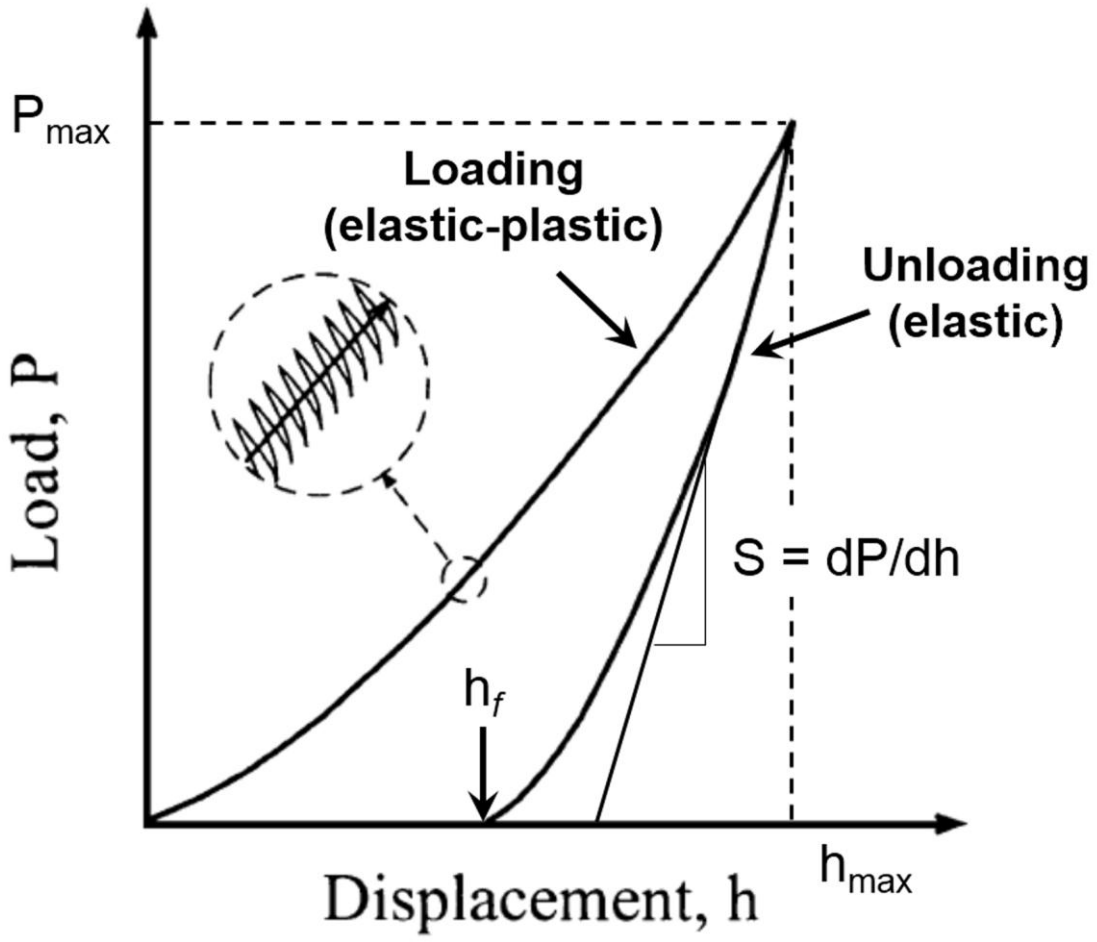

Figure 2.8 Schematic illustration of a typical load-displacement curve (*P-h* curve) obtained during the nanoindentation test of an elastic-plastic material. The inset in the circle shows the dynamic oscillation being imposed on the force signal during a test with the continuous stiffness measurement technique. The figure is adapted from Oliver et al.[151]

The vertical displacement of the contact periphery can be approximated from Equation (2.24) and the depth between the indenter and the specimen, h_c, is expressed as:

$$h_c = h_{\max} - h_s = h_{\max} - \varepsilon \frac{P_{\max}}{S} \tag{2.25}$$

The cross-section area of the indenter tip at a distance *d* back from its narrow head is carefully calibrated and described using an "area function" *F*(*d*), which then can give the contact area A by:

$$A = F(h_c) \tag{2.26}$$

Therefore, the indentation hardness is estimated from:

$$H = \frac{P_{\max}}{A} \tag{2.27}$$

Measurement of the elastic modulus is also subject to the contact area, as well as the unloading stiffness through the relation below:

$$S = \beta \frac{2}{\sqrt{\pi}} E_{eff} \sqrt{A} \tag{2.28}$$

where β is the correction factor, and E_{eff} is the effective elastic modulus defined by:

$$\frac{1}{E_{eff}} = \frac{1-\nu^2}{E} + \frac{1-\nu_i^2}{E_i} \tag{2.29}$$

where E and ν are the elastic modulus and Poisson's ratio of the specimen, respectively, and E_i and ν_i are the elastic modulus and Poisson's ratio of the indenter, respectively.

Over the past years, many new testing techniques has been developed for nanoindentation, among which the "continuous stiffness measurement" (CSM) technique is one of the most important. The basic idea is that stiffness is measured continuously during the loading of the indenter tip by imposing a tiny dynamic oscillation on the force (or displacement) signal and recording the amplitude and phase of the responsive

displacement (or force) signal (see the inset in Figure 2.8). This technique can dramatically reduce the reliance on the unloading curve and provide continuous results as functions of the penetration depth.[150]

An MTS Nanoindenter XP fitted with a Berkovitch indenter tip was employed to determine the room temperature modulus and hardness of the coatings. Using the CSM technique with an oscillatory amplitude of 2 nm, coating specimens, still on the substrate, were indented to a desired penetration depth, which was usually 1300 nm. This depth is constrained within 10% of the total coating thickness to minimize the substrate interference. The reported modulus and hardness values for each sample are based on the average over three separate specimens and nine distinct sampling points per specimen.

2.7.4 Abrasive wear resistance test for coatings

Abrasive wear resistance is an important parameter for assessing coating durability and overall performances. It depends on many coating properties, such as hardness, fracture toughness, extensibility and adhesion to the substrate.[152] The abrasive wear resistance of the epoxy coatings was determined by using a Taber Abraser (a schematic of the apparatus is shown in Figure 2.9) in accordance with ASTM standard D 4060-10. Coating specimens on the substrate (~ 80 μm thick PET plastic films) were cut to the appropriate size (50 mm × 70 mm) and abraded by a pair of CS-10 abrasive wheels (Taber Industries) with a 500g load on each wheel. Generally, the degree of wear is quantified by the weight loss from the coating for a given number of abrasion cycles.

However, the coating specimens in this work were too thin (coating thickness was usually 15-20 μm) to attain an appreciable weight loss.

Monitoring the optical transmission loss in the wear tracks is an effective alternative for transparent thin coatings,[152, 153] although the results cannot be directly correlated with wear resistance measured by weight loss.[154] Optical transmission was measured on a UV-vis spectrometer a wavelength of 630 nm following the ASTM standard D1003-11. The top surface of the uniformly abraded region of the specimen faced the incoming beam and the un-abraded region served as a reference (see the schematic of an abraded specimen in Figure 2.9). Lower transmitted intensity indicates a more damaged surface. As such, higher transmission is taken as an indication of a better abrasive wear resistance.[154, 155] Three separate specimens per coatings were tested, with measurements taken at least five different positions per specimen.

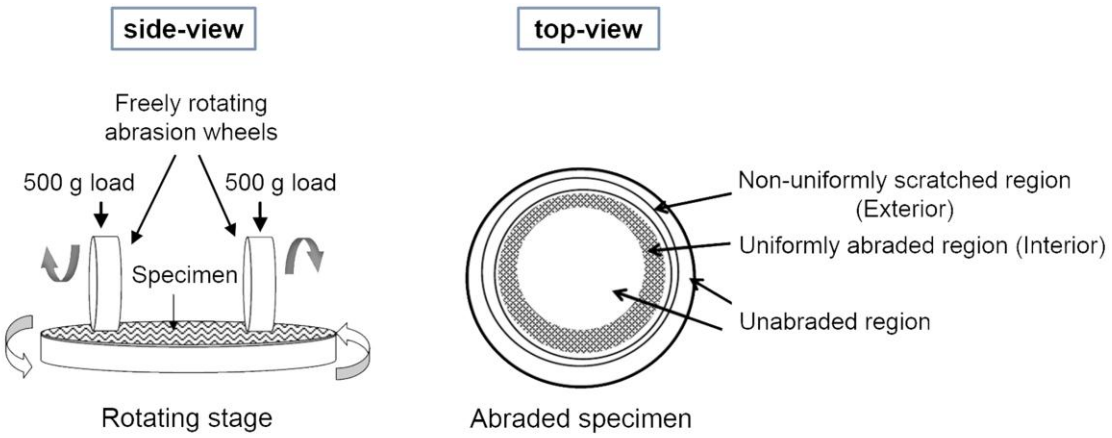

Figure 2.9 Schematic of the Taber Abraser (left) and the top surface of the abraded coating specimen (right). During abrasion tests, the rotating speed of the sample stage is about 1 cycle/s.

The surface roughness of abraded coating specimens was also measured to serve as complementary evidence of abrasive wear resistance. A Tencor P-10 Profilometer with diamond stylus tip with a radius of 5 μm was used to measure the surface roughness. A 0.5 mg load was applied. Measurements were made over the uniformly abraded regions as shown in Figure 2.9 and each specimen was first scanned with five parallel 5-mm lines separated by 5-10 mm, and then rotated by 90° for the same set of scans. Roughness is quoted as values of center line average (CLA), denoted by R_a, and root mean square average (*RMS*), denoted by R_q. Generally, there is always an increasing scatter in the roughness values as the abrasion cycles goes up, due to the spatial non-uniformity of the worn specimens. The final results are the average of three separate specimens for each sample.

2.8 Fractography

Scanning Electron Microscopy (SEM). In-depth fractography studies can reveal toughening mechanisms for block copolymer modifiers in different polymer matrices. Direct visualization of the fracture surfaces of failed compact tension specimens or the abraded surfaces of coating specimens was obtained using a JEOL 6500F field emission scanning electron microscope (FESEM). Prior to being examined under SEM, the specimen surfaces were sputtered with a thin platinum layer (ca. 5 nm) to prevent charging. The microscope was operated at an accelerating voltage of 5 *k*V and a working distance of about 10 mm.

Chapter 3

Toughening Jeffamine-epoxy bulk thermoset and coatings: a model system study*

3.1 Introduction

This chapter presents a model system study to establish the block copolymer toughening strategy in a thermoset polymer matrix, involving both bulk materials and coatings. It provides some fundamental background for the subsequent chapters. Typical areas for the utilization of commercially important epoxy resins are paintings and coatings. Epoxy coatings are widely used as protective barriers for marine, construction, aerospace and automotive components. These applications require that the coatings possess a high modulus, excellent chemical and thermal stability, great resistance to wear, and good adhesion to various substrates.[30-34] The highly crosslinked structure of epoxies imparts many of these properties, but it also leads to low fracture toughness.[16, 38]

*Reproduced in part with permission from (T. Li, et al., "Microstructure and performance of block copolymer modified epoxy coatings", *Progress in Organic Coatings*, Elsevier.)

Chapter 3

To make epoxy thermosets more effective for coating applications, a means for improving the fracture toughness is needed.

A large body of literature has shown that amphiphilic block copolymers, containing an epoxy-philic and an epoxy-phobic block, are effective second-phase modifiers for enhancing the toughness of bulk epoxy thermosets.[11, 61, 69, 87] The toughening efficacy of block copolymer modifiers is linked to their microphase separation in epoxy resins. Appropriately designed amphiphilic block copolymers self-assemble into various nanostructures, such as bi-layer vesicles, wormlike micelles, and spherical micelles, in the uncured epoxy precursor, driven by thermodynamic interactions. In most cases, these nanostructures are preserved in the cured thermosets,[49] and the curing reaction of epoxy precursors does not affect the pre-formed structures.[10] Although advances in the understanding of the performance of block copolymer toughening agents have been made during the last decade, little attention has been given to the toughening capabilities of block copolymers in epoxy coatings, with a majority of the work focused on bulk materials. In fact, the mechanical performance of rubber-toughened epoxy coatings has also been the subject of few studies.[42]

Incorporation of block copolymer toughening agents into epoxy coatings presents new challenges. For instance, Ramos et al.[86] recently showed that in the case of low block copolymer loading (< 10 wt.%), fast curing and relatively slow evaporation of casting solvents caused differential segregation of block copolymers through the thickness of epoxy films, resulting in a gradient of morphologies; however, a small thickness and faster solvent evaporation led to a homogeneous film. Garate and coworkers[83] also

investigated the block copolymer self-assembly in nanostructured epoxy thin films. They observed the block copolymer morphology transition from a short-range ordered spherical structure to some larger and less organized nano-domains as the curing reaction proceeded. While these authors did not explore the resultant influences on coating mechanical properties, their findings suggest that the block copolymer performance as a toughening agent may be affected by transitioning from bulk to coatings. As such, block copolymer modified epoxy coatings warrant study to better understand how observed property enhancement of bulk materials translates to coating applications.

This chapter presents an investigation of the performance of diblock copolymers as toughening agents in a model epoxy system. The resin being used, Jeffamine thermoset, has relatively simple characteristics in thermodynamics and curing kinetics. As mentioned in Chapter 2, two distinct diblock copolymers, poly(ethylene oxide)-*b*-poly(ethylene-*alt*-propylene) and poly(2-vinyl pyridine)-*b*-poly(1,2-butadiene), were employed. Block copolymer morphology and various properties of modified products were systematically studied in the as-prepared bulk thermoset and in solvent-cast coatings. The toughening mechanisms in bulk and coatings were also explored. The work presented in this chapter is aimed to provide a fundamental understanding of the structure-property relationship in a three-dimensional bulk state *versus* a two-dimensional thin film, which lays the basis for the subsequent chapters.

Chapter 3

3.2 Experimental

3.2.1 Materials

The chemical structures of the resin ingredients of the Jeffamine thermoset and the block copolymer modifiers being used are presented in Figure 3.1. The epoxy monomer is a diglycidyl ether of bisphenol-A (DGEBA) based epoxy monomer (Epon 828, PolySciences, Inc.). The starting material is a mixture of monomers and short oligomers with n=0 (88%), n=1 (10%), n=2 (2%). A polyether triamine (Jeffamine T-403 with x+y+z ~ 5.3, Huntsman Chemical) is used as the curing agent. As briefly mentioned in Section 2.2, this curing agent Jeffamine is designed for high temperature curing, which completes the network formation at 120 ℃. The merit of this epoxy system is that block copolymer modifiers self-assemble into different morphologies while being melt blended with the epoxy precursor, but the curing reaction would only play a role to fix those pre-formed structures. Because of this separation between the condensation of epoxy precursor and the self-assembly of block copolymers, the Jeffamine system is treated as a model system.

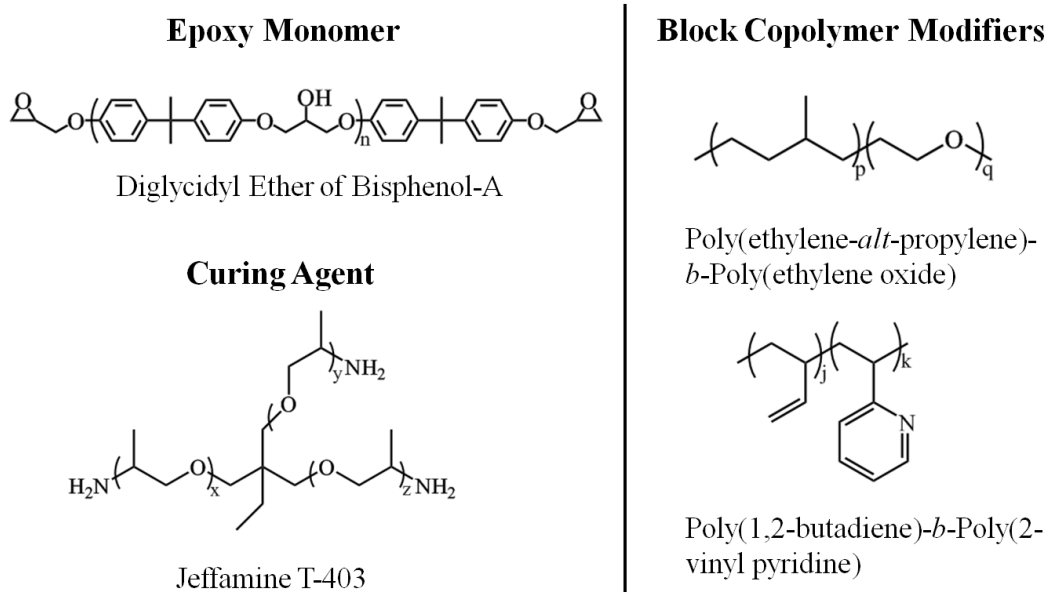

Figure 3.1 Chemical Structures of the resin ingredients of the Jeffamine thermoset and two block copolymer modifiers.

It is also mentioned in Chapter 2 that two different types of diblock copolymers, were synthesized and evaluated as the epoxy modifiers for this Jeffamine thermoset. They are poly(2-vinyl pyridine)-*b*-poly(1,2-butadiene) (P2VP-PB) and poly(ethylene oxide)-*b*-poly(ethylene-*alt*-propylene) (PEO-PEP). The polymerization protocols for both diblocks have been described in Section 2.3.1. Table 3.1 summarizes the molecular characteristics of the two block copolymer modifiers. The block copolymer composition was determined using ^{1}H NMR. The number average molecular weight and dispersity were determined by room temperature gel permeation chromatography (GPC) with polystyrene standards and tetrahydrofuran (THF) as the solvent. Both diblocks are nearly monodisperse. PEO-PEP is rich in the epoxy-philic PEO block. The molecular weight of

P2VP-PB is less than half the molecular weight of PEO-PEP and is symmetric with regards to the volume fractions of the epoxy-philic and epoxy-phobic blocks. Along with differences in composition, the chemistries of the epoxy-philic blocks impart fundamental differences between the two copolymers. P2VP can easily form hydrogen bonds with the epoxy network, which affords exothermic mixing, making it a good alternative for PEO. At room temperature, PEO is semi-crystalline with a melting point near 50 ℃, while P2VP is a rigid chain with a higher T_g (100 ℃) than PEO (–60 ℃). Both epoxy-phobic blocks produce rubbery, compliant cores in the Jeffamine thermoset matrix.

Table 3.1 Molecular characteristics of diblock copolymers for the Jeffamine thermoset.

[a]Diblocks	[b]M_n (kg/mol)	[c]$f_{epoxy\text{-}philic}$	M_w/M_n
P2VP-PB	10.3	0.50	1.05
PEO-PEP	26.5	0.57	1.09

[a] P2VP = poly(2-vinyl pyridine); PB = poly(1,2-butadiene); PEO = poly(ethylene oxide); PEP = poly(ethylene-*alt*-propylene). P2VP and PEO are the "epoxy-philic" blocks.

[b] Number average molecular weight determined by gel permeation chromatography (GPC) at 30 ℃ with THF as the mobile phase and calibrated with polystyrene standards.

[c] Volume fraction of the epoxy-philic block calculated using densities ρ_{P2VP} = 1.10 g/cm^3, ρ_{PB} = 0.91 g/cm^3, ρ_{PEO} = 1.07 g/cm^3 and ρ_{PEP} = 0.91 g/cm^3.[156, 157]

3.2.2 Sample preparation

PEO-PEP modified epoxy samples were prepared by first blending the block copolymer with the epoxy monomer at 70-75 ℃ for 24 h until full dissolution. The blend

was then cooled down to 60 ℃ and 46 phr (parts per hundred resin) of the curing agent were added to make the molar ratio of epoxide groups to reactive hydrogens on amine groups 1:1.6. The blend was stirred at 60 ℃ for 30 min before being degassed under dynamic vacuum for 5-10 min. A portion of this blend was poured into a preheated mold (60 ℃) to make bulk samples. The remaining material was used to prepare the coating solution, ensuring that bulk samples and coating samples always came from the same batch. The blend designated for the coating solution was left to pre-cure at 60 ℃ for an additional 40 min in order to build up the viscosity of the system, a step which is necessary to prevent dewetting of the coating.[158] Bulk samples also underwent the same pre-curing for consistency, but after being added to the mold due to transfer issues of the thermoset blend after the pre-cure was complete. After the pre-curing, the blend to be used for the coating solution was cooled down to room temperature and dissolved in the casting solvent, toluene, to create solutions of 30 wt.% epoxy resin. The solution was stirred at room temperature overnight until a clear coating solution was obtained.

Coatings were prepared by casting the solution onto an 80 μm polyethylene terephathalate (PET) (3M) substrate using a wire-wound rod (rod number 64) (R.D. Specialties, Inc.). The PET substrates were thoroughly rinsed with distilled water and isopropanol before use. The initial (wet) coating thickness was approximately 160 μm. As-cast coatings were allowed to dry under ambient conditions for at least 30 min to ensure the removal of toluene. Dried coatings and bulk thermosets were then cured at 80 ℃ for 1 h followed by another hour at 120 ℃, after which the oven was turned off and samples slowly cooled down to room temperature. Cured bulk samples had a thickness of

3 mm, while the thickness of the cured coating was 15 ± 2 μm as determined by digital micrometer.

A similar protocol was followed to prepare P2VP-PB modified samples. In order to reduce undesired side-reactions of the poly(1,2-butadiene) block during the mixing at high temperatures, a blending solvent, THF, was used as a co-solvent to dissolve this block copolymer in Epon 828 at room temperature overnight. A 10:1 weight ratio of the co-solvent to diblock was used. THF was completely removed from the system under dynamic vacuum at 40 ℃ for 1-2 h. After this step, the block copolymer/epoxy monomer mixture was heated up to 60 ℃ and treated following the same protocol as described above.

Neat materials (bulk thermosets and coatings) were prepared in an identical fashion, with the omission of the epoxy/block copolymer mixing step.

3.3 Results and discussion

3.3.1 Block copolymer morphology: bulk *versus* coating

Representative TEM images of the cross-sections of fully cured bulk samples and 15 μm thick coatings containing 2 and 5 wt.% PEO-PEP are presented in Figure 3.2. In both bulk and coating samples, the block copolymer self-assembles into well dispersed spherical micelles consisting of a PEP core and PEO corona. This nanostructure closely resembles that reported in previous work with this epoxy system and copolymer.[49] At

both copolymer loadings, the modified bulk samples are characterized by spheres with narrowly distributed diameters of 22 ± 5 nm (for Figure 3.2a) and 23 ± 4 nm (for Figure 3.2b). However, the sphere size in the cured coatings is reduced to half of that in bulk epoxy, 11 ± 3 nm in diameter (for Figure 3.2c and d). The size distribution of micelles was determined using ImageJ.[159]

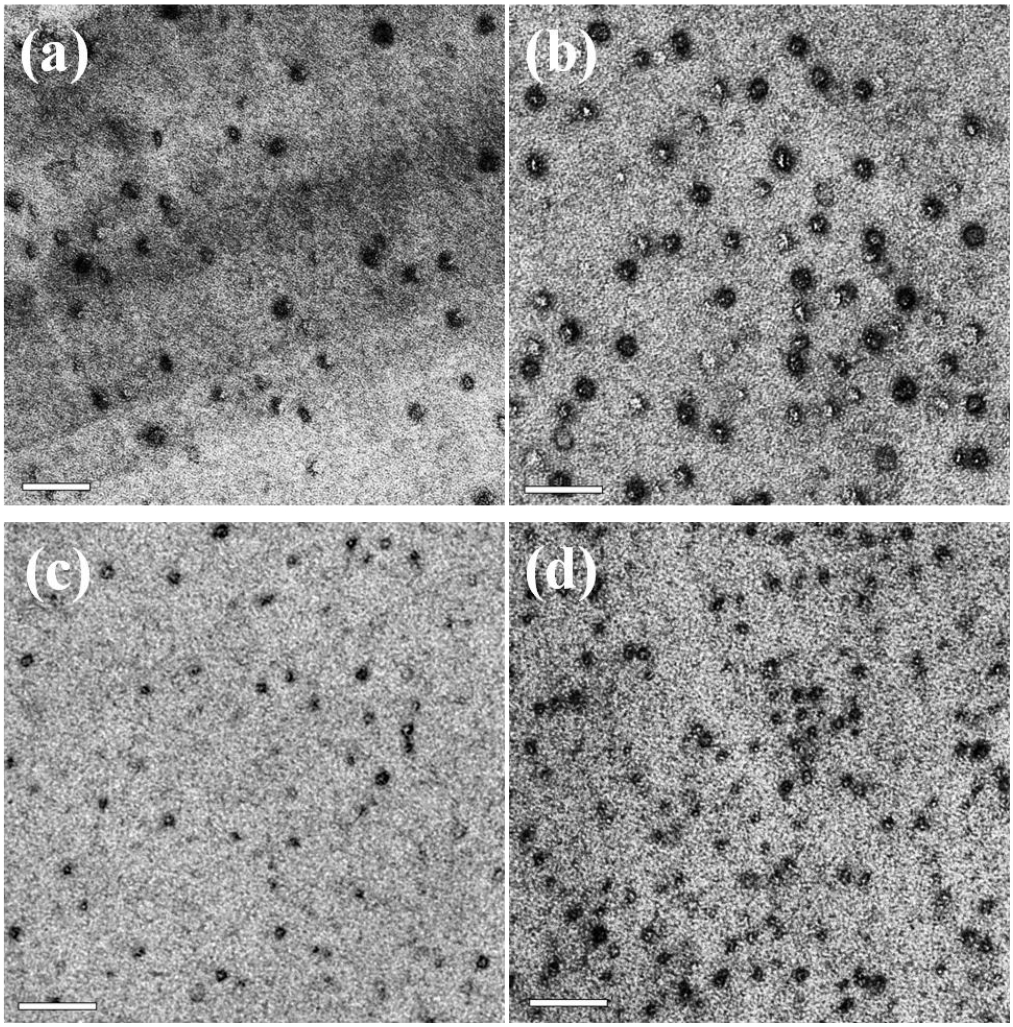

Figure 3.2 Representative TEM images of the cross-section of PEO-PEP modified (a - b) bulk epoxy thermosets and (c - d) 15 μm coatings. The block copolymer loading is 2 wt.% for (a) & (c) and 5 wt.% for (b) & (d). RuO_4, used as contrast agent, preferentially stains the PEO/epoxy interface, making brighter cores with darker coronas.[160] Scale bars represent 100 nm.

The difference in the micelle size between the bulk and coating samples most likely reflects the use of toluene as a casting solvent in the coating formulation. Previous small angle X-ray scattering results have verified the existence of PEO-PEP spherical micelles with a diameter of about 26 nm in the epoxy blend prior to curing.[95] This

indicates that the micellization of block copolymers occurs during melt-blending, and the cross-linking of epoxy monomers fixes those pre-formed structures. Based on the polymer-solvent interaction parameter, toluene is roughly a neutral solvent for PEO-PEP and the epoxy resin so that microphase separation leads to spherical micelles that are swollen with solvent. Removal of solvent results in a core diameter that is smaller than the thermodynamically preferred dimension due to kinetic limitations associated with the redistribution of block copolymer chains necessary to recover the equilibrium condition. This effect is well documented in solvent cast diblock copolymer-homopolymer blends[161] and recent experiments with PEP-PS diblock copolymer micelles dispersed in the selective solvent squalene[147, 162] quantify slow molecular exchange dynamics in this class of materials.

Figure 3.3 shows the TEM images of bulk and coating epoxy samples prepared with P2VP-PB at 2 and 5 wt.% loading. At 2 wt.% of P2VP-PB, the morphology in both bulk and coatings samples is again spherical micelles. Unlike PEO-PEP, the diameters of the spheres (11 ± 2 nm for Figure 3.3a, 10 ± 2 nm for Figure 3.3c) in bulk and coatings are about the same. Although toluene is a slightly selective solvent for PB, here, it did not affect the apparent size of micelle cores in the stained TEM specimens.

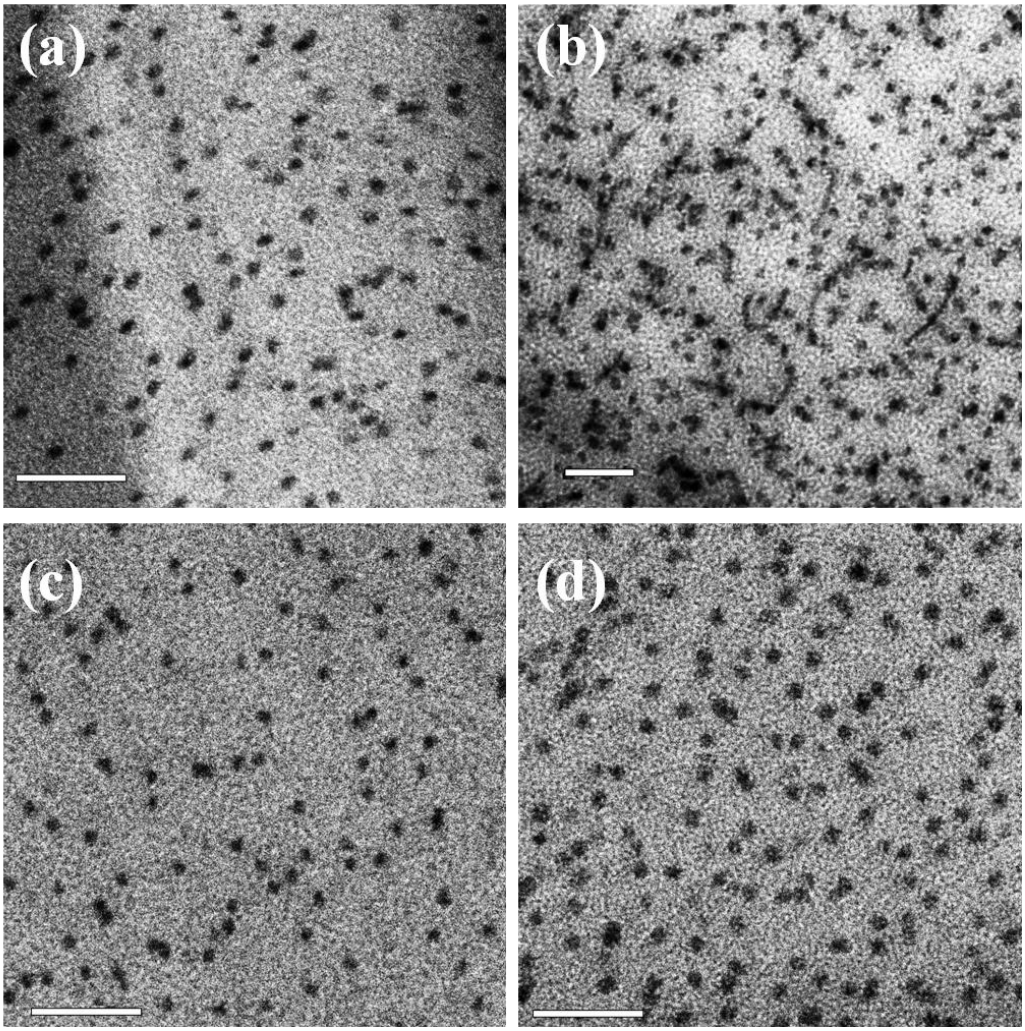

Figure 3.3 Representative TEM images of the cross-section of P2VP-PB modified (a - b) bulk epoxy thermosets and (c - d) 15 μm coatings. The block copolymer loading is 2 wt.% for (a) & (c) and 5 wt.% for (b) & (d). OsO_4, used as contrast agent, preferentially stains the PB sub-domain, making the core of spherical micelles dark. Scale bars represent 100 nm.

At a diblock loading of 5 wt.%, P2VP-PB again self-assembles into spherical micelles with a diameter of 12 ± 2 nm in coatings (Figure 3.3d). However, in the bulk samples, sparsely dispersed cylindrical structures along with spherical micelles (13 ± 3 nm in diameter) are observed (indicated by arrows in Figure 3.3b). These cylindrical

structures do not show in the bulk sample with 2 wt.% block copolymer loading. The appearance of such morphology indicates that 5 wt.% P2VP-PB may be close to a critical concentration for spherical-to-wormlike micelle morphological transition. The lack of such microstructures in the coatings suggests that the presence of toluene changes the phase behavior of the system and suppresses this transition.

In addition, all coatings maintain optical transparency owing to the small size of the block copolymer inclusions.

Compared to bulk samples, coating samples have a much larger interface area-to-volume ratio, which plays an important role in affecting the distribution or interactions between block copolymer micelles. Therefore, we are also interested in the coating microstructure with respect to the micelle distribution throughout thickness. Figure 3.4 shows TEM images of the coating/substrate interface for 15 μm coatings prepared with PEO-PEP and P2VP-PB. The arrows indicate the position of the coating/substrate interface prior to removing the coating from the substrate. Images of the bulk portion and free surfaces of coatings prepared with either copolymer show random distribution of micelles with no segregation to the free surfaces. However, images shown here reveal a higher micelle concentration near the coating/substrate interface. Figure 3.4c and d show that a single layer of P2VP-PB micelles appears at the interface for both 2 and 5 wt.% loading. In Figure 3.4a and b, a less distinct preference of the PEO-PEP micelles is observed for the coating/substrate interface. Neat epoxy coatings prepared in the same manner were also examined as controls to confirm the observed segregation is not an artifact of staining.

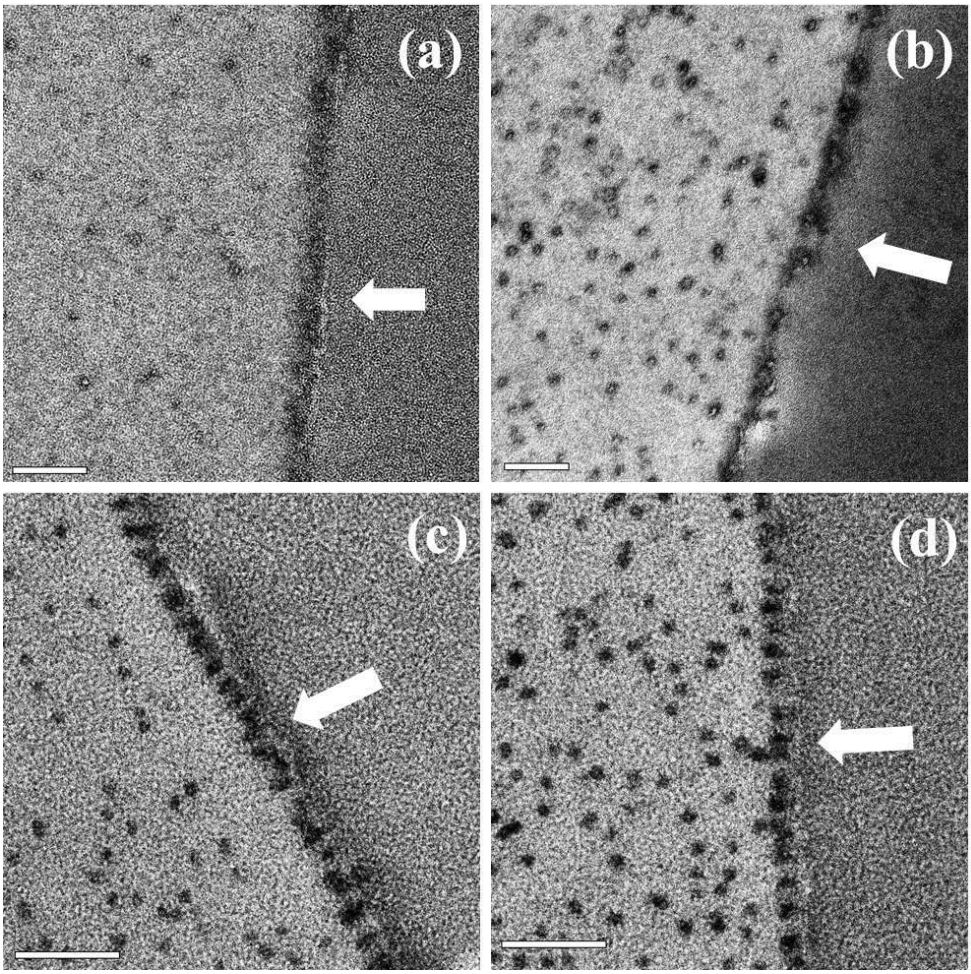

Figure 3.4 Representative TEM images of the cross-section of 15 μm epoxy coatings modified with (a) 2 wt.% and (b) 5 wt.% PEO-PEP; (c) 2 wt.% and (d) 5 wt.% P2VP-PB. The coating/substrate interface is indicated with white arrows. For PEO-PEP modified samples, RuO_4 preferentially stains the PEO/epoxy interface. For P2VP-PB modified ones, OsO_4 preferentially stains the micelle core. Scale bars represent 100 nm.

Table 3.2 summarizes the experimental data from the literature for the surface energy (γ) of each component in the epoxy system and the PET substrate. The surface energy of epoxy resin generally is lower than that of PEO or P2VP block and hence there is no preference for micelles on the free surface. There are several approaches to estimate

interfacial energies.[163] In Table 3.2, estimations of the interfacial energy between P2VP, PEO or epoxy with PET from Antonow's rule[164, 165] are listed. This rule approximates the interfacial energy between two phases α and β, $\gamma_{\alpha/\beta}$, as the absolute value of the difference between the two surface energies, γ_α and γ_β.

Table 3.2 Surface and interfacial energy of different component in the formulation.

Component	Surface energy (mJ/m^2)	[a]Interfacial energy (mJ/m^2)
PEO	46.7 [166]	$\gamma_{PEO/PET}$ = 3.1
P2VP	50 [167]	$\gamma_{P2VP/PET}$ = 0.2
Epoxy (amine cured DGEBA)	43-47 [168]	$\gamma_{epoxy/PET}$ = 2.8-6.8
Commercial PET film	49.8 [169]	--

[a] Estimations of the interfacial energy were calculated based on Antonow's rule.[164, 165]

The interfacial energy between P2VP and PET, $\gamma_{P2VP/PET}$ is 0.2 mJ/m^2, compared to $\gamma_{epoxy/PET}$, which ranges from 2.8 to 6.8 mJ/m^2. Thus, there is an energetic preference for the single layer of P2VP-PB micelles along the coating/substrate interface. On the other hand, there is no significant energy preference for PEO-PEP micelles to segregate to the coating/substrate interface, because $\gamma_{PEO/PET}$ is comparable to $\gamma_{epoxy/PET}$. The free energy argument serves as a possible explanation for the micelle distribution observed in the epoxy coatings. However, other underlying factors may also influence this phenomenon. A more detailed exploration of block copolymer segregation in epoxy coatings and its potential implications on coating properties is a subject of future research.

3.3.2 Mechanical and thermal properties: bulk *versus* coating

The mechanical properties and glass transition temperatures (T_g) of neat and modified bulk epoxy samples are summarized in Table 3.3. Statistically significant changes in T_g are not observed upon the addition of either block copolymer to bulk epoxy. In P2VP-PB modified samples, at either copolymer loading, the elastic modulus does not show a statistically significant change. While the modulus of the bulk materials containing 2 or 5 wt. % PEO-PEP is statistically lower than that of the neat materials, the drop is only between 7 and 9%. These results are consistent with previously reported observations for PEO-PEP modified epoxy thermosets.[49, 50, 170]

Table 3.3 Properties of bulk epoxy samples with different block copolymer loadings

Sample	E' (GPa)	K_{Ic} (MPa·$m^{1/2}$)	G_{Ic} (J/m^2)	T_g (℃)
Neat	2.31 ± 0.05	0.98 ± 0.13	368 ± 98	79 ± 3
2 wt.% PEO-PEP	2.14 ± 0.09	1.78 ± 0.21	1309 ± 314	79 ± 4
5 wt.% PEO-PEP	2.10 ± 0.10	1.91 ± 0.05	1536 ± 109	78 ± 3
2 wt.% P2VP-PB	2.31 ± 0.09	1.94 ± 0.06	1441 ± 105	76 ± 7
5 wt.% P2VP-PB	2.22 ± 0.08	2.00 ± 0.07	1594 ± 125	77 ± 4

Both PEO-PEP and P2VP-PB are effective in improving the toughness of the bulk epoxy thermoset. At either 2 wt. % or 5 wt.% of loading, the addition of PEO-PEP approximately doubled K_{Ic}, and caused a nearly four-fold increase in G_{Ic}. The toughening effect does not depend on the copolymer concentration. These agree with the results in a previous publication.[49] The addition of the P2VP-PB copolymer led to comparable

increases in K_{Ic} and G_{Ic}. Though the average K_{Ic} and G_{Ic} values of the PEO-PEP loaded and P2VP-PB loaded samples are different, the toughening effects are not statistically different.

As a comparison, the mechanical and thermal properties of neat and modified epoxy coatings are summarized in Table 3.4. Modulus (*E*) and hardness (*H*) of cured 15 μm thick coatings were determined by nanoindentation. To obtain stable and valuable results, only data points after 200 nm penetration depth were used to calculate *E* and *H*. The t-test concluded that coatings modified with 2 wt.% of P2VP-PB had a modulus similar to that of the neat ones, while 5 wt.% of P2VP-PB caused a statistical drop by 7% in coating modulus. Coatings loaded with 2 and 5 wt.% of PEO-PEP were also found to be statistically different than the neat one, exhibiting a 5% and 9% decrease in modulus, respectively. On the other hand, the hardness values for all modified coatings are statistically lower than those of the neat epoxy, by 7-12%. The small decrease in these properties is consistent with the bulk epoxy results.

The trends in the modulus for bulk and coating samples agree, but quantitative comparison is not possible due to the different characterization techniques employed (three-point bending *versus* nanoindentation). Several researchers have reported that the Young's modulus determined by a three-point bending test is generally lower than that obtained with nanoindentation, due to various factors, including the difference in material volumes sampled, surface and substrate effects during indentation, among others.[171-173]

Additionally, the glass transition temperatures of the neat and modified coatings are also listed in Table 3.4. Again, the T_g is not affected by the presence of either copolymer at any concentration. This trend is in agreement with the bulk results.

Table 3.4 Properties of epoxy coatings with different block copolymer loadings

Coating sample	E (GPa)	H (GPa)	T_g (℃)
Neat	3.54 ± 0.09	0.223 ± 0.009	82 ± 2
2 wt.% PEO-PEP	3.35 ± 0.05	0.204 ± 0.002	80 ± 4
5 wt.% PEO-PEP	3.23 ± 0.15	0.197 ± 0.004	79 ± 3
2 wt.% P2VP-PB	3.49 ± 0.05	0.208 ± 0.003	81 ± 4
5 wt.% P2VP-PB	3.29 ± 0.13	0.196 ± 0.003	80 ± 2

3.3.3 Abrasive wear resistance of epoxy coatings

Abrasive wear resistance is an important parameter for assessing coating durability. It depends on many coating properties, such as hardness, fracture toughness, friction, extensibility, adhesion to the substrate, and the hardness and size of debris.[174, 175] Furthermore, displacement of material occurs as carbide particles or asperities move against the coating surface with a variety of mechanisms playing a role in deforming the coating, including plastic deformation (from plowing), asperity scratching, debris particle scratching, coating fracture and delamination.[154] As such, quantification of the wear resistance is an effective means for determining the overall performance of the block copolymer modifiers in improving the protective properties of the epoxy coatings.

The abrasive wear resistance of neat and modified epoxy coating samples was determined by an abrasion test as described in detail in Section 2.7.4. Here, Figure 3.5

shows the loss in optical transmission of coatings with the number of abrasive wear cycles. For all abraded samples, the reported transmission is normalized relative to the transmission of the un-abraded portion of each specimen. The transmitted intensity of neat epoxy coating decreases to less than 50% of its initial value over the course of 500 wear cycles. During the abrasion test, P2VP-PB modified coatings behave similarly to PEO-PEP modified ones. At the early stage of the abrasion (up to 30 cycles), the abrasion resistance of the block copolymer modified coatings is the same as that of the neat epoxy coatings. However, beyond 30 cycles, coatings containing block copolymer display greater resistance to abrasive wear. As the number of wear cycles increases, coatings loaded with 5 wt.% block copolymer perform better than those loaded with 2 wt.% modifier. At 500 cycles, the improvement in transmission is about 22% for 2 wt.% of block copolymer loading and 44% for 5 wt.% of loading, compared with the neat.

To better understand the implications of the abrasive wear resistance in terms of fracture resistance, a simplified relationship between the abrasive wear resistance and fracture energetics developed by Lee[176] for the abrasive wear of brittle polymers is considered:

$$V_w = k\left(\frac{\sigma_y \gamma^{3/2}}{G_{Ic} H^{3/2}}\right) L \tag{3.1}$$

where V_w is the wear volume, k is a constant, L is the sliding distance, σ_y is the yield strength, γ is the surface energy, H is the indentation hardness and G_{Ic} is the mode I critical strain energy release rate. According to Equation (3.1), if the yield strength and surface energy of the epoxy coatings are assumed to remain unchanged after block

copolymer modification, a tougher and harder coating would exhibit a higher abrasive wear resistance. The indentation hardness was almost unaffected by the addition of PEO-PEP or P2VP-PB block copolymers in the coating. Therefore, it is reasonable to suggest that the abrasive wear resistance findings in Figure 3.5 show that modified coatings have higher fracture toughness relative to the neat coating.

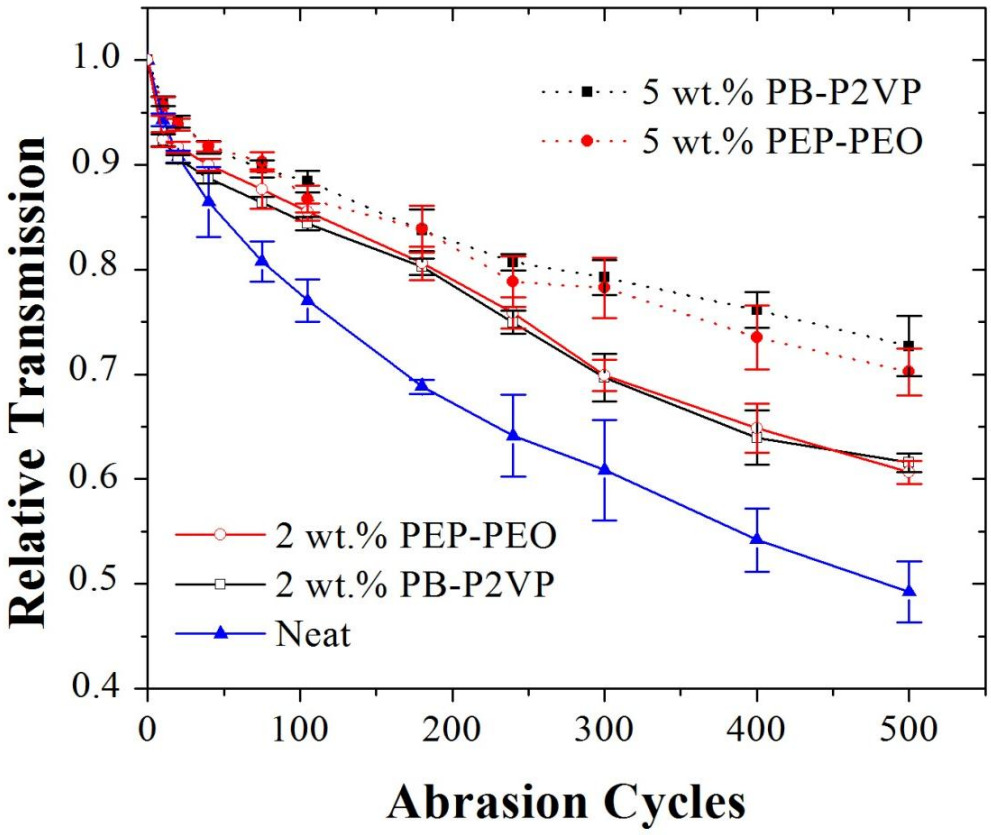

Figure 3.5 Optical transmission (at a wavelength of 630 nm) of coatings after different abrasion cycles relative to an unabraded portion of the specimen.

To further quantify the extent of damage during abrasive wear cycles, the surface roughness of neat and block copolymer-loaded coatings were measured. The surface

roughness of coatings as a function of abrasion cycles is presented in Figure 3.6. Both R_a and R_q increase as the number of cycles increases. This result indicates that that the abrasion did cause damage to coating surfaces. There is greater scatter in the results at higher cycles, indicating an increasing surface inhomogeneity with continued abrasion.

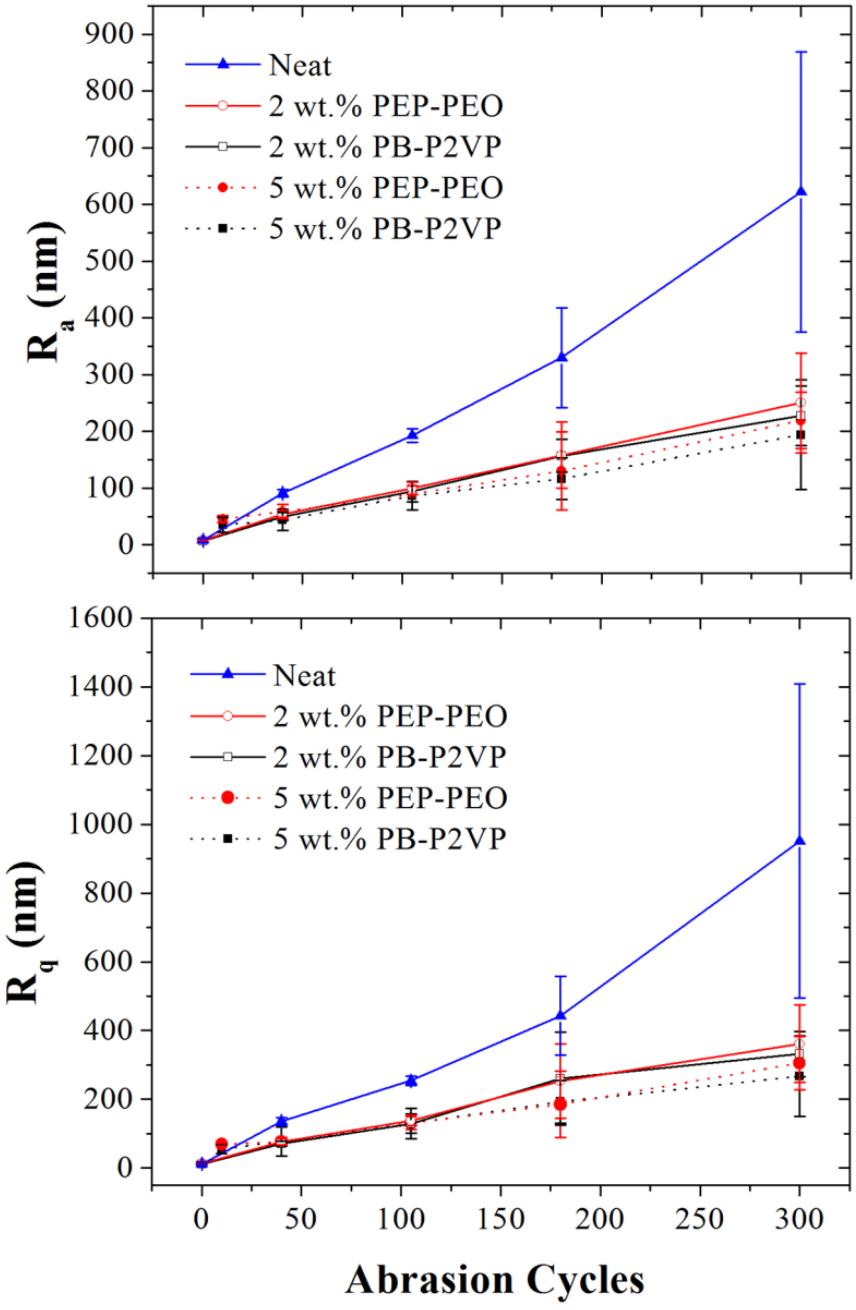

Figure 3.6 The surface roughness of coatings with increasing abrasion cycles.

After the same number of abrasion cycles, the surface of neat coatings was consistently rougher than those of modified coatings. Up to 100 abrasion cycles, the

scatter in the data is sufficiently small that a significant improvement in the performance of the modified coatings is apparent based on the average R_a and R_q values. At higher cycle counts, the extent of improvement upon the addition of copolymer modifier cannot be quantified based on the average R_a and R_q values given the scatter in the data. Nonetheless, in general, the roughness of the modified samples is still lower than that of the neat sample within the error of the measurements. Up to 300 cycles, the difference in surface roughness between the two types of modifiers and the two loadings is small. However, a major limitation of these measurements is that that all the roughness values were measured using a 5 μm radius stylus. As such, only large damage to the coatings was measureable, while small features were likely missed, providing only an estimation of the overall roughness of the abraded coating surface. These smaller features likely do contribute to the transmission loss, giving rise to some of the discrepancy observed between the transmission and abrasion experiments.

SEM images of abraded neat and PEO-PEP or P2VP-PB-modified coatings are shown in Figure 3.7. These low magnification images of wear tracks show many scratches in a cross-hatched pattern, typical of abrasion from a Taber Abraser. Only images of the samples in the initial stage of wear (after 75 abrasion cycles), in which individual scratches are still distinguishable, are presented here. Comparison of Figure 3.7 (a) and (b) or (c) shows that there were fewer visible scratches on the surface of block copolymer modified coatings, and those scratches also caused less damage there. These SEM images are in a good agreement with optical transmission and surface roughness results.

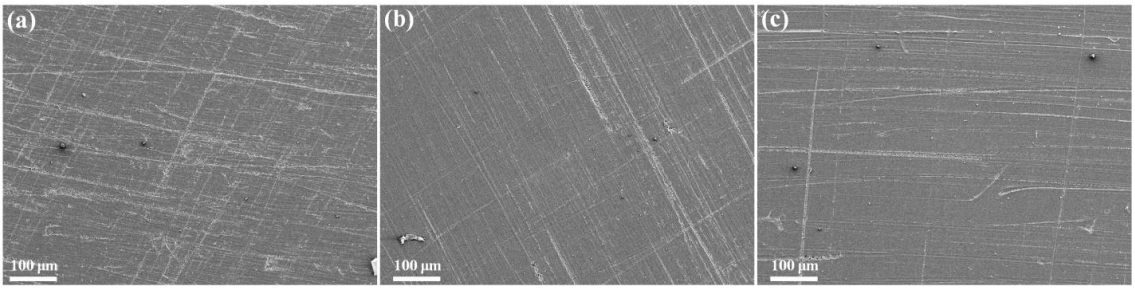

Figure 3.7 Representative SEM images of the abraded surfaces of (a) neat, (b) 5 wt. % PEO-PEP modified and (c) 5 wt.% P2VP-PB modified epoxy coatings with 15µm thickness and 75 abrasion cycles.

3.3.4 Toughening mechanisms for micelles: bulk *versus* coating

In bulk epoxy thermosets, the toughening mechanism for rubbery core spherical micelles has been well documented in the literature.[93, 96] During fracture tests, as the primary crack propagates, the nano-sized micelles in the process zone are easily cavitate within their rubbery cores (PB or PEP) under a tri-axial stress state. This cavitation can effectively promote the shear band formation, facilitating the shear yielding in the thermoset matrix. Consequently, the enhanced matrix plastic deformation in the form of accelerated shear banding and void growth creates great energy penalty for crack propagation, and therefore leads to a significant improvement in the material fracture toughness. In a previous work,[49] additional contribution to toughness enhancement was proposed to come from network disruption. The presence of a zone of disrupted network material arising due to the mixing of the corona chains with the epoxy can also facilitate the initiation of shear yielding in the matrix, although to a lesser extent than that induced by cavitation. He et al.[177] presented evidences to support this network disruption

mechanism. They reported two different T_1 relaxation times in NMR experiments associated with the aromatic carbons of an epoxy resin containing block copolymers endowed with either PEO or polycaprolactone (epoxy-philic) blocks. The slow and fast relaxation times were attributed to carbon atoms in the "perfect" network and those in the locally damaged network, respectively. However, in this study, we do not observe a significant difference in the toughening efficacy between the two types of spherical micelles, even though their coronas are believed to be very different in properties. We conjecture that the network disruption caused by the high-T_g P2VP corona chains is probably still similar to that caused by PEO corona chains.

Based on the understanding of toughening mechanisms in a three-dimensional bulk state, we are interested to see how those mechanisms translate to a two-dimensional thin film. TEM images of abraded coatings provide further insight into the improved abrasion resistance of block copolymer coatings. Figure 3.8 shows the cross-section TEM images of abraded coatings containing 5 wt.% of P2VP-PB block copolymers subjected to 500 abrasion cycles. Close to the abraded surface, the micelles are deformed into elongated rod shapes. This observation indicates plastic deformation of the coating in response to the stress field generated by the abrasive particles. Similar, though less vivid, elongated structures were also observed in the PEO-PEP modified coatings. During the abrasion test, when the carbide particles penetrate into the coating, they produce a stress field that results in material damage and removal. Micelles in this area are subjected to the stress field, which causes the rubbery core of the spherical micelles to deform. Deformation of the rubbery core facilitates epoxy matrix shear yielding, which is still believed to be the

primary toughening mechanisms in block copolymer-modified epoxy coatings. A consequence of the shear yielding is that the dissipation of the stress reduces the extent of crack propagation of the damaged zone into the coating. Ultimately, the damage incurred during abrasion of modified coatings is less than that of unmodified coatings.

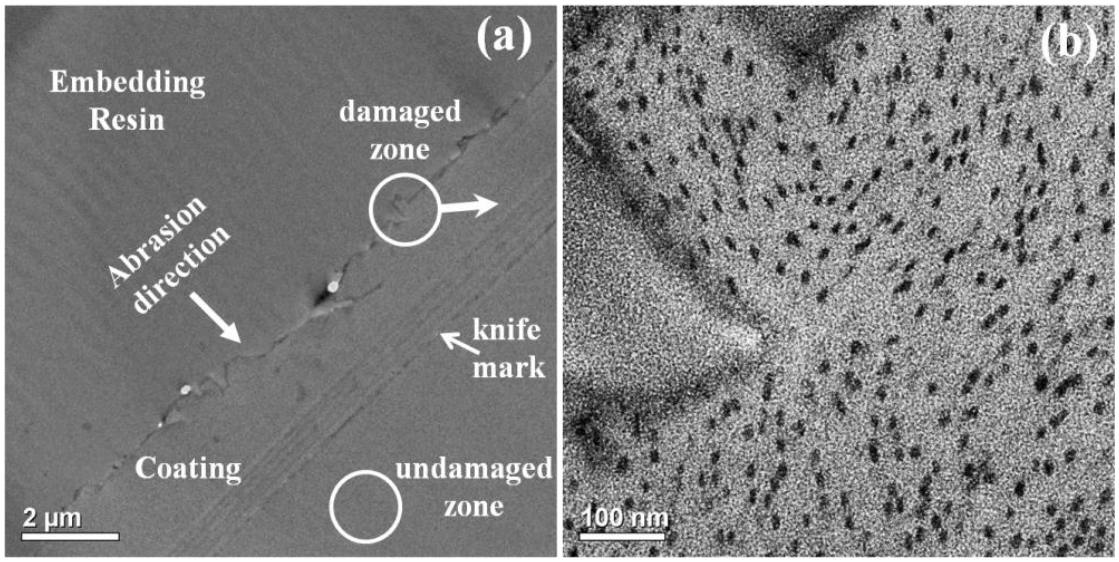

Figure 3.8 Representative TEM images of the cross-section of 15 μm epoxy coatings modified with 5 wt. % P2VP-PB after 500 abrasion cycles. The interface between the embedding resin and the coating is shown in (a), where the direction of abrasion damage is indicated. Image (b) shows damaged zone. The undamaged zone is similar to Figure 4.4 (d), not shown here.

3.4 Summary

In this chapter, two diblock copolymers, poly(ethylene oxide)-*b*-poly(ethylene-*alt*-propylene) (PEO-PEP) and poly(2-vinyl pyridine)-*b*-poly(1,2-butadiene) (P2VP-PB) were employed as modifiers for a model epoxy resin, Jeffamine thermoset, and their

effect on the mechanical properties of bulk thermosets and 15 μm thick coatings was investigated. In the bulk epoxy thermosets, both block copolymers self-assembled into spherical micelles and effectively improved the fracture toughness.

In coatings, spherical micelles were also formed and distributed throughout the coating with some segregation at the coating/substrate interface. The use of a casting solvent affected the micelle size in PEO-PEP modified epoxy coatings.

The presence of block copolymer modifiers also influenced the mechanical properties of the epoxy coatings. The hardness and modulus of the modified samples slightly decreased by increasing modifier loading, while the glass transition temperature of samples was not changed significantly. These results are in good agreement with previous findings for bulk block copolymer toughened epoxy materials. The abrasive wear resistances of coatings were also improved. Abrasion test results revealed that the abrasive wear was improved by as much as 20 and 40% upon the addition of 2 and 5 wt.% copolymer loading over neat coatings. This improvement appears to be linked to the higher fracture toughness of modified coatings. Similar toughening mechanisms as those noted in block copolymer toughened bulk epoxies still hold in modified coatings, including micelle cavitation and promoted matrix shear yielding.

Chapter 4

Toughening Cardolite thermoset with PEO-PBO block copolymers: a commercially viable system*

4.1 Introduction

The work on a block copolymer toughened Jeffamine thermoset described in Chapter 3 dealt with a model system, laying the basis for exploring commercially viable epoxy systems that are more complex thermodynamically but industrially relevant. The commercial importance of epoxy resins continues to grow with an annual increase of 7.7% in the overall demand during 2009-2013. The global market for epoxy resins is projected to reach 3.03 million tons by the year of 2017.[29] Epoxy resin formulations are available with a wide variety of curing agents,[10, 26] which benefits the utilization of epoxy resins for various kinds of services, such as adhesives, protective paints and coatings, automative components, and encapsulating materials.[31, 32, 36] However, epoxy resins are

*Reproduced in part with permission from (T. Li, et al., "Engineering superior toughness in commercially viable block copolymer modified epoxy resin", *Journal of Polymer Science, Part B: Polymer Physics*, John Wiley & Sons Inc.)

intrinsically brittle and prone to fracture failutre, which limits their applications.[16, 38] Therefore, amphiphilic block copoymers have emerged recently as efficient additives for improving the fracture toughness of epoxy thermosets without sacrificing other properties like resin modulus and glass transition temperautre.[11, 61, 69, 87, 96]

The toughening efficacy of block copolymers is found to be dependent on the associated microphase separated nanostructures in the cured epoxy resins, including bi-layer vesicles, wormlike micelles and spherical micelles. Several authors[51-53, 61] have demonstrated that wormlike micelles are more desirable for toughening than spherical micelles with a difference of up to 250% in critical stress intensity factor (K_{Ic}) in favor of the former. On the other hand, the toughening effect of vesicles varies a lot among different epoxy systems.[11, 45, 52, 53, 61] The precise control of block copolymer final morphlogy is crticial for the goal of toughening the resultant epoxies.

Over the last decade, a large body of literature has been devoted to the field of block copolymer modified epoxies, and specifically to the phase behavior and formation mechanisms of nanostructures, and to the underlying toughening mechanisms. However, most of those reported studies have focused on the application of block copolymers designed to be compatible with several model systems,[10, 11] with potentially limited practical utility. Although diglycidyl ether-based epoxy monomers and novolac epoxies are commonly employed in commercial thermoset products, the hardeners or curing agents that have been widely investigated in the literature, such as MOCA (4,4'-Methylenebis-(2-chloroaniline)) and MDA (methylene dianiline), require high temperatures (over 100 ℃) to achive complete reaction. Many industrial formulations rely

on more chemically complicated hardeners that permit curing at ambient conditions. These “industrial” epoxy resins usually possess fast curing kinetics and complex system thermodynamics that challenge existing startegies for incorporating block copolymers as effective toughening agents.

While many candidate block copolymers have been synthesized in laboratory settings[10, 11, 178, 179] few have been commercialized.[72-75, 180] Fortegra™ 100 marketed by the Dow Chemical Company is a noteworthy exception. This product is a poly(ethylene oxide-*b*-butylene oxide) (PEO-PBO) diblock copolymer with appropriately designed molecular weight and composition to be used as an effective toughening agent for epoxy resins. Although this compound has been shown to induce significant toughness at relatively low concentration (3-8% by volume) in certain epoxy materials,[181, 182] the origin and versatility of the toughness improvement is still not well documented partially because it tends to be used in complex coating formulations that do not lend themselves to fundamental studies. Further, commerical formulations frequently are designed around complex curing agents, such as the bio-derived hardener Cardolite NC-541LV, an amphiphilic compound containing a phenol/diamine headgroup and an unsaturated tail.[26, 183] The work reported in this chapter was motivated by a desire to develop new strategies to adapt PEO-PBO to the challenging Cardolite system.

This chapter presents a summary of our successful engineering of the PEO-PBO block copolymer modifiers in concert with improvements to the processing of the Cardolite thermoset resulting in a bulk product with superior toughness and coating product with exceptional abrasieve wear resistance. We investigate various processing

variables with respect to their morphological and mechanical property consequences in cured resins. Specifically, two approaches of formulating cured plaques are developed with different combinations of processing variables and systematically compared. The first approach (Route A) is based on the recommendation by the curing agent manufacturer for this epoxy; however, with this protocol the block copolymer additive leads to little or no improvement in fracture toughness over the neat plastic. This finding originally motivated our exploration of an expanded set of process parameters, resulting in the modified approach (Route B) that leads to well-dispersed spherical, cylindrical and branched wormlike micelles and significant improvements in the fracture toughness.

This chapter approaches the design of enhanced toughness in thermoset plastics through the comprehensive integration of mixing thermodynamics, curing kinetics, and optimization of structure formation in a commercially viable epoxy resin. Also, this chapter is organized in a way that “poor results” come first followed by the stepwise progression into a final “working” solution. We believe this pedagogical way of presenting reveals important and universal engineering priciples that will be useful for designing other materials.

4.2 Experimental

4.2.1 Materials

The chemical structures of the resin ingredients of the Cardolite thermoset and the block copolymer modifier being used are presented in Figure 4.1. The epoxy monomer is again diglycidyl ether of bisphenol-A (DGEBA) (Epon 828, PolySciences, Inc.), same as the one employed in the Jeffamine thermoset in Chapter 3. The curing agent here is a widely used commercial product, Cardolite NC-541LV (C541) (Cardolite Corp.). Amine-based curing agents, such as aliphatic and aromatic amines, polyamides and polyether amine (e.g. Jeffamine T-403 in Chapter 3), have been well studied as model systems for block copolymer modified epoxy materials.[26] Unlike these relatively simple compounds, C541 is a phenalkamine endowed with multiple desirable properties, including the ability to achieve high crosslink density, being active at low temperature, and having good chemical and water resistance.[183, 184] However, the amphiphilic molecular structure of C541 (i.e., a non-polar hydrocarbon tail and a polar phenol and ethylenediamine head group) leads to complex curing kinetics and complicated thermodynamic interactions when mixed with epoxy monomers and the PEO-PBO toughening agent. The curing accelerator DMP-30 (Ted Pella) is mainly composed of tris-(dimethylaminomethyl) phenol, which promotes epoxy to epoxy or hydroxyl to epoxy reactions and does not serve as a direct crosslinking agent.[183]

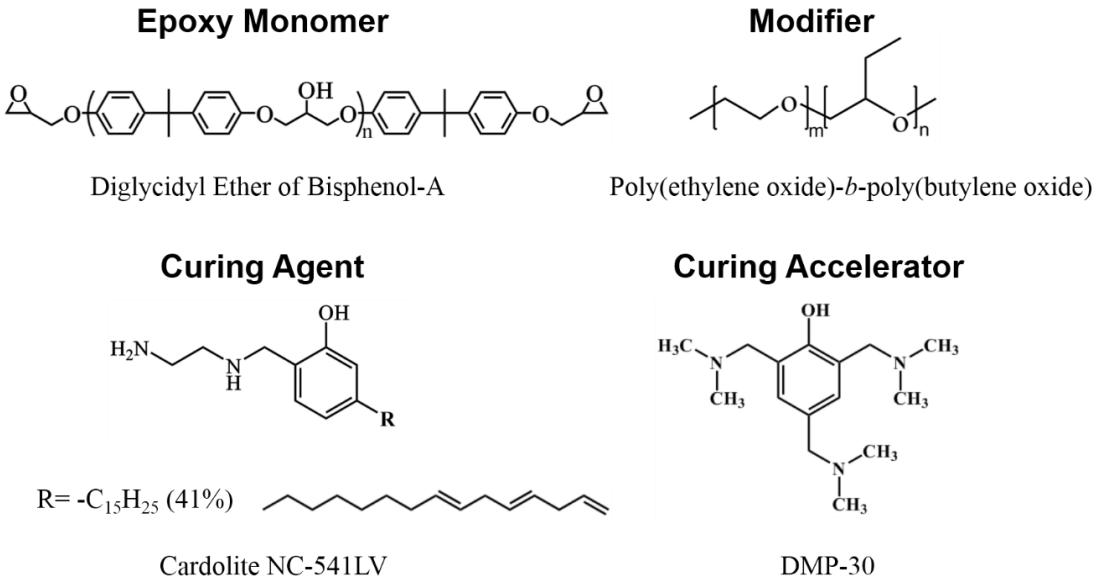

Figure 4.1 Chemical structures of ingredients in the Cardolite thermoset and block copolymer modifier.

It is mentioned in Chapter 2 that the diblock copolymer poly(ethylene oxide)-*b*-poly(butylene oxide) (PEO-PBO) is employed as the modifier for this Cardolite thermoset. In this Chapter 4, the PEO-PBO diblocks are also referred to as EB. A series of EB diblocks were synthesized via sequential anionic ring-opening polymerization as described in Section 2.3.3. They are at fixed composition (31 ± 1% by volume PEO) but varying molecular weight expanding on a commercially available PEO-PBO compound marketed by the Dow Chemical Company under the tradename Fortegra™ 100.

Table 4.1 summarizes the molecular characteristics of four EB diblock copolymers employed in this chapter, identified as EB-1 to EB-4. The block copolymer composition and number average molecular weight were determined using ^{1}H NMR and end-group

analysis. The dispersity was determined by room temperature GPC with polystyrene standards and THF as the solvent. All diblock copolymers are nearly mono-disperse, containing 34 ± 1.4 % by weight PEO, and overall number average molecular weight between 7 and 48 kg/mol. PEO is semi-crystalline with a melting point near 50 ℃ and expected to form the micelle corona when mixed with the epoxy monomer. Epoxy-phobic PBO with a glass transition temperature around –60 ℃ is expected to produce rubbery, compliant cores in the Cardolite thermoset matrix.

Table 4.1 Molecular characteristics of diblock copolymers for the Cardolite thermoset

[a]Identification	[b]Composition	[c]M_n (kg/mol)	M_w/M_n	[d]f_{PEO}	[e]w_{PEO}
EB-1	$EO_{56}BO_{63}$	7.0	1.10	32	35
EB-2	$EO_{89}BO_{105}$	11.5	1.03	31	34
EB-3	$EO_{161}BO_{210}$	22.2	1.09	30	32
EB-4	$EO_{382}BO_{433}$	48.0	1.10	32	35

[a] EB = poly(ethylene oxide)-*b*-poly(butylene oxide) (PEO-PBO)

[b] Subscripts indicate number of repeat units.

[c, e] Number average molecular weight and weight fraction of PEO blocks, calculated based on ^{1}H NMR and end-group analysis.

[d] Volume fraction of PEO blocks calculated using densities ρ_{PEO} = 1.067 g/cm^3 and ρ_{PBO} = 0.923 g/cm^3.[65, 95]

4.2.2 Sample preparation

As briefly mentioned in Section 2.4, processing variables during sample preparation can greatly affect the microstructure formation and consequent mechanical properties in

the final product for this Cardolite system. Herein, we present a detailed description of engineering an optimized processing route for this Cardolite system in order to achieve improved mechanical performance.

Full epoxy formulations were obtained by preparing the base (epoxy) batch and hardener batch separately. For the base batch, EB block copolymers were blended at a certain loading with the epoxy monomer DGEBA at 70-75 ℃ until full dissolution. These clear and transparent blends were degassed to remove residual air, and then cooled to 60 ℃ for mixing with the hardener. Two recipes were adopted for the hardener batch: (*i*) pure curing agent C541, and (*ii*) a mixture of C541 and the curing accelerator DMP-30, referred to as C541/DMP-30, which was formulated by drop-wise addition of DMP-30 to C541 at 60 ℃ where the amount of DMP-30 was adjusted to represent 1 wt.% in the final epoxy formulation.

The weight ratio of the base batch to the hardener batch was a critical parameter in this investigation, because it both controls the curing kinetics and intrinsic properties of the epoxy matrix itself, and dictates the path of block copolymer self-assembly by affecting the system thermodynamics. Table 4.2 summarizes two formulation recipes, A and B, used in this study. A specific amount of hardener (batch (*i*) or (*ii*)) was added to the base batch (a mixture of EB in DGEBA), and mixed at 60 ℃ producing a homogeneous state. Then, the full epoxy formulation was tranferred to a pre-heated aluminum mold (at 60 ℃) for the curing step. Two different curing protocols were employed as listed in Table 4.2. Route A is based on a recommendation by the curing agent manufacturer, and route B is selected from preliminary studies that explored a

wider range for formulation and curing protocols, which are described in detail in the Appendix B (See Appendix B, Figure B1 and B2).

Overall we explored the consequences on product morphology and toughness of various combinations of four formulation and processing variables: (*i*) the amount of EB in the final product, (*ii*) the choice of harener batch, (*iii*) the weight ratio of the base batch to hardener batch, and (*iv*) the curing protocol.

Table 4.2 Summary of sample preparation routes for the Cardolite thermoset

Identification	[a]Base batch	[b]Hardener batch	[c]Curing agent amount	[d]Stoichiometry	Curing protocol
A	EB in	(*i*)	65 phr	1:1	25 ℃ 24h, 50 ℃ 24h
B	DGEBA	(*ii*)	40 phr	2:3	60 ℃ 8h

[a] The EB concentrations in DGEBA were determined by making the block copolymer loading in final epoxy formulations as 1.5 wt.%, 2.5 wt.% and 5 wt.%, respectively.

[b] (*i*) is pure C541, and (*ii*) is DMP-30/C541 mixture with a 1:24 DMP-30:C541 weight ratio, resulting in 1 wt.% DMP-30 in the final epoxy formulations.

[c] phr stands for "parts per hundred resin", meaning how many grams of curing agent, C541, are needed per hundred grams of epoxy monomer, DGEBA.

[d] The stoichiometry between the reactive hydrogens from the primary and secondary amine groups in C541 and the epoxide group from DGEBA. The epoxide equivalent weight (EEW) of DGEBA is about 200 g/eq,[185] and the amine hydrogen equivalent weight (AHEW) of C541 is about 125 g/eq.[183]

The preparation of modified coating samples followed a solvent casting protocol. Full epoxy formulations were first obtained via Route B as shown in Table 4.2, and then they were allowed to pre-cure at 60 ℃ for 30 min and cool to room temperature before being dissolved in the casting solvent chloroform. The solution was cast onto an 80 μm polyethylene terephthalate (PET) (3M) substrate using a wire-wound rod (rod number 28)

(R.D. Specialties, Inc.). The PET substrates were thoroughly rinsed with distilled water and isopropanol before use. As-cast coatings were allowed to dry under ambient conditions for 30 min to ensure the removal of chloroform. Dried coatings were then cured following the protocol B as in Table 4.2, and the thickness of the cured coating was 10 ± 2 μm.

4.3 Results and analyses

In this section we first present results obtained from bulk Cardolite thermosets (subsections 4.3.1 to 4.3.3), and then show results from modified coatings (4.3.4). In 4.3.1, we investigate the phase behavior of the EB diblock copolymers when mixed individually with the DGEBA epoxy monomer and C541 hardening agent. Subsequently, in 4.3.2 and 4.3.3, the morphological and mechanical property consequences of formulating cured plaques using two different approaches, denoted route A and route B (see Table 4.2), are described. Route A results in thermoset materials with little or no improvement in fracture toughness over the neat plastic, which originally motivated this study. Route B leads to well-dispersed spherical, cylindrical and branched micelles endowed with significantly improved fracture toughness, as much as a ten-fold increase in G_{Ic} at 5% by weight loading of diblock copolymer. Lastly, in 4.3.4, modified coatings prepared via Route B are explored with respect to the microstructure and overall performance.

4.3.1 Phase behavior of block copolymer/epoxy precursor mixtures

Figure 4.2 shows DSC traces of pure EB diblock copolymers. All four diblock copolymers exhibit a PBO glass transition at about −70 ℃. The traces from EB-2, EB-3 and EB-4 clearly show PEO melting peaks at around 50 ℃, shifting to slightly higher temperatures with increasing PEO block molecular weight. Pure EB-1 has a PEO crystallization peak at around −50 ℃ and a broad PEO melting peak between −30 ℃ to 20 ℃; this low melting temperature can be attributed to the low molecular weight of EB-1.

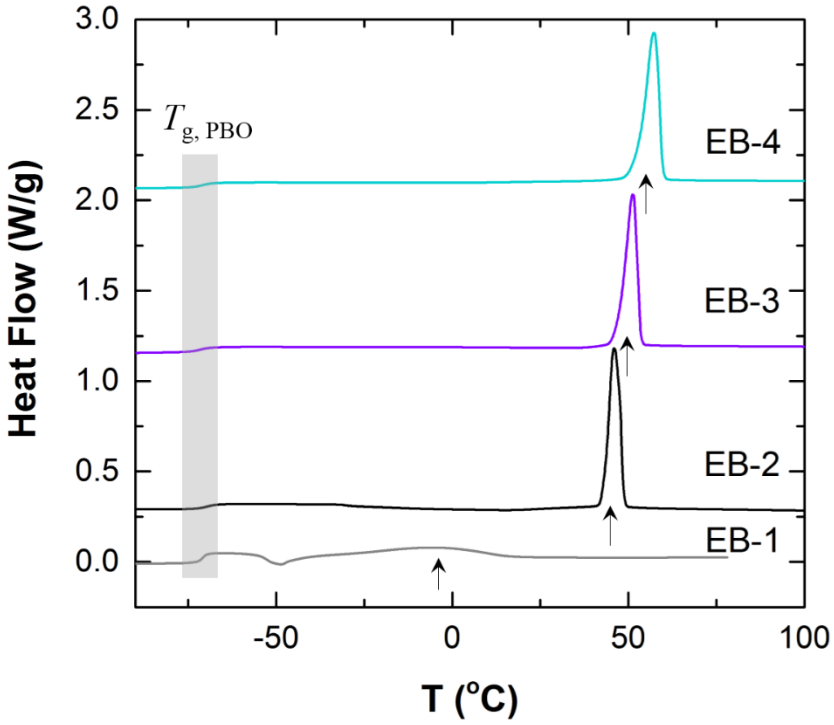

Figure 4.2 DSC traces (exo down) of pure EB diblock copolymers (EB-1 to EB-4, from bottom to top). Shaded region shows the glass transition of the PBO block. Arrows denote the PEO melting peaks. Curves were shifted vertically for clarity.

Figure 4.3 displays DSC traces obtained from blends of 5 wt.% EB mixed individually with DGEBA and C541. Based on the presence of single glass transition temperatures and complete absence of melting peaks in Figure 4.3a we tentatively conclude that all four EB modifiers are dissolved in the epoxy monomer DGEBA. On the other hand, the presence of PEO melting peaks in Figure 4.3b indicate that EB-2, EB-3 and EB-4 do not completely mix with the curing agent C541 at room temperature and up to at least 50 ℃.

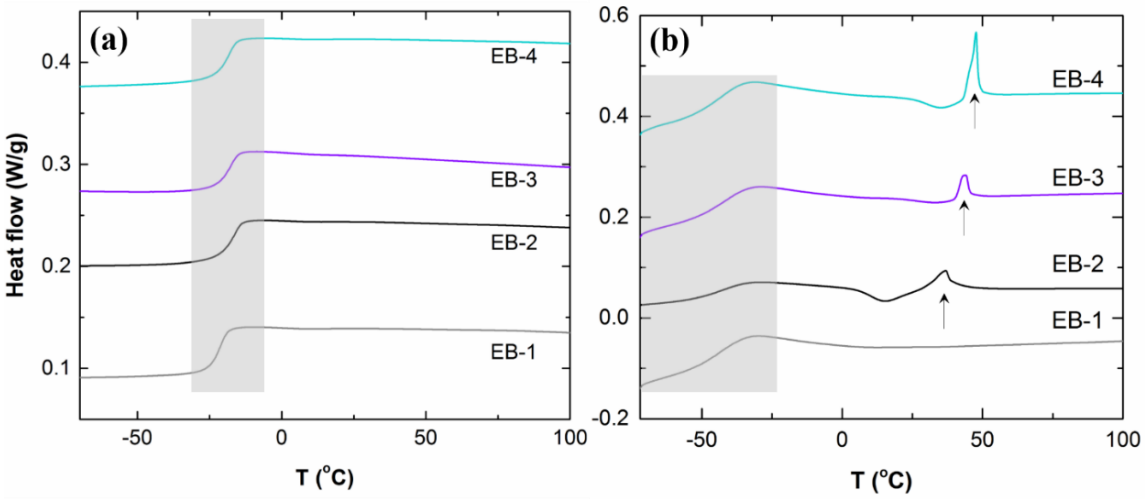

Figure 4.3 DSC traces (exo down) of (a) blends of EB block copolymers in DGEBA and (b) blends of EB in C541. The block copolymer concentration is 5 wt.% in all blends. Shaded regions show the glass transition of EB/DGEBA mixture and EB/C541 mixture in (a) and (b), respectively. Arrows in (b) denote the PEO melting peaks. Curves were shifted vertically for clarity.

Representative SAXS profiles obtained from mixtures containing 7 wt.% of the EB diblock copolymers in DGEBA at room temperature and 60 ℃ are presented in Figure 4.4a and c, respectively. (This concentration reflects the amount of diblock copolymer

that must be dissolved in the epoxy monomer to produce a 5 wt.% loading in the fully formulated and cured resin). At both temperatures a single weak and broad peak characterizes the EB-1 mixture indicating the absence of any well-defined microstructure, which we attribute to the low molecular weight of this diblock copolymer. Conversely, the SAXS patterns obtained from the blends of DGEBA with EB-2, EB-3 and EB-4 provide evidence of nanoscale structure, including a low-q structure factor peak and oscillating bumps at higher q that we associate with form factor scattering from relatively mono-disperse spherical or cylindrical micelles (see below).[63, 186] As the total molecular weight increases these features move to lower values of q, consistent with this interpretation. Upon heating to 60 ℃ the SAXS patterns from the EB/DGEBA blends retain essentially the same peak shapes and positions, with a slight reduction in overall intensity, indicative of little change in the solution morphology. Also, these mixtures are optically clear to the eye at both temperatures.

Mixing 15% by weight of the EB diblock copolymers with C541 plus the curing accelerator DMP-30 (1 part DMP-30 per 24 parts C541 by weight, see Table 4.2), or with pure C541 (similar results, not shown), leads to qualitatively different SAXS patterns as illustrated in Figures 4.4b and d. (Here again the diblock copolymer concentration was chosen in order to assess the phase behavior if all the diblock copolymer was delivered into the final formulated resin through the hardening agent). The presence of DMP-30 produces a broad rounded peak in the high q region ($0.1 < q < 0.4$ Å^{-1}); this was confirmed by results obtained with C541/DMP-30 alone (data not shown). At 60 ℃ all four mixtures produce relatively featureless SAXS patterns indicating that the block

copolymer is completely dissolved in the hardener at this temperature. This conclusion is reinforced by the fact that these mixtures are clear to the eye. At room temperature diffraction peaks are evident in the mixtures containing EB-2, EB-3, and EB-4, consistent with a layered (e.g. lamellar) microstructure. The DSC results shown in Figure 4.2 show clearly that some fraction of the PEO blocks are crystalline at this temperature. Significantly, the principle peak position q^* does not seem to vary with molecular weight suggesting that crystallization (chain folding) dictates the periodic structure (See Figure B3 in Appendix B). We believe crystallization leads to macroscopic phase separation of the diblock copolymer from the hardening agent at room temperature; this conclusion is supported by the morphological results obtained from the formulated material initially cured at room temperature (see below). Also, with the exception of the EB-1 solution (which was clear to the eye), the three higher molecular weight EB/C541/DMP-30 (and EB/C541) mixtures are opaque, indicative of macroscopic phase separation.

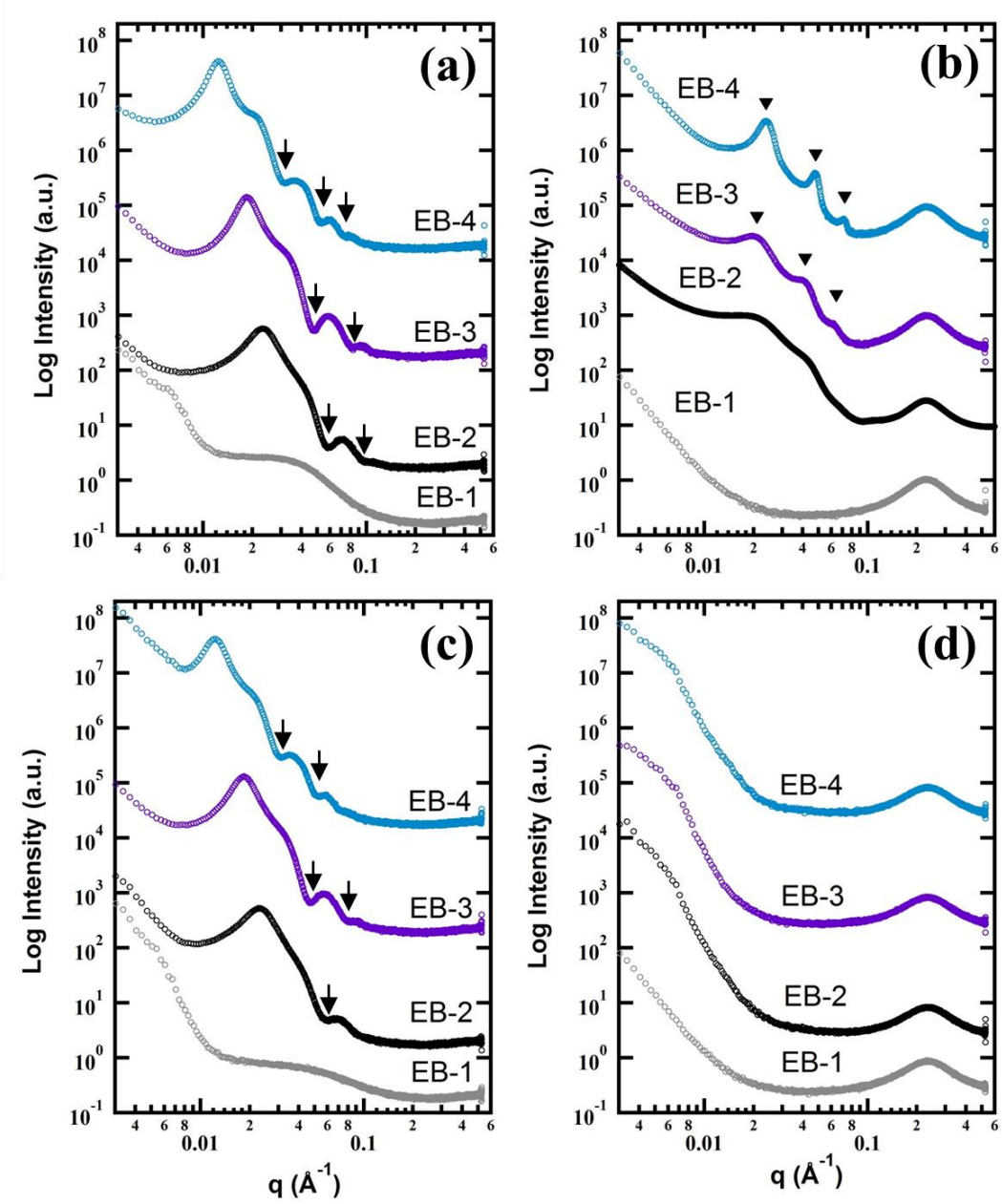

Figure 4.4 1D SAXS profiles of (a) room temperature EB/DGEBA blends, (b) room temperature EB/C541/DMP-30 blends, (c) 60 ℃ EB/DGEBA blends, and (d) 60 ℃ EB/Hardener (*ii*) blends. Arrows in (a) and (c) indicate the positions of the form factor minima. Characteristic scattering peaks are also denoted in (b). The block copolymer concentration is 7 wt.% for EB/DGEBA blends and 15 wt.% for EB/Hardener (*ii*) blends. Both concentrations were determined by keeping 5 wt.% of block copolymers in the final epoxy formulations following route B. Curves were shifted vertically for clarity.

4.3.2 Processing dependent microstructure formation in bulk epoxies

EB Modified Bulk Epoxies Prepared via Route A. Figure 4.5 shows representative TEM micrographs obtained from cured epoxies loaded with 5 wt.% of the EB modifiers prepared following route A (Table 4.2). EB-1 produced no microstructure (Figure 4.5a) and we conclude that the block copolymer is mostly dissolved into the epoxy matrix. The three higher molecular weight modifiers (EB-2, EB-3, EB-4) phase separate macroscopically, as evidenced by the micrometer-scale domains distributed throughout the matrix in Figures 4.5b, c and d. (Some of the block copolymer rich macrodomains have been pulled away from the TEM film during sectioning leaving voids).[72] Obviously, the block copolymer has precipitated from these mixtures during processing, also manifested through the appearance of cloudiness. The phase separated materials display little or no enhanced toughness *versus* the unmodified cured resin (data not shown). Although the EB-1 modified epoxy plaques were clear and transparent by appearance, fracture toughness improvement was quite limited; the K_{Ic} of neat epoxies prepared with route A was determined to be 0.48 ± 0.05 MPa·√m, while adding 5 wt.% of EB-1 increased this value to 0.57 ± 0.07 MPa·√m.

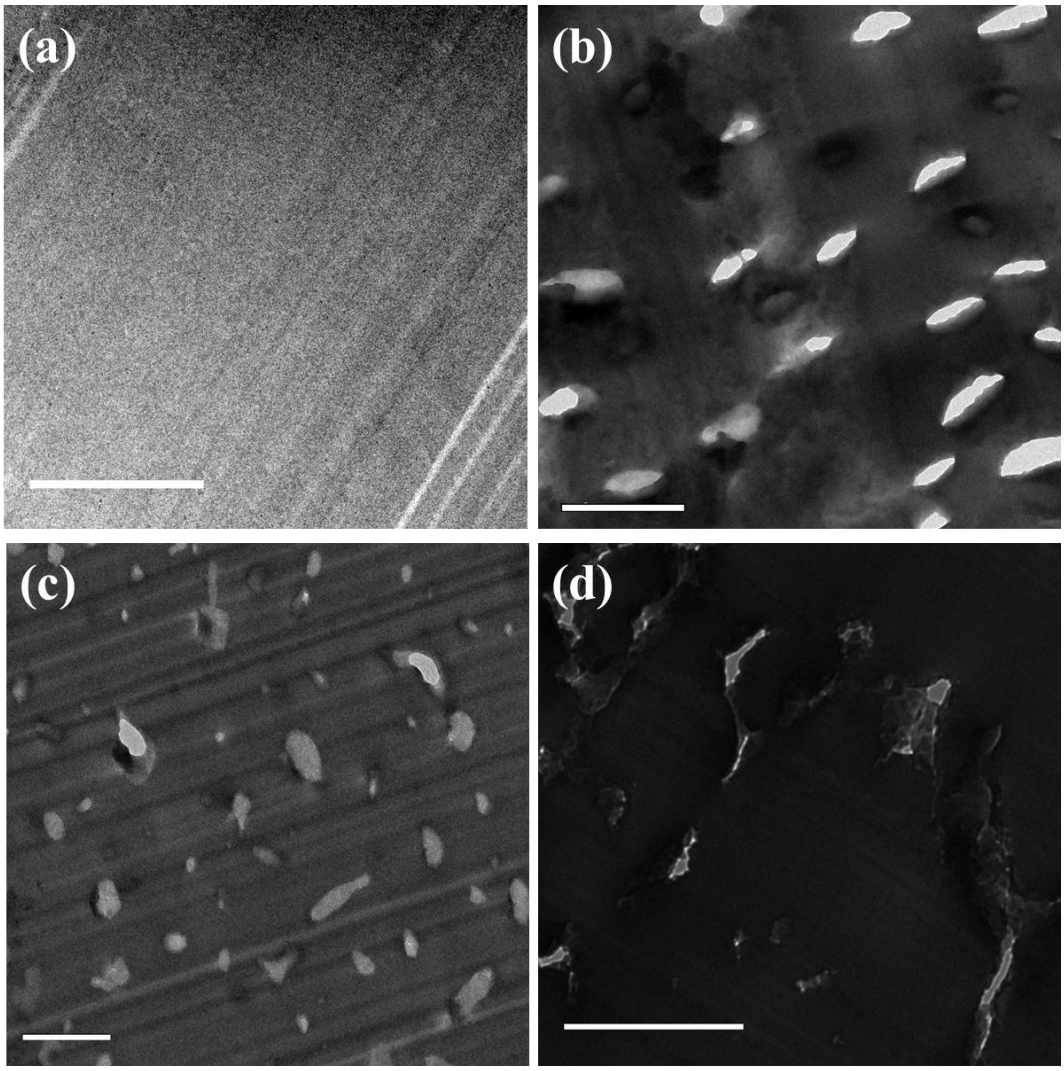

Figure 4.5 Representative TEM images of cured epoxy resins (route A) containing 5 wt.% of (a) EB-1, (b) EB-2, (c) EB-3, and (d) EB-4. RuO_4, used as a contrast agent, preferentially stains the PEO/epoxy interface. Scale bars represent 1 μm.

The corresponding DSC traces of the epoxy resins prepared via route A are shown in Figure 4.6. Cured resins modified with EB-2, EB-3, and EB-4 exhibit endothermic peaks that are clearly associated with the melting of PEO, consistent with the conclusion that the block copolymer is segregated from the cured epoxy matrix. The trace of EB-1

does not contain a melting endotherm due to the low molecular weight of this compound, which suppresses crystallization. These results suggest that crystallization may contribute to phase separation.

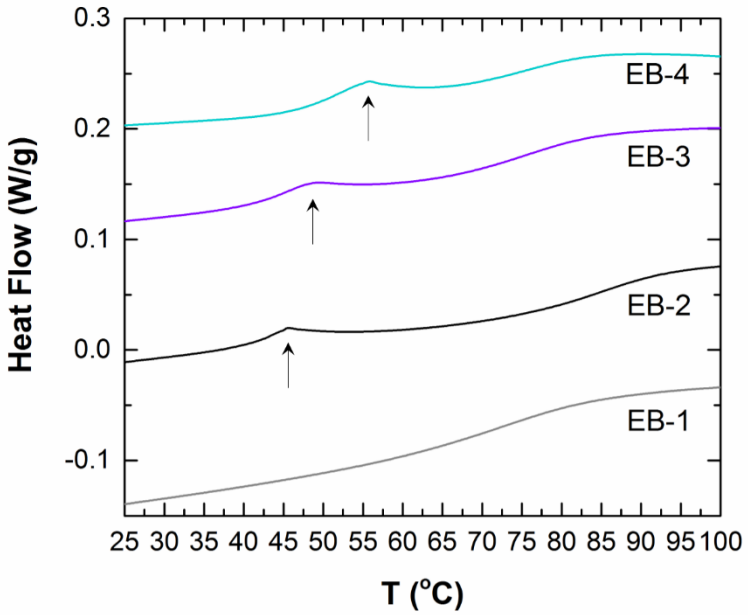

Figure 4.6 DSC traces (exothermal down) of cured epoxies (route A) containing EB modifiers. Epoxies were loaded with 5 wt.% of EB-1, EB-2, EB-3 and EB-4, respectively (from bottom to top). Arrows denote the melting peak of PEO. Curves were shifted vertically for clarity.

EB Modified Bulk Epoxies Prepared via Route B. Route B was developed to prepare epoxy resins containing nanoscale micelle morphologies and Figure 4.7 shows representative cross-section TEM images of cured samples containing 5 wt.% of modifiers. As targeted, all four EB block copolymers generate micelle structures in the cured epoxies. EB-1 forms ill-defined micelles and their size and shape are quite polydisperse, as evident in Figure 4.7a. We believe this reflects the weak segregation

between the low molecular weight block copolymer and the epoxy, which is examined in more detail below based on time-resolved SAXS experiments. On the other hand, EB-2 to EB-4 all generate well-defined micelle structures in the cured resin, transitioning from branched wormlike micelles (Figure 4.7b), to a mixture of cylindrical and spherical micelles (Figure 4.7c), and finally to mono-disperse spherical micelles (Figure 4.7d) with increasing EB molecular weight. We rationalize this sequence of morphologies based on the increasing segregation strength between the block copolymer and the epoxy resin, which accompanies the increasing total molecular weight.

To the best of our knowledge this is the first time that branched wormlike micelles have been generated in a commercially viable epoxy resin. Significantly, this was accomplished by adjusting the total molecular weight and processing conditions rather than tuning the composition of the block copolymer. The diameter of the elongated PBO cores in Figure 4.7b is 9 ± 2 nm, and of the short cylinders in Figure 4.7c this dimension is 12 ± 2 nm. The diameter of the spherical PBO cores in Figure 4.7c and 4.7d are 14 ± 2 nm and 20 ± 4 nm, respectively. All size distributions of micelles were determined using ImageJ.[159]

These TEM results confirm that route B is an effective method for generating nanoscale micelle morphologies in the C541 based epoxy resin. More TEM images showing EB micelles at different loadings are presented in Figure B4 (see Appendix B).

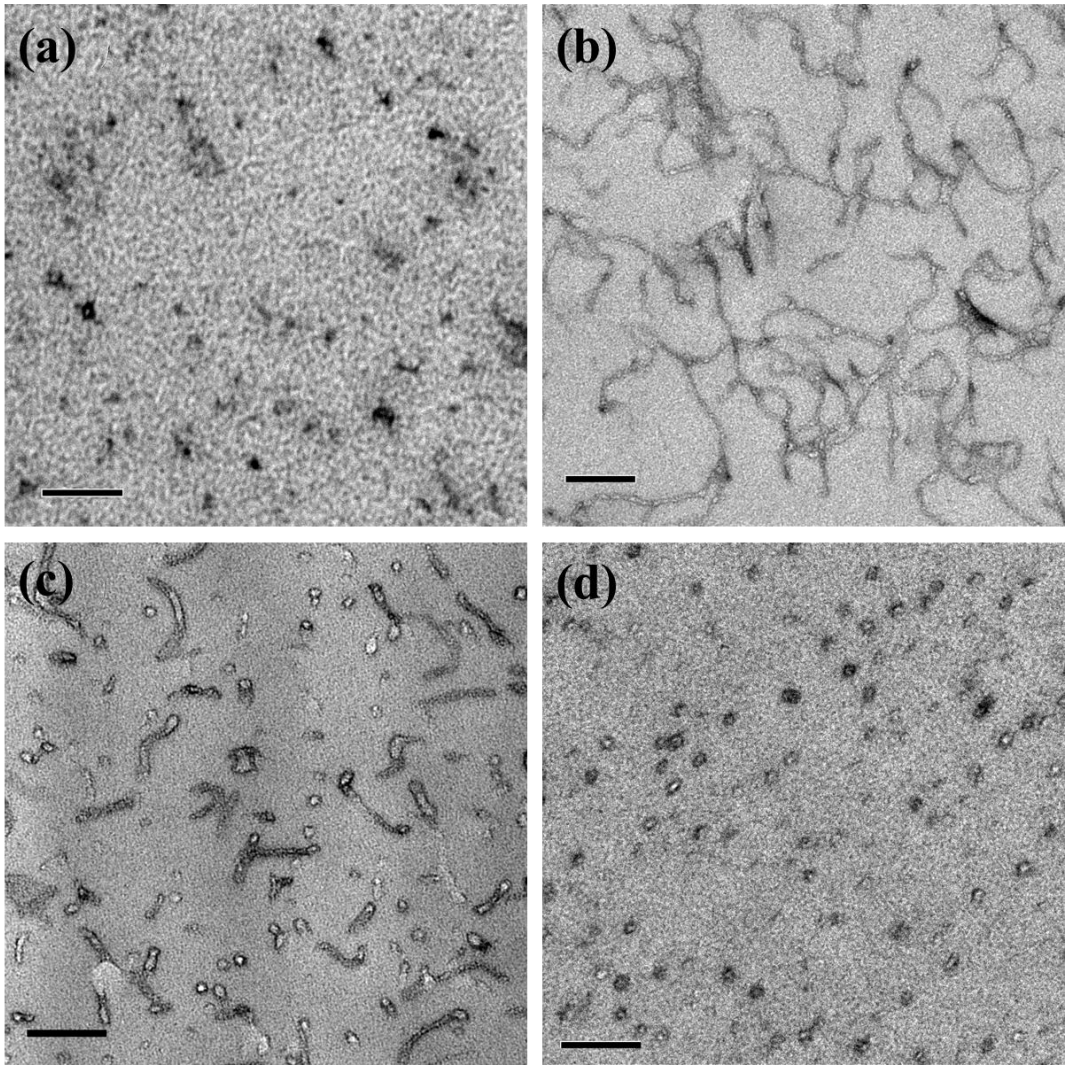

Figure 4.7 Representative TEM images of cured epoxy resins (route B) containing 5 wt.% of (a) EB-1, (b) EB-2, (c) EB-3, and (d) EB-4. RuO_4, used as a contrast agent, preferentially stains the PEO/epoxy interface, making relatively brighter PBO cores with darker PEO coronas. Scale bars represent 100 nm.

The microstructure development in Cardolite thermosets prepared via route B was further explored with time-resolved SAXS experiments. Representative 1D SAXS data are displayed in Figure 4.8. The 5 min scattering pattern in Figure 4.8a clearly shows no microstructural features consistent with complete dissolution of EB-1 in the monomer mixture. (Recall that the broad peak at high q is associated with the hardener, see above). As the curing reaction proceeds, evidence of structure appears between about 15 and 30 minutes in the form of a broad weak peak (0.01-0.04 $Å^{-1}$), which subsequently moves to lower q values as the specimen cures. These results evidence formation of some nanoscale structure consistent with the TEM image shown in Figure 4.7a. However, we are not able to quantitatively model these subtle scattering features.

SAXS patterns obtained while curing resins containing 5 wt.% of EB-2, EB-3 and EB-4 are shown in Figures 4.8b, c and d, respectively. All three mixtures contain nanoscale structure in the uncured state evidenced by peaks in the range $0.01 < q < 0.1$ $Å^{-1}$. The highest molecular weight block copolymer, EB-4, produces a well-defined scattering pattern that contains a secondary peak at 0.045 $Å^{-1}$ that can be quantitatively interpreted using a spherical form factor (see Section 4.4.2 below) with a PBO core radius of 13.2 ± 1.4 nm (see Figure 4.16 below). This morphology persists upon curing with little change in the micelle dimension (core radius of 12.3 ± 0.9 nm after 60 minutes as modeled in Figure 4.16). A similar scattering pattern emerges at about 10 minutes of curing with the EB-3 mixture. After 60 minutes of curing, we interpret the scattering pattern using a cylindrical form factor combined with a spherical form factor, based on the TEM image in Figure 4.7c, with a core radius of 8.1 ± 1.6 nm for cylinders and a core

radius of 6.3 ± 0.5 nm for spheres (see Figure 4.15 below). Similarly, the scattering patterns obtained from the resin made with EB-2 initially contain a single broad peak but develop a form factor peak at the later stages of curing, which modeling translates into a cylindrical core radius of 5.1 ± 0.9 nm (Figure 4.14), also consistent with the image in Figure 4.7b.

Taken together, the results in Figure 4.8 demonstrate the consequences of increasing the molecular weight of the EB additives at constant composition. In the unreacted state elevating the molecular weight drives the mixture through the critical micelle condition at room temperature. As the mixtures cure the effective segregation strength increases, most likely due to partial expulsion of the corona PEO blocks from the crosslinked matrix. The transition from disorder to a cylindrical morphology then spherical micelles with increasing M_n is anticipated by the trends found with amphiphilic poly(butadiene)-*b*-poly(ethylene oxide) diblock copolymers dispersed in water.[187] We cannot state with any certainty why the fascinating branched structure seen in Figure 4.7b forms, nor can we establish whether this morphology exists in the unreacted mixture or forms during curing.

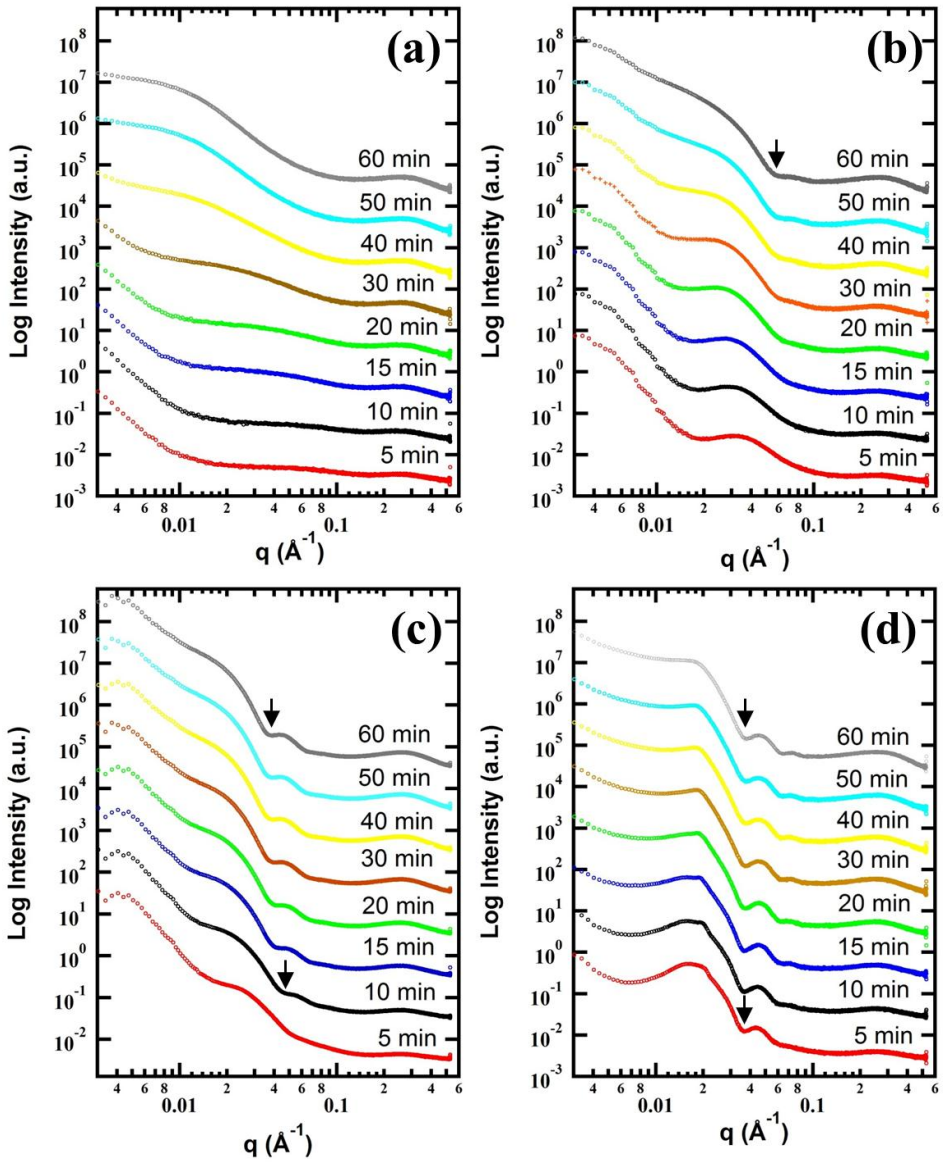

Figure 4.8 Time-resolved 1-D SAXS profiles of epoxy resins containing 5 wt.% of (a) EB-1, (b) EB-2, (c) EB-3 and (d) EB-4. Samples were prepared via route B at 60 ℃. All traces have been shifted vertically for clarity. The time labelled above each curve tells how much time has elapsed from the onset of mixing the base batch and the hardener batch until the time point of collecting the associated scan. Sample preparations took about five minutes, so the first scattering run was from 5 min instead of 0 min. For all cases, their scattering patterns did not change after 60 minutes and the curing extent at 60 min was measured to be close to that at 8 hours, so the last scattering traces shown here were from 60 min instead of 8 hours. Arrows denote the onset of the first peak associated with form factor scattering.

4.3.3 Mechanical and thermal properties of bulk thermosets

As mentioned above, the fracture toughness improvement with the processing route A is quite limited due to the macrophase separated block copolymer modifiers. Therefore, route A is not desirable for this Cardolite system. On the other hand, development of the nanoscale micelle morphology in the cured bulk epoxies using route B leads to significant enhancement in the fracture toughness of these materials. Figure 4.9 compares the critical strain energy release rate (G_{Ic}) values recorded for block copolymer loadings of 1.5, 2.5 and 5% by weight with the unmodified Cardolite bulk thermoset ($G_{Ic} = 55 \pm 10$ J/m^2). Their fracture toughness (K_{Ic}) values are also summarized in Table B1 (See Appendix B). All four EB diblocks produce a significant improvement in G_{Ic}, which in each case increases nearly two-fold between 1.5 and 5 wt.% concentration. The most dramatic increase in toughness is realized with the branched wormlike morphology associated with EB-2, i.e. twice the toughness obtained with EB-1. This trend mirrors earlier reports from our group that document roughly twice the G_{Ic} value with wormlike *versus* spherical micelles at constant block copolymer loading.[11, 48, 50, 51] The greatest improvement is obtained with 5 wt.% EB-2, which shows approximately a 900% increase in G_{Ic} over the unmodified material.

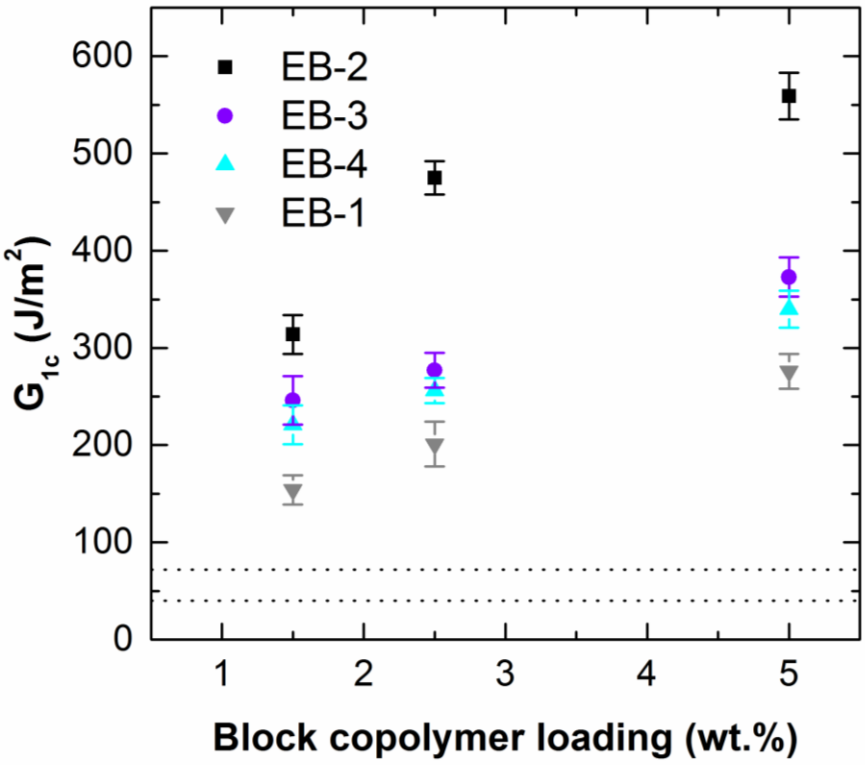

Figure 4.9 Critical strain energy release rate (G_{Ic}) for modified epoxy resins as a function of block copolymer loading. EB-2 forms entangled wormlike micelles; EB-3 forms a mixture of spherical and cylindrical micelles, and EB-4 forms spherical micelles. Each data point reflects an average value based on at least five specimens and the error bars indicate the standard deviation. The range of values obtained from the neat epoxy material are identified by the dotted lines.

The fracture surfaces of broken compact tension specimens were examined by SEM to investigate possible toughening mechanisms, and representative micrographs are presented in Figure 4.10 and Figure B5 (See Appendix B). Figures 4.10a (for EB-1) and 4.10d (for EB-4) show similar fracture surface topographies, characterized by relatively smooth surfaces with some fine (ca. 100 nm scale) texture; a subtle difference in the EB-4 based material suggests sub-100 nm holes probably caused by the cavitation and

pullout of spherical micelles. The fracture surfaces are much rougher for the EB-2 and EB-3 modified specimens (Figures 4.10b and c), particularly EB-2, which exhibits leaf-like texture evidencing massive local disruption of the thermoset material due to crack deflection.[52, 65] There is also evidence of "wormholes" in Figure 10b and both "sphere holes" and "wormholes" in Figure 4.10c.

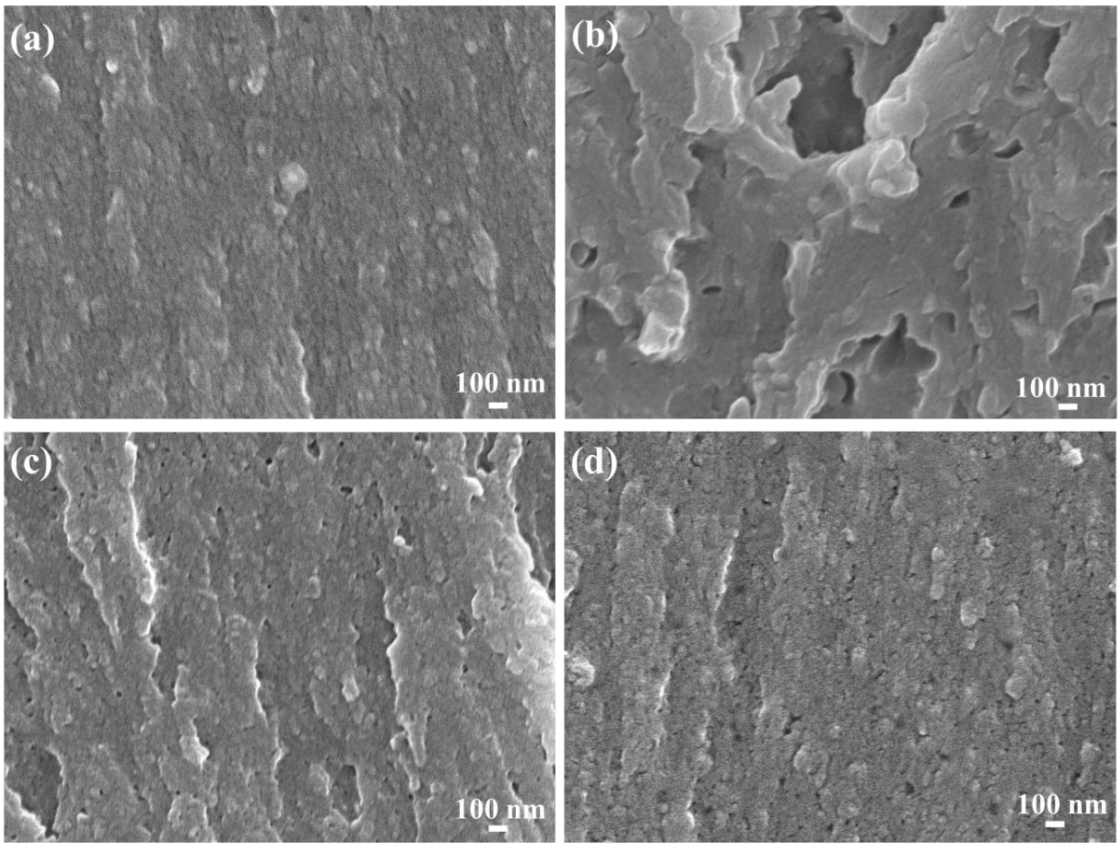

Figure 4.10 Representative SEM images of the fracture surfaces of epoxy resins loaded with 5 wt.% of (a) EB-1, (b) EB-2, (c) EB-3 and (d) EB-4. Scale bars represent 100 nm.

Apparently, the wormlike micelles affect sample failure in a manner that is not operative with the spherical micelles. We have shown elsewhere that deformation in

spherical rubbery micelle modified epoxies is accompanied by core cavitation, augmented by network disruption caused by the corona chains, which triggers local deformation of the matrix, and shear yielding that is believed to be the major energy absorbing process during fracture.[96] The presence of high aspect ratio wormlike micelles apparently enhances this effect. We speculate that the beneficial disruption of the crosslinked epoxy network is more expansive with wormlike micelles creating a more effective zone for triggering. Therefore, the triggering events from those localized sites are amplified, facilitating plastic deformation and shear yielding as reflected in the leaf-like texture of the fracture surface. This conjecture awaits further validation and will be the subject of future investigations.

Tables 4.3 and 4.4 summarize the room temperature elastic modulus and glass transition temperature of cured epoxies prepared via route B, respectively. There is a small but statistically significant decrease in the elastic modulus associated with the inclusion of EB diblock copolymer, roughly 10% reduction with 5 wt.% added. However, within experimental uncertainty addition of up to 5 wt.% EB does not affect the glass transition temperature of the epoxy matrix.

Table 4.3 Room temperature elastic modulus (in GPa) of cured bulk epoxies prepared via route B.

Modifier	1.5 wt.%	2.5 wt.%	5 wt.%
Neat		2.28 ± 0.04	
EB-1	2.20 ± 0.03	2.14 ± 0.08	2.11 ± 0.07
EB-2	2.16 ± 0.04	2.09 ± 0.02	2.03 ± 0.05
EB-3	2.19 ± 0.07	2.10 ± 0.05	2.06 ± 0.12
EB-4	2.17 ± 0.05	2.08 ± 0.05	2.04 ± 0.04

Table 4.4 Glass transition temperature (T_g in ℃) of cured bulk epoxies prepared via route B.

Modifier	1.5 wt.%	2.5 wt.%	5 wt.%
Neat		88 ± 3	
EB-1	88 ± 2	88 ± 3	87 ± 1
EB-2	88 ± 1	87 ± 2	84 ± 4
EB-3	88 ± 3	88 ± 2	84 ± 3
EB-4	89 ± 2	87 ± 3	87 ± 2

4.3.4 Microstructure and properties of modified epoxy coatings

The major industrial application for the Cardolite thermoset is protective coating and painting. Therefore, we further evaluated the toughening efficacy of EB modifiers in Cardolite coatings with route B as the formulation protocol.

Representative TEM images of the cross-section of cured 10 μm thick coatings containing 5 wt.% EB modifiers are displayed in Figure 4.11. In general, the morphology characteristics have been retained in cured coatings compared to their bulk counterparts.

EB-1 still forms ill-defined micelles as denoted by the red arrow in Figure 4.11a, and EB-2 to EB-4 present a morphological transition from branched wormlike micelles (Figure 4.11b), to a mixture of spherical micelles and a few short rod-like micelles (Figure 4.11c), and finally to dispersed spherical micelles (Figure 4.11d). However, for all diblocks, the size of formed micelles is significantly smaller than that of micelles in bulk thermosets as shown in Figure 4.7. Here, the diameter of the elongated PBO cores in Figure 4.11b is 7 ± 2 nm, and of the spherical PBO cores in Figure 4.11c and 4.11d are 9 ± 3 nm and 10 ± 2 nm, respectively. Additionally, in cured coatings there is a remarkable decrease in the number of observable ill-defined micelles (Figure 4.11a) and elongated structures, namely, wormlike micelles (Figure 4.11b) or cylindrical micelles (Figure 4.11c).

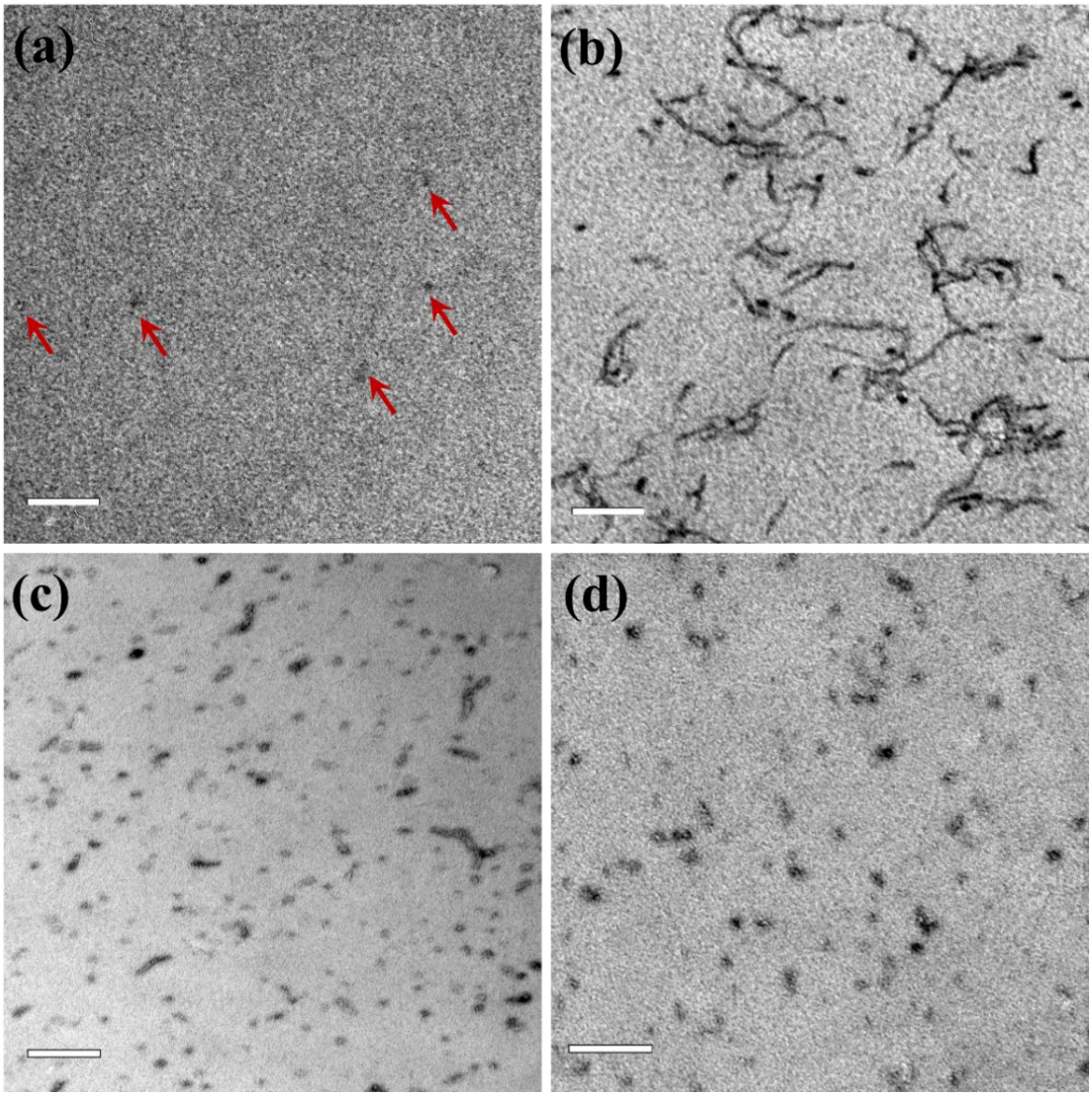

Figure 4.11 Representative TEM images of the cross-section of modified epoxy coatings prepared via route B containing 5 wt.% of (a) EB-1, (b) EB-2, (c) EB-3 and (d) EB-4. RuO_4, used as a contrast agent, preferentially stains the PEO/epoxy interface, making relatively brighter PBO cores with darker PEO coronas. Scale bars represent 100 nm. Red arrows in (a) denote the ill-defined micelles formed by EB-1.

These differences in the micelle size and shape most likely reflects the use of chloroform as a casting solvent during coating preparation. Time-resolved SAXS results (Figure 4.8) have confirmed that after 30 min of pre-curing EB-1 just generates some

weakly-segregated phases, and EB-2 and EB-3 do not complete their structure evolution, while EB-4 has already formed some spherical micelles resembling the ones in cured bulk epoxies. At this point, addition of chloroform, a good solvent for EB and the resin, can swell or disrupt those structures. Removal of solvent results in a core diameter that is smaller than the thermodynamically preferred dimension or even prohibits the formation of elongated structures due to kinetic limitations associated with the redistribution of block copolymer chains necessary to recover the equilibrium condition. This is similar to the case of obtaining size-reduced micelles in Jeffamine coatings as shown in Chapter 3.

The mechanical and thermal properties of neat and modified epoxy coatings are summarized in Table 4.5. Modulus (*E*) and hardness (*H*) of cured 10 μm thick coatings were determined by nanoindentation. The *t*-test concluded that coatings modified with 5 wt.% of EB diblocks did not cause a statistical drop in coating modulus. On the other hand, the hardness values for coatings modified with EB-2, EB-3 and EB-4 were statistically lower than those of the neat epoxy, by 5-10%. The small decrease in these properties is consistent with the bulk epoxy results. Additionally, the glass transition temperatures of the neat and modified coatings are also listed in Table 4.5. Again, the T_g is not affected by the presence of either copolymer at any concentration. This trend is also in agreement with the bulk results.

Table 4.5 Indentation modulus (E in GPa), hardness (H in GPa) and glass transition temperature (T_g in ℃) of cured epoxy coatings prepared via route B.

Modifier	E (GPa)	H (GPa)	T_g (℃)
Neat coating	3.52 ± 0.03	0.248 ± 0.005	87 ± 2
EB-1	3.45 ± 0.14	0.242 ± 0.013	84 ± 2
EB-2	3.39 ± 0.07	0.223 ± 0.006	83 ± 4
EB-3	3.49 ± 0.05	0.237 ± 0.007	85 ± 3
EB-4	3.50 ± 0.03	0.234 ± 0.013	85 ± 2

The overall performance of neat and modified epoxy coatings was evaluated by the abrasive wear test as described in Section 2.7.4. Figure 4.12 shows the loss in optical transmission of coatings with the number of abrasive wear cycles. For all abraded samples, the reported transmission is normalized relative to the transmission of the un-abraded portion of each specimen. The relative transmitted intensity of neat epoxy coating decreases to almost 60% of its initial value over the course of 460 wear cycles. At the early stage of the abrasion (up to 40 cycles), EB modified coatings have similar abrasion resistance, which is already significantly greater than that of the neat epoxy coating. As the number of wear cycles increases, EB-2, EB-3 and EB-4 modified coatings behave similarly to each other, and they start to outperform the EB-1 modified coating. Beyond 280 cycles, the coating loaded with 5 wt.% EB-1 display a resistance comparable to that of the neat coating. At 460 cycles, the best result comes from EB-2 modified coatings, showing a nearly 30% improvement in transmission, compared with the neat. Following the rationale detailed in Chapter 3, it is reasonable to suggest that the abrasive wear resistance findings in Figure 4.12 indicate a higher fracture toughness for EB

modified coatings relative to the neat one. Also, there is a subtle difference in the toughening efficacy of micelles with different morphologies. Consistent with the trend observed in bulk epoxies, wormlike micelles (EB-2) again perform better than the others in coatings, while herein the EB-1 formed ill-defined micelles impart almost no improvement in toughness to the modified coating.

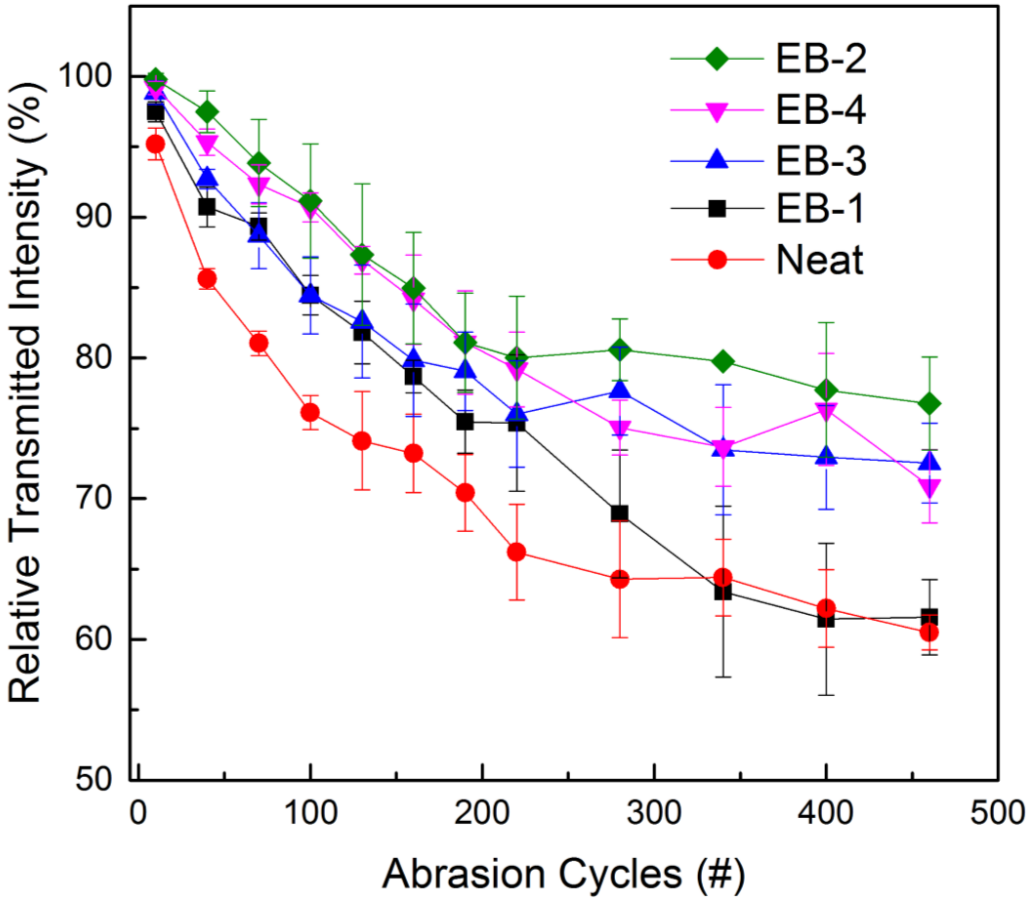

Figure 4.12 Optical transmission (at a wavelength of 630 nm) of coatings after different abrasion cycles relative to an unabraded portion of the specimen. The modifier loading is 5 wt.% in all cases.

4.4 Discussions

4.4.1 Role of processing history: route A *versus* route B

Route A. The TEM micrographs in Figure 4.6 provide clear evidence that processing route A does not lead to nanoscale structured morphologies when EB diblock copolymer is added to the DGEBA/C541 epoxy system. EB-1 is completely miscible with the epoxy matrix due to its low molecular weight. As the block copolymer molecular weight increases, from EB-1 to EB-4, the thermodynamically unfavorable interactions between the PBO block and the epoxy matrix become stronger, which promotes segregation. However, EB-2, EB-3 and EB-4 do not form discrete micelles in the cured product as desired. Instead these polymers macroscopically phase separate when mixed with the standard formulation of epoxy and hardener. We rationalize this behavior based on the local interactions that can be characterized using the solubility parameter approach.

Figure 4.13 identifies the solubility parameters associated with DGEBA, C541, PEO and PBO. The hardening agent C541 is an amphiphilic molecule comprised of a polar phenol-amine moiety and a non-polar aliphatic tail (see Figure 4.1). We believe the complications encountered with dispersing EB in the formulated resin stem from this complex molecular structure. While the average solubility parameter of C541 lies close to those of PBO and PEO, the individual pieces of this molecule lie well below and above the range of values associated with either polymer block. Because each part of the C541 molecule is relatively large with respect to the PBO and PEO repeat units, treating local

interactions using an average molecular solubility parameter in the context of Flory-Huggins theory is not appropriate. The results shown in Figures 4.3b and Figures 4.4b and 4.4d demonstrate that the higher molecular weight EB diblock copolymers tend to not form discrete micelles in C541. Because DGEBA and C541 are relatively low molecular weight compounds, they mix at a molecular level, notwithstanding these factors. Unfortunately, the balances of thermodynamic interactions that govern the mixed resin, exacerbated by the tendency for PEO to crystallize, do not allow EB-2, EB-3 and EB-4 to be dispersed as micelles using processing route A. We hypothesized that the highly amphiphilic nature of C541 would make compatibility with EB susceptible to subtle variations in the resin formulation and processing history, and such variations might tip the balance in favor of producing the desired morphologies. Based on these considerations, we explored the effects of a wide range of processing variables on final phase structure and properties of cured resins. Detailed descriptions and analyses can be found in the Appendix B (Figure B1 and B2). From the results of these investigations, we designed an improved processing route-Route B.

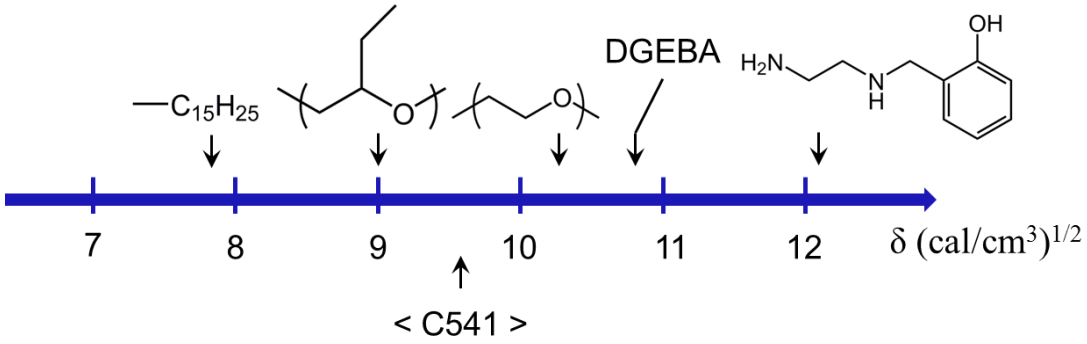

Figure 4.13 Estimations of solubility parameters (δ) of components in the epoxy system. $-C_{15}H_{25}$ is the aliphatic side group of the curing agent C541; its δ is close to 7.8 $(cal/cm^3)^{1/2}$. δ(BO) = 9 $(cal/cm^3)^{1/2}$, δ(EO) = 10.3 $(cal/cm^3)^{1/2}$, and the epoxy monomer, δ(DGEBA) = 10.8 $(cal/cm^3)^{1/2}$. The phenol-amine moiety of C541 has the largest δ value that is about 12.1 $(cal/cm^3)^{1/2}$. A crude estimation on the average δ value of C541 (shown as < C541 > above) is close to 9.6 $(cal/cm^3)^{1/2}$. All values were estimated via functional group contribution method.[156]

Route B. The improved process, route B, is summarized in Table 4.2. Firstly, the ratio of DGEBA to C541 was adjusted: the stoichiometry of reactive hydrogens in C541 (from primary and secondary amines) to epoxide groups in DGEBA was lowered from 1:1 to 2:3. This shifted the balance of thermodynamic interactions in the resin in favor of mixing with the PEO blocks, and this amelioration of mixing thermodynamics determines the phase structure in cured resins, leading to the formation of micellar structures (see Figure B1 in Appendix B). Secondly, the accelerator DMP-30 was added to the formulation (1 part per 24 parts C541 by weight) to speed up the rate of gelation in order to trap potentially metastable morphologies before nucleation and growth of macrophases as the molecular weight increases during curing. The addition of DMP-30 alone is not enough to mitigate the modifier macrophase separation (refer to Figure B1 in Appendix B), modification of the formulation and curing protocol are necessary. Thirdly, the curing

protocol was modified. Instead of allowing the resin to react for a day at 25 °C followed by a day at 50 °C, we cured the route B formulation for 8 hours at 60 °C. This avoids the possibility of PEO crystallization, which was implicated in the macroscopic phase separation of EB in the route A procedure (see Figure 4.5). Figure B2 (refer to Appendix B) summarizes the effects of curing temperature on the final morphology. The formation of dispersed micelles occurs only in samples cured at temperatures above the PEO melting point, indicating that the PEO crystallization is mainly influenced by the curing temperature.

Table 4.6 summarizes the consequences of switching from route A to route B. Both methods lead to 63% extent of reaction as determined by DSC. Significantly, following route B increases the glass transition temperature to 88 ± 3 °C versus 73 ± 3 °C based on route A. Also shown in Table 4.6 are the results of representative control experiments that show the effects on the extent of reaction and T_g with individual changes in each of the three variables. Based on this experimental design matrix we were able to simultaneously maximize T_g and produce materials with the desired nanoscale morphology and superior fracture toughness.

Table 4.6 Summary of the influences from processing variables on the neat epoxy curing extent and glass transition temperature

Identification	[a]C541 amount	[b]Hardener batch	[c]Curing	[d]Curing extent	[e]T_g (℃)
route A	Normal	(*i*)	Room temp.	63%	73 ± 3
route B	Reduced	(*ii*)	Elevated temp.	63%	88 ± 3
control-A1	Normal	(*i*)	Elevated temp.	65%	76 ± 1
control-A2	Normal	(*ii*)	Elevated temp.	73%	74 ± 2
control-A3	Normal	(*ii*)	Room temp.	67%	70 ± 2
control-B1	Reduced	(*i*)	Elevated temp.	44%	87 ± 3
control-B2	Reduced	(*i*)	Room temp.	41%	85 ± 4
control-B3	Reduced	(*ii*)	Room temp.	44%	85 ± 3

[a] The amount of C541 is based on the values of C541-to-DGEBA weight ratios from Table 2, where "Normal" amount is 65 phr used in route A, and "Reduced" amount is 40 phr used in route B.

[b] The selection of hardener batch is either (*i*) pure curing agent C541, or (*ii*) curing accelerator DMP-30 is added into C541.

[c] The curing protocols here are also from Table 2. "Room temp." refers to "25 °C curing for 24 h followed by 50 ℃ post-curing for 24 h" used in route A, and "Elevated temp." means "60 °C curing for 8 h" used in route B.

[d] The curing extent values were estimated from the integrated area of the exothermic curing peak (apex at around 220 ℃) on the first DSC heating trace of each sample.

[e] Glass transition temperatures were determined from the second DSC heating trace.

4.4.2 Mechanisms for microstructure formation

The time-resolved SAXS results presented in Figure 4.8 provide insight into the mechanisms responsible for producing the morphologies shown in Figures 4.7 and Figure B4 (see Appendix B).

EB-1 dissolves in the route B formulated resin but is driven to microphase separate into ill-defined micelles (Figure 4.7a), likely late in the course of network formation. When mixed with the uncured resin, EB-2 mostly dissolves in the resin, although concentration fluctuations produce the high q ($0.02\ Å^{-1} < q < 0.1\ Å^{-1}$) broad peak in the SAXS pattern (Figure 4.8b). The rise in intensity with decreasing q ($0.005\ Å^{-1} < q < 0.02\ Å^{-1}$) is probably caused by some weakly segregated block copolymer clusters that turn into micelles in the later stages of curing. Figure 4.14 presents the modeling of this SAXS pattern, which yields a correlation length of 1.8 nm that we associate with block chain/liquid resin interactions. This correlation length is found to increase with time, consistent with increased composition fluctuations when approaching phase separation. After about 50 minutes of curing a higher order peak is seen to develop indicative of a higher state of core-corona segregation that is associated with the branched cylindrical micelles evident in Figure 4.7b. Apparently, this fascinating morphology is induced by the curing reaction, which causes an increasing effective χ between EB-2 and the growing epoxy network, drawing any initially dissolved EB-2 into the continuous crosslinked matrix as micelles.

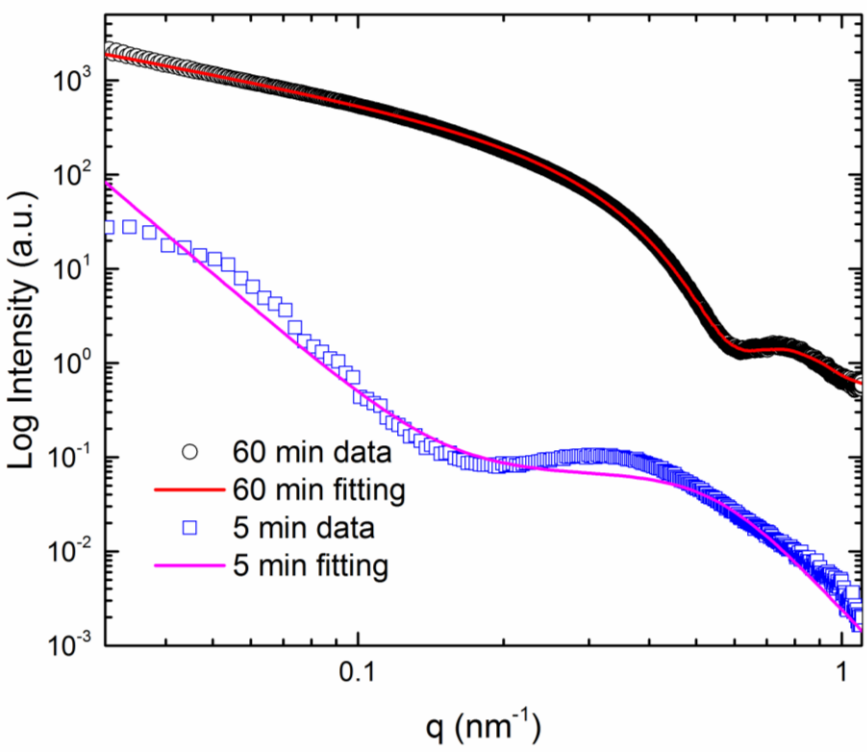

Figure 4.14 Model fitting for the 1D SAXS profile of the epoxy containing 5 wt.% EB-2. The experimental data shown here are the 5 min and 60 min curves in Figure 4.8b. The scattering from the neat epoxy has been subtracted prior to data fitting. The 5 min fitting curve is based on the correlation length model, which gives a correlation length λ = 1.84 nm. The 60 min fitting curve is based on the core-shell cylinder model, and the fitting results are: mean core radius R_c = 5.06 nm, core radius standard deviation σ_{Rc} = ± 0.90 nm, core length L = 468 nm, shell thickness t = 10.0 nm. Details about the fitting models have been described in Section 2.5.2.

Further increasing the EB molecular weight to EB-3 moves the transition from dissolution or weak segregation to consolidated micelles at an earlier point during the curing process as is evident in Figure 4.8c, where a higher order form factor peak emerges at 10 minutes. This is due to a stronger segregation associated with higher molecular weight, as evidenced by a larger correlation length of EB-3, which is 3.3 nm as shown in Figure 4.15, compared to EB-2 (1.8 nm) at the early stage of curing.

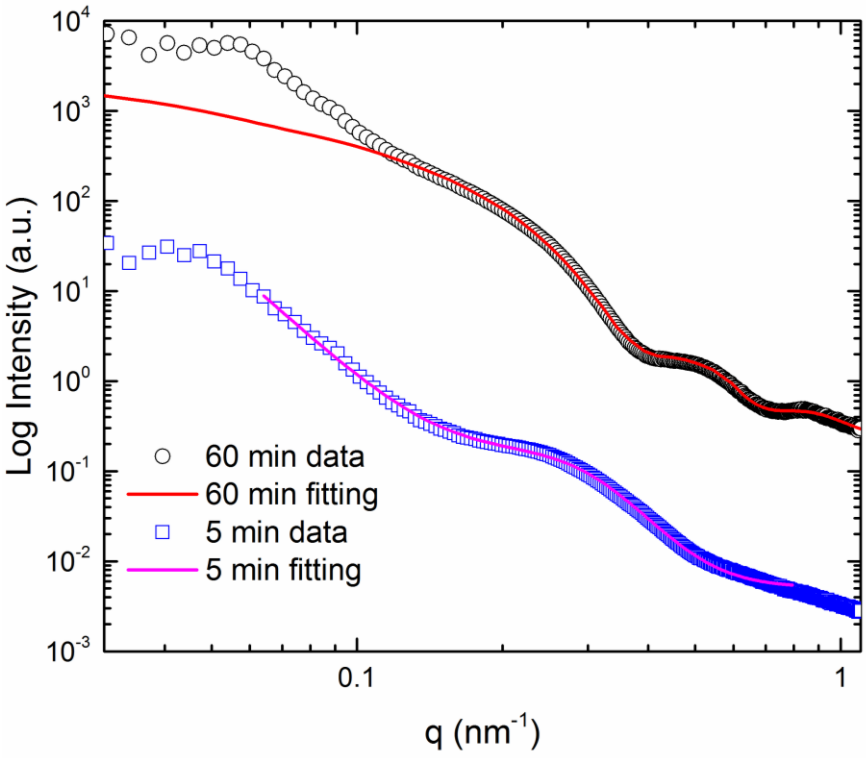

Figure 4.15 Model fitting for the 1D SAXS profile of the epoxy containing 5 wt.% EB-3. The experimental data shown here are the 5 min and 60 min curves in Figure 4.8c. The scattering from the neat epoxy has been subtracted prior to data fitting. The 5 min fitting curve is based on the correlation length model, which gives a correlation length λ = 3.28 nm. The 60 min fitting curve is based on the combination of the core-shell cylinder model and the hard sphere model, and the fitting results are: mean core radius of cylinders R_c = 8.06 nm, cylinder core radius standard deviation σ_{Rc} = ± 1.55 nm, cylinder core length L = 101 nm, shell thickness t = 5.0 nm, mean core radius of spheres $R_{c,s}$ = 6.29 nm, sphere core radius standard deviation $\sigma_{Rc,s}$ = ± 0.46 nm. Details about the fitting models have been described in Section 2.5.2.

EB-4, the highest molecular weight additive, forms well-defined spherical micelles in the unreacted resin, with an average core radius of 13.2 nm based on the model fitting results shown in Figure 4.16. Upon curing a second form factor peak emerges along with a modest variation in the structure factor, and the micelle size in the cured matrix is

similar to that in the beginning. Therefore, the epoxy condensation only slightly affects those pre-formed micelles driven by the strong segregation strength between EB-4 and the epoxy precursor.

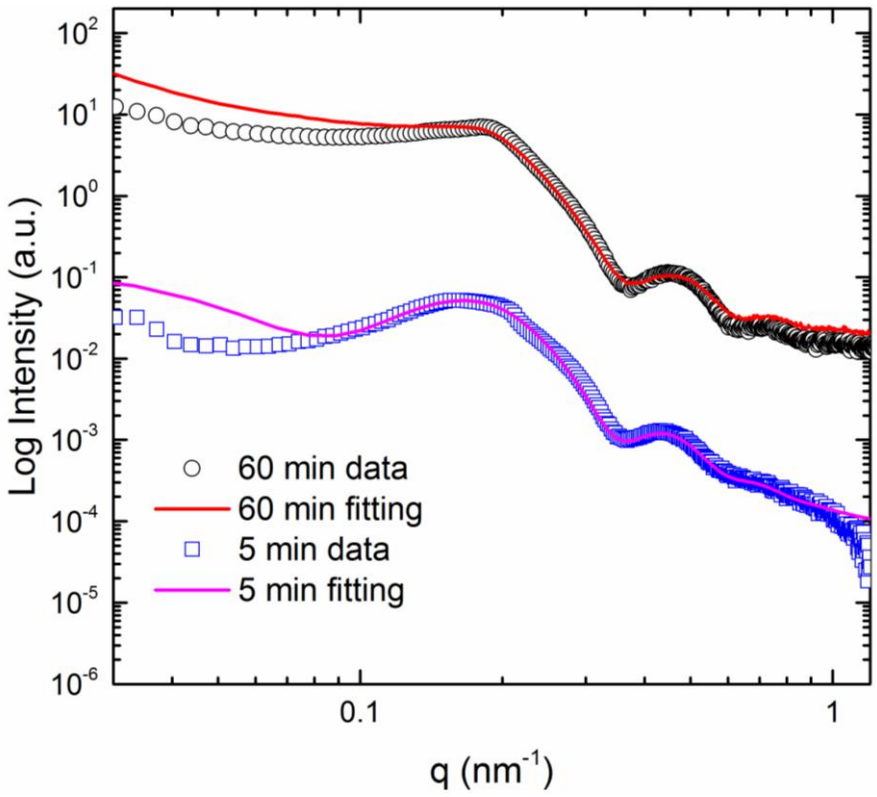

Figure 4.16 Model fitting for the 1D SAXS profile of the epoxy containing 5 wt.% EB-4. The experimental data shown here are the 5 min and 60 min curves in Figure 4.8d. The scattering from the neat epoxy has been subtracted prior to data fitting. The 5 min and 60 min fitting curves are both based on the hard sphere model, and the fitting results are: for the 5 min data, mean core radius of spheres $R_{c,s}$ = 13.2 nm, sphere core radius standard deviation $\sigma_{Rc,s}$ = ± 1.37 nm; for the 60 min data, mean core radius of spheres $R_{c,s}$ = 12.3 nm, sphere core radius standard deviation $\sigma_{Rc,s}$ = ± 0.87 nm. Details about the fitting models have been described in Section 2.5.2.

We believe the balance of thermodynamic and kinetic factors operative with processing route B provide a general strategy for engineering block copolymer modified thermoset plastics endowed with the optimal cylindrical morphology. The combination of EB composition (34 wt.% PEO) and tailored molecular weight balanced against the monomer composition, and augmented by the judicious use of a reaction accelerator and proper curing temperature enables the Fortegra™ 100 product to be extended to Cardolite hardened systems. Similar engineering strategies should be applicable to other thermoset systems, perhaps based on other commercially viable block polymers.

4.5 Summary

In this chapter, we have shown that a commercially viable block copolymer epoxy toughening agent can be engineered to provide superior toughness in combination with the bio-derived Cardolite NC 541LV (C541) curing agent. The phase behavior of four poly(ethylene oxide)-*b*-poly(butylene oxide) (PEO-PBO) diblock copolymers with similar composition but varying molecular weight were investigated by SAXS and TEM. The lowest molecular weight compound, EB-1, dissolves in the formulated epoxy resin mixture, leading to a cured product with little improvement in fracture toughness. Unfavorable thermodynamic interactions between the higher molecular weight block copolymers and C541, exacerbated by the tendency for PEO to crystallize, led to macroscopic phase separation in the room temperature cured epoxies and virtually no improvement in fracture toughness over the neat epoxy resin. Modifications to the resin

formulation and curing procedures resulted in well-defined micelles dispersed in the crosslinked epoxy matrix, and control over the micelle microstructure with variations in the block copolymer molecular weight. A branched wormlike morphology in cured resin containing 5 wt.% PEO-PBO produced a nine-fold increase in the strain energy release rate, G_{Ic}, over the standard product formulation, and a modest increase in the glass transition temperature, without significant reduction in the elastic modulus. Additionally, the morphology dependent toughening effect was retained in modified coatings so that coatings loaded with 5 wt.% wormlike micelles exhibited a remarkable improvement in the abrasive wear resistance.

Furthermore, we have elucidated the mechanism of block copolymer micelle formation in these materials based on SAXS and DSC analyses of the phase behavior of the PEO-PBO block copolymers when mixed with the individual monomer ingredients and the formulated resins in the initial unreacted state and during the curing process, and TEM and DSC evaluation of the final crosslinked products. Balancing the block copolymer molecular weight and temperature-dependent thermodynamic interactions between the components, and adjusting the monomer composition and curing rate, resulted in the optimal wormlike morphology in the cured product. This structure generated twice the fracture toughness reflected in G_{Ic} relative to spherical micelles, which is rationalized based on previously documented failure mechanisms associated with local cavitation and shear yielding.

The investigation presented in this chapter advances the field of block copolymer toughened thermoset plastics in three significant ways. Firstly, our work has the practical

benefit of extending the use of the product Fortegra™ 100 to another specific group of commercially important epoxy resins. Secondly, we have shown that suppression of block crystallization for specific curing conditions is necessary and can be effected either by modifying the processing route or selecting a non-crystallizable block. Thirdly, and most significantly, we have demonstrated a methodology for adapting an existing block copolymer, optimized for use with a restricted class of epoxies, to a broader range of commercially viable resins based on fundamental scientific and engineering principles. This approach should be valuable in designing other materials endowed with superior properties at manageable cost.

Chapter 5

Toughening graphene/block copolymer/epoxy ternary composites: hybrid toughening effects

5.1 Introduction

A large body of literature has been devoted to improving the mechanical properties of neat epoxies and major toughening strategies can be roughly classified into two categories: (i) modification with soft additives, including liquid rubbers[16, 38] and amphiphlic block copolymers,[43, 63, 65, 179] and (ii) modification with rigid fillers, including silica particles[188], carbon nanotubes,[189-191] clays[192-194] and graphenes.[195-198] Soft additives, like liquid rubbers have been added at high loadings (ca. 20 wt.%) to achieve a satisfactory toughness improvement (e.g. the fracture toughness, K_{Ic}, increases by 50%). However, the rubbery phase tends to macrophase separate from the matrix, forming micron-sized or even larger domains. The resultant epoxy products possess reduced elastic modulus, hardness and glass transition temperature (T_g), and they are also likely to lose optical transparency, rendering them unfit for many applications especially coating

products.[41, 61] In previous chapters, we have shown that amphiphilic block copolymers are more efficient and better epoxy toughening agents than liquid rubbers, at modest loadings (2-10 wt.%). However, typical block copolymer modifiers designed for epoxy resins contain rubbery epoxy-phobic blocks because they have better toughening efficacy than those with glassy epoxy-phobic blocks.[49, 96] Unfortunately, the addition of rubbery phases would inevitably sacrifice the matrix modulus and T_g.

In rigid filler toughened epoxies, the loading of modifiers is usually 1-5 wt.% or even lower due to the limitations on the processability. In a recent review, Pearson et al.[199] categorized rigid fillers from most to least effective as nanoplatelets (e.g. exfoliated clay) followed by nanofibers (e.g. carbon nanotube) followed by nanospheres (e.g. silica nanoparticles). Koratkar et al.[200] reported that at 0.1 wt.% exfoliated graphene raises the G_{Ic} of cured epoxies to 2.3 times that of the unmodified material. This enchancement is significantly greater than the ~ 1.2 times improvement obtained from other fillers at such low loadings (< 0.3 wt.%). The authors attributed the toughening effectiveness of graphene to its planar structure, which led to more effective crack deflection compared with one-dimensional carbon nanotubes or low-aspect-ratio nanoparticles. Additionally, the extremly high Young's modulus (~1 TPa) of graphene leads to an increase in composite modulus relative to that of the neat matrix.[201] Moreover, the widely used route to prepare graphene oxide (GO) from graphite involves functionalization of single-atom-thick carbon sheets,[202-207] which further improves exfoliation[205] and dispersion.[205, 206, 208, 209] The compatibility of functionalized graphenes with the matrix also enhances filler/matrix interfacial strength.[205, 208, 210]

Recognizing the advantagies and limitations of modifiers from each category stated above, ternary composites that combine soft additives and rigid fillers in epoxies have attracted considerable interest.[199] In such a ternary composite, the toughness may increase over the binary systems provided that the coexistance of soft and rigid fillers does not impair the individule toughening mechanism, and the modulus and T_g might be higher than in a binary composite containing just soft additives. If the toughening mechanisms from the two additives function simultaneously and independently, then the ternary composite toughness increases in an additive fashion. However, if one modifier's toughening effect is amplified by the addition of the other modifier, or some new toughening events take place, then an even higher, synergistic toughness could be achieved in the ternary composite.

Silica/rubber/epoxy ternary composites have been used as model systems for the exploration of epoxies modified by both soft and rigid fillers.[211-218] In most of these studies, addition of silica nanoparticles to a rubber modified epoxy matrix (containing either micron- or nano-scale soft particles) boosted G_{Ic} of the ternary composites, where the hybrid toughening effect varied, from synergistic[214, 215, 218] to simply additive.[216, 217] Synergistic toughening has been proposed to involve one or both of the following factors: (i) enhanced plastic deformation of the matrix, over and above the contribution associated with rubber cavitation alone; (ii) largely different interparticle spacings between the silica nanoparticles *versus* the micron-size rubber particles.

The simultaneous addition of rubber and nanoclay platelets into epoxies has also been studied,[219-222] and one report recently appeared describing toughening of epoxy with

graphene and rubber.[223] The fracture toughness of clay/rubber/epoxy ternary composites have been reported to be larger,[221] equal,[222] or smaller[219, 220] than the addtive toughening obtained from the corresponding binary composites. Factors influencing the performance include the dispersion of clay particles and the interaction of the soft and rigid additives. For example, Liu et al.[222] found that the toughening effects in the ternary composites depend on the relative amount of clay or rubber particles. Because the toughening mechanisms compete with each other and toughness is dominated by the additive that causes more failure feactures. Huang et al.[223] recently showed that the addition of graphene nanoplatelets enhanced the toughness of a liquid rubber modified epoxy, where larger sized graphene platelets showing the greatest effect. Toughness improveemnt was attributed to crack deflection and layer breakage/delamination of graphene particles, along with rubber cavitation and matrix shear banding. However, the authors did not report the behavior of the graphene/epoxy binary composites. Therefore, the toughening effect in the ternary composites, whether synergistic or additive, cannot be ascertained.

Although there is evidence of a synergy between soft and rigid fillers, the underlying mechanisms and generality of these effects are not well understood.[199, 214] In this chapter, we combine two highly effective additives for epoxy toughening, nanoscale block copolymer micelles with rubbery cores and micron-scale graphene (lateral dimension), in an epoxy matrix with controlled crosslink density with the goal of advancing the understanding of the factors that lead to synergistic toughening.

To the authors' knowledge, this is the first report to explore toughening effects in graphene/block copolymer/epoxy ternary composites. This chapter describes a

comprehensive investigation of the mechanical properties of composites formed by mixing an exfoliated amine-functionalized graphene oxide (GA) and poly(ethylene oxide)-*b*-poly(ethylene-*alt*-propylene) (OP) diblock copolymer into an epoxy matrix with tunable crosslink density. Comparison of the performance of binary composites containing only GA or OP, with the behavior of the ternary blends with both additives, reveals synergistic toughening of the thermoset plastic.

5.2 Experimental

5.2.1 Materials

The chemical structures of the epoxy resin ingredients and the block copolymer modifier used in this study are presented in Figure 5.1. The epoxy monomer is diglycidyl ether of bisphenol A (D.E.R. 332) provided by the Dow Chemical Company. The hardener is a mixture of two components: the trifunctional crosslinker 1,1,1-tris(4-hydroxyphenyl)ethane (THPE, Aldrich) and difunctional chain extender bisphenol A (Parabis, Dow Chemical). Both of these components react with the epoxy monomer; the ratio of the crosslinker to chain extender in the formulation was varied to systematically alter the crosslink density of the resulting network. Ethyltriphenylphosphonium acetate (70% in methanol, Alfa Aesar) was used as a catalyst to decrease curing time and to afford greater control of network branching, leading to a more uniform epoxy network.[60]

Chapter 5

Two additives were used to modify the epoxy. The first is a model poly(ethylene oxide)-*b*-poly(ethylene-*alt*-propylene) (PEO-PEP) diblock copolymer, also referred to as OP. A full description of the synthesis of PEO-PEP diblock copolymers has been provided in Chapter 2. The number-average molecular weight (M_n) of the OP diblock being used is 29 kg/mol, with the molecular weight dispersity (M_w/M_n) being 1.14, and the weight fraction of PEO is 43%. In cured epoxies, this OP diblock forms spherical micelles with the epoxy-philic PEO as the micelle corona and the epoxy-phobic PEP as the rubbery micelle core. The second modifier is a graphene oxide (GO) surface-modified with amine-terminated poly(butadiene-acrylonitrile) (ATBN), also indentified as GA.

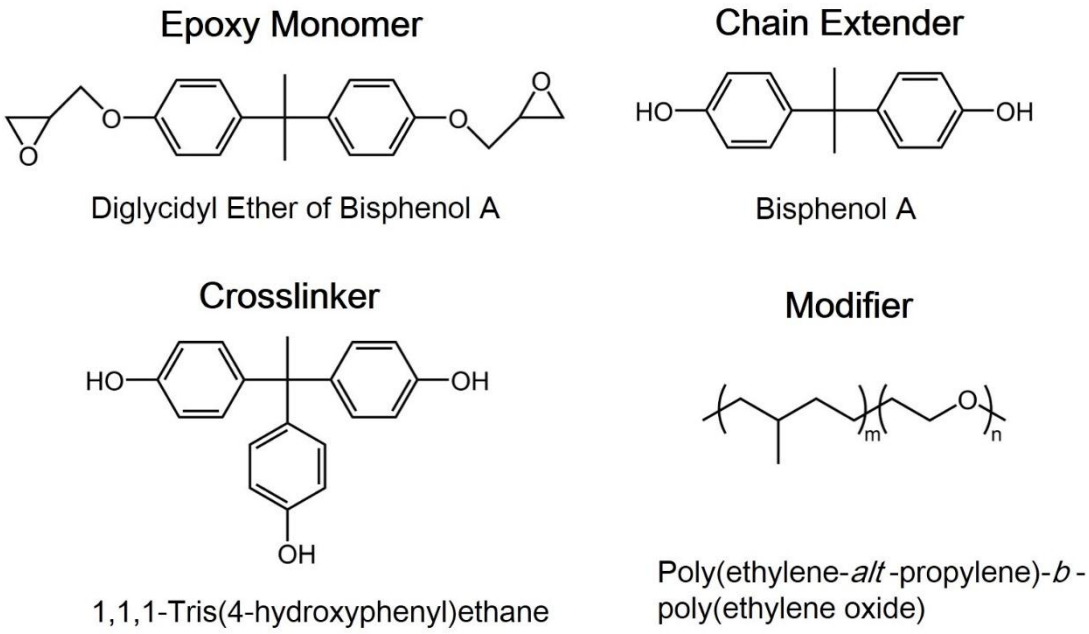

Figure 5.1 Chemical structures of epoxy resin ingredients and block copolymer modifier.

5.2.2 Preparation of amine-functionalized graphene oxide (GA)

GO was prepared from natural graphite and then grafted with ATBN following a similar protocol as reported previously.[206] ATBN chains (Hypro™ 1300 × 42 ATBN, with molecular weight 3.8 kg/mol, Emerald Performance Materials) were grafted onto GO using 4,4'-methylene diphenyl diisocynate (MDI, Sigma-Aldrich) as the coupling agent. GO (200 mg) and MDI (4 g) were placed in a 250 mL round-bottom flask, which was then purged with nitrogen for 30 min. Anhydrous dimethylformamide (DMF) was injected into the flask, and the mixture was magnetically stirred for 15 min followed by bath sonication to disperse the GO. The reaction was carried out in an oil bath at 60 ℃ and completed after 24 h, and then the mixture was flocculated by adding anhydrous toluene. The solid product was washed with anhydrous toluene at least five times to remove any excess MDI, and then was redispersed in DMF (100 mL) without drying, and a solution of 10 wt.% ATBN in DMF (20 g) was added into the dispersion while stirring. The reaction was carried out at 60 ℃ for 24 h with nitrogen purging. Acetone was used to flocculate the mixture, and then the solid product was collected by centrifugation. After washing with acetone at least five times, GA was washed twice with *tert*-butanol and redispersed in it, which was then freeze-dried, resulting in a dry powder.

5.2.3 Sample preparation

In this chapter, we explored the consequences on composite microstructure and toughness of three formulation variables: cured epoxy modified with (i) GA, (ii) OP, (iii) GA and OP, and (iv) the crosslink density of the epoxy network. Neat epoxy thermosets, GA/epoxy or OP/epoxy binary composites and GA/OP/epoxy ternary composites were prepared using similar procedures. The block copolymer OP was first dissolved in approximately 40 mL of acetone at room temperature, and then the modifier GA was added into the same round-bottom flask. To help the dispersion of GA, the mixture was bath sonicated for 30 minutes; this step was also conducted for epoxy formulations without GA for consistency. Resin components were then added and homogeneously mixed in the following order: D.E.R. 332, Parabis and THPE. Then, acetone was completely removed under dynamic vacuum by maintaining the formulation at 90 ℃ for 1 h, then at 110 ℃ for 1 h, and finally at 130 ℃ for another hour. The catalyst (ethyltriphenylphosphonium acetate) was then added and mixed for 1-2 min prior to transferring the full formulation into a preheated mold maintained at 130 ℃. The resulting plaque was cured at 200 ℃ for 2 h, and allowed to slowly cooled down to room temperature inside the oven.

The crosslink density of the epoxy network is described in terms of the average molecular weight between crosslinks (M_c), which is inversely proportional to crosslink density. The theoretical value of M_c was estimated based on the following relationship,[96]

$$M_c = \frac{2(M_e + \sum_{f=2}^{\infty} \frac{M_f \Phi_f}{f})}{\sum_{f=3}^{\infty} \Phi_f} \quad (5.1)$$

where M_e is the epoxide equivalent weight (EEW) of the epoxy monomer, *i.e.*, the ratio of the epoxy monomer molecular weight and the number of epoxide groups in the molecule, M_f is the molecular weight of a molecule with functionality f in the hardener mixture, and Φ_f is the mole fraction of hydrogens provided by the f functional molecule in the hardener mixture. Equation (5.1) assumes complete conversion of all functional groups and an exact stoichiometry between the reactive hydrogens from the hardener mixture and the epoxide group from the epoxy monomers. Given that all epoxy networks are composed of the same three basic ingredients as shown in Figure 5.1, variations in M_c are solely determined by the ratio of the crosslinker to the chain-extender in the hardener mixture, which is captured by the parameter Φ_f in Equation (5.1). For our experiments we selected four different Φ_f values, resulting in the following theoretical M_c values: 700, 1550, 3050 and 6100 g/mol. Following previously established nomenclature,[227] we refer to the four epoxy materials as CET-700, CET-1550, CET-3050 and CET-6100, respectively, where CET stands for chain extended thermoset.

5.2.4 Determination of matrix crosslink density

Employing the theory of rubber elasticity (see below), the crosslink densities of cured samples were also experimentally estimated by measuring their equilibrium storage

moduli in the rubbery state using dynamic mechanical analysis (DMA) tests with a temperature ramp from 30 to 200 ℃ (ramping rate = 5 ℃/min) on a RSA-G2 solid analyzer (TA Instruments). Rectangular strips (50 mm × 4 mm × 0.5 mm, length × width × thickness) cut from fully cured epoxy plaques were dried in vacuum at room temperature and mounted between tensile fixtures. During each test, a static pretension on the specimen was maintained at 45 g force with a sinusoidal strain amplitude of 0.005%. The dynamic tensile storage moduli (*E'*) and tan δ curves were plotted as functions of temperature (See Appendix C, Figure C1). The *E'* value at 180 ℃ (E_r, see Appendix C, Table C1) was used as the equilibrium storage modulus in the rubbery state to quantify the M_c value experimentally (see below). The temperature at the peak in the tan δ curve was recorded as the T_g for comparison with the T_g values obtained from DSC measurements (see Appendix C, Table C1).

The density of cured epoxy samples was measured at room temperature using the displacement method in accordance with ASTM D792-91. For the immersion of samples, isopropyl alcohol with a known density of 0.785 g/cm^3 was used. The density of epoxy samples was determined by the equation,

$$\rho = \frac{w_a}{w_a - w_i}\rho_i \tag{5.2}$$

where w_a is the weight of sample in air, w_i is the weight of sample in isopropyl alcohol, and ρ_i is the density of isopropyl alcohol. Density values were summarized in Table C1 (see Appendix C).

5.3 Results and Analyses

5.3.1 Dispersion of GA in binary composites

Figure 5.2 shows representative TEM micrographs obtained from fully cured epoxies with different crosslink densities, and different loadings of GA. The presence of reactive amine groups from grafted ATBN chains improves the compatibility and facilitates the interfacial interaction between the graphene particles and the epoxy matrix.[205, 206, 209] At a low loading (0.04 wt.%), the high-aspect-ratio GA particles are well dispersed, as shown in Figure 1a and 1c. Good dispersion of GA was also noted in SEM of fracture surfaces, as shown below. Dispersed and randomly oriented graphene particles with lateral dimensions in the range of 0.5 - 2 μm and thicknesses of ~ 30 nm are found throughout the matrix, without any particle aggregates or observable debonding at the graphene/matrix interface. Although the number of graphene layers associated with each particle is not discernible due to graphene corrugation, we speculate there is coexistance of single-layered and multilayered GA sheets. These figures along with those in Figure S2 reveal that the crosslink density of the epoxy matrix does not affect the dispersion state of GA. At higher GA loading (0.16 wt.%) more graphene nanosheet stacks are apparent (Figure 1b and 1d), leading to agglomerates with larger dimensions relative to those in the lower loading composite (Figure 1a and 1c). However, based on TEM the overall dispersity is similar to that in a different epoxy matrix reported previously.[206]

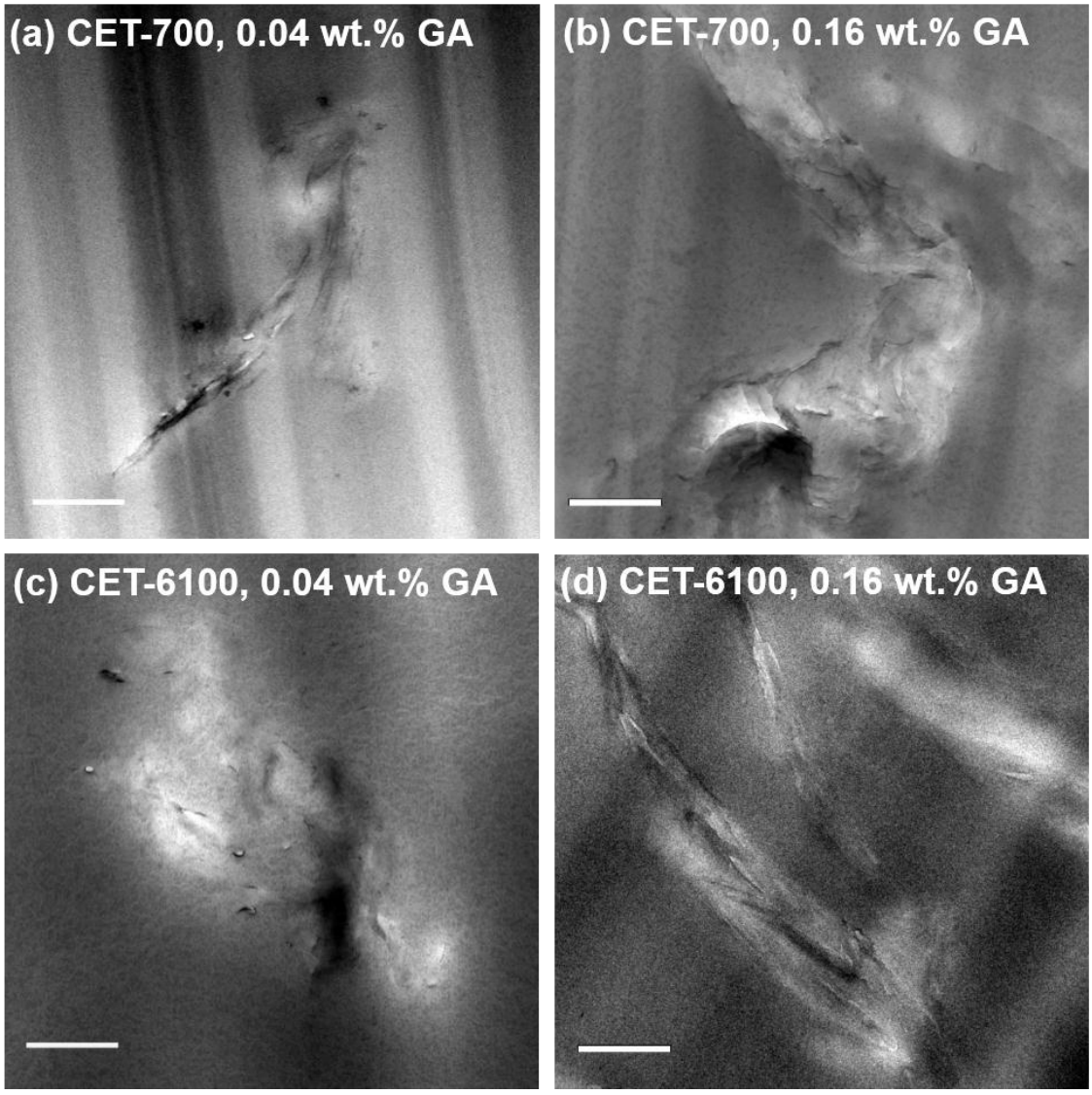

Figure 5.2 Representative TEM images of cured GA/epoxy binary composites with the theoretical crosslink density (a, b) M_c = 700g/mol, and (c, d) M_c = 6100 g/mol. The loading of GA is 0.04 wt.% in (a, c) and 0.16 wt.% in (b, d). Scale bars represent 0.5 μm.

5.3.2 Mechanical and thermal properties of GA/epoxy binary composites

Figure 5.3, Figure 5.4 and Table C1 (see Appendix C) summarize the room temperature elastic moduli and glass transition temperatures of neat epoxies and GA/epoxy binary composites at different modifier loadings and matrix crosslink densities. The elastic modulus of binary composites increases with the loading of GA up to 0.16 wt.%, as shown in Figure 5.3a, data for two epoxy matrices with different crosslink densities (theoretical M_c = 700 g/mol and 6100 g/mol). At 0.16 wt.% of GA, the increase in the elastic modulus is about 9% and 11% for the CET-700 and CET-6100 systems, respetively, which is comparable to the reported results in different epoxy composites containing graphene particles.[208, 224]

Because of the approximately linear increase, a modified rule of mixtures was empolyed to determine the effective modulus, E_{eff}, of the modifier GA in each composite,[208, 224]

$$E_c = E_m V_m + E_{eff} V_{GA} \tag{5.3}$$

where E_c and E_m are the elastic moduli of the binary composite and epoxy matrix, respectively. V_m and V_{GA} are the volume fractions of the epoxy matrix and the modifier GA, with $V_m + V_{GA} = 1$. Following this relationship, Figure C3a (see Appendix C) displays the linear regression of the data in Figure 5.3a, providing that for CET-700, E_{eff} = 250 GPa and for CET-6100, E_{eff} = 303 GPa. Furthermore, E_{eff} can be related to E_{GA} (the modulus of GA particle) through the relationship $E_{eff} = E_{GA}\eta_0\eta_1$ where η_0 is the Krenchel orientation factor, which depends on the average orientation of particles within the

matrix; η_1 is the length parameter allowing for poor stress transfer at the particle/matrix interface for particles with small lateral dimensions (η_1 = 1 for perfect stress transfer and η_1 = 0 for no stress transfer).[224] There is no observable difference between CET-700 and CET-6100 binary composites in terms of the GA particle orientation within the matrix, according to TEM. Therefore, the fact that CET-6100 has a higher E_{eff} value than CET-700 suggests that a better stress transfer at the GA/matrix interface may exist in a less crosslinked matrix.

The elastic modulus of the neat epoxy decreases as the molecular weight between crosslinks (M_c) increases, as shown in Figure 5.3b. A higher theoretical M_c value corresponds to fewer chemical crosslinks within the network. Consequently, polymer chains are less constrained and relax more readily under applied stress, resulting in a smaller elastic modulus. Likewise, binary composites based on CET-6100 have lower average moduli than corresponding composites based on CET-700 with the GA loading; however the statistically significant differences were only noted for composites 0.02 wt.% GA.

The moduli of 0.04 wt.% GA modified binary composites in Figure 5.3b shows that the moduli of these composites is appreciably higher than the neat epoxy but not significantly affected by M_c. According to Equation (5.3), the data can be interpreted as the effective modulus of GA as a function of M_c. Figure C3b (see Appendix C) summarizes the results and displays that E_{eff} increases with the theoretical M_c. However, given the scatter in the fitting results, we cannot be definitive about the dependence of the stress transfer on the matrix M_c.

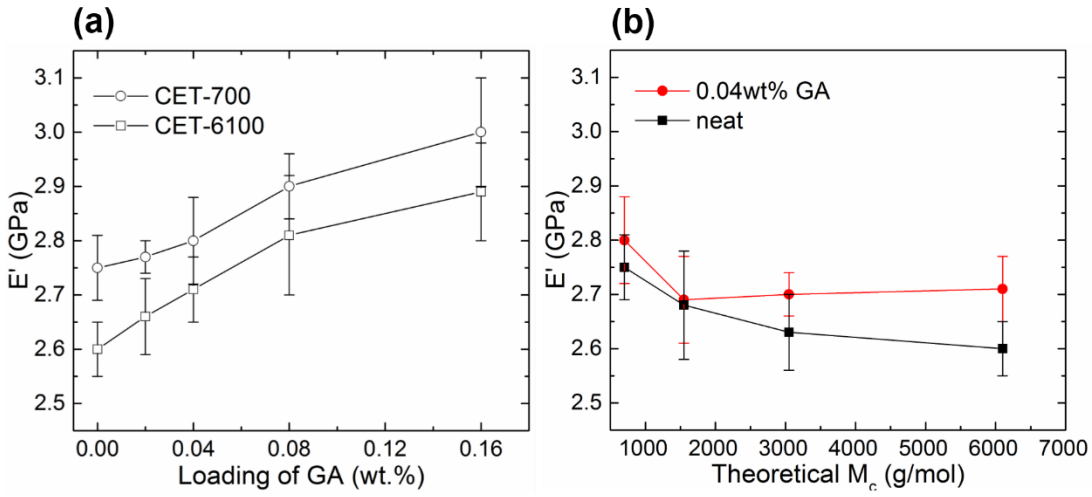

Figure 5.3 Room temperature elastic modulus (*E'*) of GA/epoxy binary composites. (a) *E'* as a function of GA loading for epoxy networks with the theoretical M_c = 700 g/mol and 6100 g/mol; (b) *E'* as a function of the network theoretical crosslink density for neat and 0.04 wt.% GA modified epoxies. Solid lines are to guide the eye.

Glass transition temperatures for the GA/epoxy binary composites are presented in Figure 5.4. The addition of low loadings of GA modifiers does not significantly affect the T_g of the epoxy matrix, as evidenced in Figure 5.4a. On the other hand, Figure 5.4b shows that neat epoxies and 0.04 wt.% GA modified composites both exhibit a ~ 40 ℃ decrease in T_g as the network M_c increases from 700 g/mol to 6100 g/mol ($1/M_c$ decreases from 1.4×10^{-3} mol/g to 1.6×10^{-4} mol/g). Based on the addition and redistribution of network free volume, Ellis et al.[225] proposed a linear relationship between the T_g (in Kelvin) of a network with varying crosslink density and $1/M_c$:

$$T_g = T_{g,\infty} + \frac{\varsigma}{M_c} \tag{5.4}$$

where $T_{g,\infty}$ is the glass transition temperature (in Kelvin) of the linear polymer backbone at infinite molecular weight and ζ depends on the molecular weight of the unreacted resin

and the ratio of incremental free volume contributions from the resin and the curing agent.[226] The linear regression of the experimental data in Figure 5.4b gives $T_{g,\infty}$ = 94 ℃ and ζ = 33 *k*g K/mol for the neat epoxy materials, close to the values reported previously for this epoxy resin.[227] The 0.04 wt.% GA modified epoxies have $T_{g,\infty}$ = 94 ℃ and ζ = 35 *k*g K/mol, according to the linear fitting results.

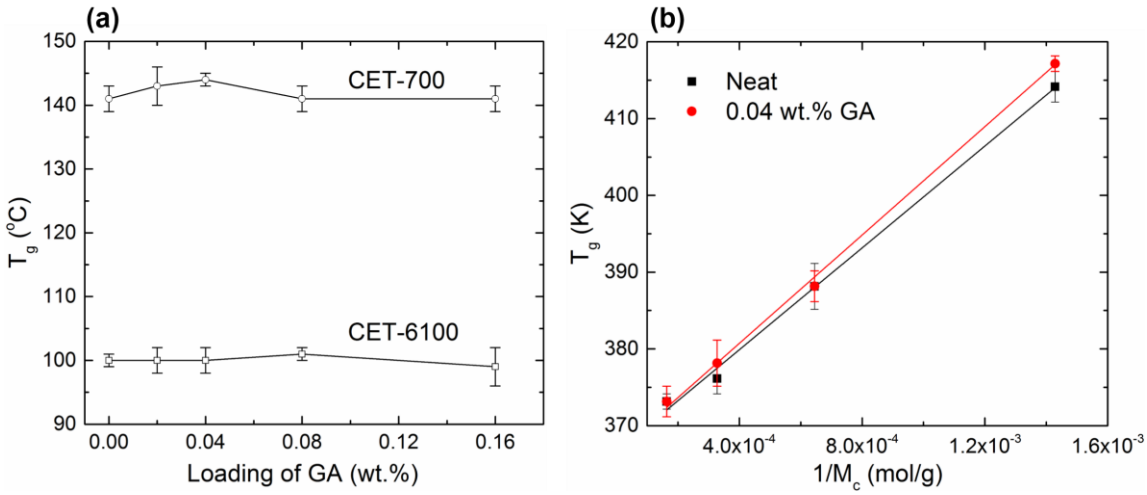

Figure 5.4 Glass transition temperature (T_g) of GA/epoxy binary composites. (a) T_g as a function of GA loading for epoxy networks with the theoretical M_c = 700 g/mol and 6100 g/mol; (b) T_g as a function of the reciprocol of the theoretical M_c for neat and 0.04 wt.% GA modified epoxies. Solid lines in (a) are to guide the eye, but in (b) they are the fitting lines of the data according to Equation (5.4).

5.3.3 Experimental crosslink densities of GA/epoxy binary composites

As described earlier, the theoretical M_c values of cured samples were calculated according to Equation (5.1). The crosslink density of each sample was estimated by

measuring the shear modulus in the rubbery state and relating it to M_c using the rubber elasticity theory:[39]

$$M_c = \frac{\rho RT}{G_r} \tag{5.5}$$

where ρ is the sample density; and R and T are the gas constant (8.314 J/K·mol) and temperature (in Kelvin), respectively. In the calculation of Mc, we have estimated the density in the rubbery state (180 ℃) based on the combined effects of thermal expansion above and below T_g (thermal expansion coefficients $\alpha_{rubbery} \cong 7.5\times10^{-4}$ ℃$^{-1}$, $\alpha_{glassy} \cong 2\times10^{-4}$ ℃$^{-1}$) and the measured density at room temperature (Table C1, Appendix C).[39] G_r is related to the tensile modulus E_r measured by DMA (see Appendix C, Table C1 and Figure C1),

$$G_r = \frac{E_r}{2(1+\nu)} \tag{5.6}$$

where ν = 0.5 is the Poisson's ratio for a rubber. Table C1 (see Appendix C) lists the theoretically and experimentally determined M_c values for all the samples.

Figure 5.5 presents the experimental M_c against the loading of GA. There is a modest difference between the theoretical and experimental M_c values, which is not surprising given the assumptions associated with both calculations. Similar results have been reported previously with this epoxy resin.[60] All GA/epoxy binary composites follow a similar trend, where the experimental M_c values decrease slightly with increasing loading of GA. This may be due to a reaction between the amine groups from the grafted ATBN chains on GA particles and the epoxy monomer, which imparts more crosslinks to

the network, and results in a lower average molecular weight between crosslinks. However, the effect of GA on increasing the crosslink density is not statistically significant.

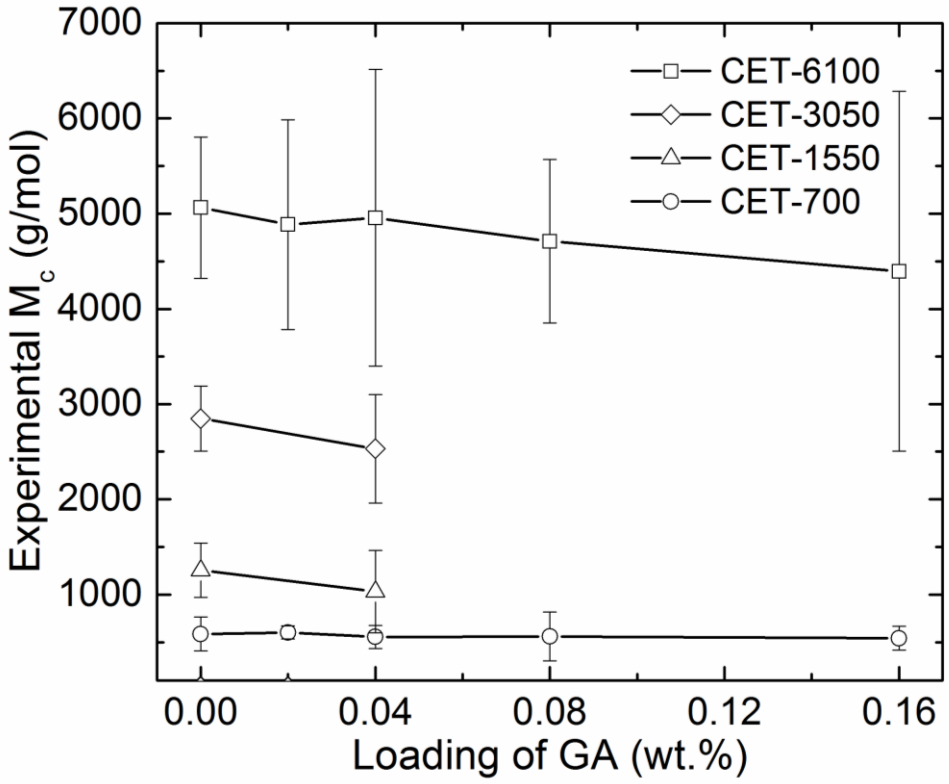

Figure 5.5 Experimental crosslink densities of GA/epoxy binary composites as a function of the loading of GA. Legends indicate the theoretical M_c values for different epoxy networks and solid lines are to guide the eye.

5.3.4 Fracture toughness of GA/epoxy binary composites

In Figure 5.6 the fracture toughness and critical strain energy release rate of GA/epoxy binary composites are plotted against the loading of GA and the theoretical crosslink density of the matrix. For both CET-6100 and CET-700 systems, the K_{Ic} and G_{Ic} increase with the loading of GA up to 0.04 wt.% and then at higher GA loadings, within experimental uncertainty, K_{Ic} and G_{Ic} values reach a plateau, as displayed in Figure 5.6a and c. It is evident that the CET-6100 system exhibits a better toughening effect than CET-700. In the CET-6100 system, 0.04 wt.% GA gives a 1.3-fold increase in K_{Ic} and a corresponding 1.7-fold increment in G_{Ic}, relative to unmodifed epoxies. This is an impressive improvement in fracture toughness, close to the preivously reported results in a different epoxy resin toughened by the GA particles.[206] The difference in tougheness improvement between the CET-700 and CET-6100 systems is reinforced by Figure 5.6b and d, where the GA loading is kept constant at 0.04 wt.%. Both K_{Ic} and G_{Ic} of the composites increase roughly linearly with the matrix M_c, but the K_{Ic} and G_{Ic} values of the neat epoxies do not change with the matrix crosslink density.

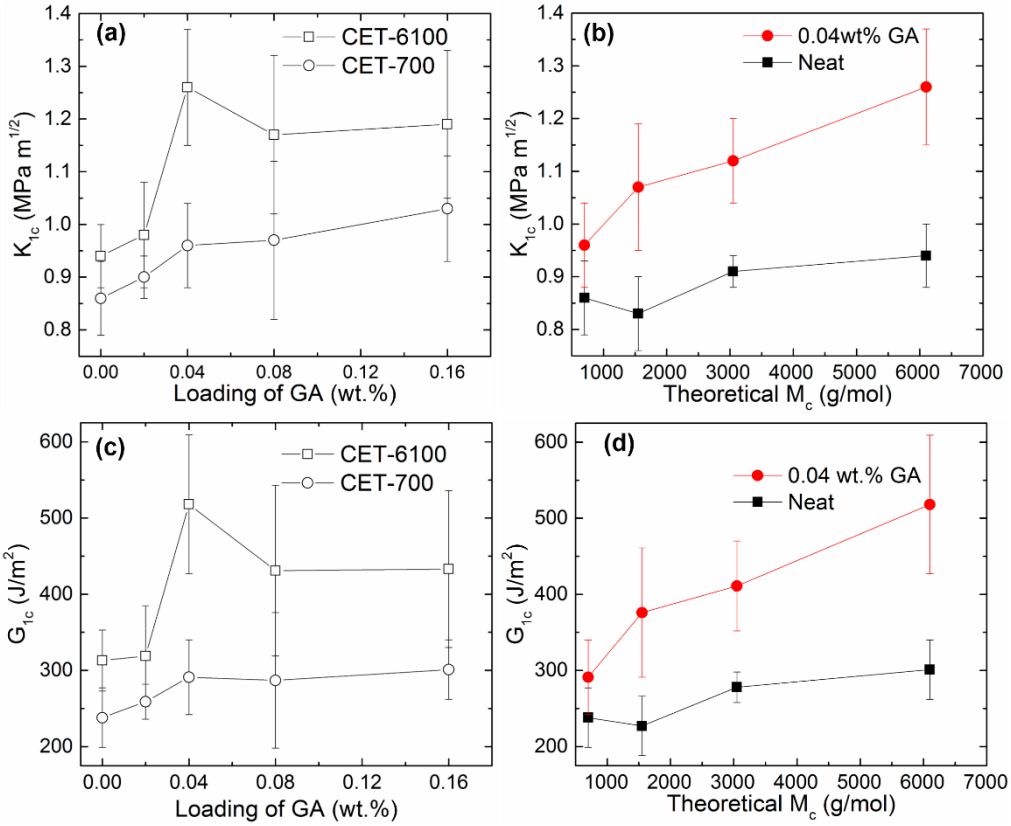

Figure 5.6 Fracture toughness K_{Ic} (a, b) and critial strain energy release rate G_{Ic} (c, d) of GA/epoxy binary composites. (a, c) K_{Ic} or G_{Ic} as a function of GA loading for epoxy networks with the theoretical M_c = 700 g/mol and 6100 g/mol; (b, d) K_{Ic} or G_{Ic} as a function of the network theoretical crosslink density for neat and 0.04 wt.% GA modified epoxies. Solid lines are to guide the eye.

5.3.5 Toughening mechanisms in GA/epoxy binary composites

The fracture surfaces of broken compact tension specimens were examined under SEM; representative micrographs are presented in Figure 5.7, as well as Figure C4 to C6 (see Appendix C). In neat epoxies with different crosslink densities, the fracture surfaces in the region of rapid growth are very smooth with no apparent plastic deformation, consistent with the brittleness of these material (see Figure C4 in Appendix C). However,

very fine lines perpendicular to the direction of crack propagation (indicated the by white arrows) are distributed thoughout the fracture surafce of the neat-6100 (as denoted by the red arrows in Figure C4d, C4f) as well as on the GA/epoxy composites prepared with CET-6100 (Figure 5.7a, b, f, and Figure C5 and C6). These features may be crack arrest lines, and each line is actually an extended band with an average width of ~ 5 μm under higher magnification (see Figure C4f and C6). In this region, marks with irregular lips are caused by the material being peeled, indicating the occurrence of a ductile fracutre and "slow" crack growth. The areas between the lines are featureless and relatively smooth, and a brittle fracture and fast crack growth occur in these regions.[15] The presence of arrest lines typically reveals a stick/slip mode for the crack propagation;[228] however, no indication of this sort of propagation was found in the load vs. displacement data. Moreover, the neat epoxies with different crosslink densities have similar fracture toughness (see Figure 5.6b and d). Hence, the unique features on the fracture surface of CET-6100 indicates an intrinsic difference from the more densely crosslinked counterparts, but the origin of these marks is not clear.

Additional features appear on the fracture surfaces of GA/epoxy composites. In Figure 5.7a and b, the "tail" markings are evident on the fracture surfaces; these markings are generated by the crack pinning effect of rigid GA particles.[206] At a higher magnification (micrographs shown in Figure C6), delamination between the GA particles and the matrix is clearly observed.

Crack pinning and crack deflection have been proposed as the major toughening mechanims in graphene modified epoxies.[199] The rough surfaces observed on the fracture

topographs provided in Figure 5.7 and Figure C5, C6 are consistent crack pinning by rigid GA particles and crack deflection. Further, at higher magnification (Figure C6), it appears that there has been debonding and void formation at the particle/matrix interface, indicating additional contribution to the toughness. As reported in previous work,[206] the grafted ATBN rubber chains can store elastic energy and their covalent bonding with the matrix further increases the energy dissipation to form delamination. The effects of GA loading and the crosslink density on the toughness merits further discussion as below.

As the loading of GA increases, there are clearly more observable crack pinning sites (Figure C5 in Appendix C). At loadings higher than 0.04 wt.%, the crack-pinning sites are closer to each other. This proximity may lead to a possible coalesence of secondary cracks formed around the particles, which would facilitate the propagation of the primary crack and lessen the crack resistance of the binary composites.[206] This may explain the the increase in K_{Ic} and G_{Ic} against the GA loading that is less steep after 0.04 wt.%. To verify this hypothesis, we estimated the plane strain plastic zone size, r_y, for the GA/epoxy binary composites by using the Irwin model:[3]

$$r_y = \frac{1}{6\pi}\left(\frac{K_I}{\sigma_{ys}}\right)^2 \tag{5.7}$$

where σ_{ys} is the material yield strength. According to the reported tensile properties of this epoxy thermoset,[91] the σ_{ys} of neat materials is ~ 80 MPa. By assuming 0.04 wt.% GA only slightly increases the σ_{ys},[206] and $\sigma_{ys} \cong 80$ MPa, we obtain $r_y \cong 12\mu m$ for the CET-6100 epoxy containing 0.04 wt.% GA. Based on SEM of the fracture surfaces, the average distance between each two neighboring sites of crack-pinning is around 13 μm,

close to the estimated plastic zone size. Therefore, the microcrack zones are likely to coalesce as stated above.

Additionally, in Figure 5.7c the tails around particles are very short and less evident, suggesting that GA particles have weak interactions with the primary crack in the densely crosslinked CET-700 matrix. As the matrix M_c increases, the tails become longer and the number density of visible crack-pinning sites also increases as revealed in Figure 5.7d to f. It indicates an increasing effect of the GA particles to pin and deflect the primary crack, contributing to the growing fracture toughness with increasing M_c (Figure 5.6b and d).

In fact, it has been well known in rubber modified epoxies, the toughening efficacy of the rubber particles improves with the decrease of the network crosslink density.[39, 227] The epoxy resins with lower crosslink density are more ductile, which means the matrix can endure more plastic shear deformation and dissipate more strain energy upon the rubber cavitation. Several researchers[282, 283] also reported rigid particle modified epoxies have a similar dependence on the matrix ductility. The increase of toughening effect in these systems with the increasing matrix ductility has been attributed to the increasing particle debonding and the shear yielding in the matrix. We note that the ductility of the epoxy matrix is controlled by two independent factors: the crosslink density and the intrinsic rigidity of the backbone. The studies cited above usually adjust the matrix ductility by changing the epoxy resin components, so the findings are actually subject to the combined effects of these two factors.

With our epoxy system neither the ductility nor backbone rigidity (i.e., chemistry) are not altered as M_c is varied. We speculate that the change in toughness with M_c in the

GA/epoxy binary composites involves molecular level events related to the mobility and relaxation of polymer chain segments between crosslinks when stressed. For example, with increasing M_c the matrix modulus drops slightly, leading to larger amounts of deformation of the matrix near the rigid particle/matrix interface, which facilitates debonding.[219] Additional studies are needed to resolve this issue.

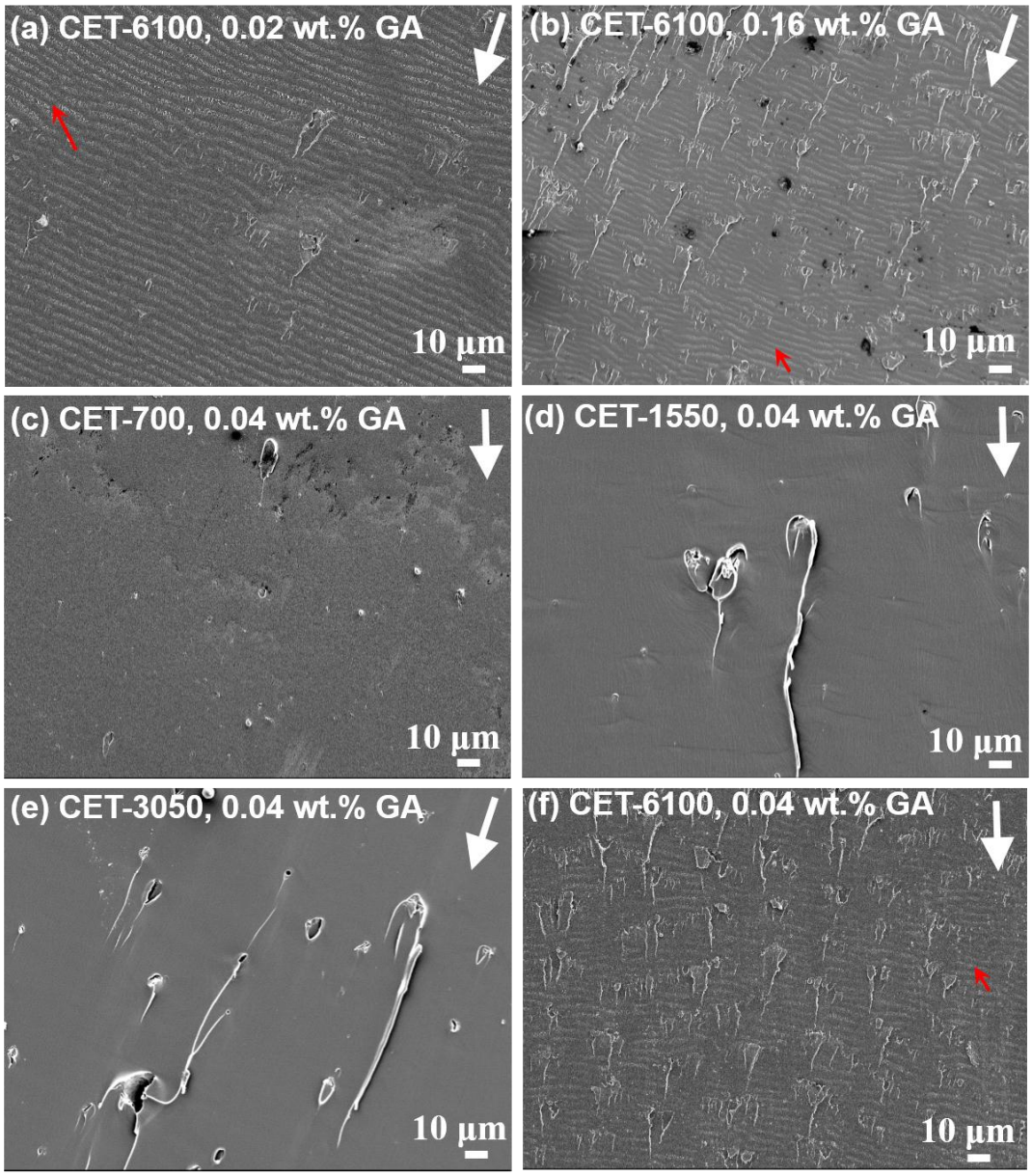

Figure 5.7 SEM fractographs of GA/epoxy binary composites with the theoretical M_c = 6100 g/mol containing (a) 0.02 wt.% GA and (b) 0.16 wt.% GA; (c–f) the GA loading is 0.04 wt.%, but the theoretical crosslink density varies (c) M_c = 700 g/mol, (d) M_c = 1550 g/mol, (e) M_c = 3050 g/mol, (f) M_c = 6100 g/mol. White arrows indicate the crack propagation direction. The red arrows in (a), (b) and (f) denote the crack arrest line within the matrix.

5.3.6 Microstructure of GA/block copolymer/epoxy ternary composites

Considering the good tougheing effect in binary composites with low GA loadings, we kept the GA loading at 0.04 wt.% but varied the block copolymer OP loading in GA/OP/epoxy ternary composites. Figure 5.8 and C7 (see Appendix C) show representative TEM images of cured ternary composites. In all cases, the dispersion of GA particles is similar to that in the binary composites, and the diblock OP self-assembles into well-dispersed spherical micelles composed of a PEO corona and PEP core. This nanostructure closely resembles that reported in previous work with this epoxy system and block copolymer.[227] In the CET-700 matrix, at both 0.04 wt.% and 5 wt.%, the OP micelles are spheres with narrowly distributed diameters of 38 ± 9 nm (Figure 5.8a) and 35 ± 6 nm (Figure 5.8b). In the CET-6100 matrix, the sphere size is slightly different, 31 ± 8 nm (Figure 5.8c) and 32 ± 5 nm (Figure 5.8d) in diameter. Figure C7 (see Appendix C) further confirms that the matrix crosslink density only has a small effect on the micelle size and does not affect the micelle distribution. Another important conclusion from TEM is that the the two types of modifiers do not exibit any observable interactions and their coexistence does not intefere with each other in terms of dispersity, particle shape and dimension. This is actually desirable for the goal of toughening a hybrid ternary system containing micron and nano-sized modifiers.

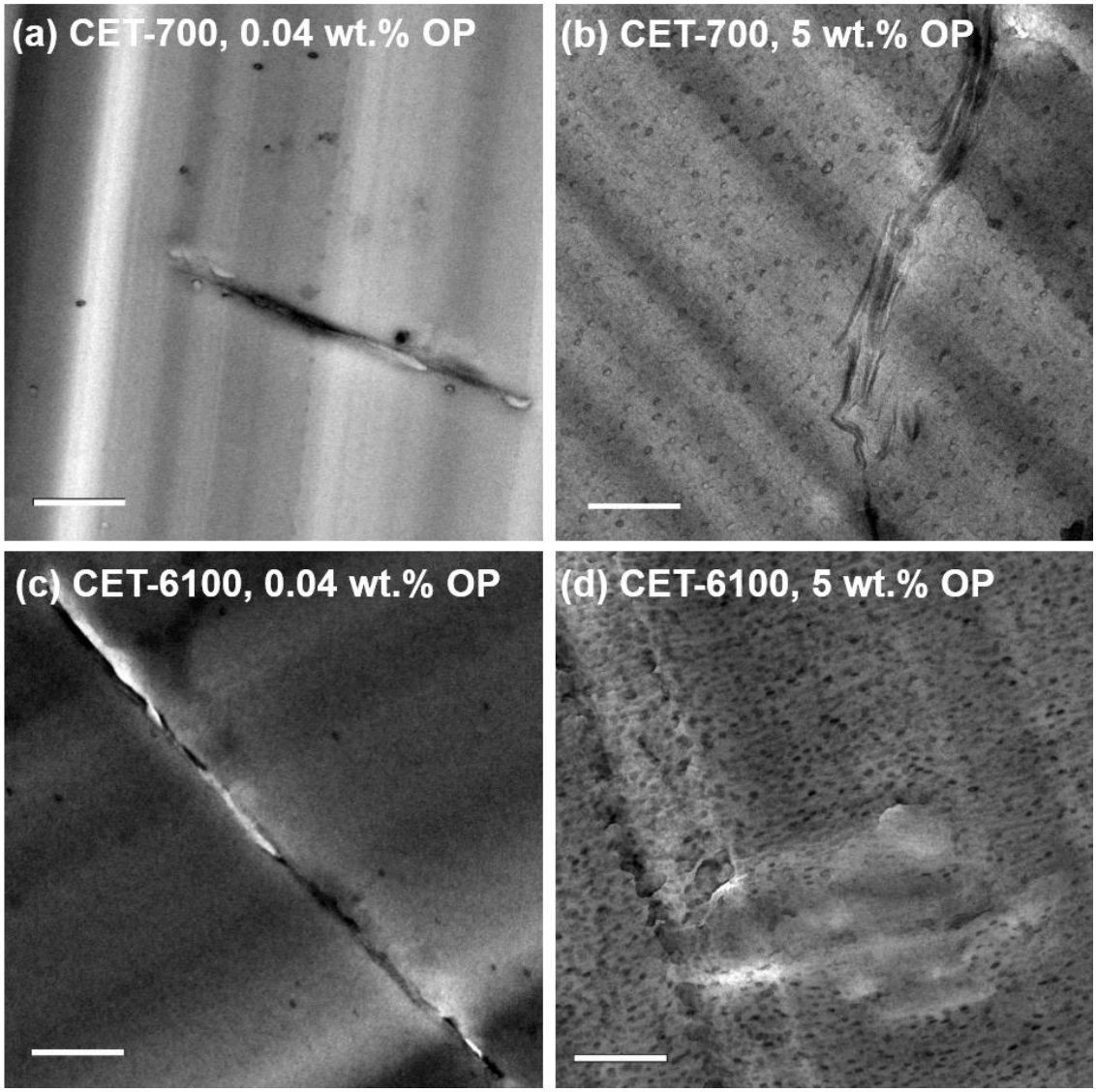

Figure 5.8 Representative TEM images of cured GA/OP/epoxy ternary composites with the theoretical crosslink density (a, b) M_c = 700g/mol and (c, d) M_c = 6100 g/mol. The loading of GA is 0.04 wt.% in all cases, and the loading of OP is 0.04 wt.% in (a) and (c), and 5 wt.% in (b) and (d). RuO_4, used as a contrast agent, preferentially stains the PEO/epoxy interface, making relatively brighter PEP cores with darker PEO coronas. Scale bars represent 0.5 μm.

5.3.7 Mechanical and thermal properties of ternary composites

Figure 5.9 and Table C2 (see Appendix C) summarize the room temperature elastic moduli of the GA/OP/epoxy ternary composites with different loadings of OP. Table C2 also lists the moduli of OP/epoxy binary composites for comparison. All values have been normalized relative to the associated neat epoxy moduli. The incorporation of low loadings of OP (0.04 and 0.4 wt.%) causes less than 5% decrease in the moduli of the OP/epoxy binary composites for both CET-700 and CET-6100 systems, while the ternary counterparts exhibit almost no sacrifice in the moduli. This effect tends to be more evident for the case of 5 wt.% OP, where the drop in binary composite moduli is usually 8 ~ 10%. The ternary composites exhibit moduli within 97% of the values of neat epoxy (see Figure 5.9 and Figure C8 in Appendix C). The addition of a small amount of GA modifier effectively compensates for the small loss in stiffness that accompanies addition of the block copolymer.[35]

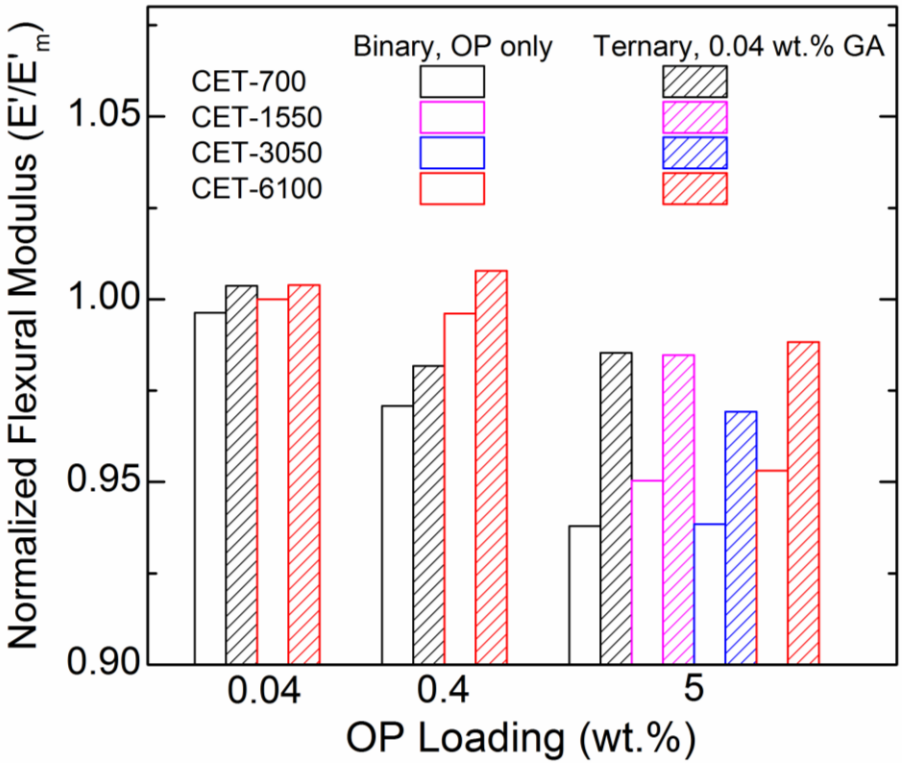

Figure 5.9 Normalized elastic modulus (*E'*) of OP/epoxy binary composites and GA/OP/epoxy ternary composites. All normalized values are relative to the associated neat epoxy E'_m values. The loading of GA is 0.04 wt.% in all ternary composites, and the loading of OP varies.

The glass transition temperatures of OP/epoxy binary composites and OP/GA/epoxy ternary composites determined by DSC are summarized in Figure 5.10. There is no statistically significant change in T_g after the addition of any amount of GA or OP modifiers for different epoxy systems (the T_g's of neat epoxies are denoted by the dotted lines with the same color). Table C2 (see Appendix C) lists T_g values estimated from the temperature at maximum tan δ (=*E'/E''*) during the DMA tests. These results also confirm that T_g is virtually unchanged with the addition of modifiers and is mainly a function of the M_c of the epoxy matrix, as characterized by Equation (5.4).[61]

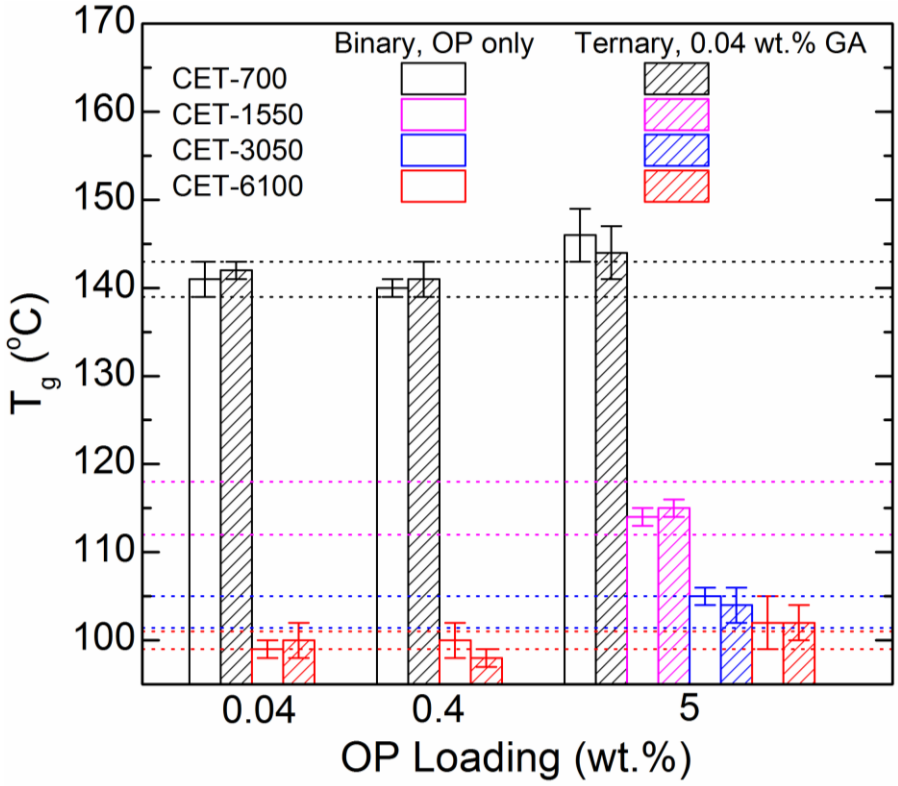

Figure 5.10 Glass transition temperature (T_g) of OP/epoxy binary composites and GA/OP/epoxy ternary composites. The loading of GA is 0.04 wt.% in all ternary composites, and the loading of OP varies. The dotted lines in the same color denote the T_g (with experimental uncertainty) of the neat epoxy with associated theoretical M_c value.

5.3.8 Experimental crosslink densities of GA/OP/epoxy ternary composites

The crosslink density of OP/epoxy binary composites and ternary composites was experimentally determined in a similar manner as described above for GA/epoxy binary composites, and the results are presented in Figure 5.11 and Table C2 (see Appendix C). As the OP loading increases from 0.04 wt.% to 5 wt.%, the experimental M_c value tends to slightly decrease in the binary and ternary composites. However, the decreasing effect

is small in general, because there are no significant differences in the experimental M_c of neat epoxies and binary and ternary composites.

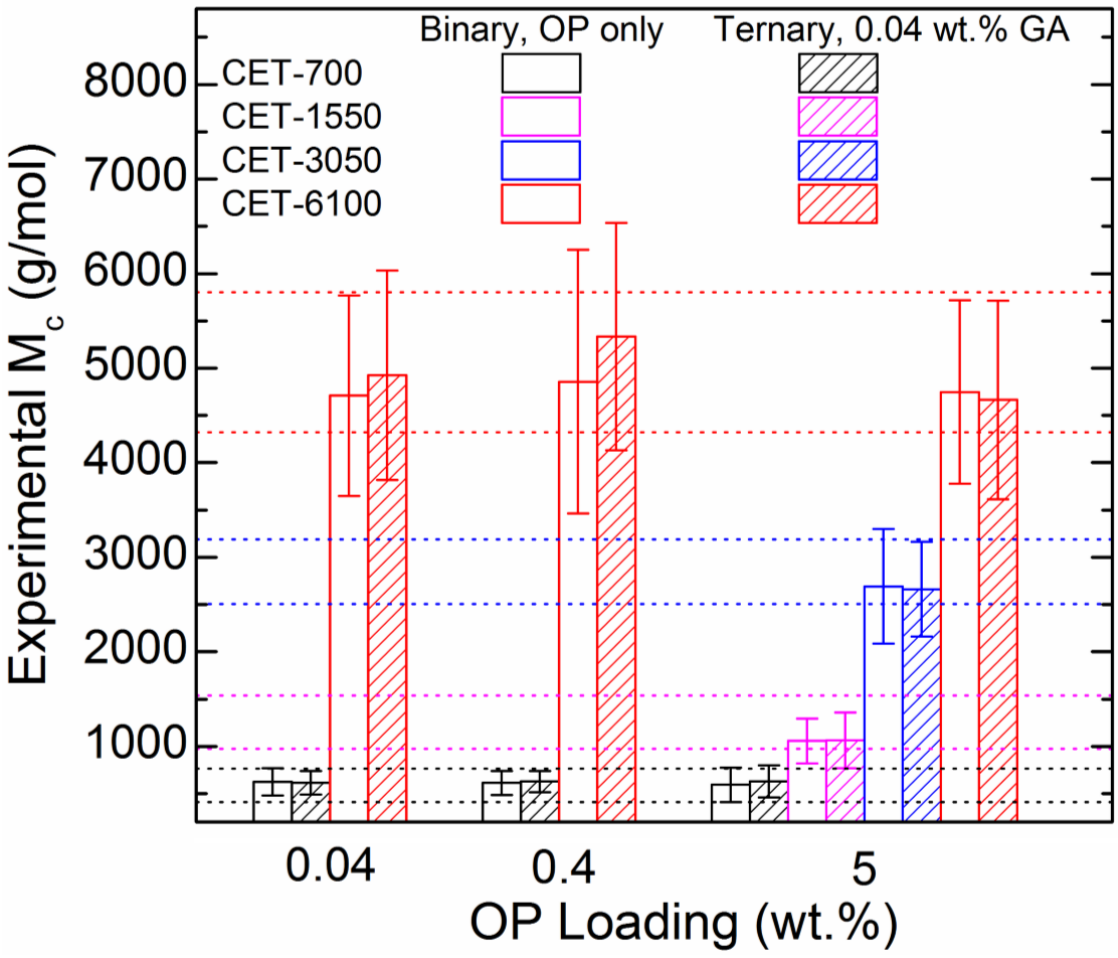

Figure 5.11 Experimental M_c values of OP/epoxy binary composites and GA/OP/epoxy ternary composites. The loading of GA is 0.04 wt.% in all ternary composites, and the loading of OP varies. The dotted line in the same color denotes the experimentally measured M_c value (with experimental uncertainty) of the neat epoxy materials.

5.3.9 Fracture toughness of GA/OP/epoxy ternary composites

Figure 5.12 shows the fracture toughness (K_{Ic}) and critical strain energy release rate (G_{Ic}) for the ternary composites containing 5 wt.% OP and 0.04 wt.% GA against the theorectical matrix M_c. Data from binary composites containing either 0.04 wt.% GA or 5 wt.% OP are also shown for comparison. Table C3 (Appendix C) lists the K_{Ic} and G_{Ic} of all ternary composites with different modifier loadings and M_c values. The results show that the block copolymer OP is very effective in toughening the epoxy materials and the toughening effect in the OP/epoxy binary composites also depends on the OP loading. Taking the CET-6100 system as an example, 0.04 wt.% OP only boosts the K_{Ic} of neat CET-6100 resin by ~ 20%, less than the toughening effect of 0.04 wt.% GA in the GA/epoxy binary composite, while 5 wt.% OP imparts a 320% increase to the K_{Ic} and improves the G_{Ic} by more than an order of magnitude. These toughening results are similar to the values from previous studies on this epoxy resin containing OP spherical micelles.[91, 227]

Figure 5.12 shows that the ternary composites exhibit increasing K_{Ic} and G_{Ic} with incresaing theoretical M_c, similar to both types of binary composites. Saturation of the improvement in the OP/epoxy binary composites at $G_{Ic} \cong 2800$ J/m^2 above M_c of 3050 g/mol is consistent with previous studies on this same epoxy resin system.[48] At M_c of 6100 g/mol, the ternary composite has extraordinary mechanical properites with G_{Ic} reaching about 5300 J/m^2 and a modest elastic modulus of 2.5 GPa (see Appendix C,

Table C2). To the best of our knowledge, this result exceeds any previously reported toughness for this epoxy resin.

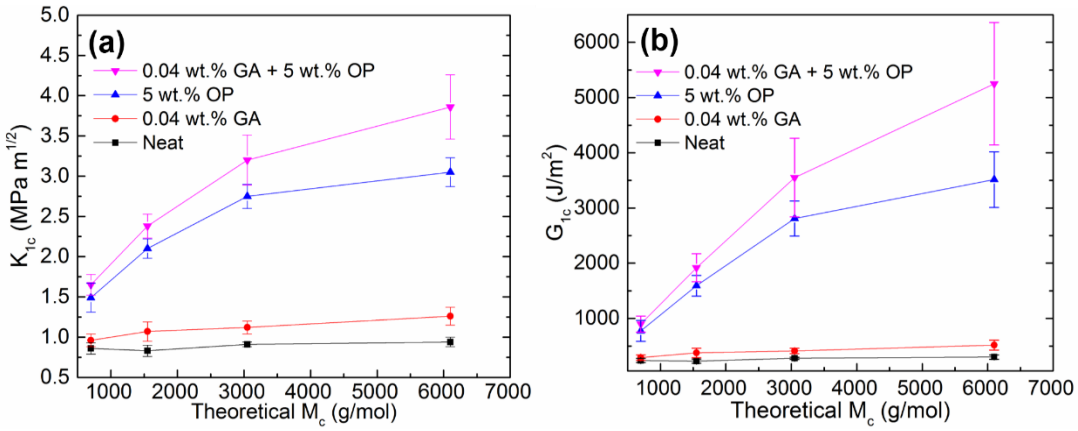

Figure 5.12 Fracture toughness (a) and critical strain energy release rate (b) as functions of the epoxy theoretical M_c. For binary composites, the modifier is either 0.04 wt.% GA (●) or 5 wt.% OP (▲). Ternary composites (▼) contain both 0.04 wt.% GA and 5 wt.% OP. Solid lines are to guide the eye.

Figure 5.13 displays the nomarlized K_{Ic} and G_{IC} relative to that of associated neat epoxy matrices ($K_{Ic,m}$ and $G_{Ic,m}$), based on the data shown in Figure 5.12. There is a compound toughening effect in ternary composites and it becomes more evident as the matrix M_c increases. At M_c of 3050 g/mol, the ternary composite increases G_{Ic} by 12 times relative to the neat epoxy while the OP/epoxy and GA/epoxy binary composites provide a 9-fold and 1.5-fold increases, respectively. At M_c of 6100 g/mol, the enhancement in ternary composite goes up to 18-fold while the boosts are 12-fold and 1.7-fold in the OP/epoxy and GA/epoxy, respectively. We speculate that an increase in the matrix ductility through decreasing the crosslink density not only benefits the

toughening efficacy of each modifier in its individule binary composite, but also promotes some synergistic micromechanical toughening mechanisms in ternary composites (see below).

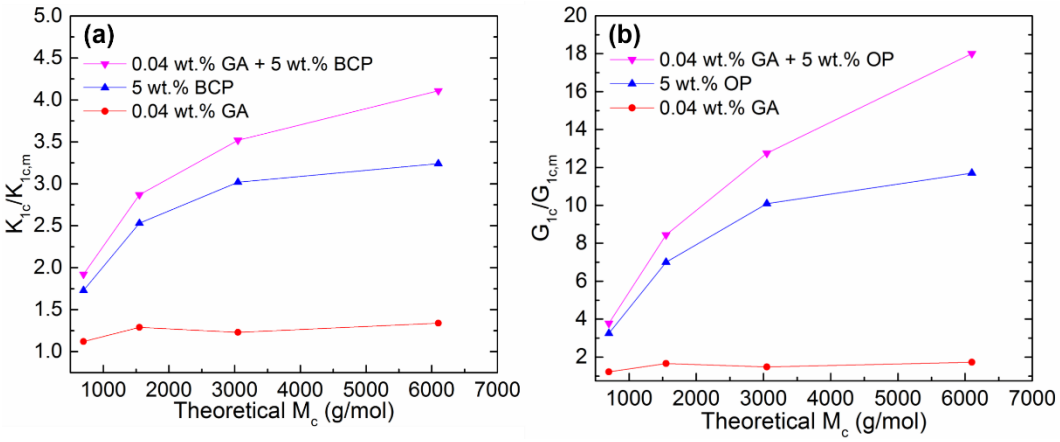

Figure 5.13 Normalized fracture toughness (a) and normalized critical strain energy release rate (b) as functions of the epoxy theoretical M_c. All normalized values are relative to the associated neat epoxy $K_{Ic,m}$ and $G_{Ic,m}$. For binary composites, the modifier is either 0.04 wt.% GA (●) or 5 wt.% OP (▲). Ternary composites (▼) contain both 0.04 wt.% GA and 5 wt.% OP. Solid lines are to guide the eye.

5.3.10 Fractographs of GA/OP/epoxy ternary composites

Representative SEM images comparing the fracture surfaces of the binary and ternary composites from the CET-6100 system are presented in Figure 5.14 and Figure C9, C10 (see Appendix C). The fracture surface topographies for GA/epoxy binary composites have been provided in Figure 5.7 and Figure C5 and C6 (Appendix C). At the lowest magnification, the fractographs are remarkably different (see Figure C9 in

Appendix C): from the neat epoxy to 0.04 wt.% GA/epoxy binary composite, and 5 wt.% OP/epoxy binary composite to the ternary composite, the surface becomes rougher and more textured. The fracture surfaces of the ternary composite (Figure C9d in Appendix C) shows leaf-like pattern that breaks the surface into small domains with an average diameter of ~ 140 μm; the surface displays evidence for massive local disruption of the matrix due to crack deflection and coalescence.[58] By comparison, the OP/epoxy binary composite (Figure C9c in Appendix C) shows a more "continuous" fracture surface with less crack pinning or deflection.

Figure 5.14 and Figure C10 (Appendix C) presents the fine features at higher magnifications. Figure 5.14a shows that the OP/epoxy binary composite is characterized by a relatively smooth surface with dispersed sub-100 nm holes, caused by the cavitation and pullout of rubbery core spherical micelles (as highlighted in the red circle in Figure 5.14c). Those features have also been observed previously in many epoxy materials toughened with spherical micelles (see Chapter 4). On the other hand, Figure 5.14b shows that in the ternary composites, at the boundaries between the leaf-like structures there are crack-pinning sites caused by GA particles, similar to those feactures observed on GA/epoxy fracture surfaces. In the further magnified images, Figure 5.14d exhibits a stack of GA layers with an orientation probably perpendicular to the crack propagation direction, revealing some evidence for interlayer separation and layer breakage within the stack, which are believed to dissipate energy and enhance the fracture toughness.[223] In this image, the micelle holes are still evident in the matrix and the ones in the region close to GA particles appear to be stretched (highlighted by the red circle), compared to

the ones highlighted in Figure 5.14c. This suggests the micelles located in the region near to the GA particles may be subject to some additional stress field due to the stress concentration around GA particles, compared to the micelles in a OP/epoxy binary composite. More micrographs of the ternary composites are presented in Figure C10 (see Appendix C), clearly showing the debonding/delamination of GA particles and also the stretched micelle holes in the matrix.

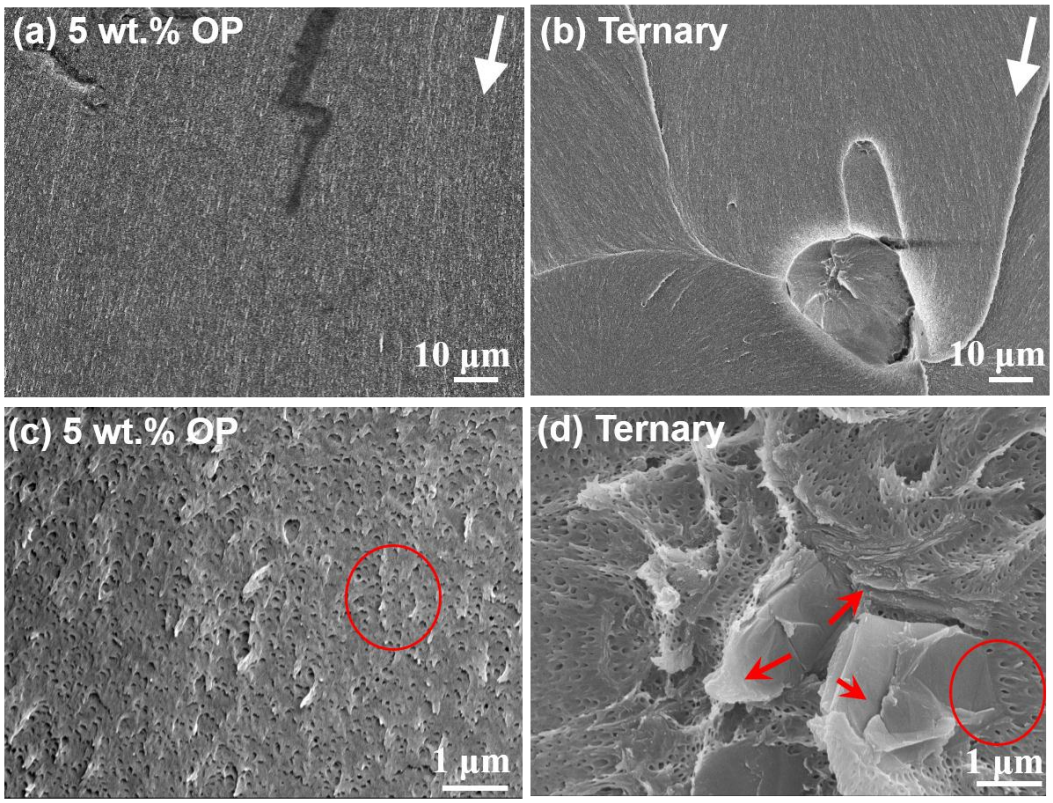

Figure 5.14 SEM fractographs of (a, c) OP/epoxy binary composites with 5 wt.% OP; (b, d) GA/OP/epoxy ternary composites with 0.04 wt.% GA and 5 wt.% OP. The network is the CET-6100 resin in all cases. The white arrows in (a, b) indicate the direction of crack propagation. The red arrows in (d) denote the GA particles. The red circles in (c, d) highlight the micelle holes.

5.4 Discussion

Synergistic toughening in GA/OP/epoxy ternary composites. We analyze composites based on CET-700 and CET-6100 with 0.04 wt.% GA to assess the synergistic toughening effect in the ternary composites as shown in Figure 5.12. To reveal the relative increase, the value of fracture toughness (K_{Ic}) for the composite is compared and normalized to that of the neat epoxy ($K_{Ic,m}$):

$$\Delta K_{Ic} = \frac{K_{Ic} - K_{Ic,m}}{K_{Ic,m}} \tag{5.8}$$

Likewise, the critical strain energy release rate (G_{Ic}) is compared and normalized to that of the neat epoxy ($G_{Ic,m}$) in the parameter ΔG_{Ic}, which is defined analogously to Equation (5.8) A positive value of ΔK_{Ic}(ΔG_{Ic}) indicates a toughening effect in the composites. Figure 15 displays the ΔK_{Ic} and ΔG_{Ic} for the binary and ternary composites against the OP loading.

For both epoxy systems, the ΔK_{Ic} and ΔG_{Ic} for the OP/epoxy binary composites increases dramatically with the OP loading, similar to the values from previous studies on this epoxy resin containing PEP-PEO micelles.[61, 91, 227] To reveal the combined toughening effects of GA and OP, we estimated the "additive toughening" values for the ternary composites according to the modified Kitagawa's model:[229]

$$\Delta K_{ter} = \Delta K_{GA} + \Delta K_{OP} \tag{5.9}$$

where K is short for K_{Ic} and the definition of ΔK still follows Equation (5.8); the subscripts *ter*, GA, OP stand for ternary composite, GA/epoxy and OP/epoxy binary composite, respectively. This model is based on a simple rule of mixtures.

The additive values for the ternary composites calculated from Equation (5.9) are shown as blue columns in Figure 5.15. Synergistic toughening is typically defined as toughening that exceeds the amount predicted by an additive model; this comparison is easily made in Figure 5.15. In the CET-700 system with 0.04 wt.% GA (Figure 5.15a and c), at any OP loading, the actual values of ΔK_{Ic} and ΔG_{Ic} for the ternary composites always exceed the additive values according to Equation (5.9); however, the synergy is small and the absolute values of K_{Ic} and G_{Ic} for these composites are modest. On the other hand, in the CET-6100 system (Figure 5.15b and d), at low OP loadings, the actual values of ΔK_{Ic} and ΔG_{Ic} for the ternary composites are close to the additive values, but at 5 wt.% of loading the actual values are much higher than the additive ones. These results suggest that the two types of modifiers function simultaneously without interfering with each other. In fact, for the case of CET-6100 the combination of 0.04 wt.% GA and 5 wt.% OP shows the largest synergistic effect.

Table C4 (see Appendix C) briefly summarizes the synergistic toughening effects reported in the recent literature for ternary composites modified by rigid and soft additives. For each reference, only the largest toughness improvement observed in the composites is listed in the table. According to the results, synergy is usually more prominent in systems containing modifiers that have a large discrepancy in dimensions (e.g. silica nanoparticles of ~ 20 nm diameter with micron-size CTBN liquid rubbers, or

micro-size organo-clay agglomerates with nanoscale block copolymer particles). Our GA/OP/epoxy ternary composites also follow this trend. The ΔK_{Ic} of the CET-6100 ternary composites exhibits a ~ 21% increase over the additive toughening results. While there is one other study with a higher increase, the composites reported here develop high toughness at the lowest modifier loading, compared to the literature.

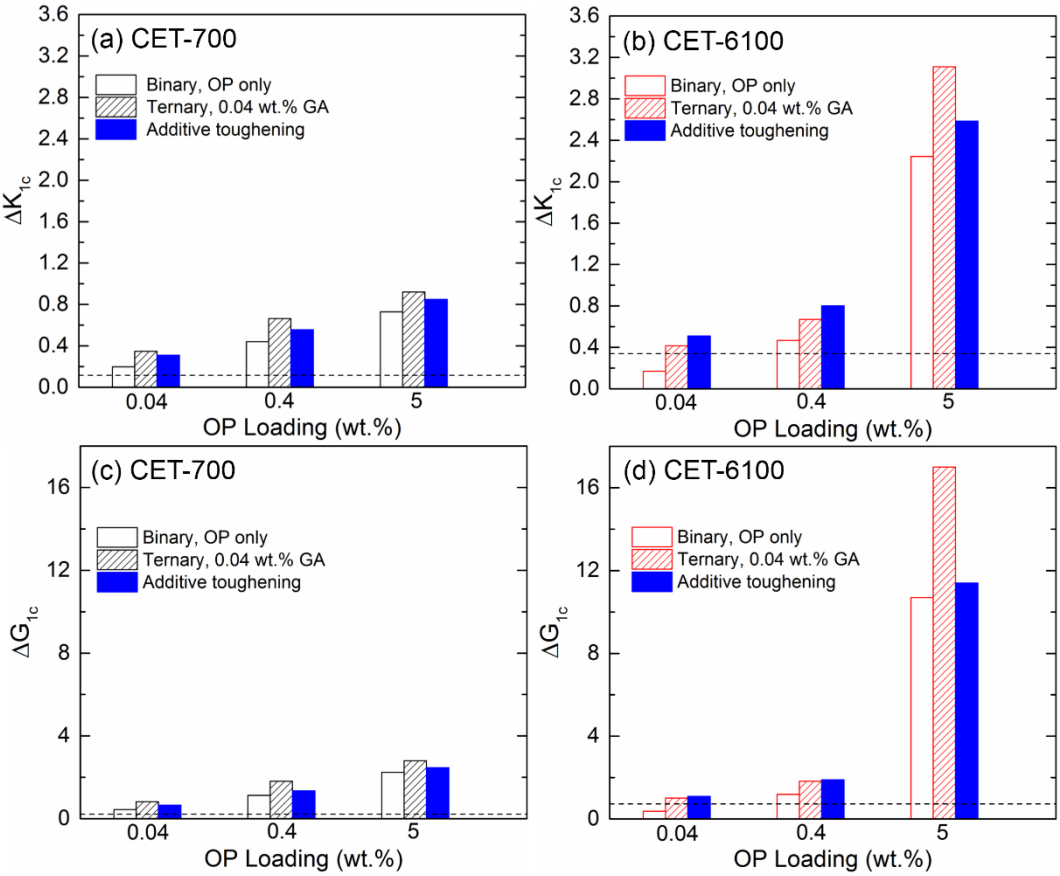

Figure 5.15 (a, b) ΔK_{Ic} and (c, d) ΔG_{Ic} as functions of the OP loading for the CET-700 (a, c) and CET-6100 (b, d) systems. ΔK_{Ic} and ΔG_{Ic} are defined according to Equation (8). The dotted lines denote the ΔK_{Ic} and ΔG_{Ic} values for GA/epoxy binary composites containing 0.04 wt.% GA. For ternary composites, the GA loading is kept constant at 0.04 wt.% in all cases. The estimated values for additive toughening (blue columns) are based on Equation (5.9).

Toughening Mechanisms in GA/OP/Epoxy Ternary Composites. Fractography results indicate that additional toughening mechanisms are active in the ternary composites apart from those found in binary composites containg GA particles or OP micelles alone. As the primary crack propagates, the nanoscale micelles in the process zone cavitate under a hydrostatic stress state, which promotes the formation of shear bands, facilitating matrix plastic deformation.[48, 52] Shear yielding is reflected in the texture and roughness of the fracture surface. Apart from interacting with micelles, the primary crack encounters graphene particles with different orientations and degrees of exfoliation, leading to interactions that involve crack deflection, layer breakage, interlayer separation and microcrack formation around the particles.[223] These interactions create tortuous crack pathways and lead to the micron sized leaf-like pattern revealed by SEM. The nanoscale mechanisms associated with micelles together with the micron-scale mechanisms of the graphene particles combine to produce the compound toughening effect in ternary composites. Moreover, it has been reported that in some ternary composites the modifiers actually can assist each other to promote toughening.[199, 215] This synergistic effect is evident in our results. There are several possible scenarios for the origin of this intriguing high synergy in the lightly crosslinked epoxy matrix (CET-6100):

First, compared with a OP/epoxy binary composite, the stiff GA particles act as stress concentrators, effetively amplifying the local stress. Consequently, rubber-core micelles close to the GA particles would be more ready to cavitate. In return, the change in the stress state caused by micelle cavatation leads to a lower driving force for GA particles to debond with the matrix.[215, 219] This promoted delamination at the interface of

a rigid phase and polymer is helpful to further relieve the hydrostatic tensile stress from the matrix, facilitating the matrix plastic deformation.[219] In brief, the toughening efficacy of both modifiers has been boosted at the presence of each other, resulting in the synergy in toughening.

Second, we have already shown that a lightly crosslinked matrix is easier to toughen for both modifiers. This increase in the matrix plasticity is also poposed to benefit crack blunting, which is credited for contributing to toughness enhancement.[214, 230] As mentioned above, $\sigma_y \cong 80$ MPa for this epoxy resin, independent of the matrix M_c and the yield stress drops to ~ 70 MPa with the addition of 5 wt.% PEP-PEO diblock copolymer.[91] In the ternary composite, we can treat the OP modified epoxy as an "effective matrix", which is modified by the GA particles, and use Irwin model (Equation (5.7)) to estimate the plastic zone size: by assuming negligible influences on σ_y from 0.04 wt.% GA, and σ_y = 70 MPa and K_{Ic} = 3.88 MPa $\sqrt{m}$, we obtain r_y of ~ 160 μm. This is over an order of magnitude higher than the r_y (~ 12 μm) for the GA/epoxy binary composites, and this expanded plastic zone can shield the crack tip and therfore improve the fracture toughness.

Third, Adachi et al.[231] reported that the toughness enhancement (ΔK_{Ic}) is proportional to the reciprocal of the square root of the interparticle distance. The toughening effect in our ternary composites may be attributed to the substantial difference in the interparticle distance of the micron-size GA particles and nanoscale OP micelles. The interparticle distance τ (surface to surface), shown in Equation (5.10) for a

cubic distribution and ideal dispersion, would dramatically increase with the particle size.[214]

$$\tau = d[(\frac{\pi}{6\Phi_p})^{\frac{1}{3}} - 1] \quad (5.10)$$

where d is the particle diameter and Φ_p is the particle volume fraction. In ternary composites with 5 wt.% OP and 0.04 wt.% GA, $\tau \cong 50$ nm for the spherical micelles, while the $\tau \cong 13$ μm for the graphene particle (estimated from SEM on the 0.04 wt.% GA/epoxy binary composites). It implies that there is a large amount of intact epoxy between the GA particles left for micelles to trigger more shear yielding and matrix dilation. This agrees with Pearson's work,[214, 232] where synergistic toughening effects in epoxies were only obtained with nanoscale silica particles and micron-sized rubber particles but no such effects with comparable-sized rubber nanoparticles and silica nanoparticles. Also, in a recent report,[223] Huang et al. employed micron-sized graphene particles and rubber particles with comparable sizes to toughen epoxies, but their improvement is not as effective as that in our ternary composites.

5.5 Summary

In this chapter, we have shown that a ternary graphene/block copolymer/epoxy composite with high elastic modulus and superior fracture toughness can be developed using exfoliated graphene oxide with amine functionalization (GA) and a poly(ethylene oxide)-*b*-poly(ethylene-*alt*-propylene) (OP) diblock copolymer as epoxy modifiers. The dispersion and toughening efficacy of GA was first characterized in binary composites containing this solitary rigid filler. The dispersed GA particles effectively increased the composite modulus, but did not have significant impact on the T_g and the experimentally meausred crosslink density of the epoxy network in the studied loading range. The toughening efficacy of GA was strongly affected by the matrix crosslink density, increasing in the lightly crosslinked matrices; the largest improvement was 1.7-fold in the critical strain energy release rate G_{Ic} at the low loading of 0.04 wt.% in the CET-6100 matix. The toughening mechanims for GA are believed to be debonding with the matrix and resultant microcrack formation around particles, and the crack pinning and crack deflection for primary cracks, according to the fracture surface SEM of binary composites.

Incorporation of 0.04 wt.% GA into epoxies containing different amounts of OP block copolymers created the hybrid ternary composites, in which the OP diblock formed well dispersed spherical micelles with a uniform diameter of ~ 30 nm. No interactions between GA and OP could be observed under TEM. The elastic modulus of the tenary composites was close to that of the neat epoxy matrices, unlike OP/epoxy binary

composites, in which inclusion of 5 wt.% OP reduced the matrix modulus by ~ 10%. Moreover, the T_g and experimentally measured crosslink density did not change significantly for the ternary composites. The matrix crosslink density played a critical role in determining the fracture toughness of ternary composites. All ternary composites, regardless of the crosslink density, exhibited a higher K_{Ic} and G_{Ic} compared to their binary counterparts, but in the matrix with the lowest crosslink density (CET-6100), 5 wt.% OP and 0.04 wt.% GA together drastically improved the G_{Ic} to 19 times that of the unmodified material. This improvement was significantly higher than the increase of 12-fold with just 5 wt.% OP, and even greater than the additive result of a 14-fold increase summed over the improvements in associated binary composites. We attributed the synergistic toughening effect to the fact that the toughening mechanims noted for rubbery-core micelles and rigid graphene particles can function simultaneously at different lengh scales. Furthermore, in ternary composites, the micelle core cavitation and resultant matrix shear yielding can be facilitated by the stress concentration aournd the GA particles, meanwhile, the toughening effect of GA like debonding and microcrack formation can be augumented by the change in stress state accompanying cavitation. These concomitant micromechanical prosesses resulted in the synergistic toughneing effect observed in our ternary composites.

This investigation advances the field of toughening thermoset plastics in three significant ways. Firstly, we have extended the concept of developing hybrid nanocomposites to including two new modifiers with a substantial difference in dimensions, which once again proves to benefit a synergistic toughening effect.

Secondly, our work has the practical merit of providing a feasible and potentially low-cost approach to engineer a superior toughness in epoxy thermosets without losing rigidity. Thirdly, the inclusion of graphene into a polymer matrix offers a platform for producing high-end materials with a host of special characteristics in electric, optical, thermal and mechanical properties.[210, 233-238]

Chapter 6

Toughening glassy poly(lactide) thermoplastic: extension of block copolymer toughening strategy*

6.1 Introduction

The block copolymer toughening strategy has been established in a thermoset polymer matrix in bulk and coating applications through previous chapters, from a model system study to full exploration of a commercially viable resin system, and to investigating a hybrid ternary composite. Inspired by the findings in Chapter 5 that the polymer matrix also greatly influences the toughening efficacy of modifiers, we were interested in applying the block copolymer modifier to a thermoplastic polymer matrix. Among a myriad of candidates in the category of thermoplastics, we selected poly(lactide) (PLA), a compostable bioderived polyester.

*Reproduced in part with permission from (T. Li, et al., "Toughening glassy poly(lactide) with block copolymer micelles", *ACS Macro Letters*, American Chemical Society.)

Chapter 6

Growing concerns over pollution caused by nondegradable, petroleum–derived plastics have driven the development of more sustainable alternatives.[97] By commercial volume the most successful example of a biobased degradable polymer has been PLA. It currently can be produced with only 15-25% surcharge relative to poly(ethylene terephthalate), a price difference small enough to allow its use in commercial products such as textiles and disposable containers.[98, 99] Despite possessing a high tensile strength and elastic modulus, neat poly(L-lactide) (PLLA) is intrinsically brittle, which prevents its use in applications where toughness, impact resistance, and optical clarity are essential.[99-101] PLLA shares many of the inherent limitations of the commodity thermoplastic poly(styrene) (PS).

Many of the strategies that have been successfully employed to toughen polystyrene have also been investigated to alter the mechanical properties of PLLA. These methods include plasticization,[102-105] copolymerization,[239-242] blending with flexible polymers,[107-110] addition of rigid fillers,[111-113] and changing the polymer chain orientation.[114] Among all of these toughening strategies, the key to designing inexpensive and tough PLLA materials may lie in fabricating blends. Many polymers including polycaprolactone,[107, 126] poly(butylene succinate),[127] polyurethane elastomers,[128] soybean oil derivatives,[129] linear low density polyethylene (LLDPE),[108, 130] and acrylonitrile-butadiene-styrene (ABS)[128] have been considered as modifiers for PLLA. Because the majority of these polymers are immiscible with PLLA, a compatibilizer must typically be added to stabilize the interfaces of the blend constituents.[98] One limitation of polymer-polymer blends is that the constituents can form micron-sized features, reducing the

transparency of material. To avoid this problem, others have proposed a versatile, simple, and potentially low-cost strategy to reinforce thermoplastics using block copolymer dispersions.[1, 132, 133]

Again, block copolymers have emerged as really ideal toughening agents for the PLA thermoplastic. In this chapter, we described the investigation of low molar mass poly(butylene oxide)-containing diblock copolymers as modifiers to toughen PLLA. These diblocks are low cost and can be dispersed as nanoscale micelles in PLLA using facile melt blending or solvent blending routes. As demonstrated below, these additives effectively toughen bulk PLLA thermoplastic even at loadings lower than 5% by weight, without reductions in T_g, elastic modulus or optical clarity. Their toughening efficacy can also be retained in thin films prepared via a film blowing process.

6.2 Experimental

6.2.1 Materials

The chemical structures of the poly(lactide) homopolymer and block copolymers used in this chapter are presented in Figure 6.1. As mentioned in Chapter 2, there are two PLA isomers being used as the thermoplastic matrix: isotactic poly(L-lactide) (PLLA, NatureWorks under the tradename Ingeo 2003D), and atactic poly(D,L-lactide) (PDLLA, NatureWorks, Ingeo 4060D). The PLLA and PDLLA homopolymers have similar number average molecular weight and dispersity (see Table 6.1), but the major difference

is that PDLLA cannot crystallize, which facilitates the phase behavior study on homopolymer blends with cloud point measurements (see below). It is important to note that in this chapter, modified PLLA thermoplastics were first heated to the PLLA melting temperature, and then rapidly cooled to room temperature during specimen preparation for all characterization. This process results in less than 5% PLLA crystallinity (see Table 6.2 below) and therefore the resultant glassy PLLA matrix is similar to the PDLLA matrix in various aspects (see below for more details).

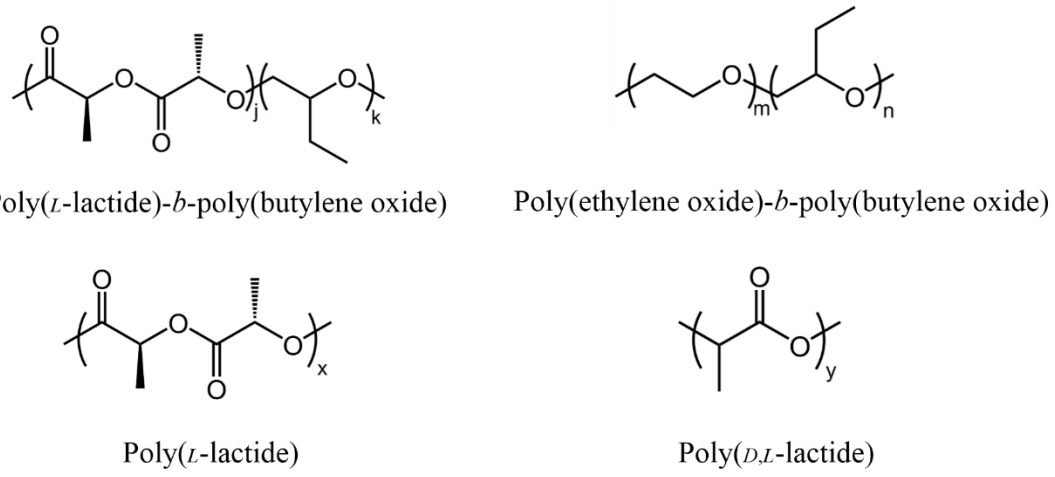

Figure 6.1 Chemical structures of block copolymer modifiers, poly(L-lactide) (PLLA) and poly(D,L-lactide) (PDLLA).

Table 6.1 summarizes the molecular characteristics of the matrix homopolymers and the block copolymers employed as toughening agents. As briefly mentioned in Chapter 2, the poly(ethylene oxide)-*b*-poly(butylene oxide) (PEO-PBO) diblock copolymer that is used for toughening the Cardolite thermoset (refer to Chaper 4) has been extended to modifying PLA thermoplastics herein. A series of PEO-PBO diblocks

identified as EB-1 to 3 were synthesized at fixed composition (69 ± 1% by volume PBO) but varying total molecular weight. A poly(L-lactide)-*b*-poly(butylene oxide) (PLLA-PBO) diblock identified as LB in Table 6.1 was also prepared with a similar total molar mass and composition as EB-1. These two different types of diblocks were designed to be amphiphilic with respect to the PLLA homopolymer matrix. Ideally, all the diblocks would form micelles in the PLLA matrix with a rubbery and compliant PBO core and a PLLA-philic block (either PEO or PLLA) as the corona.

Table 6.1 Molecular characteristics of the homopolymers and diblock copolymers.

[a]Sample ID	[b]M_n (kg/mol)	[c]$f_{PEO\ or\ PLLA}$	[d]$w_{PEO\ or\ PLLA}$	[e]M_w/M_n
PLLA	112	--	--	1.88
PDLLA	118	--	--	1.89
LB	7.8	31	38	1.15
EB-1	7.0	32	35	1.10
EB-2	11.5	31	34	1.03
EB-3	48.0	32	35	1.10

[a] PLLA = poly(L-lactide); PDLLA = poly(D,L-lactide); LB = poly(L-lactide)-*b*-poly(butylene oxide) (PLLA-PBO); EB = poly(ethylene oxide)-*b*-poly(butylene oxide) (PEO-PBO).

[b] Number average molecular weight determined by ^{1}H NMR end group analysis for the diblocks.

[c] Volume fraction of PEO and PLLA blocks calculated using densities ρ_{PEO} = 1.07 g/cm^3, ρ_{PBO} = 0.92 g/cm^3, and ρ_{PLLA} = 1.25 g/cm^3.[35, 120]

[d] Weight fraction of PEO or PLLA blocks, calculated based on ^{1}H NMR results.

[e] Dispersity and M_n for PLLA and PDLLA were determined using gel permeation chromatography (GPC) at 30 ℃ with THF as the mobile phase and calibrated with poly(styrene) standards.

6.2.2 Synthesis of PLLA-PBO diblock copolymer

PLLA-PBO (LB) and PEO-PBO (EB) diblocks were synthesized via anionic ring-opening polymerization of butylene oxide (BO) followed by reinitiation and addition of L-lactide (LLA) or ethylene oxide (EO). The polymerization protocols followed in synthesizing PBO homopolymers and EB diblock copolymers have been described in detail in Section 2.3.3. Here, we present a full description of the synthesis of PLLA-PBO diblock copolymer. In a glove box with a nitrogen atmosphere, purified PBO homopolymer (2.55 g) and L-lactide (1.79 g) were added to a 50 mL pressure vessel equipped with a mechanical stir bar. Subsequently, toluene (12 g) was added and the contents stirred at room temperature. When fully dissolved, purified $Sn(Oct)_2$ (10 mg) was added. The vessel was capped, removed from the glovebox, and heated to 120 ℃ with stirring for an hour. It was then cooled, and an aliquot was taken to determine the conversion. The polymer was diluted with 40 mL chloroform and then washed three times with 0.1 mol/L NaOH aqueous solution to remove residual monomer. After drying the organic layer over $MgSO_4$, the polymer solution was filtered and the solvent removed under reduced pressure. The polymer was further dried in a vacuum oven at room temperature for 48 hours prior to analysis.

6.2.3 Sample preparation

Preparation of Polymer Blends. The inclusion of block copolymer modifiers to the PLLA/PDLLA matrix was achieved via either a solvent-blending or melt-blending

process. The melt-blending process was only used for the preparation of impact strength testing specimens made from EB-1/PLLA blends. Both blending processes generated similar microstructures in EB-1/PLLA blends as confirmed by TEM. In the solvent-blending process, a certain amount of modifier was blended with 4g of PLLA or PDLLA pellets in about 20 mL chloroform at room temperature. Then, the polymer blend was precipitated in a large quantity of hexane (a poor solvent) and collected and completely dried under dynamic vacuum at room temperature for at least 24 hours. In the melt-blending process, large sample batches (300-500 g) were created with EB-1 for injection molding using a 16 mm twin-screw extruder (PRISM, L:D 24:1, four heating zones at 180 ℃ and a feed zone at 140 ℃, 40 rpm screw speed, 3.2 feeder screw speed). The mass flow rate and residence time distribution were measured to be 2-9 g/min and 2-7 min for all blends, respectively. Outlet pressure ranged from 50-160 psi and torques from 3-10 N·m. After steady state polymer flow was achieved, a syringe pump was used to dispense liquid EB-1 modifier (diluted in acetone to reduce viscosity, roughly 50 wt.% block polymer solution) at a controlled rate. Extrudate was chilled in a water bath, dried by air blower, pelletized, and stored in a vacuum oven for at least 48 h before further processing.

Preparation of Mechanical Property Test Specimens. The dried solid polymers from solvent-blending were melt compounded at 180 ℃ followed by rapid cooling (60-70 ℃/min) to make standard dog-bone shaped tensile bars (ASTM D1708). The EB-1 modified pellets from melt-blending were used in the preparation for notched Izod impact strength specimens with a Morgan Press injection molder (barrel temperature = 180 ℃,

nozzle temperature = 220 ℃, mold temperature = 100 ℃, ram pressure = 4.5 kpsi, pilot valve pressure = 100 psi, clamp force = 13 tons, cycle time = 45s). After being injected into the mold, specimens were quickly transferred into a water bath for rapid cooling. Notches were then created using a Tinus Olsen 899 Impact Specimen Notcher according to ASTM D256. All tensile bars and impact strength specimens were aged for 48 h in a room temperature vacuum oven prior to any characterization.

Process of film blowing. Pellets of EB-1/PDLLA blends prepared via melt-blending were fed into a lab scale extruder with a blown film die and attachment. The single-screw extruder being used has a diameter of 1 inch and a length of 25:1, L:D. The metering zone is 10:1, L:D and has a square pitch with a depth of 0.065 inch, a flight thickness of 0.14 inch and a helix angle of 17.7 degrees. The annular die has an outer diameter of 1 inch. The apparatus was operated under steady state conditions to maintain a stable bubble formation. The film produced was approximately 0.2 mm in thickness.

6.2.4 Could point measurement

The phase behavior of PDLLA/PEO homopolymer blend was investigated via a cloud point measurement with optical transmission experiment. A series of PDLLA/PEO homopolymer blends at different mixing ratios were prepared via a solvent-blending process as described above. The apparatus set-up used for optical transmission experiment has been described in detail elsewhere.[243] Raw intensity data was normalized to an arbitrary normalized transmittance scale. Changes in transmittance were interpreted

as changes of incident laser beam scattered to wider angles than can be collected at the detector. No changes in absorption are anticipated for the polymer blends in the temperature range of the experiments. In a typical test, samples were first annealed at 90 ℃ (above the T_m of PEO) for at least 15 min to reach an optically clear and transparent state, heated at 2 ℃/min to 200 ℃, then cooled at 2 ℃/min to 90 ℃. The same cycle was then repeated once more. Transmitted intensity data were collected throughout both cycles. The sharp intensity drop on the second heating cycle was identified as the cloud point for each sample.

6.2.5 Mechanical performance evaluation

Modified poly(lactide) thermoplastics were characterized using an uniaxial tensile test to evaluate the Young's modulus, yield stress, ductility (strain at break), ultimate tensile strength (UTS) and tensile toughness. Uniaxial tensile tests were performed on a Schimadzu Autograph AGSS17 X series tensile tester with a cross-head moving rate of 5 mm/min according to ASTM D1708.

The toughening efficacy of the modifier EB-1 was also evaluated through a notched Izod impact strength test. Tests were conducted using a CEAST instrumented impact strength tester (model 6545) according to ASTM D256.

The reported value for each mechanical property represents an average over at least five measurements on five identically prepared specimens from each sample. To compare

the mechanical properties of the neat materials with those of modified samples, a *t*-test with a threshold for statistical significance set to 0.05 was employed.

6.2.6 Rheology characterization

A RheometricsScientific ARES strain-controlled rheometer with the 25 mm diameter parallel plate geometry and a forced convection oven with a nitrogen atmosphere was used for the measurements. All samples were loaded to give a gap of approximately 0.5 mm, heated above the PLLA melting temperature and annealed before running frequency sweeps. Frequency sweeps were run in the range of $0.01 \leq \omega \leq 100$ rad/s. Strains were selected to maximize torque while remaining in the linear viscoelastic regime.

6.3 Results and discussion

In this section we first present results obtained from bulk thermoplastics (subsections 6.3.1 to 6.3.5), and then show results from blown films (6.3.6). In 6.3.1, we investigate the phase behavior of PEO/PDLLA homopolymer blends to verify a negative Flory-Huggins interaction parameter (χ) between PEO and PLA. Subsequently, in 6.3.2 and 6.3.3, the morphological and mechanical property consequences of blending PLLA with different diblock copolymer modifiers, are described. The negative χ(PEO/PLA) drives the dispersion of EB-1 into small micelle-like particles that impart a dramatic

toughness improvement to modified thermoplastics. Furthermore, the toughening efficacy of EB-1 is investigated in 6.3.4 and its potential influences on the melt rheological behavior of polymer blends are also studied in 6.3.5. Lastly, in 6.3.6, blown films prepared with EB-1/PDLLA blends are explored with respect to the microstructure and mechanical property.

6.3.1 Phase behavior of PEO/PLA homopolymer blend

Figure 6.2 presents a binary phase diagram for PEO/PDLLA homopolymer blends. In this phase diagram, the data points are experimentally determined from cloud point measurements as described above and the inset shows representative raw data of the optical transmission experiment. The PEO homopolymer being used (Sigma Aldrich) has a small number average molecular weight M_n = 24 kg/mol ($Đ$ = 1.06), almost one fifth of the PDLLA M_n (see Table 6.1). Therefore, the shape of this phase diagram is asymmetric with the critical point appearing at 70% by weight of PEO. It is evident that PEO and PDLLA have a lower critical solution temperature (LCST) at around 145 °C. We believe this LCST is strongly dependent on the molar mass of each homopolymer, and a higher molecular weight PEO can move this LCST to a lower temperature.

This LCST behavior suggests the presence of some attractive interactions between PEO and PDLLA molecules at low temperatures that makes these two homopolymers miscible with each other, while these interactions disappear as temperature increases, resulting in two separated phases in the blend. Hence, we propose a negative Flory-

Huggins interaction parameter, χ, between PEO and PLA, which can explain the microstructure of modified polymer blends as shown below. This conjecture awaits further verification.

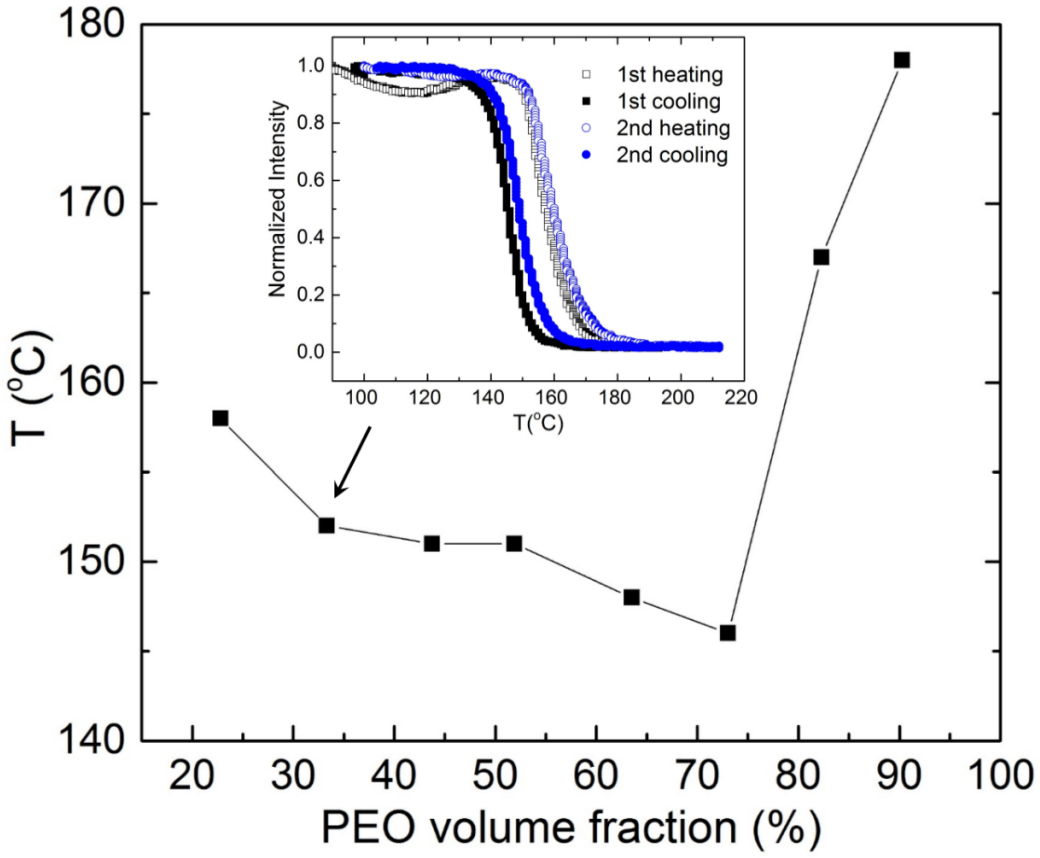

Figure 6.2 Binary phase diagram for PEO/PDLLA homopolymer blends. Experimentally determined cloud point measurements are represented as black squares. The line connecting data points is to guide the eye. The inset shows two representative curves obtained from the cloud point measurement for the 30PEO/70PDLLA blend as denoted by the arrow (the number '30' stands for 30 wt.% PEO), and the onset of the drop in transmission (on the 2nd heating trace) is taken as the cloud point for this composition.

6.3.2 Microstructure of modified polymer blends

Representative transmission electron microscopy (TEM) images of block copolymer modified PLLA are presented in Figure 6.3a-d. EB-1 generated small cylindrical micelles (PBO core diameter < 20 nm) randomly and uniformly distributed throughout the PLLA matrix. This blend retained optical clarity similar to neat amorphous PLLA. Increasing the total molecular weight of the EB modifier led to larger structures with polydisperse dimensions: blends containing EB-2 and EB-3 formed cylinders with a micron length and submicron diameter. The blend containing the LB diblock copolymer formed large and more dimensionally heterogeneous structures with roughly a spherical morphology.

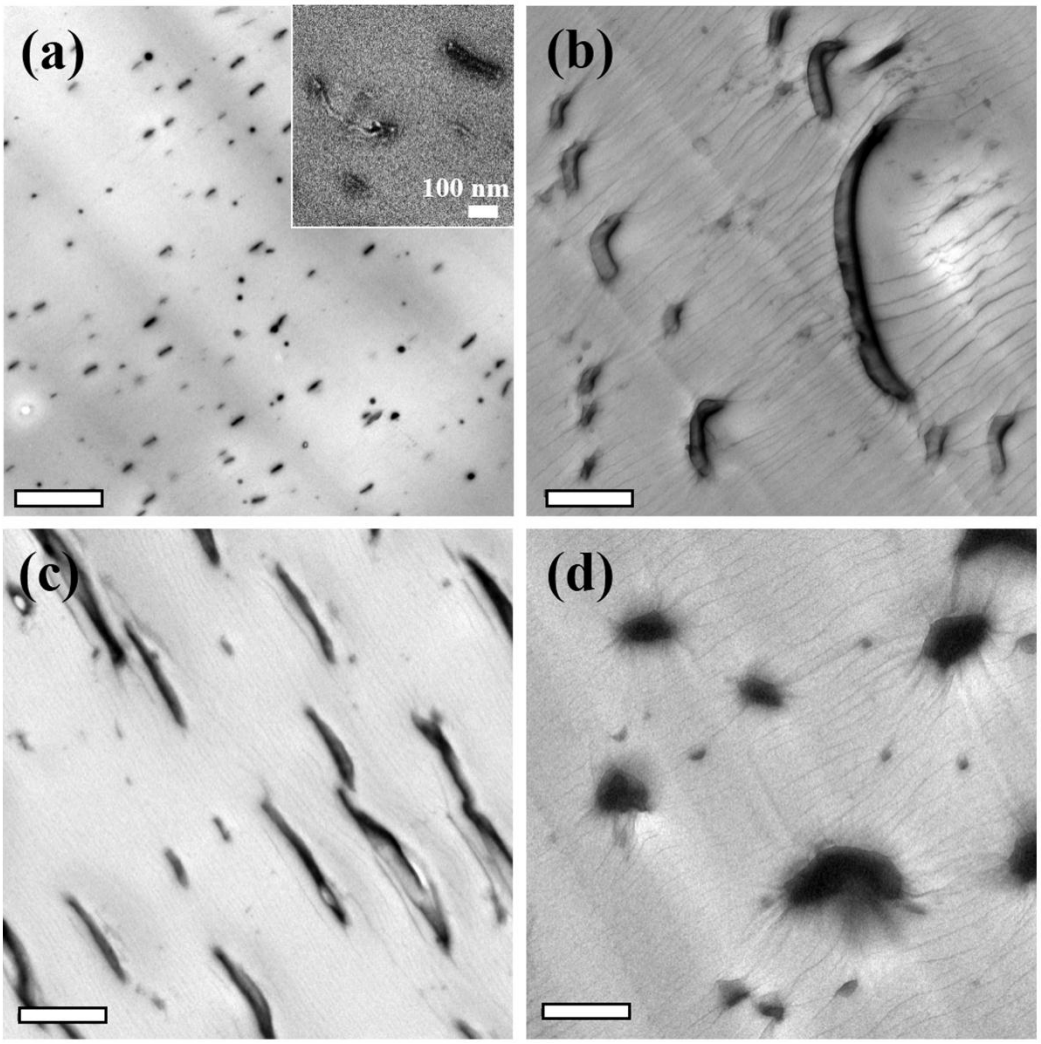

Figure 6.3 Representative TEM images of block copolymer/PLLA blends containing 5 wt.% of (a) EB-1, (b) EB-2, (c) EB-3, and (d) LB. Scale bars represent 1 μm. RuO_4, used as a contrast agent, preferentially stains the PEO/PLLA or PBO/PLLA interface. The inset in (a) clearly shows the micelle structure at a higher magnification.

The phase behavior of the EB-1/PLLA blend is surprising in the context of wet/dry brush physics of block copolymer/homopolymer blends. Typically, the presence of long homopolymer chains destabilizes the dispersion of meso-structured micelles formed by

microphase separation of the thermodynamically incompatible components of the block copolymer.[134, 135] Macrophase separation of the LB modified PLLA (Figure 6.3d) is consistent with this expected behavior. Owing to a large molar mass difference, the PLLA homopolymer chains cannot penetrate the corona formed by the short PLLA chains of the LB diblock; the PLLA blocks of LB are thus "dry brushes". Because there is minimal mixing between the PLLA of the bulk material and the PLLA blocks of the LB component, the diblock tends to macrophase separate, forming large spherical features.

As mentioned above, we believe a negative Flory-Huggins interaction parameter, χ, between PEO and PLLA drives the dispersion of EB-1 into small micelle-like particles. Melt blending experiments have previously shown that PEO and PLLA homopolymers are partially miscible.[244-246] Thermal studies by Lin et al., used to estimate χ between high molar mass PLLA and short PEO chains with different end-groups, also suggest that χ(PEO/PLLA) is negative.[247] We postulate that favorable enthalpic attractions between PEO and PLLA help to counteract the entropic effects mentioned above, enabling the high PLLA homopolymer to wet the low molar mass PEO corona.[134] This favorable enthalpic interaction thus facilitates the dispersion of EB-1 in bulk PLLA. The cylindrical shape of the micelles reduces the interfacial area per EB chain minimizing unfavorable interactions between PBO and PLLA.

Increasing the overall molecular weight of the EB additive (EB-2 and EB-3) leads to coarser dispersions, with domain sizes much larger than those expected from the assembly of individual micelles. This is likely due to the fact that PEO and PLLA have a

lower critical solution temperature (LCST) (see above). Increasing the PEO molecular weight could reduce the miscibility temperature to below the sample preparation temperature (180 °C); samples containing EB-2 and EB-3 molded at 100 °C indeed displayed a much finer dispersion consistent with this notion (results not shown here). PEO crystallization may also have an impact (see below).

6.3.3 Thermal and mechanical properties of modified blends

The thermal properties of the PLLA blends, determined by DSC, are summarized in Figure 6.4 and Table 6.2. The glass transition temperature (T_g) of PLLA in the 5 wt.% EB-1/PLLA blend was slightly reduced due to the plasticization effect of an amorphous PEO block. Although PEO crystallization in EB-1 is suppressed due to the low molecular weight,[35] blends containing EB-2 and EB-3 both exhibited PEO melting transition (T_m) at 45 ℃ and 54 ℃, respectively. Apparently the thermodynamic benefit of long-chain PEO crystallization outweighs the enthalpic benefit of mixing PEO and PLLA. This crystallization may also contribute to the coarser morphologies of EB-2 and EB-3. Reduction in T_g due to mixing of PLLA and the PEO blocks may provide the mobility necessary to allow micelles to coalescence during PEO crystallization, although this would be somewhat surprising since the specimens were cooled and vitrified rapidly to suppress PLLA crystallization (see Table 6.2).

Upon reheating the glassy PLLA crystallized (T_c > 100 ℃) followed by melting (140 ℃ < T_m < 150 ℃). For each of the EB/PLLA blends the melting transition was split

into two distinct peaks with one higher and one lower than the melting point of neat PLLA (see Figure 6.4). We attribute this phenomenon to the influence of PEO on the mechanism of PLLA crystallization, which causes the formation of two different types of crystallized domains in the matrix.[248, 249] Notably, the LB diblock does not appear to affect the melting behavior of the PLLA matrix (Figure 6.4).

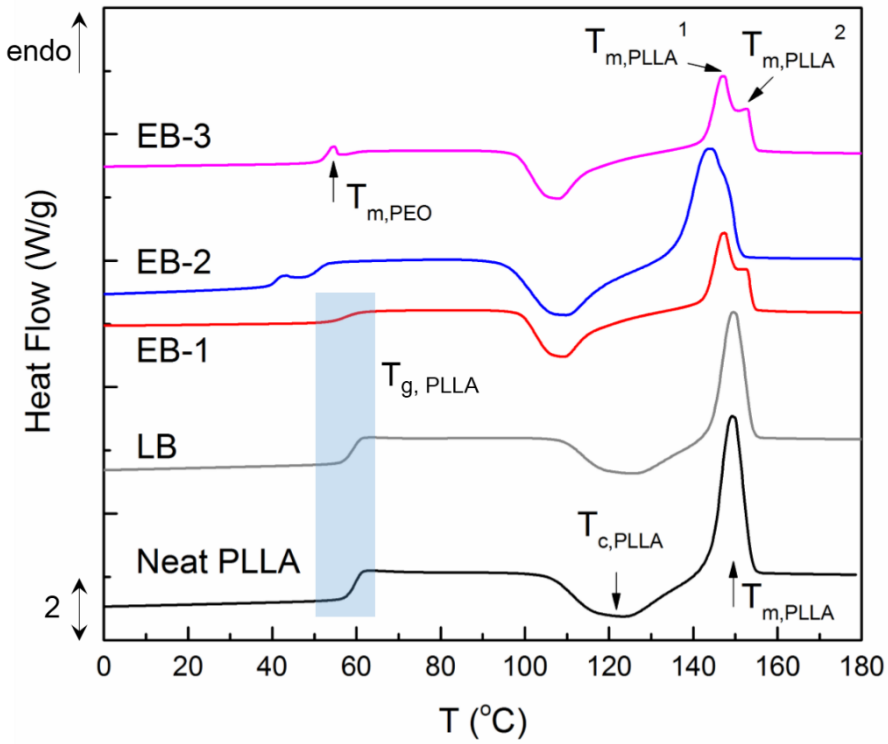

Figure 6.4 DSC traces (endo up) of neat PLLA and modified blends containing 5 wt.% diblock copolymers obtained during a second heating. Arrows denote the crystallization and melting peak of PLLA, and the PEO melting peak in blends loaded with EB-2 and EB-3. The shaded region highlights the glass transition of PLLA. Curves were shifted vertically for clarity.

Table 6.2 Summary of thermal properties of block copolymer/PLLA blends.

[a]Blend	[b]ΔH_c (J/g)	[c]ΔH_m (J/g)	[d]Φ_{PLLA} (%)	[e]$T_{g,PLLA}$ (℃)	[e]$T_{c,PLLA}$ (℃)	[f]$T_{m,PLLA}$ (℃)	
Neat	22.1	23.0	1.0	60 ± 1	103 ± 3	149 ± 1	
LB	15.8	16.6	0.9	59 ± 1	105 ± 3	149 ± 1	
EB-1	22.2	25.1	3.1	56 ± 1	96 ± 4	147 ± 2	153 ± 1
EB-2	17.6	19.5	2.0	--[g]	94 ± 2	144 ± 3	148 ± 2
EB-3	16.4	20.4	4.3	--[h]	95 ± 1	147 ± 2	153 ± 1

[a] The concentration of modifiers is 5 wt.% in all cases.

[b, c] The enthalpy of PLLA crystallization and melting were determined by the integrated area of associated crystallization and melting peaks on the first heating ramp of DSC measurements with a rate of 10 ℃/min.

[d] Crystallinity was calculated using 93.0 J/g for theoretical enthalpy of infinite PLLA crystals.[125]

[e] Glass transition, crystallization and melting temperatures were determined using DSC on the second heating ramp at a rate of 10 ℃/min. The onset of the exothermic crystallization peak was taken as the crystallization temperature of PLLA.

[f] The apex of the endothermic melting peak was taken as the melting temperature of PLLA. In the cases of EB-1, EB-2 and EB-3, the melting peak is split into two as shown in Figure 6.4.

[g, h] Accurate $T_{g,\ PLLA}$ was hard to determine, because the PLLA glass transition was merged with the PEO melting peak at 45 ℃ for EB-2 and at 54 ℃ for EB-3, as shown in Figure 6.4.

The microstructure of the modified blends critically affects the tensile properties of these glassy materials. Representative engineering stress *versus* strain curves are presented in Figure 6.5a and the associated yield strength (σ_y), elastic modulus (E), strain at break (ε_b) and toughness are summarized in Table 6.3. All blends modified with 5 wt.% loading of diblocks exhibited improved toughness and ductility over the neat PLLA. The blend prepared using EB-1 exhibited the greatest improvement relative to

neat PLLA with a 1300% increase in tensile toughness and a 2500% increase in ε_b. EB-2, EB-3 and LB were less effective in toughening the PLLA, similar to macrophase-separated rubber modifiers as reported in the literature.[138] At loadings of 5 wt.%, none of the blends exhibited a significant drop in Young's modulus. However, as is often observed with rubber toughening, the yield strength relative to neat PLLA decreased by 45% to 50%.[7]

Table 6.3 Summary of mechanical properties of block copolymer/PLLA blends.

[a]Blend	[b]σ_y (MPa)	[b]E (GPa)	[b]ε_b (%)	[c]Toughness (MJ/m^3)
Neat	52 ± 3	2.3 ± 0.1	7 ± 2	2 ± 1
LB	26 ± 3	2.2 ± 0.2	72 ± 17	12 ± 3
EB-1	28 ± 4	2.0 ± 0.1	175 ± 28	26 ± 4
EB-2	26 ± 3	2.1 ± 0.3	87 ± 35	18 ± 2
EB-3	27 ± 2	2.5 ± 0.3	26 ± 5	5 ± 1

[a] The concentration of modifiers is 5 wt.% in all cases.

[b] Yield strength (σ_y), tensile modulus (E), and strain at break (ε_b) were determined using a uniaxial tensile test with a crosshead velocity of 5 mm/min. Tensile modulus was quantified by fitting the linear elastic region of each curve before the yield point.

[c] Tensile toughness was determined by the integrated area under engineering stress-strain curve up to the breaking point.

A photograph of representative tensile specimens containing 5 wt.% EB-1 before and after stretching is presented in Figure 6.5c. Before stretching the specimen was transparent and indistinguishable from neat amorphous PLLA. Upon deformation, the gauge region showed uniform whitening and necking. This opacity is caused by the formation of micron and submicron size holes, as shown by the TEM image in Figure

6.5b. We speculate that this porous structure is formed by cavitation of the rubbery-core micelles, similar to what has been discussed in block copolymer toughened epoxy thermosets in previous chapters (Chapter 3-5). Under an applied tensile force, the micelles can cavitate, leaving nano-sized voids in the PLLA matrix, which continue to grow in size and number with increasing strain.

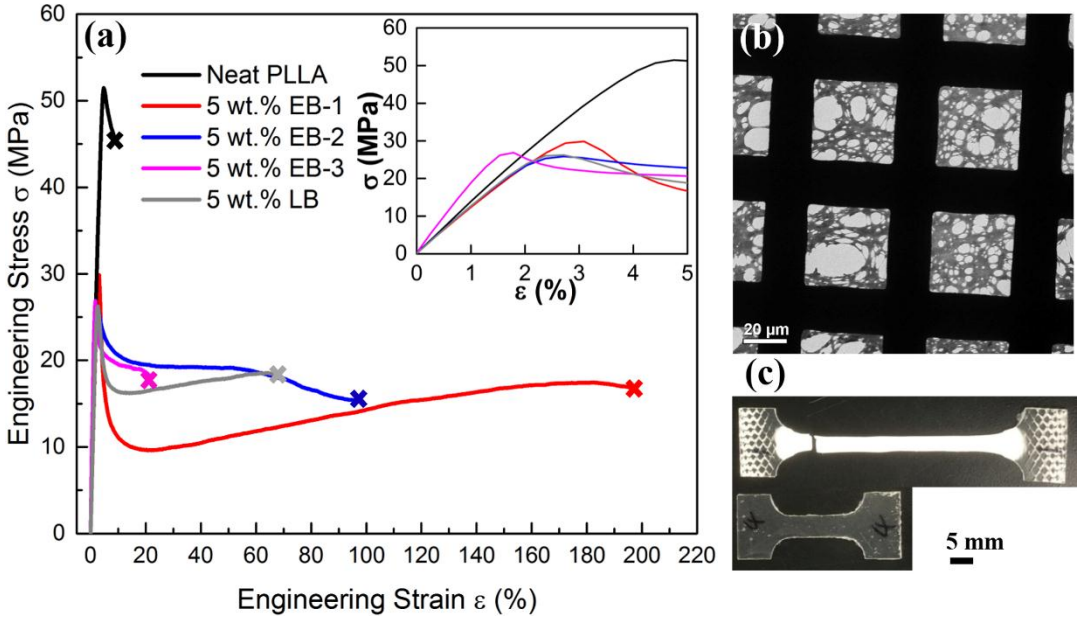

Figure 6.5 (a) Representative engineering stress *versus* strain data from tensile tests. The block copolymer loading is 5 wt.% in all cases. Inset shows the linear elastic region of each curve. (b) Representative TEM image of 5 wt.% EB-1 modified PLLA tensile specimens. Images were taken from the whitened zone (gauge region) of failed tensile specimens. (c) Representative photo of tensile specimens containing 5 wt.% EB-1 before and after deformation.

6.3.4 Toughening effect in modified blends

The effect of modifier concentration on mechanical performances was explored using blends containing EB-1. As shown in Figure 6.6a, relative to neat PLLA, adding 1.25% and 5 wt.% EB-1 dramatically improved the notched Izod impact strength by 600% and 1500%, respectively. The tensile properties, shown in Figure 6.6b and Table 6.4, were also influenced. As expected, the σ_y of the modified materials decreased but the ε_b increased drastically with EB-1 content. Addition of 2.5% and 5 wt.% EB-1 effectively increased the tensile toughness to more than 13 times that of the neat PLLA; at loadings of less than 5 wt.%, EB-1 did not significantly decrease the Young's modulus. To compare the yield stress and Young's modulus of neat PLLA and EB-1 modified blends, a *t*-test with a threshold for statistical significance set to 0.05 was used. Test results confirm that yield stress values of the blends with loadings of 1, 2.5 and 5 wt.% are significantly lower than that of neat PLLA, and higher than that of the blend with the 10 wt.% of EB-1. There are no statistically significant differences in the yield stress among these three lower loadings. When loadings are less than 5 wt.%, there is no statistically significant drop in the Young's modulus. Additionally, we observed a similar toughening effect in blends of EB-1 with PDLLA (see Table 6.1). With 2.5 wt.% of EB-1, the modified PDLLA thermoplastic exhibited $\sigma_y = 41 \pm 6$ MPa, $\varepsilon_b = 91 \pm 18$ %, and tensile toughness was 25 ± 9 MJ/m^3. These results are comparable to the tensile properties of the 2.5 wt.% EB-1/PLLA blend as shown in Table 6.4.

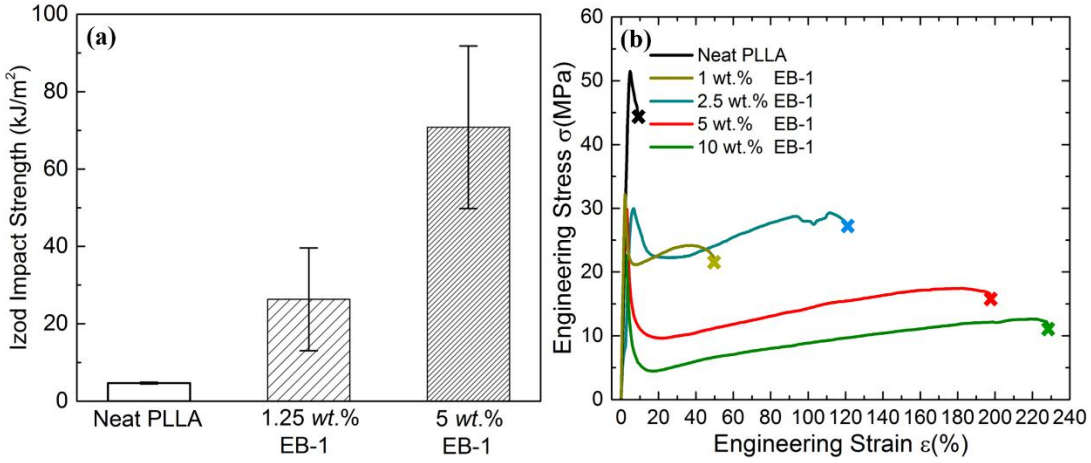

Figure 6.6 (a) Izod impact strength of neat PLLA and modified blends containing different loadings of EB-1. (b) Representative engineering stress *versus* strain data from tensile tests of PLLA/EB-1 blends. The modifier loading is from 1 to 10 wt.%.

Table 6.4 Summary of mechanical properties of EB-1/PLLA blends with different loadings of the modifier.

[a]Loading	[b]σ_y (MPa)	[b]E (GPa)	[b]ε_b (%)	[c]Toughness (MJ/m^3)
Neat	52 ± 3	2.3 ± 0.1	7 ± 2	2 ± 1
1 wt.%	33 ± 1	2.3 ± 0.2	67 ± 19	15 ± 3
2.5 wt.%	30 ± 3	2.1 ± 0.5	110 ± 30	28 ± 4
5 wt.%	28 ± 4	2.0 ± 0.1	175 ± 28	26 ± 4
10 wt.%	21 ± 2	1.8 ± 0.2	221 ± 18	20 ± 1

[a] The modifier is EB-1 in all cases.

[b] Yield strength (σ_y), tensile modulus (E), and strain at break (ε_b) were determined using a uniaxial tensile test with a crosshead velocity of 5 mm/min. Tensile modulus was quantified by fitting the linear elastic region of each curve before the yield point.

[c] Tensile toughness was determined by the integrated area under engineering stress-strain curve up to the breaking point.

Whereas pristine PLLA in the glassy state deforms first by crazing, then immediately undergoes shear banding without cavitation, the PLLA/EB blends undergo a deformation mechanism more similar to rubber-toughened thermoplastics (e.g. high impact polystyrene).[138, 250] In specimens of PLLA/EB-1 blends strained beyond the yield point, cavitation and void formation appear to trigger craze formation. Evidence of craze initiation can be seen in Figure 6.7, a TEM image of a 2.5 wt.% EB-1/PLLA specimen strained just past the yield point, where bilateral cracks emanate from the equator of micron–size voids. This voiding and crazing response helps to enhance the toughness of the blend by dissipating deformation stresses onto a large volume of the glassy matrix.[7] Rubber particle cavitation can also help promote shear deformation of PLLA, similar to the primary toughening mechanism operative with micelle-modified epoxy materials as described in previous Chapter 3-5. In the EB-1/PLLA blend all three micromechanical mechanisms: cavitation, crazing and shear yielding, produce a synergistic toughening effect.

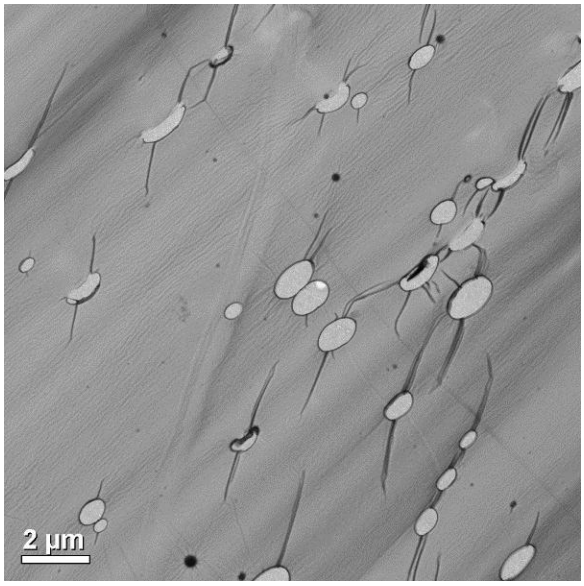

Figure 6.7 Representative cross-section TEM image of the tensile bar strained beyond the yield point. The sample was modified with 2.5 wt.% EB-1 and cryo-microtomed at −100 ℃ in the whitened zone within the gauge region. Ultrathin sections were stained with RuO_4 at room temperature before imaging. Hollow holes are caused by cavitation of micelle particles and multiple crazes are initiated from those holes. The tensile direction is perpendicular to this imaging plane.

6.3.5 Rheological behavior of modified blends

Figure 6.8 presents the influence of added EB-1 modifier on the melt rheological behavior of PLLA, and emphasis has been put on the study of complex viscosity. It is evident that addition of small quantities of EB-1 can result in a viscosity decrease, even though micelle-like particles are formed in polymer blends. This effect is more pronounced at low shear rates. Therefore, the decrease in zero shear viscosity of polymer blends relative to that of neat PLLA material is plotted as a function of EB-1 loading, which confirms the magnitude of drop grows with the EB-1 loading, and remarkable

changes as much as 45% can be attained at just 2.5 wt.% of EB-1. Within the limits of our characterization technique, we do not see evidence that this decreasing effect arises from either slip between the polymer and the instrument, or due to degradation of the PLLA.

This result is surprising, because addition of dispersed deformable spherical particles to a homopolymer is expected to increase the mixture viscosity, through deformation of the streamlines:[163]

$$\eta = \eta_s \left[1 + \left(\frac{1 + \frac{5}{2}\eta_{dr}}{1 + \eta_{dr}} \right) \phi \right] \tag{6.1}$$

where η is the apparent viscosity, η_s is the homopolymer viscosity, η_{dr} is the dispersed phase viscosity, and ϕ is the volume fraction of the dispersed phase. Unless the dispersed phase viscosity is negative, Equation (6.1) cannot predict a viscosity decrease such as we have observed. We propose that the viscosity drop may result from plasticizing effects caused by the wetting of the polymer brush on the EB-1 micelle surface with the PLLA homopolymer, since a negative χ(PEO/PLLA) is still present at 170 ℃ for the low molecular weight PEO block of EB-1. More in-depth investigations are needed for understanding this viscosity reduction effect, while it makes EB-1 a more appealing modifier for poly(lacitde) thermoplastics, because a lower viscosity can facilitate the processing of polymer blends. A good evidence is that the mixing force at 180 ℃ obtained using a twin-screw batch mixer (XPlore, DSM) was significantly decreased with the inclusion of EB-1: the mixing force for neat PLLA 2003D was about 3000 N, while it

was around 1280 N for 2.5 wt.% EB-1/PLLA blends, and about 720 N for 5 wt.% EB-1/PLLA blends.

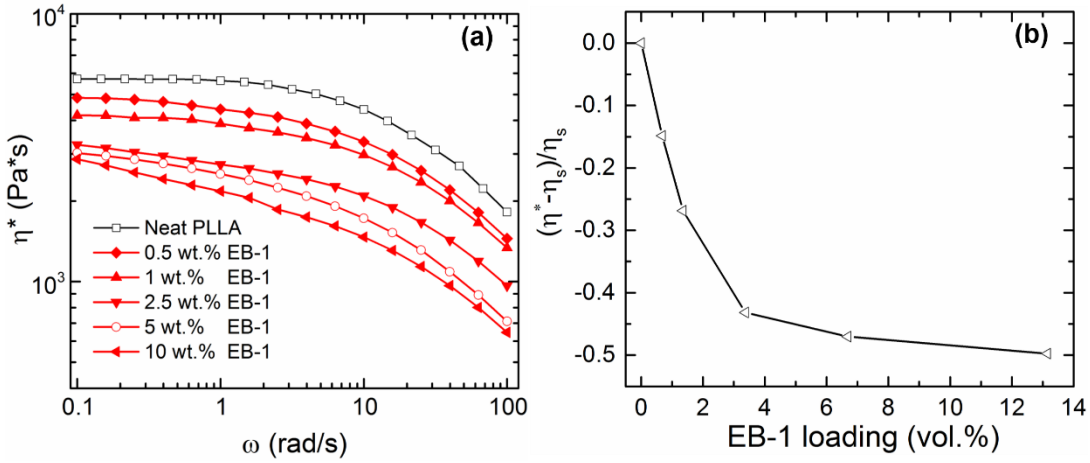

Figure 6.8 Effect of added EB-1 block copolymer on PLLA melt rheology. (a) complex viscosity (η^*) determined at 170 ℃; (b) the change in zero shear viscosity of modified blends relative to that of neat PLLA (η_s) as a function of EB-1 loading. The solid line between data points is a guide to the eye.

6.3.6 Performance of blown films prepared with modified blends*

EB-1/PDLLA polymer blends were employed in a film blowing process to further explore the toughening efficacy of this modifier in a thin thermoplastic film. Figure 6.9 shows the morphology of micelles in films produced as described above. Those 200 μm thick films were imbedded into a resin for cross-section TEM. In the process of film blowing, the films were stretched along the machine-direction (MD), so TEM was conducted in two different cross-section planes. One plane was along the machined direction, and the other one was normal to the machined direction, identified as the transverse-direction (TD). Figure 6.9a and 6.9b are in the MD, clearly showing the cylindrical micelles being stretched and aligned along the MD, as denoted by the arrow in Figure 6.9a. On the other hand, micelles in the TD tend to randomly distribute throughout the PDLLA matrix, as evidenced in Figure 6.9c and 6.9d.

(*This section was collaborated with Alex Mannion, Jacob Wright and Joseph Schaefer. Courtesy to them for conducting the film blowing process and tensile tests on the films.)

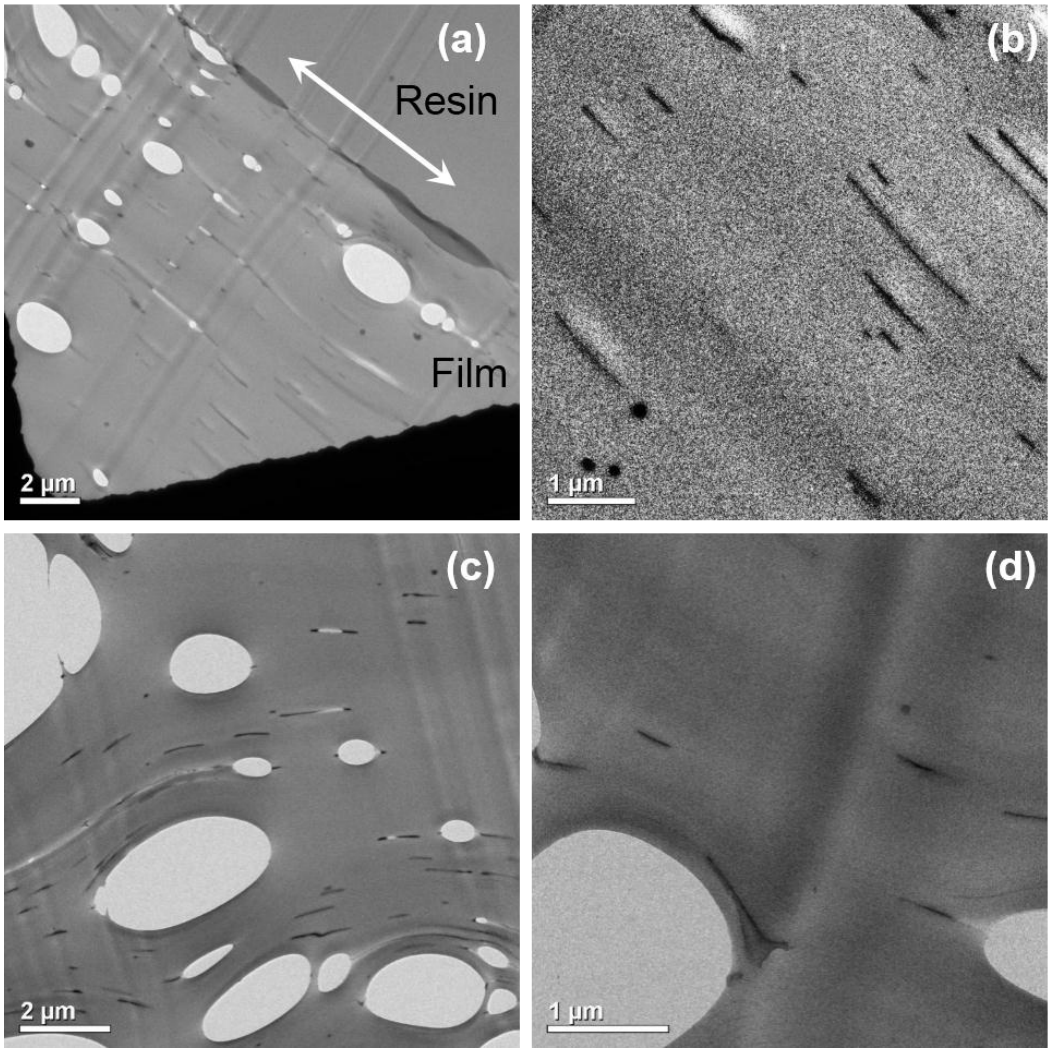

Figure 6.9 Representative cross-section TEM images of the films. (a, b) are in the machine direction (MD), *i.e.*, the direction in which films were stretched during the film bowing process, as denoted by the arrow in image (a). (c, d) are in the transverse direction (TD), namely, the direction that is perpendicular to the machined direction. RuO_4, as a contrast agent, was used to preferentially stain the PEO/PDLLA interface. The block copolymer loading is 2.5 wt% in all images.

To further verify the observed alignment and stretching of micelles, in Figure 6.10, we compare the micelle morphology in the bulk glassy PLLA (Figure 6.10a, b) with that in the blown-film along MD (Figure 6.10c, d). In the high magnification images,

Figure 6.10a and 6.10c, it is evident that cylindrical micelles have been stretched during the blown-film process, but the micelle shape and dimension are maintained. In the zoomed-out images, Figure 6.10b and 6.10d, micelle distribution in the blown-film shows the tendency of being aligned along the machine direction (MD).

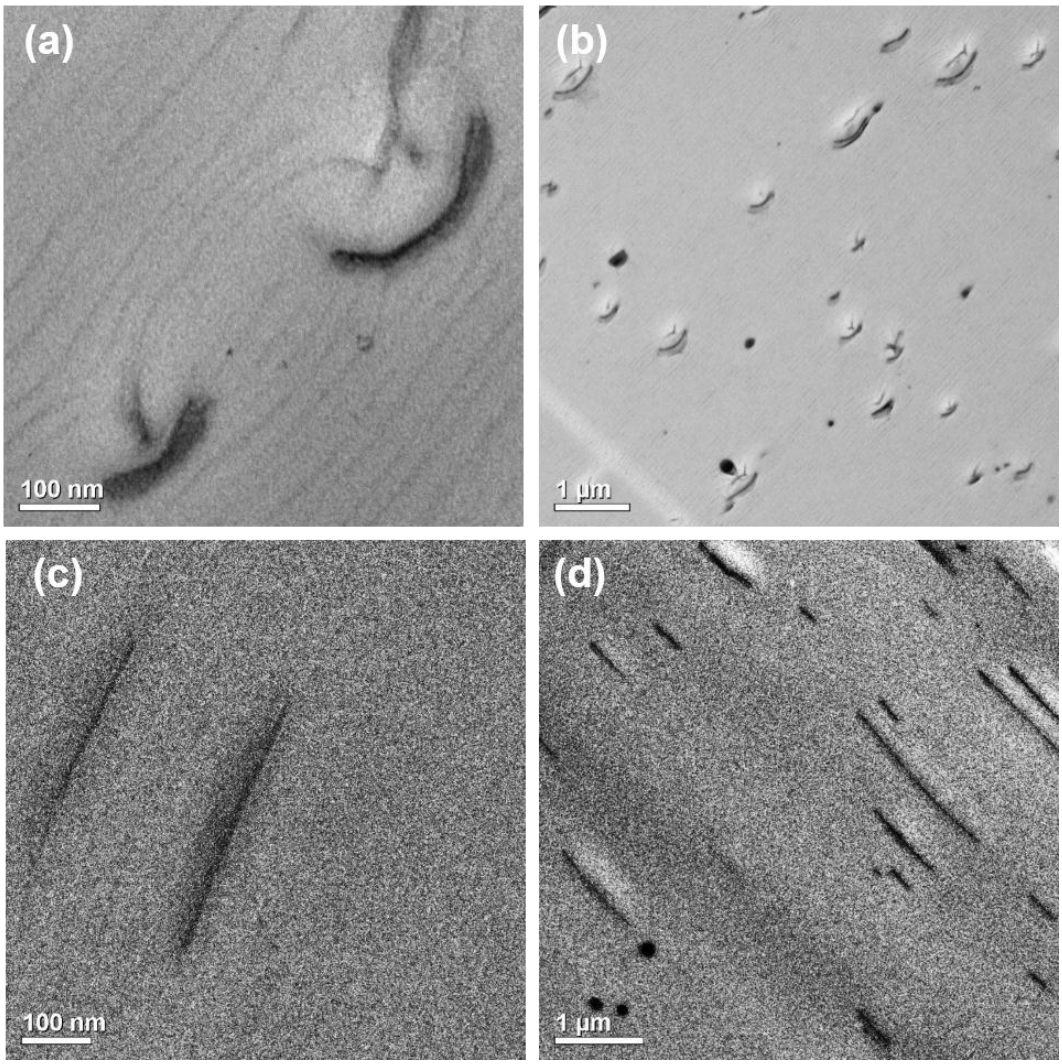

Figure 6.10 Representative TEM images of micelle morphology in polymer blends. (a, b) are EB-1/PLLA blends in the bulk state, and (c, d) are EB-1/PDLLA blends in blown-films along the machined direction. The block copolymer loading is 2.5 wt.% in all cases.

In the blown films, cylindrical micelles still can effectively toughen the PDLLA matrix. As shown in Table 6.5, in the machine direction, films modified with just 2.5 wt.% of EB-1 exhibit a 700% increase in the strain at break, and an 800% increase in the tensile toughness, compared to the unmodified film. Meanwhile, the Young's modulus and yield strength are not affected. There is a remarkable difference in the tensile properties for films in the machined direction (MD) and transverse direction (TD). As listed in Table 6.5, at the same block copolymer loading, films in MD have a toughness that is more than 300% higher than that of films in TD. We believe this difference is probably due to the alignment and stretching of micelles in the MD. As a comparison, the tensile properties of bulk specimens with 2.5 wt.% EB-1 (see above) are similar to those of the film in TD. Because micelles are randomly distributed in the PDLLA matrix for both cases.

Table 6.5 Summary of mechanical properties of blown films.*

[a] Sample	[b] E (GPa)	[b] σ_y (MPa)	[b] ε_b (%)	[c] Toughness (MJ/m^3)
Neat-MD	1.3 ± 0.4	44 ± 11	20 ± 13	6 ± 4
Neat-TD	1.6 ± 0.3	3 ± 1	6 ± 3	2 ± 1
Blend-MD	1.4 ± 0.2	43 ± 4	150 ± 30	46 ± 8
Blend-TD	1.2 ± 0.2	29 ± 2	60 ± 19	14 ± 4

* Courtesy to Alex Mannion and Jacob Wright for the data.

[a] The sample is 200 μm thick blown films. Neat = unmodified PDLLA, Blend = PDLLA modified with 2.5 wt.% EB-1, MD = machined direction, TD = transverse direction.

[b] Tensile modulus (E), yield strength (σ_y), and strain at break (ε_b) were determined using a uniaxial tensile test on punched dog-bone specimens (gauge length = 6 mm, width = 3.2 mm, thickness = 200 μm) with a crosshead velocity of 0.1 mm/s. Tensile modulus was quantified by fitting the linear elastic region of each curve before the yield point.

[c] Tensile toughness was determined by the integrated area under engineering stress-strain curve up to the breaking point.

6.4 Summary

In this chapter, we have shown that a low molecular weight PEO-PBO diblock can be uniformly dispersed as short cylindrical micelles in a commercial high molecular weight glassy PLLA or amorphous PDLLA thermoplastic matrix. This microstructure is believed to form due to a negative value of Flory-Huggins interaction parameter, χ, between PEO and PLA, which is evidenced by an experimentally observed lower critical

solution temperature (LCST) behavior for PEO/PDLLA homopolymer blend. The dispersed micelles toughen the thermoplastic matrix through concurrent cavitation, crazing and shear yielding, resulting in a greater than 10-fold increase in the tensile toughness and notched Izod impact strength over the unmodified PLLA in the glassy bulk state. At loadings as low as 2.5 wt.%, these micelles are found to effectively lower the zero shear viscosity of blends in the melt state by 45% relative to that of neat PLLA material. In plastic films prepared via a film blowing process, an eight-fold enhancement in the tensile toughness is also attained in the machined direction for block copolymer/PDLLA blends.

The work presented here advances the field of block copolymer modified thermoplastics in three significant ways. First, we have shown that a negative χ can be utilized to control microstructures in block copolymer/homopolymer blends. It is the basis for the extension of the block copolymer toughening strategy that is established in the thermoset polymer system to thermoplastic polymers. Secondly, our work has the practical benefit of providing a low-cost approach to toughening sustainable poly(lactide) materials based on a facile processing route. Finally, controlled cavitation and void formation offers a new method for producing low density porous materials with a host of potential applications.[251-253]

Chapter 7

Summary and outlook

The work presented in this dissertation has provided valuable insights for the understanding of nanostructure formation and associated toughness enhancement in block copolymer modified plastics. In this final chapter we first summarize the main results and conclusions from previous chapters (section 7.1) and then suggest possible research directions to further advance the field (section 7.2 to 7.4).

7.1 Thesis summary

Fabricating nanostructured plastics with outstanding toughness continuously arouses the interest of many researchers,[1, 2] because the nanoscale dispersed phase can minimize detrimental consequences on other highly desirable properties of the matrix material (the continuous phase) such as transparency, stiffness and use temperature.[7] In this work, we employed block copolymers as the dispersed phase to realize toughness enhancement in brittle plastics. Despite a large body of literature on polymer blends containing block copolymers, a comprehensive understanding of the toughening effect under various

conditions is still elusive. In this work, we designed different types of block copolymers in concert with several commercially important matrix plastics, including epoxy thermosets and poly(lactide) thermoplastics. Well-defined nanostructures accompanied by dramatic toughness enhancement were successfully achieved for these matrix materials in the bulk state as well as in thin films. As part of our work, we also explored such factors as processing variables, the crosslink density of the epoxy network and the presence of a second modifier in the matrix, in order to understand their influences on the nanostructure formation and toughening mechanism.

The work on nanostructured epoxy thermosets was presented first through Chapter 3 to Chapter 5. Although great advances in the understanding of block copolymer toughened epoxies have been made over the past years,[10, 11, 199] little attention has been given to the toughening effect in modified epoxy coatings, with a majority of the work focused on bulk materials.

In Chapter 3, we took advantage of a model epoxy system composed of the Jeffamine resin and two distinct diblock copolymers, PEO-PEP and P2VP-PB. In the bulk epoxies and 15 μm thick coatings, both block copolymers self-assembled into spherical micelles of 10-20 nm diameter. However, the process of solvent casting affected the micelle size and distribution throughout the coating, resulting in some micelle segregation at the coating/substrate interface. A very important conclusion is that the toughness enhancement observed in bulk materials (up to fivefold increase in G_{Ic}) can successfully translate to coatings, which was evidenced by the over 40% increase in the coating abrasive wear resistance with the addition of only 5 wt.% block copolymers.

According to TEM examination, this improvement appeared to be linked to the shear yielding promoted by micelle cavitation, similar toughening mechanisms as those in bulk epoxies. Moreover, the hardness, modulus, transparency and T_g of modified coatings were not significantly affected.

Based on this model system study, we proceeded to investigate a commercially viable block copolymer modifier, PEO-PBO, in combination with the bio-derived Cardolite curing agent. Compared to the model epoxy systems being extensively studied in literature,[10, 11] this commercial Cardolite-epoxy formulation is more complex thermodynamically, which challenges existing strategies for incorporating block copolymers as effective toughening agents.

Motivated by this practical problem, in Chapter 4, we expanded the molecular weight window for the PEO-PBO product and explored various processing variables with respect to the morphology and mechanical properties of cured resins. SAXS and TEM results showed that the lowest molecular weight PEO-PBO compound dissolved in the formulated epoxy resin mixture, leading to a cured product with little improvement in fracture toughness. Unfavorable thermodynamic interactions between the higher molecular weight block copolymers and the chemically complicated curing agent, exacerbated by the tendency for PEO to crystallize, led to macroscopic phase separation in cured epoxies and virtually no improvement in toughness over the neat material.

Modifications to the resin formulation and curing procedures resulted in well-defined micelles dispersed in the crosslinked epoxy matrix, and control over the morphology with variations in the block copolymer molecular weight. A branched

wormlike morphology in cured resin containing 5 wt.% PEO-PBO produced a nine-fold increase in G_{Ic}, over the standard product formulation, and a modest increase in T_g, without significant reduction in the elastic modulus. Furthermore, we elucidated the mechanism of block copolymer micelle formation, confirming the importance of balancing the block copolymer molecular weight and temperature-dependent thermodynamic interactions between the components, and adjusting the epoxy precursor composition and curing rate. The optimal wormlike morphology generated twice the toughness reflected in G_{Ic} relative to spherical micelles, consistent with the results of previous studies in our group.[51-53, 61] This morphology-dependent toughening effect was found to still exist in solvent-cast coatings as thin as 10 μm. The improved toughness was rationalized based on the mechanisms of shear yielding promoted by local cavitation and network disruption. A significant thrust of this work is the comprehensive integration of mixing thermodynamics, curing kinetics, and optimization of structure formation. The approach presented is valuable in designing other thermoset materials endowed with exceptional properties at manageable cost.

Typical block copolymer modifiers designed for epoxy resins contain rubbery epoxy-phobic blocks because they have better toughening efficacy than those with glassy epoxy-phobic blocks.[49, 95, 96] However, addition of rubbery phases would inevitably sacrifice the matrix modulus and T_g. To overcome this limitation of block copolymer toughened epoxies, incorporation of some rigid fillers in the matrix may be the solution. Also, there are a few studies in literature focused on the block copolymer toughening effect in the presence of a second type of modifier in the matrix.[199, 214, 219]

In Chapter 5, we advanced this field by developing a block copolymer/graphene/epoxy hybrid composite with superior toughness and no reduction in the elastic modulus. In the cured epoxy network, the rigid filler, exfoliated graphene oxide with amine-functionalization (GA), was well dispersed with no aggregation, and the diblock copolymer, PEO-PEP, formed randomly distributed spherical micelles of ~ 30 nm diameter showing no observable interactions with the graphene modifier. The crosslink density of the epoxy network was tunable, which strongly affected the toughening efficacy of both modifiers.

Hybrid ternary composites exhibited an interesting synergistic toughening effect. In the epoxy matrix with the lowest crosslink density, 5 wt.% PEO-PEP and 0.04 wt.% GA together dramatically enhanced the G_{Ic} value to 19 times that of the unmodified material, which is significantly higher than the additive result of a 14-fold increase summed over the improvements in associated binary composites containing solitary modifier. This synergy was attributed to the fact that the toughening mechanims noted for rubbery-core micelles and rigid graphene particles can function simultaneously at different lengh scales. Furthermore, in ternary composites, the micelle core cavitation and resultant matrix shear yielding can be facilitated by the stress concentration around GA particles; meanwhile, the micromechanical process of GA like debonding and microcrack formation can also be promoted by the change in the stress state accompanying micelle cavitation.

With the establishment of block copolymer toughening strategy in thermoset plastics, in Chapter 6, we extended this approach to a thermoplastic polymer matrix.

Chapter 7

Poly(lactide) thermoplastics were selected due to their sustainability, bio-degradability and growing commercial importance.[97-99] To fabricate thermodynamically stable block copolymer/homopolymer blends, amphiphilic block copolymers are typically designed to have a matrix-philic block that is chemically identical to but much longer than the homopolymer chain.[134, 135] However, addition of very high molecular weight block copolymers would significantly limit the processibility of polymer blends.

To solve this problem, we utilized the negative value of χ between PEO and PLLA to control microstructures in the modified blend. We showed that a low molar mass PEO-PBO diblock is uniformly dispersed as short cylindrical micelles in a commercial high molecular weight glassy PLLA plastic. This structure can toughen the thermoplastic matrix through concurrent cavitation, crazing, and shear yielding. At only 5 wt.% of loading, those micelles resulted in a greater than 10-fold increase in the tensile toughness and notched Izod impact strength over the pristine PLLA in the glassy state. At loadings as low as 2.5 wt.%, these micelles were found to effectively lower the zero shear viscosity of blends in the melt state by 45% relative to that of neat PLLA material. Moreover, these cylindrical micelles were stretched and aligned in plastic films prepared with PEO-PBO/PDLLA blends via a film blowing process, leading to an eight-fold enhancement in the tensile toughness over neat PDLLA films in the machined direction.

Recently there have been numerous studies concerning nanostructured plastics fabricated with block copolymers,[254-257] but there are still many research avenues open to aid our understanding of the nanostructure formation and control, and resultant consequences on the physical, chemical, and thermal properties of modified materials.

The subsequent sections of this chapter are dedicated to outlining potential opportunities that focus on further exploring the role of substrate on epoxy coating microstructure and performance, the role of thickness on the nanostructure formation and toughening effect in epoxy and PLA films, and some alternative block copolymer/homopolymer blends worthy for study beyond those previously investigated.

7.2 Role of substrate on epoxy coating structure and performance

In this dissertation, only commercial polyethylene terephthalate (PET) plastic films have been employed to prepare solvent-cast epoxy coatings, due to the requirement of abrasion test. Many researchers have shown that the selection of substrate has significant impacts on the microstructure and performance of cured epoxy coatings.[258-260] Therefore, we propose the study on the role of substrate as a promising direction for future studies.

Substrate selectivity (block copolymer/substrate interactions). When we choose different substrates for epoxy coatings, the substrate selectivity for each block may affect block copolymer distribution throughout the coating thickness. Adsorption of micelles onto the substrate from a selective solvent typically occurs when there exists strong interactions between the corona chains and the substrate.[261] As shown in Chapter 3, we have observed the segregation of P2VP-PB micelles to the coating/PET interface, since the P2VP block exhibits a preferential affinity for polar substrates.[262] The other corona block that we have used, PEO, is likely to be absorbed to hydrophilic substrates. Ideally, we would like the block copolymers and their aggregates to remain dispersed in the bulk of coating for the goal of toughening. However, it is of interest to study how to alter

coating nanostructures by tailoring the surface chemistry of substrates, which would also change the adhesion properties of the coatings. We propose using silicon substrates for epoxy coatings modified with PEO-based block copolymers. Substrates can be made hydrophilic by treatment with Piranha solution, or more hydrophobic via vapor phase silanization, but in the latter case we need to make sure there is good wetting of the substrate by the casting solutions, which can be verified by contact angle measurement. With strong attraction between selective substrates and PEO blocks, we are likely to create immobile "micelle layers" near the interface.

Curing of epoxy coatings on metals (resin/substrate interactions). For most practical applications, epoxy coatings are applied onto metallic substrates,[95] which have been observed to provoke the formation of a mixed interphase between the bulk coating and substrate during the network growth.[263] In this interphase region, amine-based curing agents can easily form organo-metallic complexes, resulting in a preferential adsorption of curing agent molecules and dissolution of the metal surface oxide or hydroxide layer. The properties of the interphase differ from the bulk coatings and it is often the weak spot of adhesive joints.[264, 265] Several researchers[263, 266] reported lower curing extent, decreased T_g and lower ductility in the interphase region between epoxy coatings and metallic substrates (aluminum, copper and titanium), and this region expanded over hundreds of nanometers. Therefore, it is worthy to explore how this interphase impacts the epoxy coating performance.

As the first step, aluminum and carbon steel can be selected as model substrates to study the influenced curing kinetics of epoxy coatings with small thickness (< 1 μm),

which allow for the utilization of *in situ* analysis techniques, such as FTIR external reflection absorption spectroscopy (ERAS).[265] Specifically, for epoxy resins cured with amine, the analysis can be based on the consumption of amine or oxirane group, or the formation of hydroxyl group. However, with the presence of different block copolymers, an appropriate IR band range must be selected to avoid overlap. To quantitatively study the conversion as a function of time and film thickness, the target band intensity should be normalized, and the phenylene ring stretching vibration at 1510 cm^{-1} is a good reference peak, since it usually exists in the epoxy monomer only.

Coating *in situ* toughness on substrates. In this dissertation, the abrasive wear resistance has been used as the indication for coating toughness. Although this result reflects the overall performance of coatings, a direct measurement to quantify the K_{Ic} and G_{Ic} value of epoxy coatings would be preferred. The small coating thickness (10-20 μm) puts challenges on fracture toughness measurement, because the conventional method by propagating a known pre-crack (e.g. ASTM standard E 399) is not suitable. Previous work[95] by Dr. Redline on the Jeffamine system reported difficulties to obtain coating fracture toughness based on the Indentation Crack Length (ICL) method that is established with ceramic films.[267-270] On the surface of epoxy coatings, radial cracks with valid shape and dimensions cannot be initiated via Nanoindenter or Triboindenter. We also tried similar experiments with the Cardolite system and other types of epoxy resins, but encountered the same issue. We believe that the coating toughness may be so high compared to the yielding of this polymeric material that the crack formation would be prohibited. In order to initiate cracks, we can conduct the experiment at a very low

temperature by using liquid nitrogen cooling, but the result cannot reflect coating toughness under ambient conditions.

Instead of employing the ICL method, we propose that the modified Vickers method developed by Xia et al.[271] may be a feasible solution to our dilemma. It is based on the microindentation technique, where Vickers indentation is performed on the substrate. Figure 7.1 illustrates the indentation geometry. The substrate is partially covered by the coating with a sharp edge. The indentation load must be large enough to ensure the initiated crack on the substrate to propagate into the coating. The length of crack that grows into the coating and the substrate is *a* and *b*, respectively. With no delamination, the coating toughness K_c is related to the substrate toughness K_s through the following equation:

$$K_c = \left\{ K_s^2 \left[1 + 0.45 \frac{(\phi b - a)}{t} \sqrt{\frac{E_c^*}{E_s^*}} \right]^2 \pm \left[1.9 \sigma_r \sqrt{t \frac{E_c^*}{E_s^*}} \right]^2 \right\}^{1/2} \tag{7.1}$$

where ϕ is the slope of *a* versus *b*, *t* is the coating thickness, σ_r is the internal stress $E_{c,s}^*$ is the effective elastic modulus given by $E_{c,s}/(1-\nu_{c,s}^2)$, subscript c and s standing for the coating and substrate respectively, ν being the Poisson ratio. The + or – signs are for tensile and compressive internal stress respectively. In this test, the epoxy coating specimen would be measured *in situ*. Again, the success relies on the crack propagation into the coating.

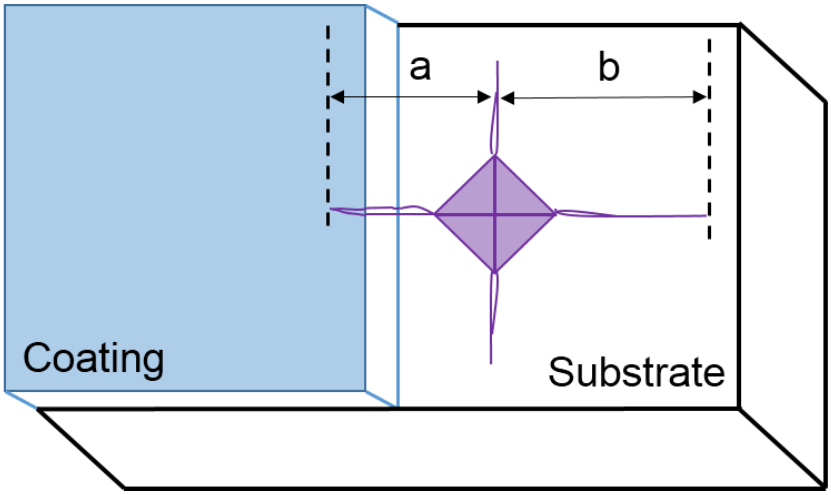

Figure 7.1 Schematic of the indentation geometry (adapted from Wang et al.[272]).

On the other hand, it has been observed that free-film failure and *in situ* failure, which is failure of the coating that happens on the substrate, can be dramatically different. This is due to the fact that free-film experiments do not account for substrate effects such as adhesion and mechanical constraint on the deformation process of coatings.[259] Therefore, we propose to determine the *in situ* fracture toughness G_{cc} of the coating system. Kim et al.[259, 260] developed a theoretical model to quantify G_{cc} from experimental data obtained with a four-point bending test. During bending tests, coatings failed by multiple-cracking and the number of cracks was recorded as a function of applied bending strain. G_{cc} is a system property, dependent on intrinsic properties of both coating and substrate, and even coating thickness. It is directly connected to practical applications as coating products.

7.3 Role of thickness on nanostructure and toughening

In thin films prepared with AB/A block copolymer/short-chain homopolymer blends, surface segregation of block copolymer chains or micelles has been observed, which is attributed to an attractive interaction between polymer brushes and the free surface.[262, 273] Similar phenomena are also possible to occur in our solvent-cast epoxy coatings and PLA films via film blowing, because the matrix-phobic blocks (PB, PEP, and PBO) possess lower surface energy than that of matrix polymers. In the early stage of thermal curing or at the outlet of melt-blending extruder, system viscosity is low, making micelle migration easy.

Thickness plays an important role in affecting the distribution of the dispersed phase, resulting in nanostructure variations. In a recent work, Ramos et al.[86] reported a morphological transition of block copolymers with the thickness in a solvent-cast epoxy coating. When coating thickness was small, spherical micelles occurred due to a faster solvent evaporation, while larger wormlike morphology was developed via the coalescence of small micelles with longer time in contact with the solvent. They also stated that films thinner than 30 μm would lead to homogeneous nanostructure.

It is of interest to study how thickness affects micelle distribution or even interaction. Take the PEO-PBO diblock/PDLLA melt blend just exiting from the extruder as an example. For simplification, we ignore the influence from shearing and assume an effective size D for the micelle. The thickness H of solidified film is assumed to be the same with that of film in the melt state. The annealing time t characterizes the interval for

micelles to stay mobile before the blend is vitrified, mainly dependent on the cooling rate. Micelle diffusion constant is scaled as:

$$D_m \sim \frac{kT}{3\pi\eta D} \tag{7.2}$$

where η is the blend viscosity at particular temperature. The typical displacement of a micelle during annealing time can be described as:

$$L_t \sim \sqrt{2D_m t} \tag{7.3}$$

The displacement before it meets another micelle is characterized by:

$$L_\phi \sim \frac{D}{\phi_c^{1/2}} \tag{7.4}$$

where ϕ_c is the volume fraction of block copolymer micelles in the blend. If H is not too large, e.g., $H < 2L_t$, most of the micelles would migrate to the surface, so the average number of "micelle layer", n, near the surface is determined by:

$$n \sim \frac{H\phi_c}{2D} \tag{7.5}$$

When the thickness is approaching the micelle size, a single layer of micelles can be achieved.[274] For thicker coatings, i.e., $H >> L_t$, most of the micelles will not have enough time to reach the surface and remain in the bulk portion of the film. Pairs or clusters of micelles are likely to appear in the bulk when $L_t >> L_\phi$.

Based on these simple scaling relationships, we propose to vary the thickness of epoxy coatings or PDLLA films to investigate the potential segregation of micelles and resultant changes in surface properties and toughness. It is of particular interest to study

the thickness influences in the block copolymer/graphene/epoxy ternary composite. The platelet shape and micron-scaled lateral dimension of graphene particles would challenge the theoretical analyses listed above and also the process of making thin coatings. Nevertheless, this study has direct implications for promising applications like anti-static coatings or conductive coatings.

7.4 Alternative block copolymer/homopolymer blends

We have found in Chapter 6 that a negative χ can be utilized to control microstructures in block copolymer/homopolymer blends. To verify the versatility of this approach, we propose to test more polymer blends in which the thermoplastic polymer matrix (C) and the matrix-philic block (A) of a block copolymer exhibit a negative χ when they are combined in the melt.

Firstly, the measurement of a χ parameter needs to be conducted. The most precise approach is to isotopically label polymer A or C with deuterium and use small angle neutron scattering (SANS) techniques. Based on the random phase approximation (RPA) theory,[275] χ (A/C) can be evaluated from the intermolecular component of the scattering from binary mixtures of A and C. Russell et al.[276] clearly demonstrated the utility of SANS for measuring negative χ values for mixtures of PEO with protio- and deuterio-poly(methyl methacrylate) (PMMA). Specific examples of the A/C combinations that have potential practical utility include PEO/PMMA, poly(vinyl methyl ether)/PS, and

poly(4-vinyl pyridine)/poly(acrylic acid), etc. The matrix-phobic block should be rubbery to allow cavitation to occur in the matrix, which greatly contributes to the toughness enhancement.

The architecture of block copolymers is another important factor that controls the microstructure formation and influences different properties of the polymer blend. For example, linear multiblock copolymers can afford impressive toughness by bridging individual microdomains and therefore facilitating the stress transfer within the matrix.[124, 125] However, it is generally challenging to process these materials due to their high melt viscosity, let alone to disperse them into another plastic.[277, 278] More complex architectures such as star and graft polymers may be utilized. These branched structures tend to have lower viscosities at high shear rates and improved processibility compared to linear chains with similar molecular weight.[279, 280] This inherent advantage along with the tunability in chemistry[255, 281] make star or graft block copolymers good candidates for the dispersed phase to fabricate tough nanostructured plastics.

Bibliography

1. Leibler, L. *Progress in polymer science* **2005,** 30, (8), 898-914.
2. Ruzette, A.-V.; Leibler, L. *Nature materials* **2005,** 4, (1), 19-31.
3. Janssen, M.; Zuidema, J.; Wanhill, R., Fracture Mechanics, 2nd. Taylor & Francis Group, London and New York: 2004.
4. Argon, A.; Cohen, R. *Polymer* **2003,** 44, (19), 6013-6032.
5. Argon, A. S., *The physics of deformation and fracture of polymers*. Cambridge University Press: 2013.
6. Bucknall, C. B., *Toughened plastics*. Springer: 1977.
7. Bartczak, Z.; Galeski, A., Mechanical Properties of Polymer Blends. In *Polymer Blends Handbook*, Springer: 2014; pp 1203-1297.
8. Milner, S. T. *MRS Bulletin* **1997,** 22, (01), 38-42.
9. Creton, C.; Kramer, E. J.; Brown, H. R.; Hui, C.-Y., Adhesion and Fracture of Interfaces Between Immiscible Polymers: from the Molecular to the Continuum Scal. In *Molecular Simulation Fracture Gel Theory*, Springer: 2001; pp 53-136.
10. Zheng, S. In *Nanostructured epoxies by the use of block copolymers*, Wiley-VCH Verlag GmbH & Co. KGaA: 2010; pp 81-108.
11. Ruiz-Perez, L.; Royston, G. J.; Fairclough, J. P. A.; Ryan, A. J. *Polymer* **2008,** 49, (21), 4475-4488.
12. Bates, F. S.; Fredrickson, G. H. *Annual Review of Physical Chemistry* **1990,** 41, (1), 525-557.
13. Bates, F. S.; Hillmyer, M. A.; Lodge, T. P.; Bates, C. M.; Delaney, K. T.; Fredrickson, G. H. *Science* **2012,** 336, (6080), 434-440.
14. Haward, R. N., *The physics of glassy polymers*. Springer Science & Business Media: 2012.

15. Kinloch, A. J., *Fracture behaviour of polymers*. Springer Science & Business Media: 2013.

16. Bagheri, R.; Marouf, B. T.; Pearson, R. A. *Polymer Reviews* **2009,** 49, (3), 201-225.

17. Muratoglu, O.; Argon, A.; Cohen, R.; Weinberg, M. *Polymer* **1995,** 36, (5), 921-930.

18. Kayano, Y.; Keskkula, H.; Paul, D. *Polymer* **1998,** 39, (13), 2835-2845.

19. Michler, G. H.; Balta-Calleja, F. J., *Nano-and micromechanics of polymers: structure modification and improvement of properties*. Carl Hanser Verlag GmbH Co KG: 2012.

20. Michler, G. H.; Balta-Calleja, F., *Mechanical properties of polymers based on nanostructure and morphology*. CRC Press: 2005; Vol. 71.

21. Kim, G.-M.; Michler, G. *Polymer* **1998,** 39, (23), 5689-5697.

22. Kim, G.-M.; Michler, G. *Polymer* **1998,** 39, (23), 5699-5703.

23. Bartczak, Z.; Argon, A.; Cohen, R.; Weinberg, M. *Polymer* **1999,** 40, (9), 2331-2346.

24. Oleinik, E. *Polymer science. Series C* **2003,** 45, 17-117.

25. Meijer, H.; Govaert, L.; Smit, R. In *Toughening of Plastics: Advances in Modeling and Experiments*, ACS Symposium Series; 2000; pp 50-70.

26. Ding, C.; Matharu, A. S. *ACS Sustainable Chemistry and Engineering* **2014,** 2, (10), 2217-2236.

27. Flick, E. W., *Epoxy resins, curing agents, compounds, and modifiers: an industrial guide*. William Andrew: 2012.

28. Meeks, A. C. *Polymer* **1974,** 15, (10), 675-681.

29. Auvergne, R.; Caillol, S.; David, G.; Boutevin, B.; Pascault, J.-P. *Chemical Review* **2014,** 114, (2), 1082-1115.

30. Pascault, J.-P.; Sautereau, H.; Verdu, J.; Williams, R. J. J.; Editors, *Thermosetting Polymers*. Marcel Dekker, Inc.: 2002.

31. Dickie, R. A.; Labana, S. S.; Bauer, R. S.; Editors, *ACS Symposium Series 367: Cross-Linked Polymers: Chemistry, Properties, and Applications.* American Chemical Society: 1988.

32. Kinloch, A. J. *MRS Bulletin* **2003,** 28, (6), 445-448.

33. Drake, R. S.; Egan, D. R.; Murphy, W. T. In: Bauer, R. S.; Ed.; Epoxy Resin Chemistry II, American Chemical Society: Washington, DC, **1983,** 221, pp 1-20.

34. Bauer, R. S. Epoxy Resin Chemistry II; Ameican Chemical Society: Washington, DC, **1983,** 221, ix-x.

35. Li, T.; Heinzer, M. J.; Francis, L. F.; Bates, F. S. *Journal of Polymer Science Part B: Polymer Physics* **2016,** 54, (2), 189-204.

36. Li, T.; Heinzer, M. J.; Redline, E. M.; Zuo, F.; Bates, F. S.; Francis, L. F. *Progress in Organic Coatings* **2014,** 77, (7), 1145-1154.

37. Riew, C. K.; Kinloch, A. J. *Toughened plastics I: science and engineering*; American Chemical Society, Washington, DC: 1993.

38. Unnikrishnan, K. P.; Thachil, E. T. *Designed Monomers and Polymers* **2006,** 9, (2), 129-152.

39. Pearson, R.; Yee, A. *Journal of materials science* **1989,** 24, (7), 2571-2580.

40. Pearson, R. A.; Yee, A. F. *Journal of Materials Science* **1991,** 26, (14), 3828-3844.

41. Heng, Z.; Chen, Y.; Zou, H.; Liang, M. *RSC Advances* **2015,** 5, (53), 42362-42368.

42. Yahyaie, H.; Ebrahimi, M.; Tahami, H. V.; Mafi, E. R. *Progress in Organic Coatings* **2013,** 76, (1), 286-292.

43. Hillmyer, M. A.; Lipic, P. M.; Hajduk, D. A.; Almdal, K.; Bates, F. S. *Journal of the American Chemical Society* **1997,** 119, (11), 2749-2750.

44. Hillmyer, M. A.; Lipic, P. M.; Hajduk, D. A.; Almdal, K.; Bates, F. S. In *Amphiphilic block copolymers as nanocomposite templates*, 1997; American Chemical Society: 1997; pp 340.

45. Dean, J. M.; Lipic, P. M.; Grubbs, R. B.; Cook, R. F.; Bates, F. S. *Journal of Polymer Science, Part B: Polymer Physics* **2001,** 39, (23), 2996-3010.

46. Grubbs, R. B.; Broz, M. E.; Dean, J. M.; Bates, F. S. *Macromolecules* **2000,** 33, (7), 2308-2310.

47. Matsen, M. *Macromolecules* **1995,** 28, (17), 5765-5773.

48. Thompson, Z. J.; Hillmyer, M. A.; Liu, J.; Sue, H.-J.; Dettloff, M.; Bates, F. S. *Macromolecules* **2009,** 42, (7), 2333-2335.

49. Declet-Perez, C.; Redline, E. M.; Francis, L. F.; Bates, F. S. *ACS Macro Letters* **2012,** 1, (2), 338-342.

50. Liu, J.; Sue, H.-J.; Thompson, Z. J.; Bates, F. S.; Dettloff, M.; Jacob, G.; Verghese, N.; Pham, H. *Macromolecules* **2008,** 41, (20), 7616-7624.

51. Liu, J.; Thompson, Z. J.; Sue, H.-J.; Bates, F. S.; Hillmyer, M. A.; Dettloff, M.; Jacob, G.; Verghese, N.; Pham, H. *Macromolecules* **2010,** 43, (17), 7238-7243.

52. Wu, J.; Thio, Y. S.; Bates, F. S. *Journal of Polymer Science, Part B: Polymer Physics* **2005,** 43, (15), 1950-1965.

53. Thio, Y. S.; Wu, J.; Bates, F. S. *Macromolecules* **2006,** 39, (21), 7187-7189.

54. Dean, J. M.; Grubbs, R. B.; Saad, W.; Cook, R. F.; Bates, F. S. *Journal of Polymer Science, Part B: Polymer Physics* **2003,** 41, (20), 2444-2456.

55. Lipic, P. M.; Bates, F. S.; Hillmyer, M. A. *Journal of the American Chemical Society* **1998,** 120, (35), 8963-8970.

56. Grubbs, R. B.; Dean, J. M.; Broz, M. E.; Bates, F. S. *Macromolecules* **2000,** 33, (26), 9522-9534.

57. Dean, J. M.; Bates, F. S.; Pham, H. Q.; Vergese, N. E. Curable flame retardant epoxy resin compositions with block copolymer for toughness, coated article, prepreg, and laminate. US20040247881A1, 2004.

58. Pham, H. Q.; Verghese, K. E.; Bates, F. S. Amphiphilic block copolymer-toughened epoxy vinyl ester and unsaturated polyester resins with good fracture resistance. WO2006052728A1, 2006.

59. Liu, J.; Sue, H.-J.; Thompson, Z. J.; Bates, F. S.; Dettloff, M.; Jacob, G.; Verghese, N.; Pham, H. *Acta Materialia* **2009,** 57, (9), 2691-2701.

60. Liu, J.; Sue, H.-J.; Thompson, Z. J.; Bates, F. S.; Dettloff, M.; Jacob, G.; Verghese, N.; Pham, H. *Polymer* **2009,** 50, (19), 4683-4689.

61. Dean, J. M.; Verghese, N. E.; Pham, H. Q.; Bates, F. S. *Macromolecules* **2003,** 36, (25), 9267-9270.

62. Grubbs, R. B.; Dean, J. M.; Bates, F. S. *Polymeric Materials: Science and Engineering* **1999,** 81, 153-154.

63. Guo, Q.; Dean, J. M.; Grubbs, R. B.; Bates, F. S. *Journal of Polymer Science, Part B: Polymer Physics* **2003,** 41, (17), 1994-2003.

64. Thio, Y. S.; Wu, J.; Bates, F. S. *Journal of Polymer Science, Part B: Polymer Physics* **2009,** 47, (11), 1125-1129.

65. Wu, J., Structures and properties of diblock copolymer modified epoxy. University of Minnesota: Minneapolis, MN, 2005.

66. Fan, W.; Zheng, S. *Polymer* **2008,** 49, (13-14), 3157-3167.

67. Yu, R.; Zheng, S.; Li, X.; Wang, J. *Macromolecules* **2012,** 45, (22), 9155-9168.

68. Wang, L.; Zhang, C.; Cong, H.; Li, L.; Zheng, S.; Li, X.; Wang, J. *The Journal of Physical Chemistry B* **2013,** 117, (27), 8256-8268.

69. Yang, X.; Yi, F.; Xin, Z.; Zheng, S. *Polymer* **2009,** 50, (16), 4089-4100.

70. Cong, H.; Li, J.; Li, L.; Zheng, S. *The Journal of Physical Chemistry B* **2014**.

71. Zhu, L.; Zhang, C.; Han, J.; Zheng, S.; Li, X. *Soft Matter* **2012,** 8, (26), 7062-7072.

72. Ritzenthaler, S.; Court, F.; David, L.; Girard-Reydet, E.; Leibler, L.; Pascault, J. P. *Macromolecules* **2002,** 35, (16), 6245-6254.

73. Ritzenthaler, S.; Court, F.; Girard-Reydet, E.; Leibler, L.; Pascault, J. P. *Macromolecules* **2003,** 36, (1), 118-126.

74. Rebizant, V.; Abetz, V.; Tournilhac, F.; Court, F.; Leibler, L. *Macromolecules* **2003,** 36, (26), 9889-9896.

75. Rebizant, V.; Venet, A.-S.; Tournilhac, F.; Girard-Reydet, E.; Navarro, C.; Pascault, J.-P.; Leibler, L. *Macromolecules* **2004,** 37, (21), 8017-8027.

76. Garate, H.; Goyanes, S.; D'Accorso, N. B. *Macromolecules* **2014,** 47, (21), 7416-7423.

77. Pandit, R.; Michler, G. H.; Lach, R.; Grellmann, W.; Saiter, J. M.; Berkessel, A.; Adhikari, R. In *Epoxidation of Styrene/Butadiene Star Block Copolymer by Different Methods and Characterization of the Blends with Epoxy Resin*, Macromolecular Symposia, 2014; Wiley Online Library: 2014; pp 67-74.

78. Kishi, H.; Kunimitsu, Y.; Nakashima, Y.; Abe, T.; Imade, J.; Oshita, S.; Morishita, Y.; Asada, M. *Express Polymer Letters* **2015,** 9, (1).

79. Belmonte, A.; Daebritz, F.; Ramis, X.; Serra, A.; Voit, B.; Fernández‐Francos, X. *Journal of Polymer Science Part B: Polymer Physics* **2014,** 52, (18), 1227-1242.

80. Francis, R.; Baby, D. K. *Industrial & Engineering Chemistry Research* **2014,** 53, (46), 17945-17951.

81. Leonardi, A. B.; Zucchi, I. A.; Williams, R. J. *European Polymer Journal* **2014**.

82. Hu, C.; Yu, J.; Huo, J.; Chen, Y.; Ma, H. *Polymers for Advanced Technologies* **2015**.

83. Garate, H.; Mondragon, I.; D'Accorso, N. B.; Goyanes, S. *Macromolecules* **2013,** 46, (6), 2182-2187.

84. Naguib, M.; Sangermano, M.; Capozzi, L. C.; Pospiech, D.; Sahre, K.; Jehnichen, D.; Scheibner, H.; Voit, B. *Progress in Organic Coatings* **2015,** 85, 178-188.

85. Acebo, C.; Picardi, A.; Fernández-Francos, X.; De la Flor, S.; Ramis, X.; Serra, À. *Progress in Organic Coatings* **2014,** 77, (8), 1288-1298.

86. Ramos, J. A.; Esposito, L. H.; Fernandez, R.; Zalakain, I.; Goyanes, S.; Avgeropoulos, A.; Zafeiropoulos, N. E.; Kortaberria, G.; Mondragon, I. *Macromolecules* **2012,** 45, (3), 1483-1491.

87. Hydro, R. M.; Pearson, R. A. *Journal of Polymer Science, Part B: Polymer Physics* **2007,** 45, (12), 1470-1481.

88. Gerard, P.; Boupat, N. P.; Fine, T.; Gervat, L.; Pascault, J. P. In *Toughness properties of lightly crosslinked epoxies using block copolymers,* Macromolecular Symposia, 2007; Wiley Online Library: 2007; pp 55-64.

89. George, S. M.; Puglia, D.; Kenny, J. M.; Causin, V.; Parameswaranpillai, J.; Thomas, S. *Industrial & Engineering Chemistry Research* **2013,** 52, (26), 9121-9129.

90. Tang, H. S.; Hermel‐Davidock, T. J.; Hahn, S. F.; Murray, D. J.; Cieslinski, R. C.; Verghese, N. E.; Pham, H. Q. *Journal of Polymer Science Part B: Polymer Physics* **2009,** 47, (4), 393-406.

91. Declet-Perez, C. Toughness in block copolymer modified epoxies. University of Minnesota: Minneapolis, MN, 2014.

92. Redline, E. M.; Declet-Perez, C.; Bates, F. S.; Francis, L. F. *Polymer* **2014,** 55, (16), 4172-4181.

93. Declet-Perez, C.; Francis, L. F.; Bates, F. S. *ACS Macro Letters* **2013,** 2, (10), 939-943.

94. Redline, E. M.; Francis, L. F.; Bates, F. S. *Journal of Polymer Science, Part B: Polymer Physics* **2011,** 49, (7), 540-550.

95. Redline, E. M. Addition of Block Copolymer to Radical Cured Thermosets. University of Minnesota: Minneapolis, MN, 2011.

96. Declet-Perez, C.; Francis, L. F.; Bates, F. S. *Macromolecules* **2015,** 48, (11), 3672-3684.

97. Jamshidian, M.; Tehrany, E. A.; Imran, M.; Jacquot, M.; Desobry, S. *Comprehensive Reviews in Food Science and Food Safety* **2010,** 9, (5), 552-571.

98. Liu, H.; Zhang, J. *Journal of polymer science part B: Polymer Physics* **2011,** 49, (15), 1051-1083.

99. Miller, S. A. *ACS Macro Letters* **2013,** 2, (6), 550-554.

100. Anderson, K. S.; Schreck, K. M.; Hillmyer, M. A. *Polymer Reviews* **2008,** 48, (1), 85-108.

101. Perego, G.; Cella, G. D.; Bastioli, C. *Journal of Applied Polymer Science* **1996,** 59, (1), 37-43.

102. Murariu, M.; Da Silva Ferreira, A.; Alexandre, M.; Dubois, P. *Polymers for Advanced Technologies* **2008,** 19, (6), 636-646.

103. Ljungberg, N.; Wesslen, B. *Journal of Applied Polymer Science* **2002,** 86, (5), 1227-1234.

104. Ljungberg, N.; Wesslén, B. *Biomacromolecules* **2005,** 6, (3), 1789-1796.

105. Martino, V.; Ruseckaite, R.; Jiménez, A. *Journal of thermal analysis and calorimetry* **2006,** 86, (3), 707-712.

106. Grijpma, D. W.; Pennings, A. J. *Macromolecular Chemistry and Physics* **1994,** 195, (5), 1649-1663.

107. Vilay, V.; Mariatti, M.; Ahmad, Z.; Pasomsouk, K.; Todo, M. *Journal of applied polymer science* **2009,** 114, (3), 1784-1792.

108. Anderson, K. S.; Lim, S. H.; Hillmyer, M. A. *Journal of Applied Polymer Science* **2003,** 89, (14), 3757-3768.

109. Liu, H.; Chen, F.; Liu, B.; Estep, G.; Zhang, J. *Macromolecules* **2010,** 43, (14), 6058-6066.

110. Liu, H.; Song, W.; Chen, F.; Guo, L.; Zhang, J. *Macromolecules* **2011,** 44, (6), 1513-1522.

111. Urayama, H.; Ma, C.; Kimura, Y. *Macromolecular Materials and Engineering* **2003,** 288, (7), 562-568.

112. Chen, G. X.; Yoon, J. S. *Journal of Polymer Science Part B: Polymer Physics* **2005,** 43, (5), 478-487.

113. Hasook, A.; Tanoue, S.; Iemoto, Y.; Unryu, T. *Polymer Engineering & Science* **2006,** 46, (8), 1001-1007.

114. Grijpma, D. W.; Altpeter, H.; Bevis, M. J.; Feijen, J. *Polymer international* **2002,** 51, (10), 845-851.

115. Jacobsen, S.; Fritz, H.-G. *Polymer Engineering & Science* **1999,** 39, (7), 1303-1310.

116. Baiardo, M.; Frisoni, G.; Scandola, M.; Rimelen, M.; Lips, D.; Ruffieux, K.; Wintermantel, E. *Journal of Applied Polymer Science* **2003,** 90, (7), 1731-1738.

117. Hu, Y.; Rogunova, M.; Topolkaraev, V.; Hiltner, A.; Baer, E. *Polymer* **2003,** 44, (19), 5701-5710.

118. Hu, Y.; Hu, Y.; Topolkaraev, V.; Hiltner, A.; Baer, E. *Polymer* **2003,** 44, (19), 5711-5720.

119. Labrecque, L.; Kumar, R.; Dave, V.; Gross, R.; McCarthy, S. *Journal of Applied Polymer Science* **1997,** 66, (8), 1507-1513.

120. Xiong, M.; Schneiderman, D. K.; Bates, F. S.; Hillmyer, M. A.; Zhang, K. *Proceedings of the National Academy of Sciences* **2014,** 111, (23), 8357-8362.

121. Martello, M. T.; Burns, A.; Hillmyer, M. *ACS Macro Letters* **2011,** 1, (1), 131-135.

122. Wanamaker, C. L.; O'Leary, L. E.; Lynd, N. A.; Hillmyer, M. A.; Tolman, W. B. *Biomacromolecules* **2007,** 8, (11), 3634-3640.

123. Lin, J.-O.; Chen, W.; Shen, Z.; Ling, J. *Macromolecules* **2013,** 46, (19), 7769-7776.

124. Lee, I.; Panthani, T. R.; Bates, F. S. *Macromolecules* **2013,** 46, (18), 7387-7398.

125. Panthani, T. R.; Bates, F. S. *Macromolecules* **2015,** 48, (13), 4529-4540.

126. Semba, T.; Kitagawa, K.; Ishiaku, U. S.; Hamada, H. *Journal of applied polymer science* **2006,** 101, (3), 1816-1825.

127. Harada, M.; Ohya, T.; Iida, K.; Hayashi, H.; Hirano, K.; Fukuda, H. *Journal of applied polymer science* **2007,** 106, (3), 1813-1820.

128. Li, Y.; Shimizu, H. *Macromolecular bioscience* **2007,** 7, (7), 921-928.

129. Robertson, M. L.; Chang, K.; Gramlich, W. M.; Hillmyer, M. A. *Macromolecules* **2010,** 43, (4), 1807-1814.

130. Anderson, K. S.; Hillmyer, M. A. *Polymer* **2004,** 45, (26), 8809-8823.

131. Li, Y.; Shimizu, H. *European Polymer Journal* **2009,** 45, (3), 738-746.

132. Knoll, K.; Nießner, N. In *Styrolux+ and styroflex+ – from transparent high impact polystyrene to new thermoplastic elastomers: Syntheses, applications and blends with other styrene based polymers*, Macromolecular Symposia, 1998; Wiley Online Library: 1998; pp 231-243.

133. Adhikari, R.; Michler, G. H. *Progress in polymer science* **2004,** 29, (9), 949-986.

134. Borukhov, I.; Leibler, L. *Physical Review E* **2000,** 62, (1), R41.

135. Borukhov, I.; Leibler, L. *Macromolecules* **2002,** 35, (13), 5171-5182.

136. Martin, T. B.; Mongcopa, K. I. S.; Ashkar, R.; Butler, P.; Krishnamoorti, R.; Jayaraman, A. *Journal of the American Chemical Society* **2015,** 137, (33), 10624-10631.

137. Mao, H.; Arrechea, P. L.; Bailey, T. S.; Johnson, B. J.; Hillmyer, M. A. *Faraday discussions* **2005,** 128, 149-162.

138. Kowalczyk, M.; Piorkowska, E. *Journal of Applied Polymer Science* **2012,** 124, (6), 4579-4589.

139. Ndoni, S.; Papadakis, C. M.; Bates, F. S.; Almdal, K. *Review of scientific instruments* **1995,** 66, (2), 1090-1095.

140. Pangborn, A. B.; Giardello, M. A.; Grubbs, R. H.; Rosen, R. K.; Timmers, F. J. *Organometallics* **1996,** 15, (5), 1518-1520.

141. Hillmyer, M. A.; Bates, F. S. *Macromolecules* **1996,** 29, (22), 6994-7002.

142. Quirk, R. P.; Ma, J. J. *Journal of Polymer Science Part A: Polymer Chemistry* **1988,** 26, (8), 2031-2037.

143. Allgaier, J.; Willbold, S.; Chang, T. *Macromolecules* **2007,** 40, (3), 518-525.

144. Kline, S. R. *Journal of Applied Crystallography* **2006,** 39, (6), 895-900.

145. Hammouda, B.; Ho, D. L.; Kline, S. *Macromolecules* **2004,** 37, (18), 6932-6937.

146. Choi, S.-H.; Bates, F. S.; Lodge, T. P. *The Journal of Physical Chemistry B* **2009,** 113, (42), 13840-13848.

147. Choi, S.-H.; Lodge, T. P.; Bates, F. S. *Phys Rev Lett* **2010,** 104, (4), 047802.

148. Grillet, A. C.; Galy, J.; Gérard, J.-F.; Pascault, J.-P. *Polymer* **1991,** 32, (10), 1885-1891.

149. Schuh, C. A. *Materials Today* **2006,** 9, (5), 32-40.

150. Oliver, W. C.; Pharr, G. M. *Journal of materials research* **2004,** 19, (01), 3-20.

151. Oliver, W. C.; Pharr, G. M. *J. Mater. Res.* **1992,** 7, (6), 1564-83.

152. Wen, J.; Vasudevan, V. J.; Wilkes, G. L. *J. Sol-Gel Sci. Technol.* **1995,** 5, (2), 115-26.

153. Nishiyama, N.; Asakura, T.; Horie, K. *J. Colloid Interface Sci.* **1988,** 124, (1), 14-21.

154. Daniels, M. W. Colloidal ceramic coatings with silane coupling agents. 1999.

155. Lewis, L. N.; Katsamberis, D. *J. Appl. Polym. Sci.* **1991,** 42, (6), 1551-6.

156. Brandrup, J.; Immergut, E. H.; Editors, *Polymer Handbook, Fourth Edition*. Wiley: 1998; p 1920 pp.

157. Fetters, L.; Lohse, D.; Richter, D.; Witten, T.; Zirkel, A. *Macromolecules* **1994,** 27, (17), 4639-4647.

158. Yim, H.; Kent, M.; McNamara, W. F.; Ivkov, R.; Satija, S.; Majewski, J. *Macromolecules* **1999,** 32, (23), 7932-7938.

159. Schneider, C. A.; Rasband, W. S.; Eliceiri, K. W. *Nature Methods* **2012,** 9, 671-675.

160. Trent, J. S.; Scheinbeim, J. I.; Couchman, P. R. *Macromolecules* **1983,** 16, (4), 589-98.

161. Bates, F. S.; Berney, C. V.; Cohen, R. E. *Macromolecules* **1983,** 16, (7), 1101-8.

162. Lu, J.; Bates, F. S.; Lodge, T. P. *ACS Macro Letters* **2013,** 2, (5), 451-455.

163. Berg, J. C., *An introduction to interfaces & colloids: the bridge to nanoscience*. World Scientific: 2010.

164. Antonow, G. N. *J Chem Phys* **1907,** 5, 364-371.

165. Bahramian, A. *Fluid Phase Equilibria* **2009,** 285, (1–2), 24-29.

166. Lee, L.-H., In *Fundamentals of Adhesion and Interfaces*, DeMejo, L. P., Raima, D.S., Sharpe, L.H., Ed. Gordon and Breach: Amsterdam, The Netherlands, 1999; p 13.

167. Afshin Falsafi, S. M., Michael J. Owen, Surface and Interfacial Properties. In *Physical Properties of Polymers Handbook*, Mark, J. E., Ed. Springer: New York, NY, 2007; pp 1018.

168. George, G. A., *Polymer Surfaces and Interfaces II*. John Wiley & Sons: Hoboken, NJ, 1993.

169. Pinto, G.; de Abreu, C. A. M.; Knoechelmann, A.; de Almeida, Y. M. B. *Macromolecular Symposia* **1999,** 148, 333-343.

170. Liu, D.; Sue, H.-J.; Thompson, Z. J.; Bates, F. S.; Hillmyer, M. A.; Dettloff, M.; Jacob, G.; Verghese, N.; Pham, H. In *Nanoscaled deformations in block copolymer modified epoxies*, 2010; American Chemical Society: 2010; pp 250.

171. Zhang, Y.-F.; Bai, S.-L.; Li, X.-K.; Zhang, Z. *J. Polym. Sci., Part B: Polym. Phys.* **2009,** 47, (10), 1030-1038.

172. Payne, J. A.; Strojny, A.; Francis, L. F.; Gerberich, W. W. *Polymer Engineering & Science* **1998,** 38, (9), 1529-1535.

173. Iijima, M.; Muguruma, T.; Brantley, W. A.; Mizoguchi, I. *American Journal of Orthodontics and Dentofacial Orthopedics* **2011,** 140, (1), 65-71.

174. Holmberg, K.; Mathews, A. *Thin Solid Films* **1994,** 253, (1-2), 173-8.

175. Holmberg, K.; Ronkainen, H.; Matthews, A. *Ceram. Int.* **2000,** 26, (7), 787-795.

176. Lee, L. H. *ACS Symposium Series* **1985,** 287, 27-38.

177. He, X.; Liu, Y.; Zhang, R.; Wu, Q.; Chen, T.; Sun, P.; Wang, X.; Xue, G. *The Journal of Physical Chemistry C* **2014,** 118, (24), 13285-13299.

178. Maiez-Tribut, S.; Pascault, J.-P.; Soule, E.; Borrajo, J.; Williams, R. J. *Macromolecules* **2007,** 40, (4), 1268-1273.

179. Ocando, C.; Serrano, E.; Tercjak, A.; Pena, C.; Kortaberria, G.; Calberg, C.; Grignard, B.; Jerome, R.; Carrasco, P. M.; Mecerreyes, D. *Macromolecules* **2007,** 40, (11), 4068-4074.

180. Girard‐Reydet, E.; Pascault, J. P.; Bonnet, A.; Court, F.; Leibler, L. In *A new class of epoxy thermosets*, Macromolecular Symposia, 2003; Wiley Online Library: 2003; pp 309-322.

181. Feng, Y. L.; Gan, J.; Zhang, W. Y.; Yan, P. P., Adducts as toughening in thermosettable epoxy systems. Google Patents: 2011.

182. Valette, L.; Jiang, L. Y.; Ji, D.; Karunakaran, K. In *Novel high performances epoxy/anhydride formulations and their application in electrical insulation*, Electrical Insulation Conference (EIC), 2011, 2011; IEEE: 2011; pp 459-463.

183. Dai, Z.; Constantinescu, A.; Dalal, A.; Ford, C. *Cardolite Corporation* **1994**.

184. Pathak, S. K.; Rao, B. S. *Journal of Applied Polymer Science* **2006,** 102, (5), 4741-4748.

185. Pham, H. Q.; Marks, M. J. *Kirk-Othmer Encyclopedia of Chemical Technology* **2004**.

186. Bang, J.; Jain, S.; Li, Z.; Lodge, T. P.; Pedersen, J. S.; Kesselman, E.; Talmon, Y. *Macromolecules* **2006,** 39, (3), 1199-1208.

187. Jain, S.; Bates, F. S. *Science* **2003,** 300, (5618), 460-464.

188. Fu, S.-Y.; Feng, X.-Q.; Lauke, B.; Mai, Y.-W. *Composites Part B: Engineering* **2008,** 39, (6), 933-961.

189. Gkikas, G.; Barkoula, N.-M.; Paipetis, A. *Composites Part B: Engineering* **2012,** 43, (6), 2697-2705.

190. Spitalsky, Z.; Tasis, D.; Papagelis, K.; Galiotis, C. *Progress in polymer science* **2010,** 35, (3), 357-401.

191. Byrne, M. T.; Gun'ko, Y. K. *Advanced Materials* **2010,** 22, (15), 1672-1688.

192. Qi, B.; Zhang, Q.; Bannister, M.; Mai, Y.-W. *Composite structures* **2006,** 75, (1), 514-519.

193. Wang, K.; Chen, L.; Wu, J.; Toh, M. L.; He, C.; Yee, A. F. *Macromolecules* **2005,** 38, (3), 788-800.

194. Liu, W.; Hoa, S. V.; Pugh, M. *Composites Science and Technology* **2005,** 65, (15), 2364-2373.

195. Rafiee, M. A.; Rafiee, J.; Wang, Z.; Song, H.; Yu, Z.-Z.; Koratkar, N. *ACS nano* **2009,** 3, (12), 3884-3890.

196. Tang, L.-C.; Wan, Y.-J.; Yan, D.; Pei, Y.-B.; Zhao, L.; Li, Y.-B.; Wu, L.-B.; Jiang, J.-X.; Lai, G.-Q. *Carbon* **2013,** 60, 16-27.

197. Zaman, I.; Phan, T. T.; Kuan, H.-C.; Meng, Q.; La, L. T. B.; Luong, L.; Youssf, O.; Ma, J. *Polymer* **2011,** 52, (7), 1603-1611.

198. Chandrasekaran, S.; Sato, N.; Tölle, F.; Mülhaupt, R.; Fiedler, B.; Schulte, K. *Composites Science and Technology* **2014,** 97, 90-99.

199. Marouf, B. T.; Mai, Y.-W.; Bagheri, R.; Pearson, R. A. *Polymer Reviews* **2016,** 56, (1), 70-112.

200. Rafiee, M. A.; Rafiee, J.; Srivastava, I.; Wang, Z.; Song, H.; Yu, Z. Z.; Koratkar, N. *Small* **2010,** 6, (2), 179-183.

201. Lee, C.; Wei, X.; Kysar, J. W.; Hone, J. *Science* **2008,** 321, (5887), 385-388.

202. Lerf, A.; He, H.; Riedl, T.; Forster, M.; Klinowski, J. *Solid State Ionics* **1997,** 101–103, Part 2, 857-862.

203. Lerf, A.; He, H.; Forster, M.; Klinowski, J. *The Journal of Physical Chemistry B* **1998,** 102, (23), 4477-4482.

204. Yang, H.; Shan, C.; Li, F.; Zhang, Q.; Han, D.; Niu, L. *Journal of Materials Chemistry* **2009,** 19, (46), 8856-8860.

205. Fang, M.; Zhang, Z.; Li, J.; Zhang, H.; Lu, H.; Yang, Y. *Journal of Materials Chemistry* **2010,** 20, (43), 9635-9643.

206. Park, Y. T.; Qian, Y.; Chan, C.; Suh, T.; Nejhad, M. G.; Macosko, C. W.; Stein, A. *Advanced Functional Materials* **2015,** 25, (4), 575-585.

207. Ye, Z.; Lito, P.; Hu, L.; Efremov, M. Y.; Allen, L. H. *Thermochimica Acta* **2015,** 603, 69-78.

208. Li, Z.; Young, R. J.; Wang, R.; Yang, F.; Hao, L.; Jiao, W.; Liu, W. *Polymer* **2013,** 54, (21), 5821-5829.

209. Li, Z.; Wang, R.; Young, R. J.; Deng, L.; Yang, F.; Hao, L.; Jiao, W.; Liu, W. *Polymer* **2013,** 54, (23), 6437-6446.

210. Kim, H.; Abdala, A. A.; Macosko, C. W. *Macromolecules* **2010,** 43, (16), 6515-6530.

211. Kinloch, A.; Mohammed, R.; Taylor, A.; Eger, C.; Sprenger, S.; Egan, D. *Journal of Materials Science* **2005,** 40, (18), 5083-5086.

212. Sprenger, S. *Polymer* **2013,** 54, (18), 4790-4797.

213. Shayegan, M.; Bagheri, R. *International Journal of Nanomanufacturing* **2010,** 5, (3-4), 232-244.

214. Liang, Y.; Pearson, R. *Polymer* **2010,** 51, (21), 4880-4890.

215. Labak, A. Fracture Behavior of Silica-and Rubber-Nanoparticle-Toughed Epoxies. Dissertation, 2015.

216. Johnsen, B.; Kinloch, A.; Mohammed, R.; Taylor, A.; Sprenger, S. *Polymer* **2007,** 48, (2), 530-541.

217. Liu, H.-Y.; Wang, G.-T.; Mai, Y.-W.; Zeng, Y. *Composites Part B: Engineering* **2011,** 42, (8), 2170-2175.

218. Hsieh, T.; Kinloch, A.; Masania, K.; Lee, J. S.; Taylor, A.; Sprenger, S. *Journal of materials science* **2010,** 45, (5), 1193-1210.

219. Marouf, B.; Pearson, R.; Bagheri, R. *Materials Science and Engineering: A* **2009,** 515, (1), 49-58.

220. Fröhlich, J.; Thomann, R.; Gryshchuk, O.; Karger‐Kocsis, J.; Mülhaupt, R. *Journal of Applied Polymer Science* **2004,** 92, (5), 3088-3096.

221. Fröhlich, J.; Thomann, R.; Mülhaupt, R. *Macromolecules* **2003,** 36, (19), 7205-7211.

222. Liu, W.; Hoa, S. V.; Pugh, M. *Polymer Engineering & Science* **2004,** 44, (6), 1178-1186.

223. Wang, F.; Drzal, L. T.; Qin, Y.; Huang, Z. *Composites Part A: Applied Science and Manufacturing* **2016,** 87, 10-22.

224. Vallés, C.; Beckert, F.; Burk, L.; Mülhaupt, R.; Young, R. J.; Kinloch, I. A. *Journal of Polymer Science Part B: Polymer Physics* **2016,** 54, (2), 281-291.

225. Banks, L.; Ellis, B. *Polymer* **1982,** 23, (10), 1466-1472.

226. Vakil, U.; Martin, G. *Journal of materials science* **1993,** 28, (16), 4442-4450.

227. Thompson, Z. J. Block Copolymer Modified Epoxies: Role of Epoxy Crosslink Density. University of Minnesota, Minneapolis, MN, 2010.

228. Becker, W.; Lampman, S. *Materials Park, OH: ASM International, 2002.* **2002**, 559-586.

229. Kitagawa, H.; Yuuki, R.; Ohira, T. *Engineering Fracture Mechanics* **1975,** 7, (3), 515-529.

230. Maazouz, A.; Sautereau, H.; Gerard, J. *Journal of applied polymer science* **1993,** 50, (4), 615-626.

231. Adachi, T.; Osaki, M.; Araki, W.; Kwon, S. C. *Acta Materialia* **2008,** 56, (9), 2101-2109.

232. Liang, Y.-L., *The toughening mechanisms in epoxy-silica nanocomposites and hybrid epoxy-silica-rubber nanocomposites*. ProQuest: 2008.

233. Wang, S.; Tambraparni, M.; Qiu, J.; Tipton, J.; Dean, D. *Macromolecules* **2009,** 42, (14), 5251-5255.

234. Bortz, D. R.; Heras, E. G.; Martin-Gullon, I. *Macromolecules* **2011,** 45, (1), 238-245.

235. Stankovich, S.; Dikin, D. A.; Dommett, G. H.; Kohlhaas, K. M.; Zimney, E. J.; Stach, E. A.; Piner, R. D.; Nguyen, S. T.; Ruoff, R. S. *Nature* **2006,** 442, (7100), 282-286.

236. Zhang, H.; Bao, Q.; Tang, D.; Zhao, L.; Loh, K. *Applied Physics Letters* **2009,** 95, (14), 141103.

237. de la Rama, L. P.; Hu, L.; Ye, Z.; Efremov, M. Y.; Allen, L. H. *Journal of the American Chemical Society* **2013,** 135, (38), 14286-14298.

238. Song, W.-L.; Cao, M.-S.; Lu, M.-M.; Bi, S.; Wang, C.-Y.; Liu, J.; Yuan, J.; Fan, L.-Z. *Carbon* **2014,** 66, 67-76.

239. Grijpma, D. W.; Pennings, A. J. *Macromolecular Chemistry and Physics* **1994,** 195, (5), 1649-1663.

240. Hiljanen‐Vainio, M.; Karjalainen, T.; Seppälä, J. *Journal of applied polymer science* **1996,** 59, (8), 1281-1288.

241. Jing, F.; Hillmyer, M. A. *Journal of the American Chemical Society* **2008,** 130, (42), 13826-13827.

242. Theryo, G.; Jing, F.; Pitet, L. M.; Hillmyer, M. A. *Macromolecules* **2010,** 43, (18), 7394-7397.

243. Habersberger, B. M.; Gillard, T. M.; Hickey, R. J.; Lodge, T. P.; Bates, F. S. *ACS Macro Letters* **2014,** 3, (10), 1041-1045.

244. Tsuji, H.; Smith, R.; Bonfield, W.; Ikada, Y. *Journal of applied polymer science* **2000,** 75, (5), 629-637.

245. Lin, J.-H.; Woo, E. M. *Polymer* **2006,** 47, (19), 6826-6835.

246. Nijenhuis, A.; Colstee, E.; Grijpma, D.; Pennings, A. *Polymer* **1996,** 37, (26), 5849-5857.

247. Lai, W.-C.; Liau, W.-B.; Lin, T.-T. *Polymer* **2004,** 45, (9), 3073-3080.

248. Huang, C. I.; Tsai, S. H.; Chen, C. M. *Journal of Polymer Science Part B: Polymer Physics* **2006,** 44, (17), 2438-2448.

249. Yang, J.; Liang, Y.; Luo, J.; Zhao, C.; Han, C. C. *Macromolecules* **2012,** 45, (10), 4254-4261.

250. W. Heckmann, G. E. M., F. Ramsteiner, Structure-property relationships in rubber modified amorphous thermoplastic polymers. In *Mechanical Properties of Polymers Based on Nano-Structure and Morphology*, F. J. Balta-Calleja, G. H. M., Ed. Taylor and Francis: London, 2005; pp 429-479.

251. Hentze, H.-P.; Antonietti, M. *Reviews in molecular biotechnology* **2002,** 90, (1), 27-53.

252. Cooper, A. I. *Advanced Materials* **2003,** 15, (13), 1049-1059.

253. Su, H.; Song, F.; Dong, Q.; Li, T.; Zhang, X.; Zhang, D. *Applied Physics A: Materials Science & Processing* **2011,** 104, (1), 269-274.

254. Singh, A. N.; Thakre, R. D.; More, J. C.; Sharma, P. K.; Agrawal, Y. *Polymer-Plastics Technology and Engineering* **2015,** 54, (10), 1077-1095.

255. Zhang, J.; Li, T.; Mannion, A. M.; Schneiderman, D. K.; Hillmyer, M. A.; Bates, F. S. *ACS Macro Letters* **2016,** 5, (3), 407-412.

256. Noshay, A.; McGrath, J. E., *Block copolymers: overview and critical survey*. Elsevier: 2013.

257. Sarkar, B.; Alexandridis, P. *Progress in Polymer Science* **2015,** 40, 33-62.

258. Amiel, C.; Sikka, M.; Schneider Jr, J. W.; Tsao, Y.-H.; Tirrell, M.; Mays, J. W. *Macromolecules* **1995,** 28, (9), 3125-3134.

259. Kim, S.-R.; Nairn, J. A. *Engineering Fracture Mechanics* **2000,** 65, (5), 573-593.

260. Kim, S.-R.; Nairn, J. A. *Engineering fracture mechanics* **2000,** 65, (5), 595-607.

261. Goertz, M. P.; Marks, L. E.; Montano, G. A. *ACS nano* **2012,** 6, (2), 1532-1540.

262. Chen, X. C.; Yang, H.; Green, P. F. *Macromolecules* **2011,** 44, (14), 5758-5763.

263. Roche, A.; Bouchet, J.; Bentadjine, S. *International Journal of adhesion and Adhesives* **2002,** 22, (6), 431-441.

264. Possart, W.; Krüger, J. K.; Wehlack, C.; Müller, U.; Petersen, C.; Bactavatchalou, R.; Meiser, A. *Comptes Rendus Chimie* **2006,** 9, (1), 60-79.

265. Mersier, A. W., C.; Possart, W., In *Chemical processes during aging in ultra-thin epoxy films on metals*, Wiley-VCH Verlag GmbH & Co. KGaA: 2005; pp 445-463.

266. Bouchet, J.; Roche, A.-A. *The Journal of Adhesion* **2002,** 78, (9), 799-830.

267. Dietz, M.; Tietz, H.-D. *Journal of Materials Science* **1990,** 25, (8), 3731-3738.

268. Li, X.; Bhushan, B. *Materials characterization* **2002,** 48, (1), 11-36.

269. Zhang, S.; Sun, D.; Fu, Y.; Du, H. *Surface and Coatings Technology* **2005,** 198, (1), 74-84.

270. Zhang, S.; Zhang, X. *Thin Solid Films* **2012,** 520, (7), 2375-2389.

271. Xia, Z.; Curtin, W.; Sheldon, B. *Acta materialia* **2004,** 52, (12), 3507-3517.

272. Wang, C.; Shi, K.; Gross, C.; Pureza, J. M.; de Mesquita Lacerda, M.; Chung, Y.-W. *Surface and Coatings Technology* **2014,** 257, 206-212.

273. Winey, K. I.; Thomas, E. L.; Fetters, L. J. *The Journal of chemical physics* **1991,** 95, (12), 9367-9375.

274. Pavlopoulou, E.; Anastasiadis, S.; Kortright, J.; Bras, W.; Portale, G. IOP Conference Series: Materials Science and Engineering, 2010; IOP Publishing: 2010.

275. De Gennes, P.-G., *Scaling concepts in polymer physics*. Cornell university press: 1979.

276. Ito, H.; Russell, T.; Wignall, G. *Macromolecules* **1987,** 20, (9), 2213-2220.

277. Schindler, A.; Harper, D. *Journal of Polymer Science: Polymer Chemistry Edition* **1979,** 17, (8), 2593-2599.

278. Ukielski, R. *Polymer* **2000,** 41, (5), 1893-1904.

279. Hadjichristidis, N.; Xenidou, M.; Iatrou, H.; Pitsikalis, M.; Poulos, Y.; Avgeropoulos, A.; Sioula, S.; Paraskeva, S.; Velis, G.; Lohse, D. J. *Macromolecules* **2000,** 33, (7), 2424-2436.

280. Mannion, A. M.; Bates, F. S.; Macosko, C. W. *Macromolecules* **2016**.

281. Lin, Y.; Wang, Y.; Zheng, J.; Yao, K.; Tan, H.; Wang, Y.; Tang, T.; Xu, D. *Macromolecules* **2015,** 48, (20), 7640-7648.

282. Liang, Y.; Pearson, R. *Polymer* **2009,** 50, (20), 4895-4905.

283. Lee, J.; Yee, A. *Polymer* **2000,** 41, (23), 8375-8385.

284. Zhang, J.; Deng, S.; Wang, Y.; Ye, L. *Composites Part A: Applied Science and Manufacturing* **2016**, 80, 82-94.

Appendix A

Toughening poly(lactide) thermoplastics with sustainable block copolymer modifiers

A.1 Introduction

In Chapter 6, we have established the strategy of toughening glassy poly(lactide) thermoplastics through dispersing block copolymer modifiers in the homopolymer matrix as small micellar like structures. The work presented in this chapter still follows the same toughening strategy but the goal is to design fully sustainable block copolymer modifiers. The diblock copolymers being used in Chapter 6, poly(ethylene oxide)-*b*-poly(butylene oxide) (PEO-PBO) and poly(L-lactide)-*b*-poly(butylene oxide) (PLLA-PBO) are endowed with the rubbery PBO block as the matrix-phobic block. Although PBO can effectively afford significant toughness enhancement via cavitation, it is not bioderived or biodegradable. Recently, Xiong et al.[1] reported a total biosynthetic route to produce the branched lactone, β-methyl-δ-valerolactone (MVL). This compound, based on the functional group contribution (see Chapter 4, Section 4.4.1 for more details), is estimated

to have a solubility parameter δ close to that of the butylene oxide (BO) compound, which means poly(β-methyl-δ-valerolactone) (PMVL) and PBO would show similar thermodynamic characteristics. Additionally, PMVL has a glass transition temperature (T_g) of around −60 ℃ close to the T_g of PBO. Therefore, PMVL can be a good candidate to replace PBO as the matrix-phobic block in diblock copolymer modifiers to toughen poly(lactide) thermoplastics. More importantly, this new poly(ethylene oxide)-*b*-poly(β-methyl-δ-valerolactone) (PEO-PMVL) diblock is fully biodegradable and sustainable. Inspired by this idea, we synthesized two distinct PEO-PMVL diblock copolymers with different molecular weights but similar composition (40% PEO by volume). Then, we incorporated them into the glassy poly(L-lactide) (PLLA) homopolymer matrix following similar experimental procedures as employed in Chapter 6. The microstructure, thermal and mechanical properties of resultant polymer blends were evaluated to reflect the toughening efficacy of this new type of PLA modifier.

A.2 Experimental

A.2.1 Materials

The chemical structures of the poly(L-lactide) (PLLA) homopolymer and poly(ethylene oxide)-*b*-poly(β-methyl-δ-valerolactone) (PEO-PMVL) diblock copolymer used in this chapter are presented in Figure A.1. The plastic matrix is PLLA

homopolymer (NatureWorks under the tradename Ingeo 2003D), same as the one used in Chapter 6.

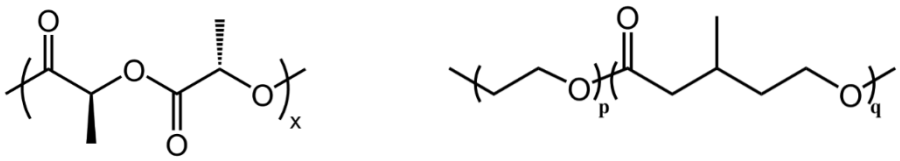

Poly(*L*-lactide) Poly(ethylene oxide)-b-poly(β-methyl-δ-valerolactone)

Figure A.1 Chemical structures of the homopolymer and block copolymer modifier.

Table A.1 summarizes the molecular characteristics of the homopolymer and block copolymer modifiers. Two distinct PEO-PMVL diblock copolymers identified as EMV-1 and EMV-2 were synthesized at fixed composition (40 ± 1% by volume PEO) but different total molecular weights. Ideally, both diblocks would form micelles in the PLLA matrix with a rubbery and compliant PMVL core and the PLLA-philic PEO block as the corona.

Appendix A

Table A.1 Molecular characteristics of the homopolymer and block copolymers.

[a]Sample ID	[b]M_n (kg/mol)	[c]f_{PEO} (%)	[d]w_{PEO} (%)	[e]M_w/M_n
PLLA	112	--	--	1.88
EMV-1	5.0	41	40	1.10
EMV-2	13.0	39	38	1.08

[a]PLLA = poly(L-lactide); EMV = poly(ethylene oxide)-*b*-poly(β-methyl-δ-valerolactone) (PEO-PMVL).
[b]Number average molecular weight determined by ^{1}H NMR end group analysis for the diblocks.
[c]Volume fraction of the PEO block calculated using densities ρ_{PEO} = 1.07 g/cm^3, and ρ_{PMVL} = 1.10 g/cm^3.[1,2]
[d]Weight fraction of the PEO block, calculated based on ^{1}H NMR results.
[e]Dispersity and M_n for PLLA were determined using gel permeation chromatography (GPC) at 30 ℃ with THF as the mobile phase and calibrated with poly(styrene) standards.

A.2.2 Block copolymer synthesis

Poly(ethylene oxide)-*b*-poly(β-methyl-δ-valerolactone) (PEO-*b*-PMVL) block copolymers with different molecular weights were synthesized using a similar method. For example, EMV-2 was synthesized by ring-opening transesterification polymerization (ROTEP). PEO (0.5 g, 0.25 mmol, M_n = 2k, hydroxyl group as one end group) was first charged into a pressure flask and then dried overnight under vacuum line. The pressure flask was then transferred into glove box. Diphenyl phosphate (25 mg, 0.1 mmol) and β-methyl-δ-valerolactone (MVL, 2.3 g, 20.1 mmol) were then charged into the flask. The mixture was stirred under room temperature for 5 hours and then was precipitated in water to remove unreacted monomers. Solids were collected and dried under vacuum.

A.2 Micelle morphology

Representative transmission electron microscopy (TEM) images of block copolymer modified PLLA are presented in Figure A.2a-d. EMV-1 completely dissolves in the PLLA matrix, showing a homogenous phase as evidenced in the high and low magnification micrographs (Figure A.2a and c). This is probably due to the fact that EMV-1 has a very short PMVL block, leading to a weak expulsion with the PLLA homopolymer. Consequently, the entire EMV-1 diblock is not able to effectively segregate out from the PLLA matrix. Increasing the diblock copolymer molecular weight can raise the segregation strength. Therefore, EMV-2 can generate small cylindrical micelles (PBO core diameter < 30 nm, evidenced in the higher magnification Figure A.2d) randomly and uniformly distributed throughout the PLLA matrix as shown in the lower magnification Figure A.2b. Both blends with EMV-1 and EMV-2 retain optical clarity similar to neat amorphous PLLA.

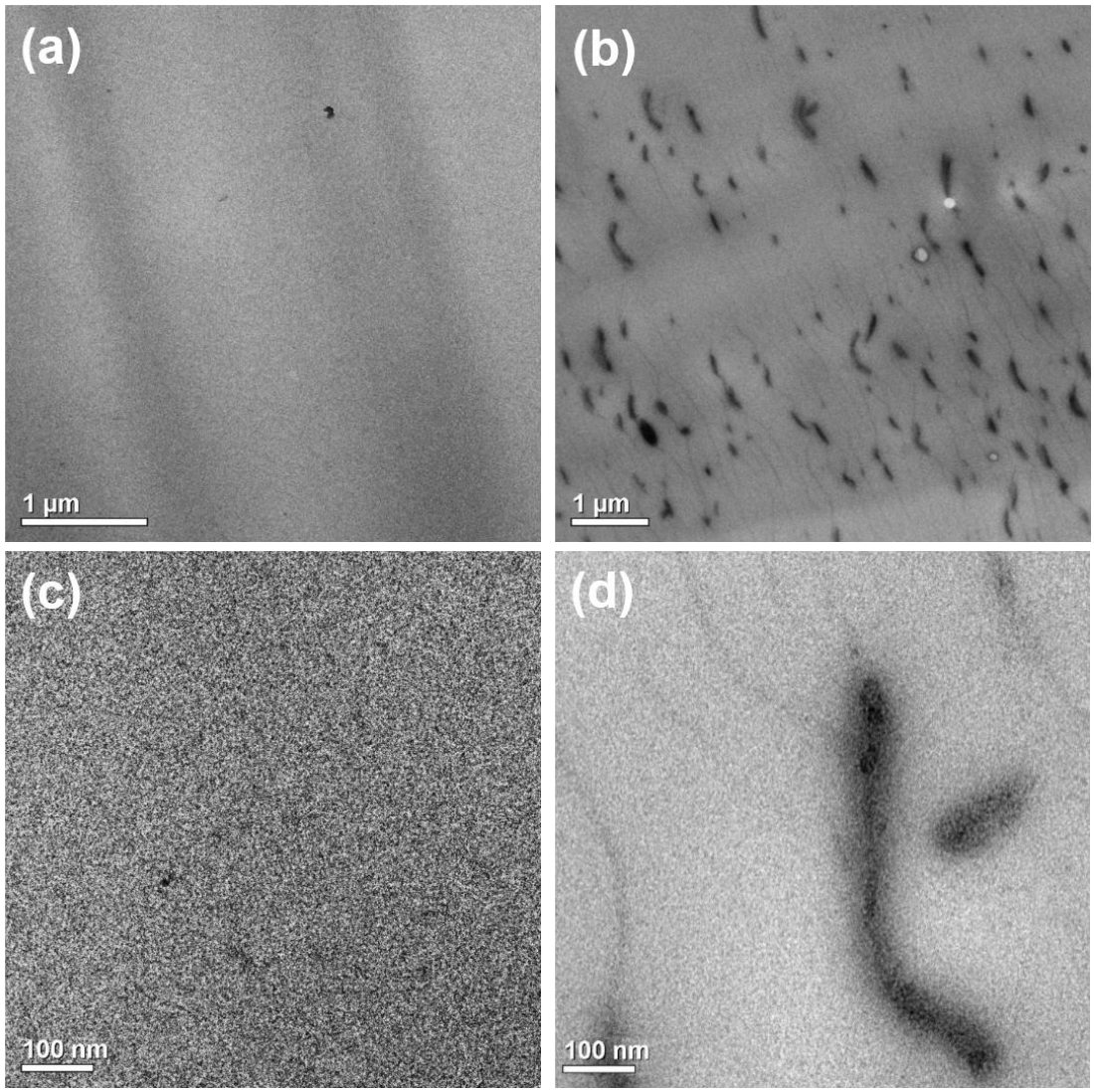

Figure A.2 Representative TEM images of block copolymer/PLLA blends containing 5 wt.% of (a, c) EMV-1 and (b, d) EMV-2. Micrographs (a and b) are at lower magnification, and (c and d) are at higher magnification. Scale bars are presented in each micrograph. RuO_4, used as a contrast agent, preferentially stains the PEO/PLLA interface.

Appendix A

A.3 Thermal and mechanical properties of modified blends

The thermal properties of the PLLA blends, determined by DSC, are summarized in Figure A.3 and Table A.2. The glass transition temperature (T_g) of PLLA in both blends containing 5 wt.% diblocks was significantly reduced due to the plasticization effect of an amorphous PEO block. This effect was more evident in the EMV-1/PLLA blend. Unlike the results presented in Chapter 6, herein PEO crystallization was not observed, since the PEO block in EMV-1 and EMV-2 is relatively short. Upon reheating the glassy PLLA crystallized (T_c > 100 ℃) followed by melting (140 ℃ < T_m < 150 ℃). The crystallization temperature (T_c) of PLLA in both blends was also remarkably decreased resulted from the PEO plasticization. For each of the EMV/PLLA blends the melting transition (T_m) was split into two distinct peaks with one higher and one lower than the melting point of neat PLLA. We attribute this phenomenon to the influence of PEO on the mechanism of PLLA crystallization, which causes the formation of two different types of crystallized domains in the matrix. It is consistent with the observation of EB/PLLA blends presented in Chapter 6.

Appendix A

Table A.2 Summary of thermal properties of block copolymer/PLLA blends.

[a]Blend	[b]$T_{g,PLLA}$ (℃)	[c]$T_{c,PLLA}$ (℃)	[d]$T_{m,PLLA}$ (℃)	
Neat	60 ±1	103 ±3	149 ±1	
EMV-1	44 ±2	84 ±3	141 ±2	148 ±1
EMV-2	53 ±1	94 ±4	145 ±2	151 ±2

[a]The concentration of modifiers is 5 wt.% in all cases.
[b]Glass transition, crystallization and melting temperatures were determined using DSC on the second heating ramp at a rate of 10 ℃/min.
[c]The onset of the exothermic crystallization peak was taken as the crystallization temperature of PLLA.
[d]The apex of the endothermic melting peak was taken as the melting temperature of PLLA.

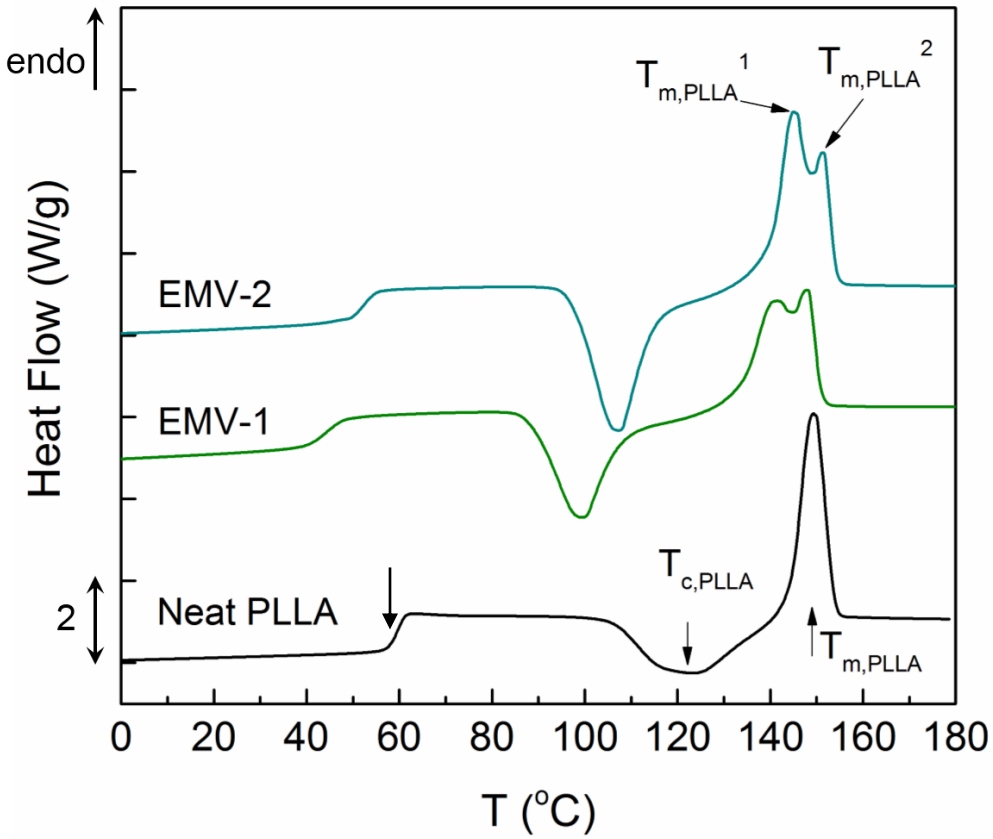

Figure A.3 DSC traces (endo up) of neat PLLA and modified blends containing 5 wt.% diblock copolymers obtained during a second heating. Arrows denote the glass transition temperature, crystallization and melting peak of PLLA. Curves were shifted vertically for clarity.

Appendix A

The microstructure of the modified blends critically affects the tensile properties of these glassy materials. Representative engineering stress *versus* strain curves are presented in Figure A.4 and the associated yield strength (σ_y), elastic modulus (E), strain at break (ε_b) and toughness are summarized in Table A.3. The blend modified with 5 wt.% of EMV-1 exhibited similar toughness and ductility to that of the neat PLLA, but caused a more than 20% drop in σ_y. This phenomenon is as expected, since EMV-1 does not form any microstructures in the PLLA matrix. On the other hand, the blend prepared using EMV-2 exhibited an impressive enhancement relative to neat PLLA with a 1100% increase in tensile toughness and a 1000% increase in ε_b. We also observed evident whitening in the stretched specimens containing EMV-2. We believe the short cylindrical micelle structure formed by EMV-2 contributes to this improvement in the mechanical performance, probably following a similar toughening mechanism as discussed in Chapter 6, i.e., concurrent cavitation, crazing and shear yielding.

Table A.3 Summary of mechanical properties of block copolymer/PLLA blends.

[a]Blend	[b]σ_y (MPa)	[b]E (GPa)	[b]ε_b (%)	[c]Toughness (MJ/m^3)
Neat	52 ± 3	2.3 ± 0.1	7 ± 2	2 ± 1
EMV-1	40 ± 3	2.0 ± 0.2	8 ± 3	1 ± 1
EMV-2	43 ± 2	2.2 ± 0.2	78 ± 8	24 ± 2

[a]The concentration of modifiers is 5 wt.% in all cases.
[b]Yield strength (σ_y), tensile modulus (E), and strain at break (ε_b) were determined using a uniaxial tensile test with a crosshead velocity of 5 mm/min. Tensile modulus was quantified by fitting the linear elastic region of each curve before the yield point.
[c]Tensile toughness was determined by the integrated area under engineering stress-strain curve up to the breaking point.

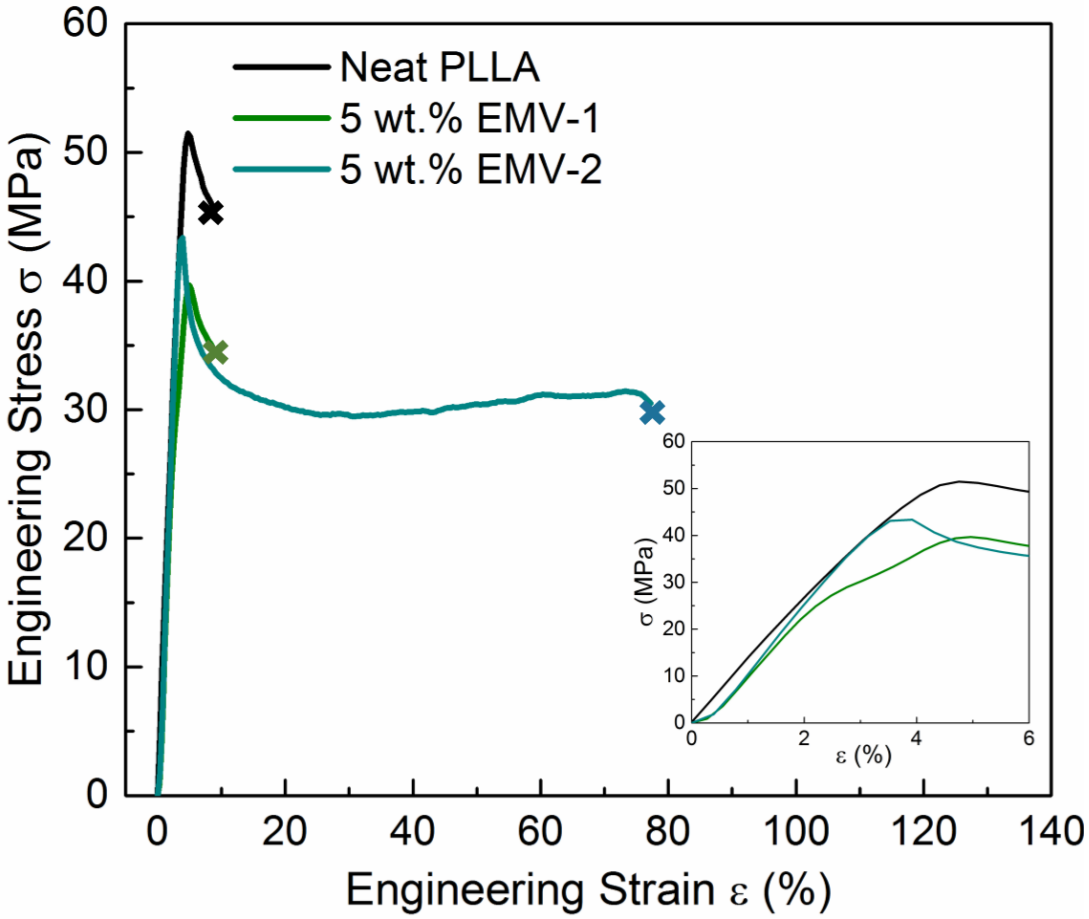

Figure A.4 Representative engineering stress *versus* strain data from tensile tests. The block copolymer loading is 5 wt.% in both blends. Inset shows the linear elastic region of each curve.

The effect of modifier concentration on mechanical performances was explored using blends containing EMV-2. As shown in Figure A.5, the tensile behavior of blends was strongly influenced by the loading of EMV-2. At loadings lower than 2.5 wt.%, there was little toughening effect observed in polymer blends. Addition of 5 and 10 wt.% EMV-2 effectively increased the tensile toughness to more than 11 times that of the neat

PLLA, but also led to a nearly 20% drop in the yield strength of blends. Additionally, EMV-2 did not significantly decrease the Young's modulus, regardless of the loading.

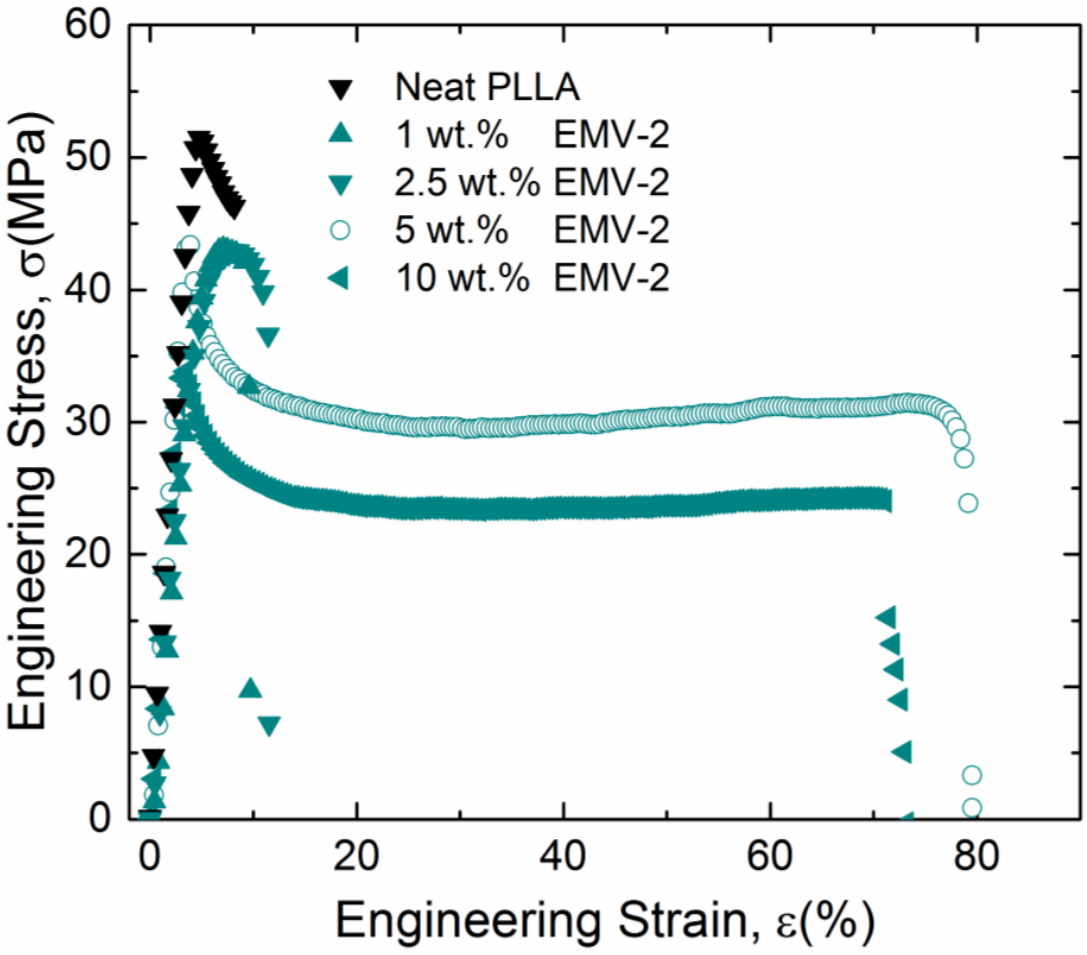

Figure A.5 Representative engineering stress *versus* strain data from tensile tests of PLLA/EMV-2 blends. The modifier loading is from 1 to 10 wt.%.

A.4 Rheological behavior of modified blends

Figure A.6 presents the influence of added EMV-2 modifier on the melt rheological behavior of PLLA, and emphasis has been put on the study of complex viscosity. It is clear that addition of only 5 wt.% EMV-2 can result in a viscosity decrease, and this effect is more evident at low shear rates. The zero shear viscosity of EMV-2/PLLA blends is about 30% lower than that of neat PLLA melt. As a comparison, the data from Chapter 6 showing the melt viscosity of EB-1/PLLA blends is also displayed here (red circle). The viscosity decreasing effect is more pronounced in the EB-1/PLLA blend compared to the EMV-2/PLLA blend. We postulate that this difference may be attributed to the discrepancy in the micelle shape and dimension between these two blend systems. More in-depth investigations will be pursued in the future.

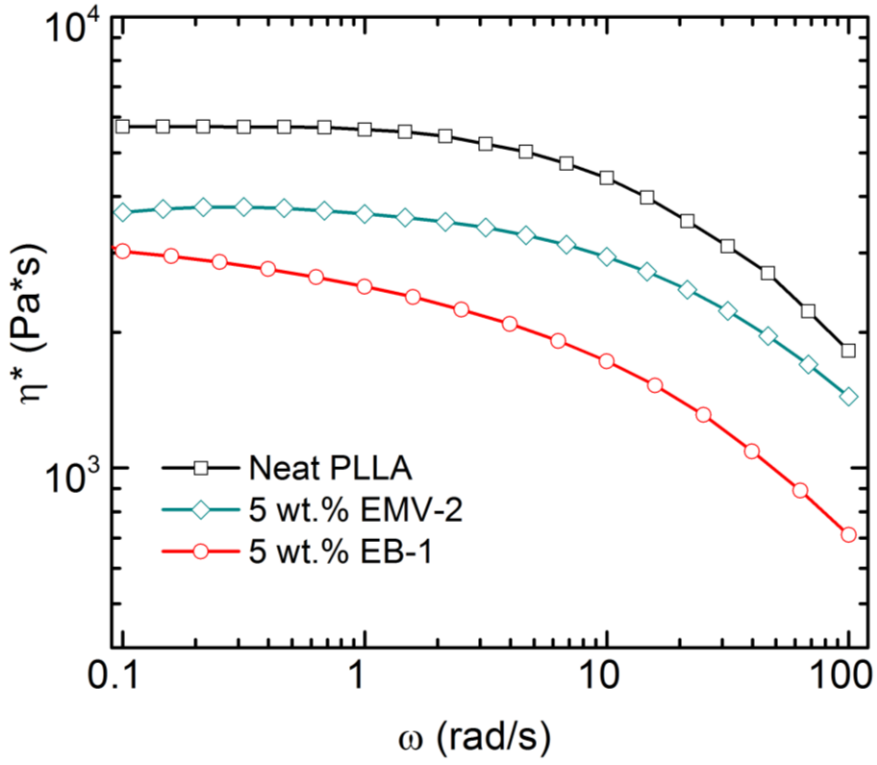

Figure A.6 Effect of added EMV-2 block copolymer on PLLA melt rheology: complex viscosity (η^*) determined at 170 ℃. The EB-1 data is from Chapter 6.

A.5 References

1. Xiong, M.; Schneiderman, D. K.; Bates, F. S.; Hillmyer, M. A.; Zhang, K. *Proceedings of the National Academy of Sciences* **2014,** 111, (23), 8357-8362.
2. Li, T.; Heinzer, M. J.; Francis, L. F.; Bates, F. S. *Journal of Polymer Science Part B: Polymer Physics* **2016,** 54, (2), 189-204.

Appendix B

Supporting Information for Chapter 4

Figure B1 summarizes the influences from processing variables on the block copolymer morphology in cured resins. Here we explored the consequences of eight different combinations of three formulation and processing variables as listed in Table 4.2 and 4.6: (*i*) the choice of hardener batch, pure C541 *versus* C541 with DMP-30; (*ii*) the stoichiometry of the reactive hydrogen from C541 to the epoxide group from DGEBA, 1:1 *versus* 2:3; (*iii*) the curing protocol, Protocol A (25 ℃ for 24h, 50 ℃ for 24h) *versus* Protocol B (60 ℃ for 8h). A single modifier EB-2 was used and kept at a 5 wt.% of loading in all cases. Figure B1 'Route A' and "Control-A1 to A3' all show many macrophase separated domains, while Figure 'Route B' and 'Control-B1 to B3' display either dispersed or aggregated wormlike micelles. It suggests that the mixing thermodynamics determines the phase structure in cured resins, since 'Route A' and 'Control-A1 to A3' uses the 1:1 stoichiometry and 'Route B' and 'Control-B1 to B3' uses the 2:3 stoichiometry. For processing variable (*ii*), the 2:3 stoichiometry is preferred for

the micelle formation. Figure B1 ‘Route B’ and ‘Control-B1’ show well-defined and dispersed wormlike micelles, while Figure ‘Control-B2 and B3’ display many large aggregated block copolymer domains. The former two are cured at elevated temperature with curing Protocol B, but the latter two are with Protocol A. It suggests that curing temperature also controls the final morphology, and for processing variable (*iii*), an elevated curing temperature is preferred. Figure B1 ‘Route B’ that contains DMP-30 shows branched wormlike micelles, while Figure ‘Control-B1’ displays more randomly dispersed cylindrical micelles. It indicates that the addition of DMP-30 to some extent affects micelle morphology as well. For processing variable (*i*), the addition of DMP-30 is preferred for a fast curing rate and maintaining the curing extent (Table 4.6). In a nutshell, the processing ‘Route B’ in Table 4.2 combines the optimized selections for all three variables.

Appendix B

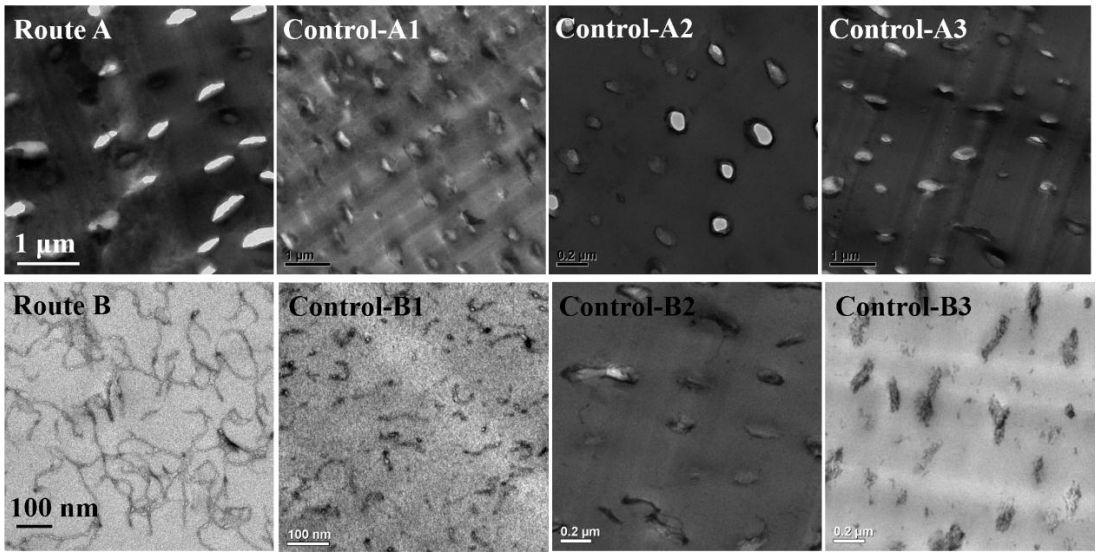

Figure B1 Representative TEM images of control samples for Route A and B in Table 4.2. All samples were loaded with 5 wt.% of EB-2. Sample identification and detailed information on processing variables are summarized in Table 4.6.

Figure B2 summarizes the morphological consequences of different curing temperatures while maintaining all the other processing variables as Route B (Table 4.2). All samples were loaded with 5 wt.% of EB-2 that has a PEO melting point at around 48 ℃. In all cases, wormlike micelles can be observed, but those nanoscale micelles start to aggregate and form submicron-sized domains as the curing temperature goes below $T_{m,\,PEO}$. It suggests that the PEO crystallization is mainly influenced by the curing temperature and it severely affects the final structure in cured resins.

Appendix B

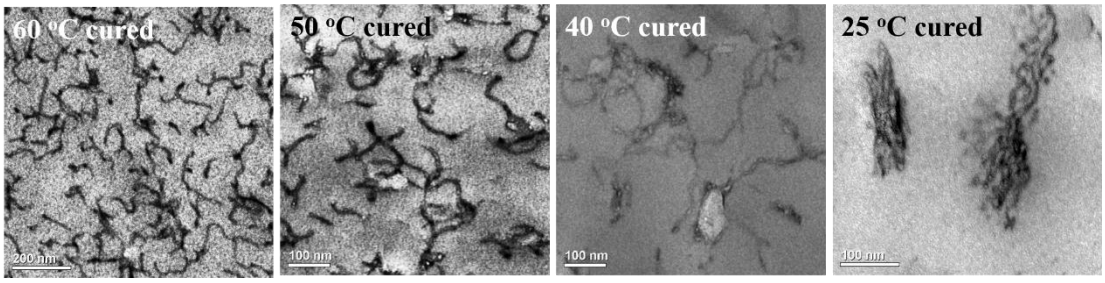

Figure B2 Representative TEM images showing the influences from curing temperatures on block copolymer morphology in cured resins. All samples were prepared via Route B (Table 4.2) except for the curing temperature. In all cases, the modifier is 5 wt.% of EB-2.

The peak positions in Figure B3 agree with some lamellar microstructures, and the principle peak position q^* just slightly shifts to lower q with increasing molecular weight suggesting that PEO crystallization dictates the periodic structure. This confirms the scattering patterns shown in Figure 4.4b. Higher order scattering peaks are not obvious in the EB-4 trace. It is probably due to the poor mobility of the chains associated with their high molecular weight, inhibiting their ability to rearrange themselves for a long-term periodic structure.

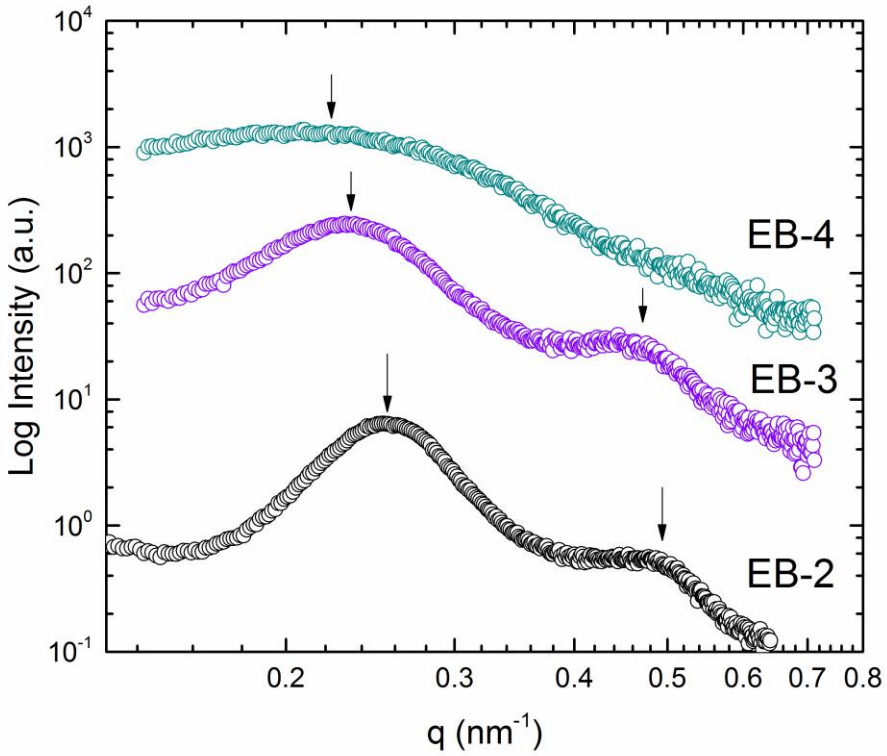

Figure B3 1D SAXS profiles of pure EB diblock copolymers at room temperature (EB-2 to EB-4, from bottom to top). Arrows denote the scattering peak positions. Curves were shifted vertically for clarity.

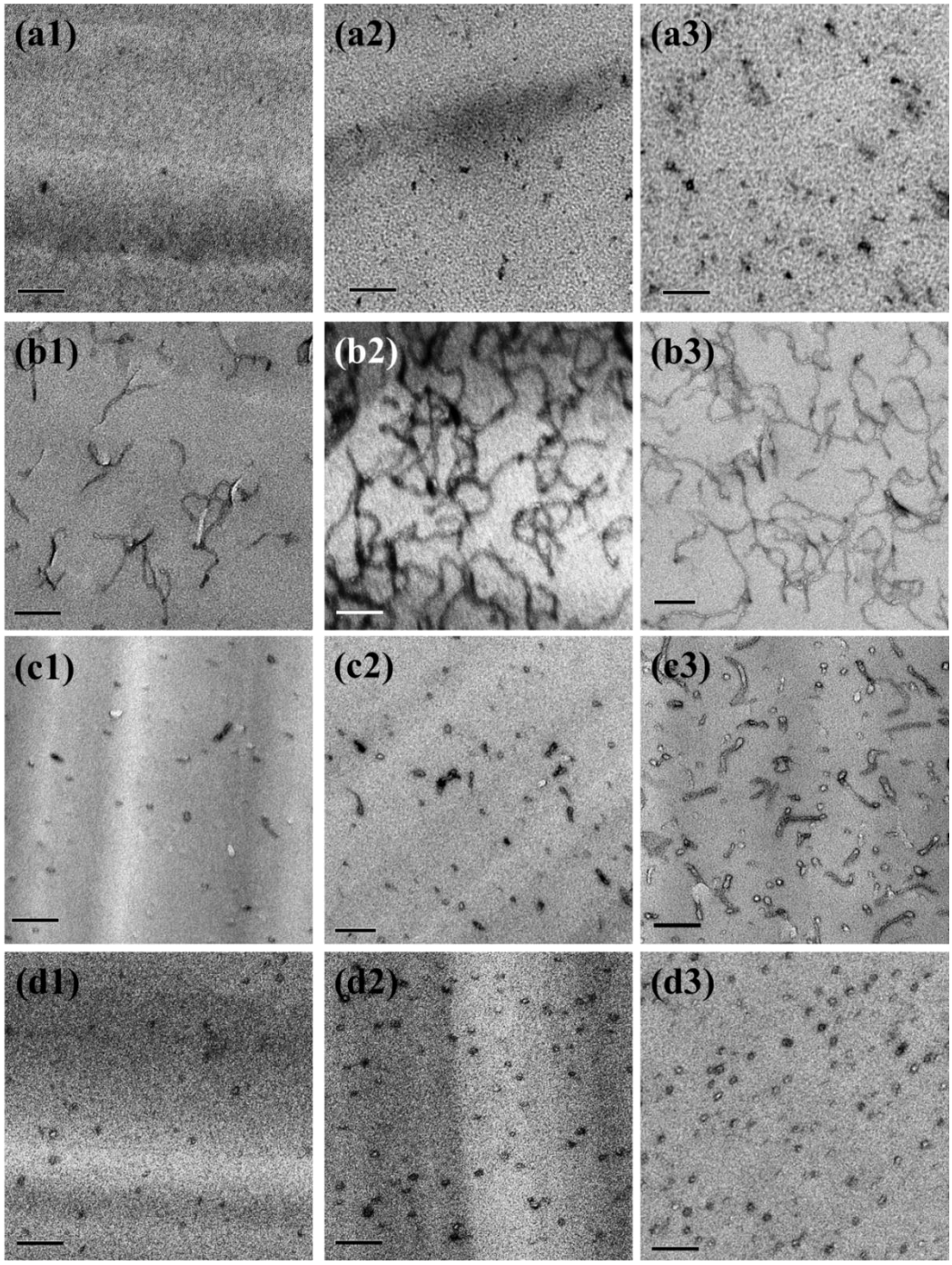

Figure B4 Representative TEM images of cured bulk epoxy resins containing (a1 – a3) EB-1, (b1 – b3) EB-2, (c1 – c3) EB-3, and (d1 – d3) EB-4. The block copolymer concentration is 1.5 wt.% for (a – d1), 2.5 wt.% for (a – d2) and 5 wt.% for (a – d3). RuO_4, used as a contrast agent, preferentially stains the PEO/epoxy interface, making relatively brighter PBO cores with darker PEO coronas. Scale bars represent 100 nm.

Appendix B

Table B1 Fracture toughness K_{Ic} (in MPa·√m) of neat and cured bulk epoxy resins prepared via route B

Modifier	1.5 wt.%	2.5 wt.%	5 wt.%
Neat		0.38 ± 0.05	
EB-1	0.62 ± 0.03	0.70 ± 0.06	0.81 ± 0.03
EB-2	0.88 ± 0.04	1.06 ± 0.02	1.13 ± 0.03
EB-3	0.78 ± 0.05	0.81 ± 0.03	0.93 ± 0.04
EB-4	0.74 ± 0.06	0.78 ± 0.02	0.89 ± 0.03

From the low magnification SEM images (Figure B5 (a2-d2)), we can clearly see a higher roughness associated with the EB-3 cylindrical (Figure B5 (c2)) and EB-2 wormlike (Figure B5 (b2)) micelles modified epoxies, when compared with the relatively smoother fracture surface of EB-4 spherical micelle (Figure B5 (d2)) modified epoxies. The ill-defined EB-1 micelles give a smooth, almost featureless fracture surface (Figure B5 (a2)).

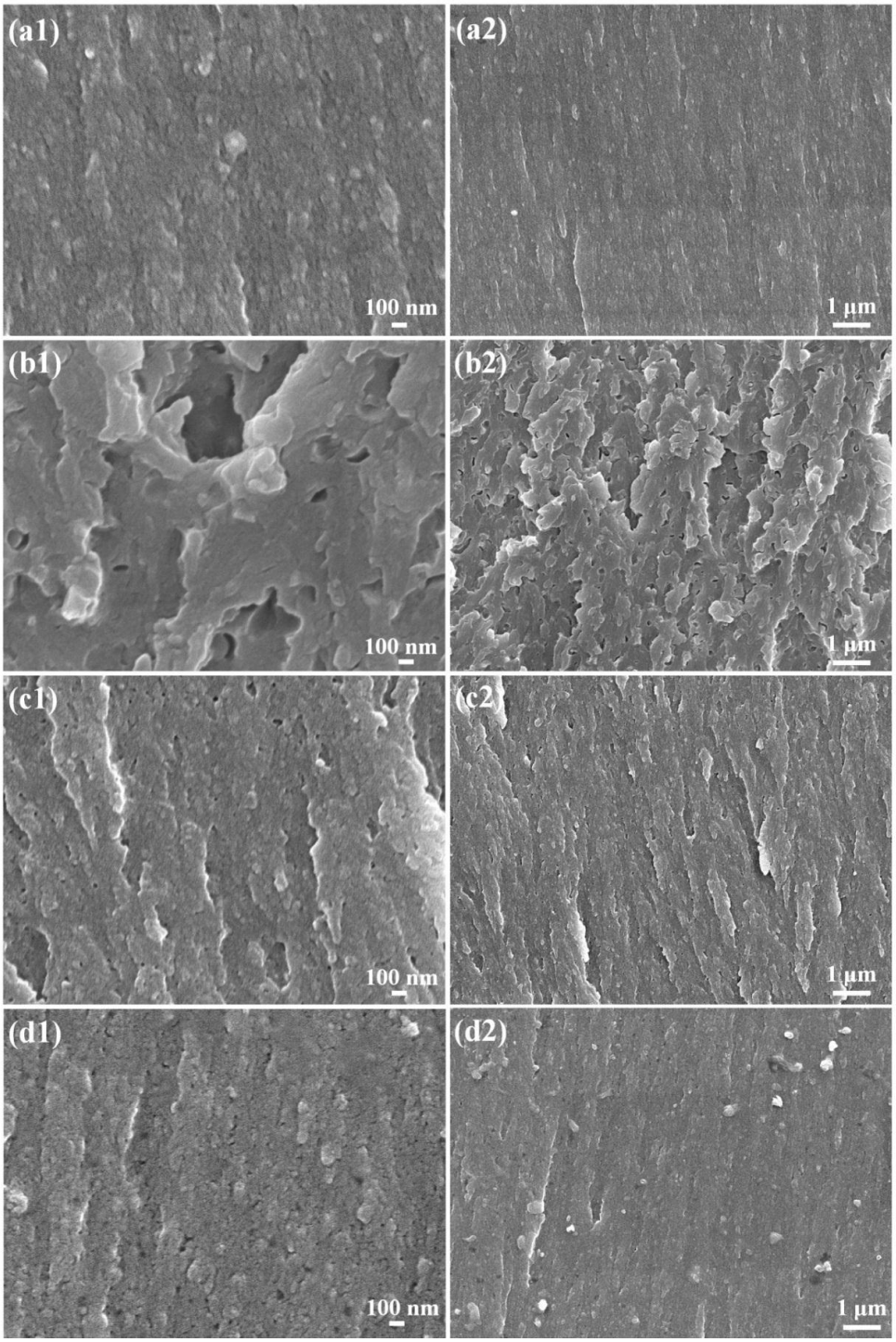

Figure B5 Representative SEM images of cured bulk epoxy resins containing (a1 – a2) EB-1, (b1 – b2) EB-2, (c1 – c2) EB-3, and (d1 – d2) EB-4. The block copolymer concentration is 5 wt.% for all cases.

Appendix C

Supporting Information for Chapter 5

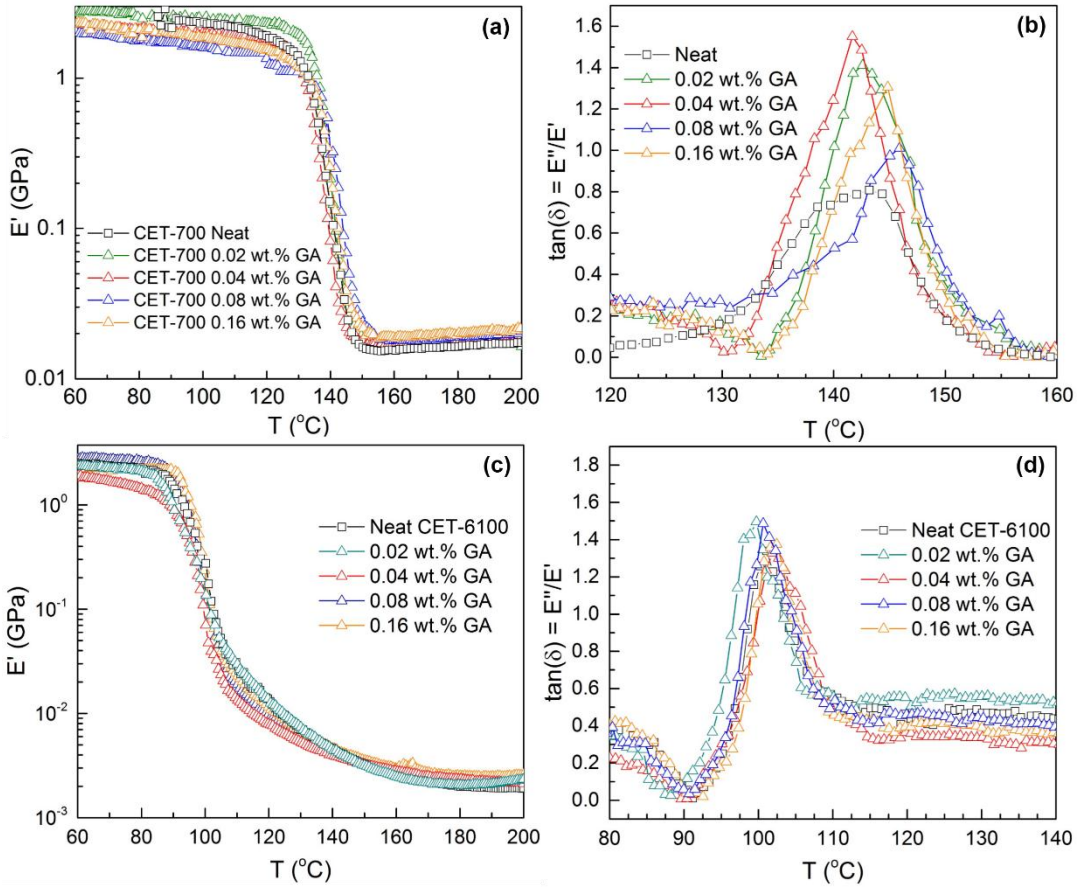

Figure C1 Representative data plots from DMA showing the tensile storage modulus (a, c) and tan δ (b, d) as functions of temperature for GA/epoxy binary composites. (a, d) are for the epoxy network with a theoretical M_c = 700 g/mol, (c, d) are for the network with theoretical M_c = 6100 g/mol.

Appendix C

Table C1. Summary of thermo-mechanical properties, experimental crosslink densities, thermal and mechanical properties of GA/epoxy binary composites.

ID	GA wt. %	DMA		ρ at 25 ℃ (g/cm^3)	Experimental M_c (g/mol)	DSC	Elastic modulus at 25 ℃ (GPa)
		E_r at 180 ℃ (MPa)	T_g by max tan δ (℃)			T_g (℃)	
700	0	16.8 ± 5.1	143 ± 2	1.203	587 ± 178	141 ± 2	2.75 ± 0.06
	0.02	17.1 ± 1.9	143 ± 1	1.258	603 ± 68	143 ± 3	2.77 ± 0.03
	0.04	17.9 ± 3.9	142 ± 4	1.214	556 ± 122	144 ± 1	2.80 ± 0.08
	0.08	18.9 ± 8.6	146 ± 3	1.293	560 ± 256	141 ± 2	2.90 ± 0.06
	0.16	19.7 ± 4.5	142 ± 2	1.305	543 ± 125	141 ± 2	3.00 ± 0.10
1050	0	8.6 ± 1.9	117 ± 2	1.320	1256 ± 283	115 ± 3	2.68 ± 0.10
	0.04	10.3 ± 4.3	117 ± 3	1.295	1032 ± 432	115 ± 2	2.69 ± 0.08
3050	0	3.4 ± 0.4	105 ± 1	1.189	2849 ± 341	103 ± 2	2.63 ± 0.07
	0.04	3.6 ± 0.8	108 ± 2	1.116	2531 ± 570	105 ± 3	2.70 ± 0.04
6100	0	2.0 ± 0.3	101 ± 2	1.242	5063 ± 740	100 ± 1	2.60 ± 0.05
	0.02	2.1 ± 0.5	100 ± 3	1.253	4886 ± 1100	100 ± 2	2.66 ± 0.07
	0.04	2.2 ± 0.7	102 ± 1	1.307	4957 ± 1558	100 ± 2	2.71 ± 0.06
	0.08	2.3 ± 0.4	101 ± 4	1.328	4711 ± 860	101 ± 1	2.81 ± 0.11
	0.16	2.5 ± 1.1	103 ± 3	1.352	4395 ± 1889	99 ± 3	2.89 ± 0.09

Appendix C

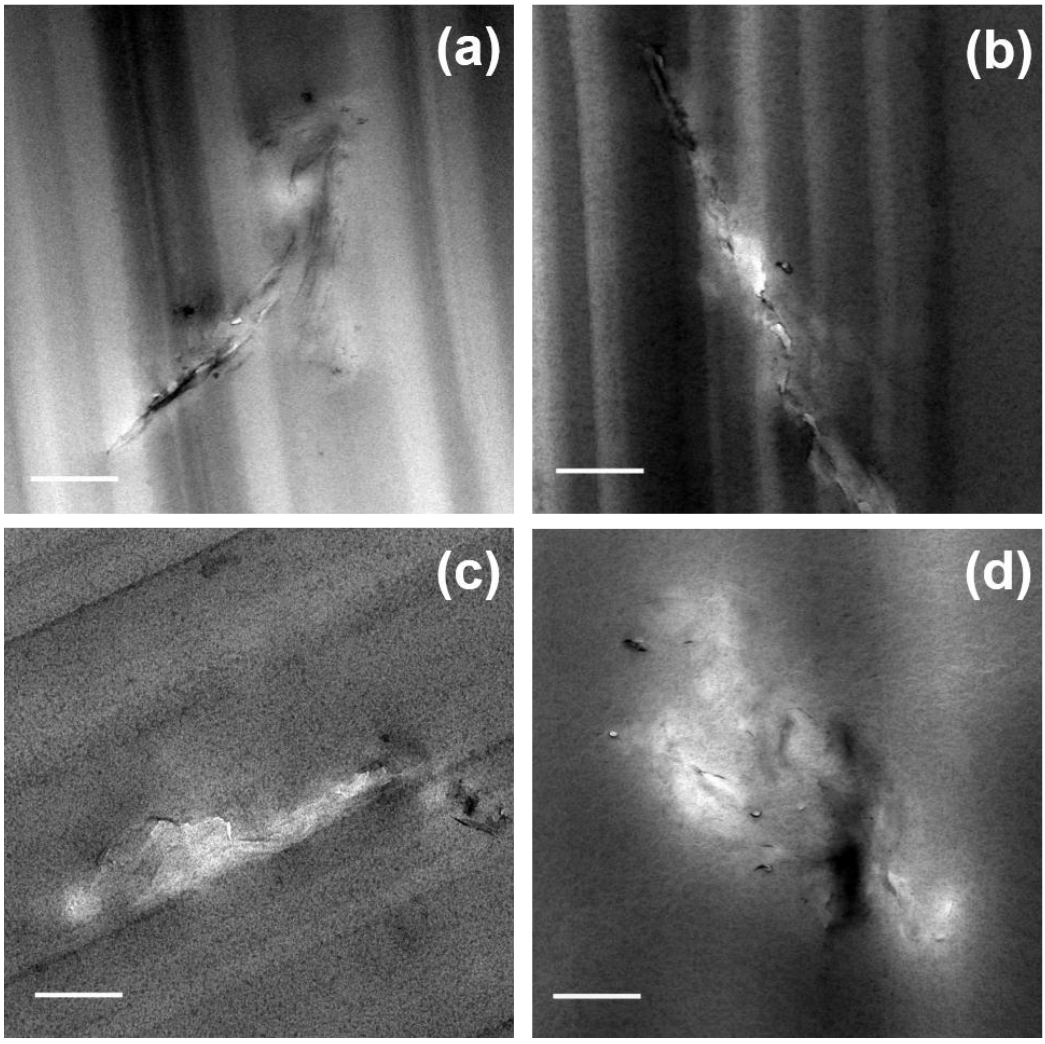

Figure C2 Representative TEM images of cured epoxy/GA binary composites with the theoretical crosslink density (a) M_c = 700g/mol, (b) M_c = 1550 g/mol, (c) M_c = 3050 g/mol, (d) M_c = 6100 g/mol. The loading of GA is 0.04 wt.% in all cases. Scale bars represent 0.5 μm.

Appendix C

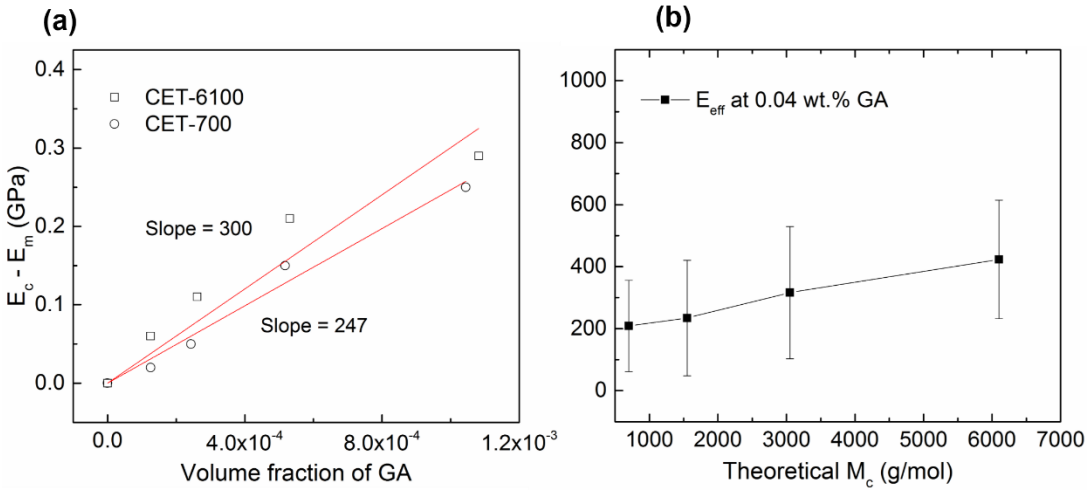

Figure C3 (a) Increment in the elastic modulus (E_c – E_m) of GA/epoxy binary composites relative to neat epoxy modulus (E_m) as a function of the GA volume fraction. Linear regressions of the data provide the effective modulus, E_{eff}, of the GA modifier in binary composites, as 250 GPa for CET-700, and 303 GPa for CET-6100, respectively. (b) E_{eff} of binary composites with 0.04 wt.% GA as a function of the matrix crosslink density. All values of E_{eff} were calculated according to equation (5.3) based on the data listed in Table C1. The solid line is to guide the eye

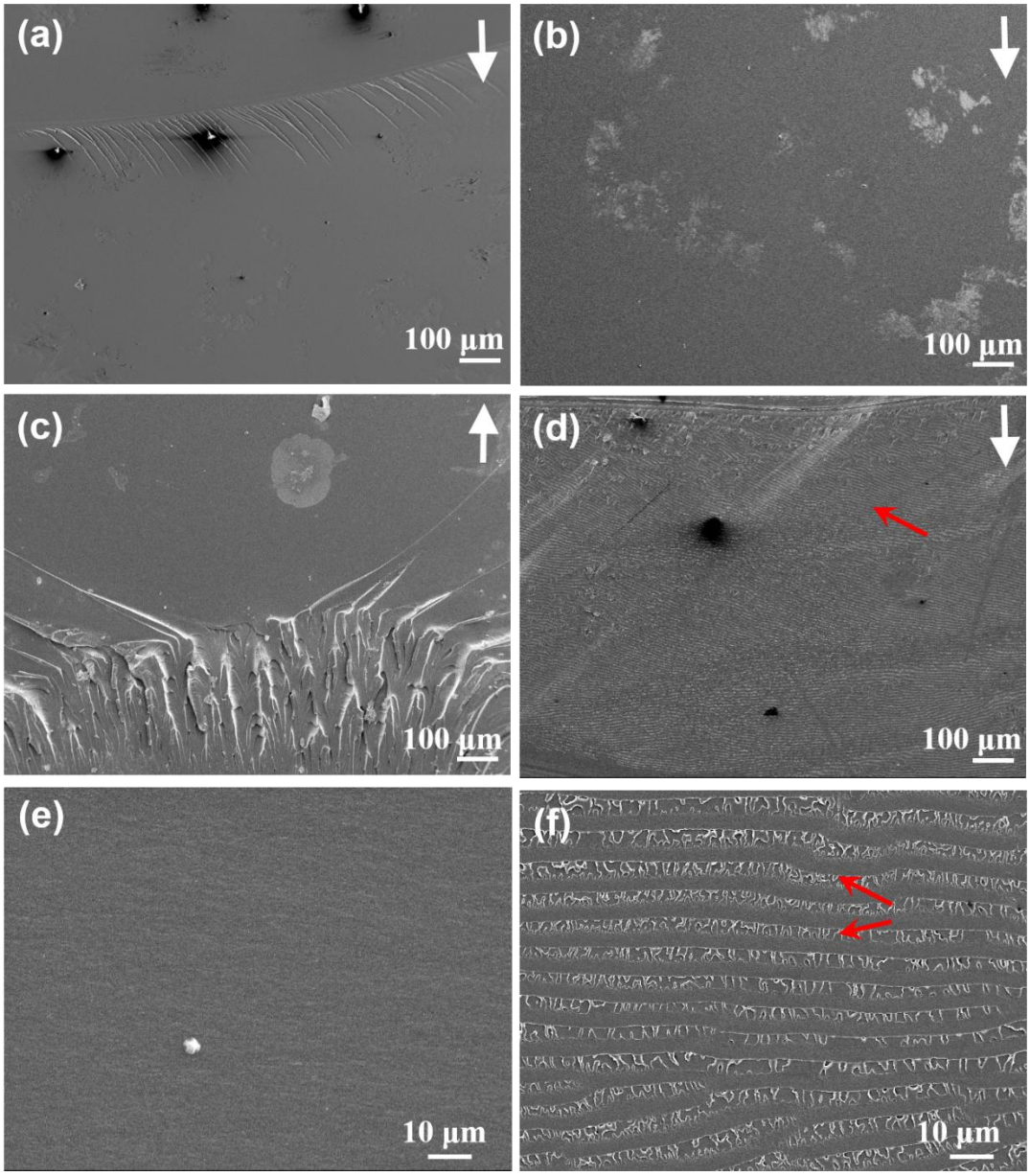

Figure C4 SEM fractographs of neat epoxies with varying theoretical crosslink densities (a) M_c = 700 g/mol, (b) M_c = 1550 g/mol, (c) M_c = 3050 g/mol, (d) M_c = 6100 g/mol. (e) and (f) are the zoomed-in micrographs of images (a) and (d), respectively. White arrows indicate the crack propagation direction. The red arrows in (d) and (f) denote the crack-arrest lines in the neat CET-6100 epoxy.

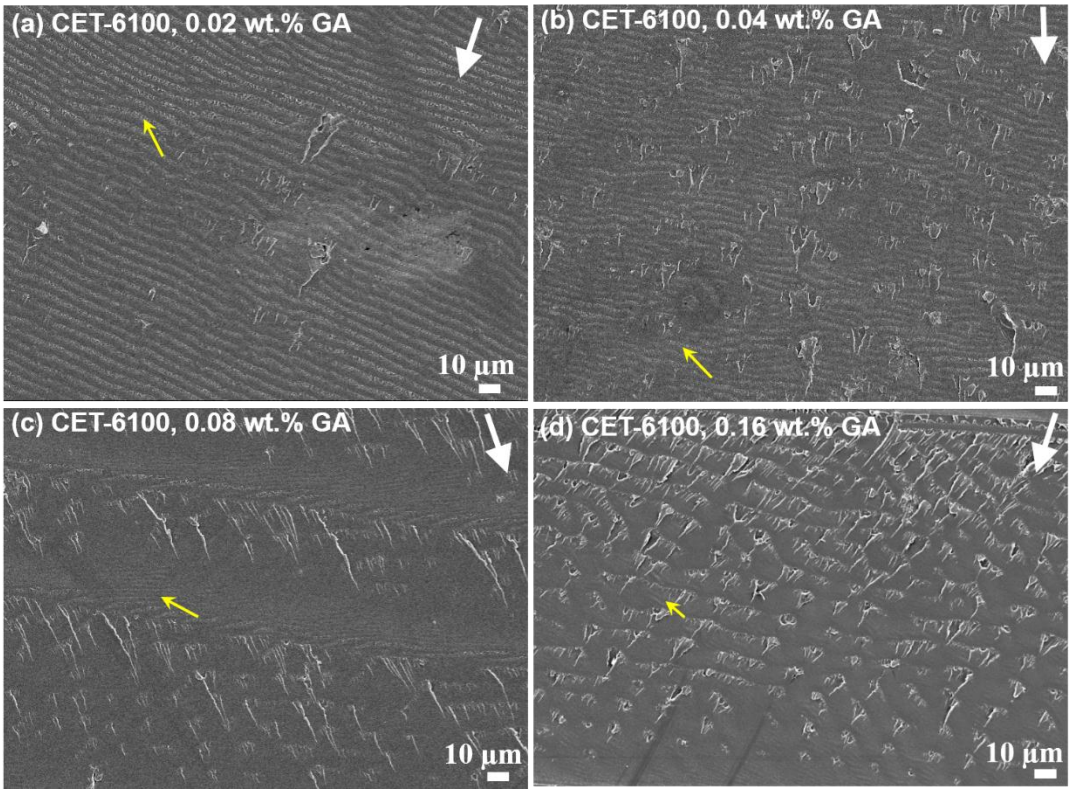

Figure C5 SEM fractographs of epoxy/GA binary composites with theoretical M_c = 6100 g/mol containing different amount of GA (a) 0.02 wt.%, (b) 0.04 wt.%, (c) 0.8 wt.%, and (d) 0.16 wt.%. White arrows indicate the crack propagation direction. Yellow arrows denote the crack arresting lines.

Appendix C

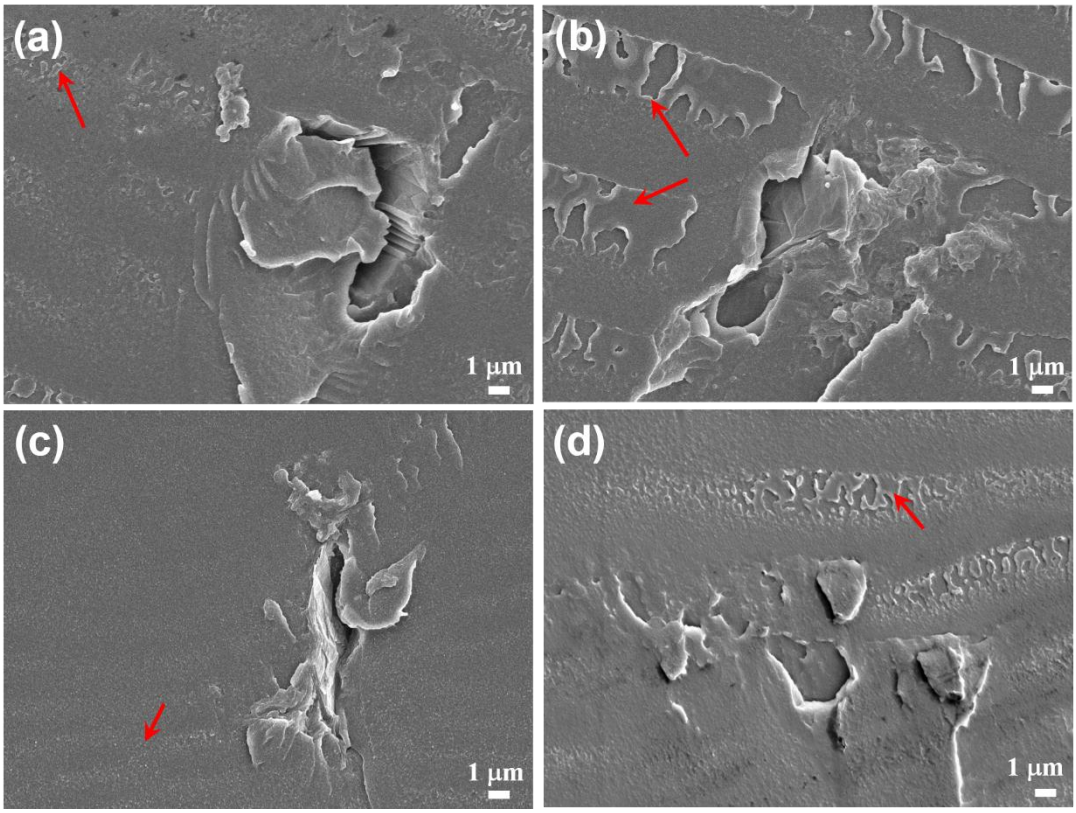

Figure C6 SEM fractographs of epoxy/GA binary composites with theoretical M_c = 6100 g/mol containing different amount of GA (a) 0.02 wt.%, (b) 0.04 wt.%, (c) 0.8 wt.%, and (d) 0.16 wt.%. Red arrows indicate the crack-arrest lines.

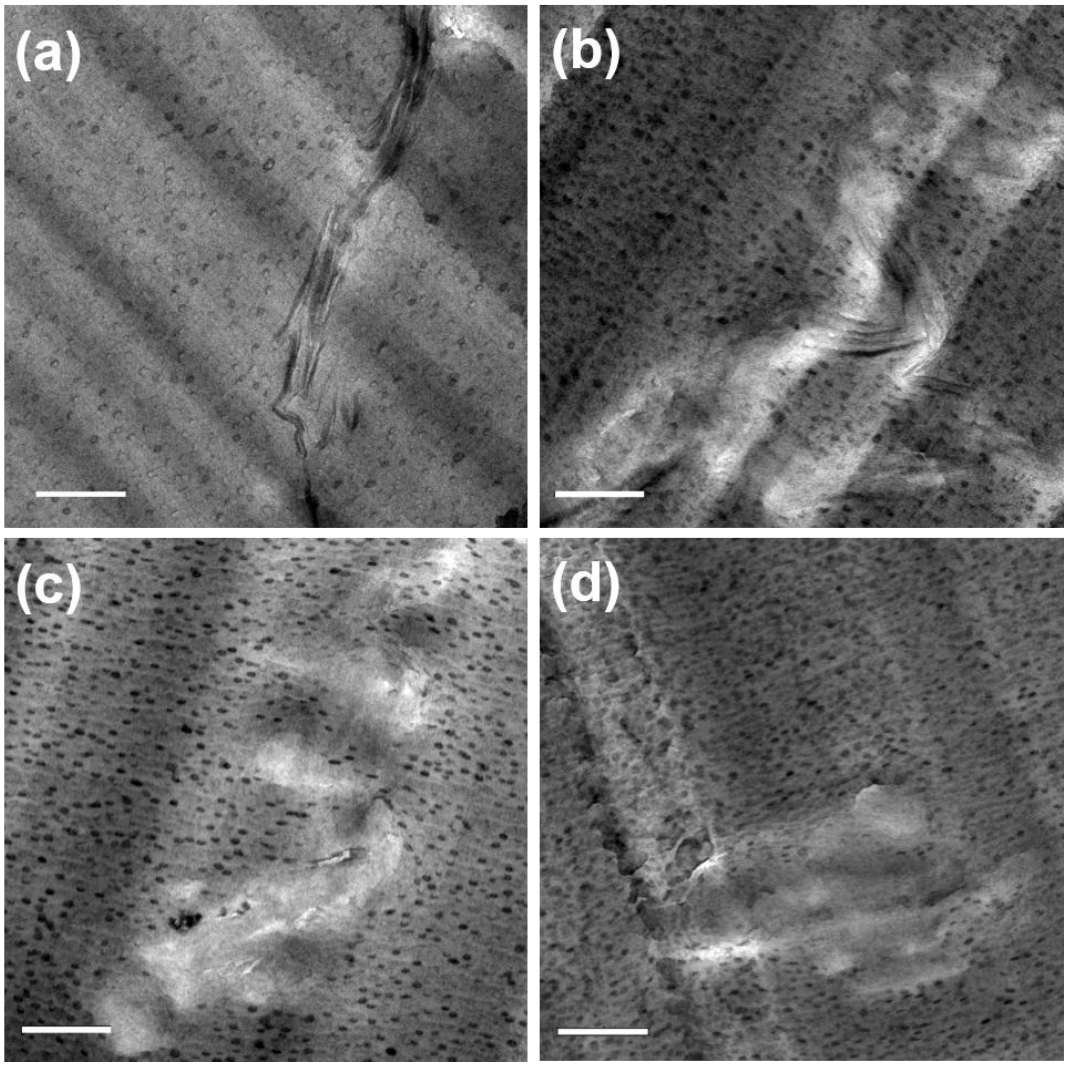

Figure C7 Representative TEM images of cured GA/OP/epoxy ternary composites with the theoretical M_c (a) 700g/mol, (b) 1550 g/mol, (c) 3050 g/mol, (d) 6100 g/mol. The loading of GA is 0.04 wt.% and the loading of OP is 5 wt.% in all cases. RuO_4, used as a contrast agent, preferentially stains the PEO/epoxy interface, making relatively brighter PEP cores with darker PEO coronas. Scale bars represent 0.5 μm.

Appendix C

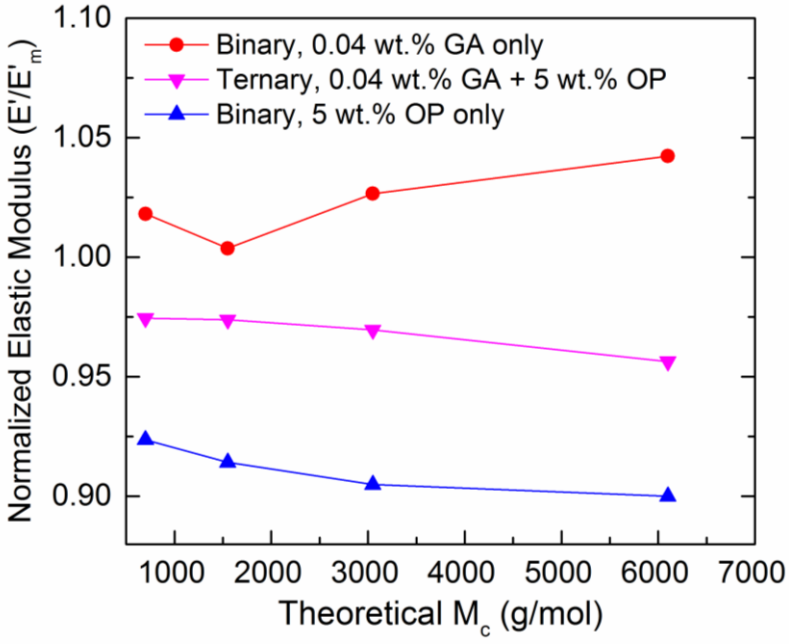

Figure C8 Normalized elastic moduli at 25 ℃ for cured composites as functions of the theoretical crosslink density of the epoxy network. For binary composites, the modifier is only 0.04 wt.% GA (●) or only 5 wt.% OP (▲). Ternary composites (▼) contain both 0.04 wt.% GA and 5 wt.% OP. All normalized values are relative to the moduli of associated neat epoxy resins. Solid lines are guide for the eye.

Appendix C

Table C2. Summary of thermo-mechanical properties, experimental crosslink densities, thermal and mechanical properties of GA/OP/epoxy ternary composites.

ID	Modifier Loading (wt.%)		DMA		ρ at 25 ℃ g/cm^3	Experimental M_c g/mol	DSC	Elastic modulus at 25 ℃ (GPa)
	GA	OP	E_r at 180 ℃ (MPa)	T_g by max tan δ (℃)			T_g (℃)	
700	0	0	16.8±5.1	143±2	1.203	587±178	141 ±2	2.75 ±0.06
		0.04	15.8±3.7	144±1	1.208	626±145	141 ±2	2.74 ±0.09
		0.4	15.7±3.2	141±2	1.176	614±126	140 ±1	2.69 ±0.10
		5	15.0±4.6	141±3	1.087	594±181	146 ±3	2.54 ±0.09
	0.04	0.04	16.6±3.3	144±1	1.251	617±124	142 ±1	2.75 ±0.08
		0.4	15.6±2.8	143±2	1.199	630±112	141 ±2	2.71 ±0.05
		5	15.4±4.1	141±2	1.189	632±169	144 ±3	2.68 ±0.10
1550	0	0	8.6±1.9	117±2	1.320	1256±283	115 ±3	2.68 ±0.10
		5	9.5±2.1	116±4	1.230	1058±238	114 ±1	2.45 ±0.07
	0.04	5	9.7±2.7	116±2	1.260	1064±294	115 ±1	2.61 ±0.10
3050	0	0	3.4±0.4	105±1	1.189	2849±341	103 ±2	2.63 ±0.07
		5	3.4±0.8	106±3	1.127	2691±606	105 ±1	2.38 ±0.07
	0.04	5	3.7±0.7	105±2	1.187	2663±500	104 ±2	2.55 ±0.13
6100	0	0	2.0±0.3	101±2	1.242	5063±740	100 ±1	2.60 ±0.05
		0.04	2.0±0.5	99±1	1.150	4709±1060	99 ±1	2.58 ±0.06
		0.4	2.1±0.6	99±1	1.233	4857±1393	100 ±2	2.55 ±0.05
		5	2.1±0.4	103±4	1.194	4748±969	102 ±3	2.34 ±0.19
	0.04	0.04	2.1±0.5	99±2	1.262	4924±1108	100 ±2	2.59 ±0.05
		0.4	1.9±0.4	98±2	1.237	5334±1201	98 ±1	2.57 ±0.08
		5	2.1±0.5	101±3	1.207	4664±1050	102 ±2	2.51 ±0.10

Appendix C

Table C3. Summary of the K_{Ic} and G_{Ic} of cured ternary composites with different network crosslink densities and modifier loadings.

Sample	Modifier Loading (wt.%)		K_{Ic} (MPa $\sqrt{m}$)	G_{Ic} (J/m^2)
	GA	OP		
CET-700	0	0	0.86 ± 0.07	238 ± 39
		0.04	1.03 ± 0.10	342 ± 67
		0.4	1.24 ± 0.12	506 ± 100
		5	1.49 ± 0.18	773 ± 189
	0.04	0	0.96 ± 0.08	291 ± 49
		0.04	1.16 ± 0.13	433 ± 98
		0.4	1.43 ± 0.07	667 ± 66
		5	1.65 ± 0.13	898 ± 145
CET-6100	0	0	0.94 ± 0.06	301 ± 39
		0.04	1.10 ± 0.14	415 ± 106
		0.4	1.38 ± 0.07	660 ± 68
		5	3.05 ± 0.18	3516 ± 504
	0.04	0	1.26 ± 0.11	518 ± 91
		0.04	1.33 ± 0.10	604 ± 92
		0.4	1.57 ± 0.13	848 ± 143
		5	3.86 ± 0.40	5250 ± 1108
CET-1550	0	0	0.83 ± 0.07	227 ± 39
		5	2.10 ± 0.12	1592 ± 188
	0.04	0	1.07 ± 0.12	376 ± 85
		5	2.38 ± 0.15	1919 ± 253
CET-3050	0	0	0.91 ± 0.03	278 ± 20
		5	2.75 ± 0.15	2810 ± 318
	0.04	0	1.12 ± 0.08	411 ± 59
		5	3.20 ± 0.31	3551 ± 712

Appendix C

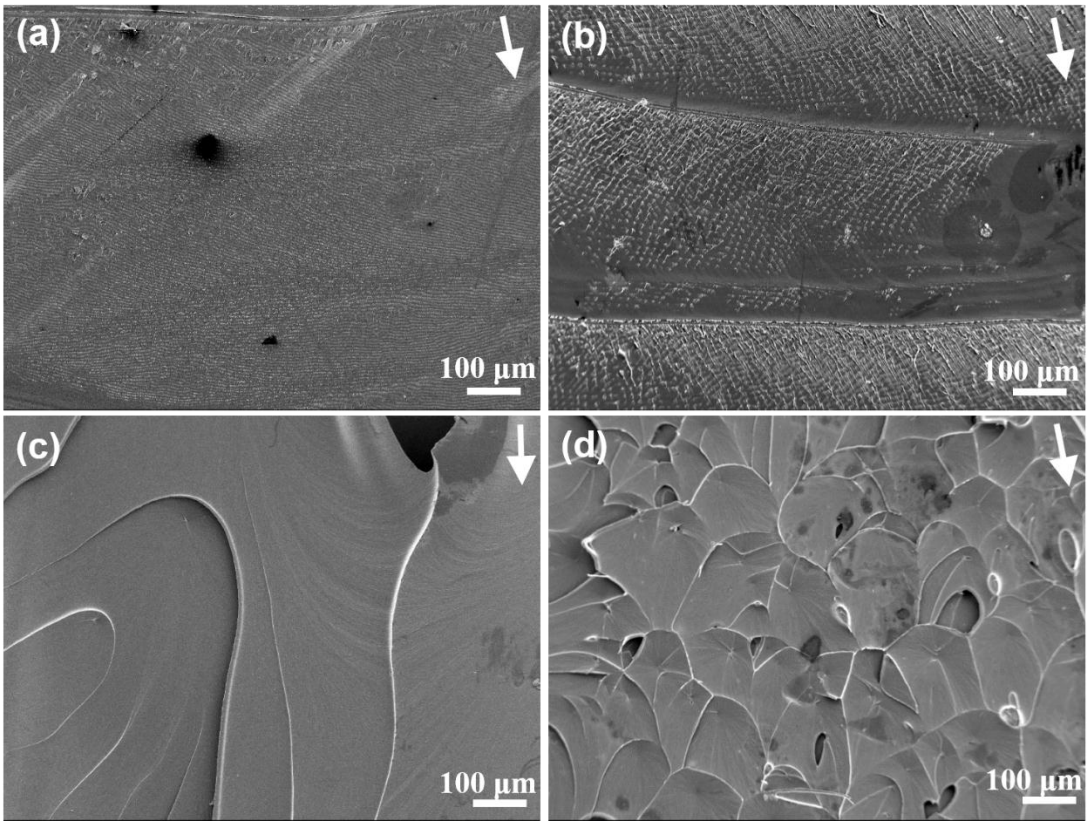

Figure C9 Zoomed-out SEM fractographs of (a) neat epoxy, (b) GA/epoxy binary composites with 0.04 wt.% GA; (c) OP/epoxy binary composites with 5 wt.% OP; (d) GA/OP/epoxy ternary composites with 0.04 wt.% GA and 5 wt.% OP. The epoxy network has the theoretical M_c = 6100 g/mol in all cases. White arrows indicate the crack propagation direction.

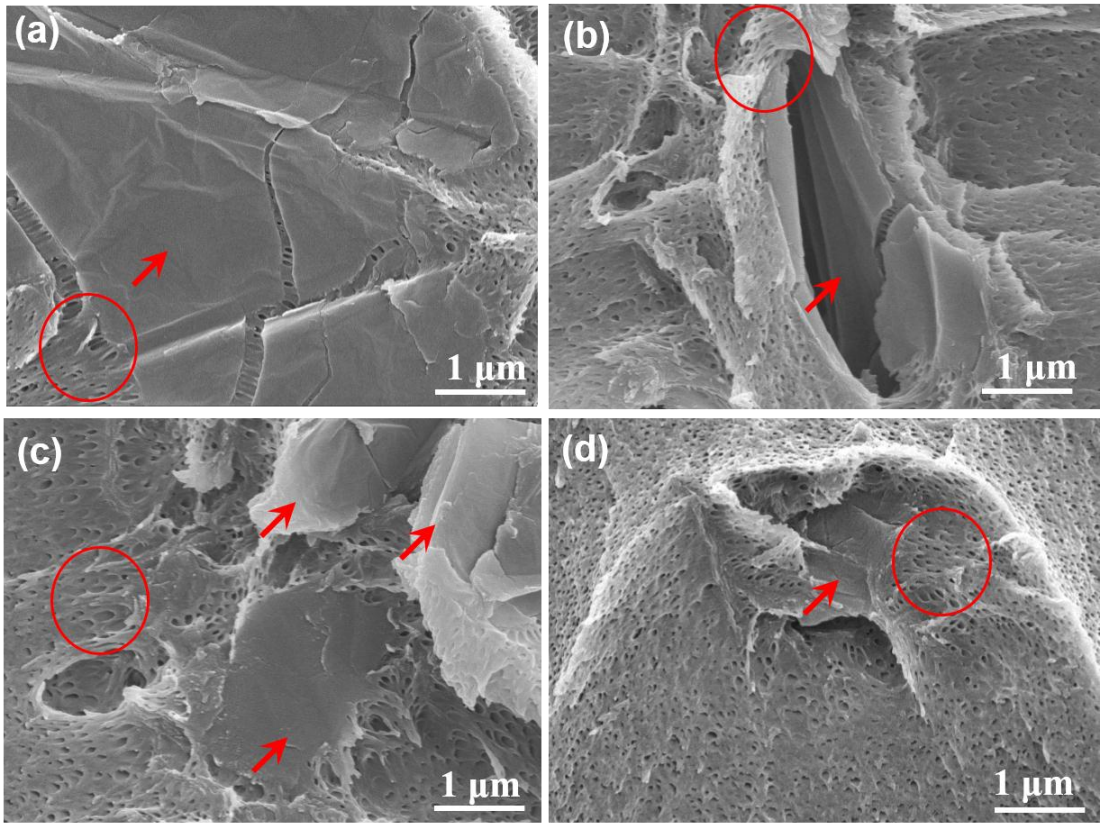

Figure C10 SEM fractographs of GA/OP/epoxy ternary composites with 0.04 wt.% GA and 5 wt.% OP. The epoxy network is the CET-6100 resin in all cases. The red arrows denote the GA particles. The red circles in highlight the micelle holes being stretched.

Appendix C

Table C4. Summary of the maximum synergistic toughening effect in epoxy-based ternary composites from the literature.

Ref	Modifier type, size and loading		[a]ΔK_{Ic}					[b]ΔG_{Ic}				
	Rigid additive	Soft additive	Rigid binary	Soft binary	[c]Additive	Ternary	Synergy (%)[d]	Rigid binary	Soft binary	[c]Additive	Ternary	Synergy (%)[d]
This work	GA, 0.04 wt.%	OP, 5 wt.%	0.34	2.24	2.58	3.11	121	0.72	10.7	11.4	16.5	145
221	Silica NP, d ~ 20nm, 14.8 wt.%	CTBN, 9 wt.%	1.19	0.88	2.07	2.71	131	2.94	3.31	6.25	13.4	214
214	Silica NP, 20 nm, 5 wt.%	CTBN, 18 wt.%	0.65	1.38	2.03	2.09	103	--	--	--	--	--
215	Silica, 5 µm, 30 vol.%	PMMA-PBA diblock copolymer, 5 phr	0.88	0.44	1.32	1.38	105	--	--	--	--	--
218	Silica NP, 20 nm, 15 wt.%	CTBN, 9 wt.%	0.63	1.84	2.47	2.51	102	1.48	7.71	9.19	11.5	125
284	Silica NP, 20 nm, 10 wt.%	CTBN, 10 wt.%	0.52	0.73	1.25	1.28	102	1.03	2.35	3.38	4.49	133
221	Interclated organoclay, agglomerates < 1 µm, 5 wt.%	PPO-PEO diblock, 50-200 nm, 10 wt.%	0.59	0.91	1.50	1.60	107	--	--	--	--	--
222	clay < 1 µm, 6phr	CTBN, 20 phr	0.72	0.55	1.27	1.14	90	1.8	2.75	4.55	6	132

284	Halloysite clusters < 1 μm, 10 wt.%	CTBN, 10 wt.%	0.49	0.73	1.22	1.28	105	1.09	2.35	3.44	4.72	137

[a,b] ΔK_{Ic} (or ΔG_{Ic}) is defined according to Equation (5.8). From each reference, only the largest increase in the toughness of the ternary systems has been reported, and the associated modifier loadings are also listed. The toughness values for the binary systems correspond to the composites containing the listed modifier loadings.

[c] The additive toughening results are estimated based on Equation (5.9).

[d] The synergy is defined as the relative difference between the ternary results and the additive toughening results. Specifically, the ternary value is divided by the additive toughening value, and then the resultant number subtracts one, followed by multiplying 100.